DESIGN AND DEVELOPMENT OF ECM-INSPIRED PEPTIDE-BASED NANOSTRUCTURES FOR BIOENGINEERING AND BIOMEDICINE

A DISSERTATION SUBMITTED TO

THE GRADUATE SCHOOL OF ENGINEERING AND SCIENCE

OF BILKENT UNIVERSITY

IN PARTIAL FULFILLMENT OF THE REQUIREMENTS FOR

THE DEGREE OF

DOCTOR OF PHILOSOPHY

IN

MATERIALS SCIENCE AND NANOTECHNOLOGY

By

ELİF ARSLAN

August 2017

DESIGN AND DEVELOPMENT OF ECM-INSPIRED PEPTIDE-BASED NANOSTRUCTURES FOR BIOENGINEERING AND BIOMEDICINE

By Elif Arslan

August 2017

We certify that we have read this dissertation and that in our opinion it is fully adequate, in scope and in quality, as a dissertation for the degree of Doctor of Philosophy.

Ayşe Begüm Tekinay (Advisor)

Yusuf Şükrü Çağlar

Aykutlu Dana

Çağlar Elbüken

Melih Önder Babaoğlu

Approved for the Graduate School of Engineering and Science:

Ezhan Karaşan

Director of the Graduate School

ABSTRACT

DESIGN AND DEVELOPMENT OF ECM-INSPIRED PEPTIDE-BASED NANOSTRUCTURES FOR BIOENGINEERING AND BIOMEDICINE

Elif Arslan

Ph.D. in Materials Science and Nanotechnology

Advisor: Ayşe Begüm Tekinay

August 2017

Advances in understanding of cell-matrix interactions and the regulation of cellular behaviors through nanobiotechnological tools have presented new perspectives for regenerative medicine. Peptide amphiphiles have been used as building blocks for development of bioactive synthetic nanofiber scaffolds for regenerative medicine applications. Biocompatibility, tailorable characteristics, and mechanical stability as well as bioactivitiy of these peptide nanostructures make them ideal candidates for biomedical applications.

To guide natural cellular activities, biomaterials should provide a microenvironment similar to that experienced by cells under natural conditions. The native extracellular matrix (ECM) not only provides a suitable physical environment but also incorporates the necessary set of biochemical and mechanical signals to ensure the normal function of cells, as well as mediating their differentiation, morphogenesis

and homeostasis by providing biological, physical, and chemical recognition signals that can trigger specific interactions with cell surface receptors.

In this thesis, different ECM-mimetic peptide nanofiber formulations were designed and developed, which were shown to have superior chondrogenic and therapeutic effect on stem cell differentiation *in vitro* and cartilage regeneration *in vivo*. Hence, the synthetic peptide nanomaterials harbor great promise in mimicking specific ECM molecules as therapeutic agents and model systems.

Keywords: Extracellular matrix, peptide nanofiber, mesenchymal stem cell, cartilage regneration, bioactive scaffold

ÖZET

BİYOMÜHENDİSLİK VE BİYOTIP UYGULAMALARI İÇİN HÜCRELER ARASI MATRİKSDEN ESİNLENİLEN PEPTİT NANOYAPILARIN TASARIMI VE GELİŞTİRİLMESİ

Elif Arslan

Malzeme Bilimi ve Nanoteknoloji, Doktora

Tez Danışmanı: Ayşe Begüm Tekinay

Ağustos, 2017

Nanobiyoteknolojik gelişmeler hücre-matriks etkileşimlerinin anlaşılmasında ve hücresel davranışların düzenlenmesinde rejeneratif tıp için yeni perspektifler sunmaktadır. Peptit amfifiller, rejeneratif tıp uygulamalarında biyoaktif sentetik nanofiber iskele geliştirilmesi için yapı taşları olarak kullanılmaktadır. Bu peptit esaslı nanoyapılardaki biyolojik uyumluluk, uyarlanabilir yapı ile mekanik stabilite ve biyolojik aktiviteler daha ileri klinik uygulamalar için ideal adaylar olmalarını sağlamaktadır. Doğal hücresel aktiviteleri yönlendirmek için, biyomalzemeler, doğal koşullar altında hücrelerin yaşadığı ortamlara benzer bir mikro ortam sağlamalıdır. Doğal hücre dışı matris (ECM) hem uygun bir fiziksel ortam sağlar hem de hücrelerin normal işlevini sağlamak için hücre yüzey reseptörleri ile spesifik etkileşimleri tetikleyebilen gerekli biyokimyasal ve mekanik sinyaller ile biyolojik,

fiziksel ve kimyasal tanıma sağlayarak farklılaşma, morfogenez ve homeostazın arabuluculuğunu yapar. Bu tezde, *in vitro* kök hücre farklılaşması ve *in vivo* kıkırdak rejenerasyonu üzerinde kondrojenik ve terapetik etkiye sahip oldukları gösterilen farklı ECM-benzeri peptit nanofiber formülasyonları tasarlanmış ve geliştirilmiştir. Dolayısıyla, sentetik peptit nanomalzemeler, spesifik ECM moleküllerini taklit ederek ilaç ve model sistemler olarak kullanılmak açısından büyük önem taşımaktadırlar.

Anahtar kelimeler: hücrelerarası matris, peptit nanofiber, mezenkimal kök hücre, kıkırdak rejenerasyonu, biyoaktif iskele

Acknowledgement

I would like to express my sincere gratitude to my advisor Prof. Ayşe Begüm Tekinay for her guidance and support to my PhD study. Her encouragement helped me develop my scientific perspective that I can carry with me throughout my professional career. I would like to thank Prof. Mustafa Özgür Güler for his scientific support during my studies. I would also like to acknowledge my jury members for their contributions to my thesis.

I would like to acknowledge the PhD scholarship and funding from TÜBİTAK (The Scientific and Research Council of Turkey) BIDEB 2211-A, 111M710, and 114S913. I would also thank to international conference supports of TÜBİTAK (in the form of 2224-A).

I would like to express my most sincere thanks to my dearest Dr. ☺ friends: Dr. Berna Şentürk, Dr. Gülcihan Gülseren, and Dr. Gülistan Tansık. I am very glad to have their lifelong friendship which has kept me motivated during this long journey. In addition, I would like to extend my special thanks to Prof. Dr. Şükrü Çağlar, Prof. Dr. Hüseyin Özkan, Dr. İhsan Doğan, Dr. Cemil Kılınç, Özge Uysal, Begüm Dikeçoğlu, Meryem Hatip Koç, Alper Devrim Özkan, Ahmet Emin Topal, Çağla Eren Çimenci, Dr. Melis Şardan Ekiz, and Dr. Seher Yaylacı for their fruitful collaborations. Especially, I would like to express my special thanks to Özge Uysal who is one of the best master students of our group, and I believe she would be great PhD student in EPFL as well. Moreover, I would also thank to my AFM partner Begüm Dikeçoğlu who achieved the difficult analyses that no one done before.

I would like to acknowledge my ODTU-friends Ceren Yaşa, Öncay Yaşa, Yasin Tümtaş, and Didem Mumcuoğlu. We have started to this long journey together after our graduation from ODTU. The first 2.5 years before they spread to Europe, we shared a lot of memories in UNAM that we will remember through all our life.

I would like to acknowledge my previous and present lab members Dr. Hakan Ceylan, Dr. Büşra Mammadov, Dr. Aref Khalily, Dr. Melike Sever, Dr. Ruslan Garifullin, Nuray Gündüz, Dr.Rashad Mammadov, Melis Göktaş, Mustafa Beter, Hepi Hari Susapto, Aygül Zengin, Nurcan Haştar, Idil Uyan, Merve Şen, Canelif Yılmaz, Zeynep Orhan, Gökhan Günay, Dr. Ashif Shaikh, Dr. Özlem Erol, and Dr. Göksu Çınar, for creating such a warm working environment. I would like to thank Suna Temiz who is smiley face of UNAM and always has cheered me up whenever I saw her. I would also thank to Zeynep Erdoğan for her technical help.

I would like to express my most sincere gratitude to my lovely family for their endless love, motivation, encouragement, support, and belief in me. I would not be where I am today without them. Thank you so much for everything. I dedicated this thesis to my beloved parents.

Contents

ABSTRACT ..... **iii**

ÖZET ..... **v**

Acknowledgement ..... **vii**

List of Figures ..... **xiv**

List of Tables ..... **xxvii**

Abbreviations ..... **xxviii**

Chapter 1. Introduction: Bioinspired Materials for Regenerative Medicine **1**

1.1 Extracellular Matrix Mimetic Scaffolds **1**

1.1.1 Self Assembling Peptide Nanofibers as ECM Mimetic Scaffolds 4

1.2 Induction of Chondrogenesis and Cartilage Regeneration Through Self Assembling Peptide Nanofibers **7**

1.2.1 Cartilage Structure 8

1.2.2 Cartilage Diseases 12

1.2.3 Cartilage Tissue Regeneration with Peptide Nanofibers 14

Chapter 2. Glycosaminoglycan-mimetic signals direct the osteo/chondrogenic differentiation of mesenchymal stem cells in a three-dimensional peptide nanofiber extracellular matrix mimetic environment **17**

2.1 Objective **17**

2.2 Introduction **18**

2.3 Experimental Section **22**

2.3.1 Materials 22

2.3.2 Synthesis and characterization of peptide amphiphile molecules 22

2.3.2 Preparation and characterization of self-assembled peptide gels for 3D cell culture experiments 24
2.3.3 3D cell culture and maintenance 26
2.3.4 Viability analyses 27
2.3.5 Sulfated glycosaminoglycan deposition analysis 27
2.3.6 Gene and protein expression analysis 27
2.3.7 Statistical analysis 30
2.4 Results and Discussion 30
2.4.1 Design, preparation and characterization of self-Assembled PA molecules and 3D PA gels 30
2.4.2 3D peptide gels provide a biocompatible environment for MSCs 43
2.4.3 Stem cell differentiation can be directed into chondrogenic and osteogenic lineages in 3D peptide gels 46
2.4.4 Immunophenotypic characterization of stem cell differentiation into osteogenic and chondrogenic lineages 51
2.5 Conclusion 64
Chapter 3. Regenerative and Protective Effects of Peptide Amphiphile - Hyaluronic Acid Hybrid Nanofiber Membranes in *in vivo* Osteoarthritis Model… 65
3.1 Objective 65
3.2 Introduction 66
3.3 Experimental Section 69
3.3.1 Materials 69
3.3.2 Synthesis of peptide amphiphile molecules 70

3.3.3 Chemical characterizations of peptide amphiphiles by LC-MS 70

3.3.4 Preparation and characterization of self-assembled peptide amphiphile-HA hybrid nanofiber membrane 70

3.3.5 Morphological analysis of hybrid nanofiber membrane by TEM imaging..... 71

3.3.6 Secondary structure analysis of hybrid nanofiber membrane by CD ... 71

3.3.7 Mechanical analysis of hybrid nanofiber membrane by oscillatory rheology..... 71

3.3.8 Morphological analysis of hybrid nanofiber membrane by SEM imaging 72

3.3.9 Cell culture experiments 72

3.3.10 *In Vivo* osteoarthritis model in rat and intraarticular hybrid nanofiber membrane treatment..... 74

3.3.11 Histological and immunohistochemical stainings of tissue sections .. 76

3.3.12 Histological scoring 77

3.3.13 Statistical analysis 78

3.4 Results 78

3.4.1 Synthesis and characterization of hybrid nanofiber membranes..... 78

3.4.2 Hybrid nanofiber membrane provide a biocompatible microenvironment for MSC and chondrocyte culturing and encapsulation in 2D and 3D *in vitro* environments 83

3.4.3 Hybrid nanofiber membrane promotes the regeneration of defected cartilage tissue in osteoarthritic rat knees 86

3.5 Discussion..... 97

3.6 Conclusion 102

Chapter 4. Supramolecular Peptide Nanofiber Morphology Affects Mechanotransduction of Stem Cells 103

4.1 Objective 103

4.2 Introduction 104

4.3 Experimental Section 107

4.3.1 Materials 107

4.3.2 Synthesis of peptide amphiphile molecules 108

4.3.3 Chemical characterizations of peptide amphiphiles by LC-MS 109

4.3.4 Secondary structure analysis of peptide nanofibers by CD 109

4.3.5 Morphological analysis of peptide nanofibers by TEM 110

4.3.6 Morphological analysis of peptide nanofibers by SAXS 110

4.3.7 Molecular dynamics simulations of peptide nanofibers 112

4.3.8 Nanomechanical analysis of peptide nanofibers by AFM 114

4.3.9 Bulk mechanical analysis of peptide nanofibers by oscillatory rheology 114

4.3.10 Morphological analysis of peptide nanofibers by SEM 115

4.3.11 *In vitro* cell culture experiments 115

4.3.12 Viability assay 116

4.3.13 Adhesion analysis 116

4.3.14 Proliferation analysis 116

4.3.15 Spreading analysis 117

4.3.16 Gene expression analysis 117

4.3.17 Protein expression analyses by flow cytometry 118

4.3.18 Immunoblotting analysis of protein expression by western blotting 119

4.3.19 Immunocytochemical analyses of protein detection by confocal microscopy 120

4.3.20 Collagen adsorption analyses by ELISA..... 120

4.3.21 Statistical analysis 121

4.4 Results 121

4.4.1 Design, preparation and characterization of self-assembled PA molecule 121

4.4.2 Peptide nanofibers provide a biocompatible environment for cell culture 144

4.4.3 Cellular proliferation and spreading is mediated by nanofiber morphology and chirality 148

4.4.4 Effects of peptide nanofibers with different morphologies on the osteochondrogenic differentiation of MSCs 153

4.4.5 Scaffold-mediated structural and chiral regulation of mechanotransduction..... 158

4.5 Discussion..... 167

4.6 Conclusion..... 176

Chapter 5. Conclusion and Future Prospects..... 177

Bibliography 181

List of Figures

Figure 1. 1 Schematic representation ECM which is composed of two main types: interstitial and pericellular matrices. Interstitial matrices contain collagen fibrils, secreted proteoglycans (PGs), hyaluronic acid (HA), and other ECM proteins. These ECM macromolecules are associated with cells through receptors such as integrins, CD44, and DDRs (discoidin domain receptor). ECM components facilitate the presentation of growth factors (GF) to cells. Matrix degradation enzymes such as MMPs (matrix metalloproteases) are responsible for the turn over of the ECM (Reproduced from [7] with permission from Elsevier). 3

Figure 1. 2 Schematic illustration of biomaterial properties and their possible impact on cell fate (Reproduced from [1] with permission from John Wiley & Sons). 5

Figure 1. 3 Schematic representation of cartilage matrix surrounding chondrocytes with pericellular, territorial, interterritorial regions with essential macromolecules of ECM. Abbrevations: CS, chondroitin sulfate; KS, keratin sulfate; CILP-1, cartilage intermediate layer protein 1; PRELP, proline-arginine-rich leucine-rich repeat protein; COMP, cartilage oligomeric matrix protein. (Reproduced from [36] with permission from Nature Publishing Group). 11

Figure 1. 4 The normal knee joint and the joint with established osteoarthritis are shown with structural elements of each stages (Reproduced from [52] with permission from Nature Publishing Group). 14

Figure 2. 1 Chemical structures of peptide amphiphile molecules. GAG-PA: Lauryl-VVAGEGD-K (p-sulfobenzoyl)-S; E-PA: Lauryl-VVAGE, K-PA: Lauryl-VVAGK; RGD-PA: Lauryl-VVAGRGD. 31

Figure 2. 2 Liquid chromatogram and mass spectra of GAG-PA, $[M-H]^-$ (calculated) = 1224.58, $[M-H]^-$ (observed) = 1226.6042 (observed $[M-2H]^{-2}$ m/z = 613.6082)... 32

Figure 2. 3 Liquid chromatogram and mass spectra of E-PA, $[M-H]^-$ (calculated) = 654.4156, $[M-H]^-$ (observed) = 654.3952 (observed $[M-2H]^{-2}$ m/z = 326.6732 $[2M-H]^-$ m/z = 1309.8437). 33

Figure 2. 4 Liquid chromatogram and mass spectra of K-PA, $[M+H]^+$ (calculated) = 654.4840, $[M+H]^+$ (observed) = 654.4998 (observed $[M+2H]^{+2}$ m/z = 327.7529, $[2M+H]^+$ = 1307.9788). 33

Figure 2. 5 Liquid chromatogram and mass spectra of RGD-PA, $[M+H]^+$ (calculated) = 983.57, $[M+H]^+$ (observed) = 982.5619 (observed $[M+2H]^{+2}$ m/z = 490.7543). 34

Figure 2. 6 STEM images of GAG and E nanofibers, scale bar = 50 nm. (B) SEM images of GAG- and E-gels, scale bar = 5 μm. 35

Figure 2. 7 SEM images of GAG- and E-gels, scale bar = 5 μm. 36

Figure 2. 8 CD spectra of peptide amphiphile solutions and gels. 36

Figure 2. 9 Rheological analyses of peptide nanofiber gels and collagen I gel, ***$p<0.001$. Equilibrium moduli of the collagen I gel are significantly less than the equilibrium moduli of peptide nanofiber gels. 37

Figure 2. 10 Mechanical characterizations of PA gels by rheology. Equilibrium storage and loss moduli of GAG- and E-gels during time, frequency and strain sweeps. 39

Figure 2. 11 Mechanical characterizations of GAG- and E-gel niche after 1 day and 14 days of cell culturing. Equilibrium storage and loss moduli of GAG- and E- gels during (A) time sweep, (B) frequency sweep, and (C) strain sweep. 40

Figure 2. 12 SEM images of cells cultured within GAG- and E-gel niches at day 3, scale bar = 30 μm for GAG-gel and scale bar = 20 μm for E-gel..... 41

Figure 2. 13 Viability analyses of rMSCs within PA gel niches for 14 days (O.D. = optical density). 41

Figure 2. 14 Rheology analyses of peptide nanofiber gel niches incubated with cells for 1 day and 14 days. 42

Figure 2. 15 Confocal microscopy analyses of cellular localization within peptide nanofiber gels following 3 and 7 days of culture. Colored-scale bars show the depth of gel niches; the corresponding cellular localizations are shown in depth-dependent colors (using a red to blue scale for surface-to bottom depth). 42

Figure 2. 16 Viability analyses of stem cells in 3D PA gel niches and cells on tissue culture plate by Live/Dead assay. Green cells are live cells, and red cells are dead cells. 45

Figure 2. 17 Morphological tracking of cells in PA gel niches for 7 days, scale bars = 100 μm. (MT Media: 10% FBS containing growth media, Low FBS Media: 2% FBS containing media)..... 47

Figure 2. 18 Chondrogenic differentiation analyses by qRT-PCR. Expressions of Sox 9 and collagen II were quantified on days 3 and 7. 48

Figure 2. 19 Quantification of GAGs by dimethyl methylene blue (DMMB) assay on days 3 and 7 in both MT (10% FBS) and low FBS medium (Low FBS) (2% FBS). GAG concentrations were normalized to DNA. Error bars indicate SEM, n = 3, *$p<0.05$. 48

Figure 2. 20 Osteogenic differentiation analyses by qRT-PCR. Expressions of Runx 2 and collagen I were quantified on days 3 and 7. 49

Figure 2. 21 Flow cytometry analyses of cells in GAG-gel within both MT and low FBS media. (A) Cell population and corresponding gating are shown for both Runx-2 and isotype labeling cells in GAG-MT niches. (B) Fluorescence signaling for corresponding gated cell populations are shown for both Runx-2 and isotype labeling. Gating is applied for subtracting isotype labeling from Runx-2 labeled populations, and percent of remaining part is considered specifically stained with Runx-2 antibody. (C) Cell population and corresponding gating are shown for both Runx-2 and isotype labeling of cells in GAG-low FBS niches. (D) Fluorescence signaling for corresponding gated cell populations is shown for both Runx-2 and isotype labeling. Gating is applied for subtracting isotype labeling from Runx-2 labeled populations, and percent of remaining part is considered specifically stained with Runx-2 antibody..... 53

Figure 2. 22 Flow cytometry analyses of cells in E-gel within both MT and low FBS media. (A) Cell population and corresponding gating are shown for both Runx-2 and isotype labeling cells in E-MT niches. (B) Fluorescence signaling for corresponding gated cell populations is shown for both Runx-2 and isotype labeling. Gating is applied for subtracting isotype labeling from Runx-2 labeled populations, and percent of remaining part is considered specifically stained with Runx-2 antibody. (C) Cell population and corresponding gating are shown for both Runx-2 and isotype labeling of cells in E-gel in low FBS media. (D) Fluorescence signaling for corresponding gated cell populations is shown for both Runx-2 and isotype labeling. Gating is applied for subtracting isotype labeling from Runx-2 labeled populations, and percent of remaining part is considered specifically stained with Runx-2 antibody..... 55

Figure 2. 23 Flow cytometry analyses of cells in GAG-gel within both MT and low FBS media. (A) Cell population and corresponding gating are shown for both Sox-9 and isotype labeling cells in GAG-MT niches. (B) Fluorescence signaling for corresponding gated cell populations are shown for both Sox-9 and isotype labeling. Gating is applied for subtracting isotype labeling from Sox-9 labeled populations, and percent of remaining part is considered specifically stained with Sox-9 antibody. (C) Cell population and corresponding gating are shown for both Sox-9 and isotype labeling of cells in GAG-low FBS niches. (D) Fluorescence signaling for corresponding gated cell populations are shown for both Sox-9 and isotype labeling. Gating is applied for subtracting isotype labeling from Sox-9 labeled populations, and percent of remaining part is considered specifically stained with Sox-9 antibody. 57

Figure 2. 24 Flow cytometry analyses of cells in E-gel within both MT and low FBS media. (A) Cell population and corresponding gating are shown for both Sox-9 and isotype labeling cells in E-MT niches. (B) Fluorescence signaling for corresponding gated cell populations are shown for both Sox-9 and isotype labeling. Gating is applied for subtracting isotype labeling from Sox-9 labeled populations, and percent of remaining part is considered specifically stained with Sox-9 antibody. (C) Cell population and corresponding gating are shown for both Sox-9 and isotype labeling of cells in E-gel in low FBS media. (D) Fluorescence signaling for corresponding gated cell populations are shown for both Sox-9 and isotype labeling. Gating is applied for subtracting isotype labeling from Sox-9 labeled populations, and percent of remaining part is considered specifically stained with Sox-9 antibody..... 59

Figure 2. 25 Immunophenotypic characterization of stem cells encapsulated in GAG- and E-gel niches for Runx-2 expression on day 7. (A) Cell population and fluorescence signaling including corresponding gating are shown for both Runx-2 labeling of cells in GAG- and E-gel niches. Gating is applied for subtracting isotype labeling from Runx-2 labeled populations, and percent of remaining part is considered specifically stained with Runx-2 antibody. (B) Cell population percentage comparison for Runx-2 expression. 61

Figure 3. 1 Chemical characterization of K-PA molecule. Liquid chromatogram and mass spectra of L-VVAK, calculated exact mass [M] = 654.4998, $[M-2H]^{-}/2$ (m/z) = 327.7529. 79

Figure 3. 2 Chemical structures of the K-PA and hyaluronic acid molecules. 80

Figure 3. 3 (A) STEM image of hybrid nanofiber membrane (HA/K-PA), scale bar = 50 nm; (B) SEM image of hybrid nanofiber membrane at 5 mM, scale bar = 20 μm. 81

Figure 3. 4 (A) CD spectra of K-PA and Hyalgan• solutions and hybrid nanofiber membrane; (B) Rheological analyses of hybrid nanofibers. 82

Figure 3. 5 (A) Live/Dead analyses of MSCs cultured on hybrid nanofiber membranes and on uncoated TCP; (B) Viability analyses of MSCs by Alamar Blue assay. 83

Figure 3. 6 Live/Dead analyses and morphology tracking of chondrocytes cultured in 3D scaffolds. 85

Figure 3. 7 Hyaline cartilage regeneration analyses through Safranin-O/Fast Green/Hematoxylin stainings of tissues for all groups. 88

Figure 3. 8 Corresponding OARSI scoring for assessment of total joint score (Osteophyte scoring was evaluated as Grade 0: Marginal zone proliferative changes <200 μm; Grade 1: small 200-299 μm; Grade 2: moderate 300-399 μm; Grade 3: large 400-499 μM; Grade 4: very large >500 μm); Total joint score for scaffolds and sham (*p< 0.05, **p<0.01, by Student's t-test, mean ± s.e.m.). 89

Figure 3. 9 Total degeneration width analyses across three zones (0%: degeneration on the cartilage surface; 50%: degeneration through the midzone; 100%: degeneration through the tidemark); Total degeneration width percent across the whole cartilage tissue for all experimental groups (*p< 0.05, by Student's t-test, mean ± s.e.m.). 90

Figure 3. 10 Analyses methods for zonal depth ratio of lesions across three zones; Depth ratios of lesions across three zones for all experimental groups (1 and 0 are maximum and minimum degeneration width, respectively) (*p< 0.05 and **p<0.01 by Student's t-test, mean ± s.e.m.). 91

Figure 3. 11 Medial tibial cartilage scoring for experimental groups (**p<0.01, by Student's t-test, mean ± s.e.m.). 92

Figure 3. 12 Medial femur cartilage degeneration scoring for experimental groups. 93

Figure 3. 13 Tibial cartilage significant degeneration width analyses for experimental groups (**p<0.01, *** p<0.001 by Student's t-test, mean ± s.e.m.). .. 94

Figure 3. 14 Collagen deposition analyses; Collagen II immunostaining and Sirius Red stainings are shown for all experimental groups. 95

Figure 3. 15 (A) Total cartilage degeneration score for late osteoarthritis groups; (B) Tibial cartilage degeneration score for late osteoarthritis groups; (C) Total cartilage

degeneration width for late osteoarthritis groups (*p<0.05 by Student's t-test, mean ± s.e.m.) 96

Figure 3. 16 (A) Significant cartilage degeneration width for late osteoarthritis groups; **(B)** Femur cartilage degeneration score for late osteoarthritis groups; **(C)** Depth ratio of lesions for late osteoarthritis groups (1 & 0 are max. and min. degeneration width, respectively) (*p< 0.05, by Student's t-test, mean ± s.e.m.). 97

Figure 4. 1 Starting structures of the PA nanofibers for MD simulations. Nanofiber structures were built using 18 layers. Each layer contains 12 PAs that were placed by 30° angle separation. Adjacent layers contain only either glutamic acid (red) or lysine (blue) containing PAs and are constructed by 15° angle rotation with respect to each other..... 113

Figure 4. 2 Liquid chromatogram and mass spectra of L-VVEE, calculated exact mass [M] = 783.4742, $[M-H]^-$ (m/z) = 782.4586, $[M-2H]^-/2$ (m/z) = 390.7025..... 123

Figure 4. 3 Liquid chromatogram and mass spectra of D-VVEE, calculated exact mass [M] = 783.4742, $[M-H]^-$ (m/z) = 782.4580, $[M-2H]^{-2}/2$ (m/z) = 390.7023..... 124

Figure 4. 4 Liquid chromatogram and mass spectra of L-FFEE, calculated exact mass [M] = 879.4742, $[M-H]^-$ (m/z) = 878.4614, $[M-2H]^{-2}/2$ (m/z) = 438.7034..... 124

Figure 4. 5 Liquid chromatogram and mass spectra of D-FFEE, calculated exact mass [M] = 879.4742, $[M-H]^-$ (m/z) = 878.4661, $[M-2H]^{-2}/2$ (m/z) = 438.7059. ... 124

Figure 4. 6 Liquid chromatogram and mass spectra of L-VVKK, calculated exact mass [M] = 781.5789, $[M+H]^+$ (m/z) = 782.5905, $[M+2H]^{+2}/2$ (m/z) = 391.8014. 125

Figure 4. 7 Liquid chromatogram and mass spectra of D-VVKK, Calculated Exact Mass [M]= 781.5789, $[M+H]^+$ (m/z) = 782.5911, $[M+2H]^{+2}/2$ (m/z) = 391.8015.. 125

Figure 4. 8 Liquid chromatogram and mass spectra of L-FFKK, calculated exact mass [M] = 877.5789, $[M+H]^+$ = 878.5897 (m/z), $[M+2H]^{+2}/2$ (m/z) = 439.7974. 125

Figure 4. 9 Liquid chromatogram and mass spectra of D-FFKK, calculated exact mass [M] = 877.5789, $[M+H]^+$ (m/z) = 878.5908, $[M+2H]^{+2}/2$ (m/z) = 439.8017. 126

Figure 4. 10 Schematic representations of peptide nanofibers and their corresponding STEM images, scale bar = 100 nm (L-VV and D-VV), scale bar = 50 nm (L-FF and D-FF). L-VV: Lauryl-VVAGEE-Am / Lauryl-VVAGKK-Am, D-VV: Lauryl-vvaGee-Am / Lauryl-vvaGkk-Am, L-FF: Lauryl-FFAGEE-Am / Lauryl-FFAGKK-Am, D-FF: Lauryl-ffaGee-Am / Lauryl-ffaGkk-Am..... 127

Figure 4. 11 TEM images showing diameter (top) and pitch size (bottom) measurements of L-FF networks. n =100 for diameter analysis, and n = 90 for pitch size analysis. Scale bars = 50 nm. 128

Figure 4. 12 STEM images showing diameter (top) and pitch size (bottom) measurement of D-FF networks. n = 100 for diameter analysis, and n = 90 for pitch size analysis. Scale bars = 50 nm (left), scale bars = 100 nm (right)..... 129

Figure 4. 13 SAXS patterns for unmixed PAs in aqueous solution, as indicated (open symbols) along with model form factor fits (solid lines) to describe nanotape structures, as described in the text, (A) VVxx series (data for D-VVEE multiplied by 5 for ease of comparison), (B) FFxx series. 130

Figure 4. 14 SAXS patterns for gel mixtures, as indicated. 131

Figure 4. 15 CD spectra of peptide nanofibers..... 132

Figure 4. 16 CD difference spectra between L-FF and L-VV ensembles (black), and D-FF and D-VV ensembles (red). 133

Figure 4. 17 Time series for non-bonded interaction energies for the last 20 ns of the simulations. (A) Energy calculation between PAs. (B) Energy calculations for the atom pairs of the side-chain atoms of the first and second residues on PAs. 135

Figure 4. 18 Time series of hydrogen bond number for the last 20 ns of the simulations. 136

Figure 4. 19 Radial distribution function (RDF) plots. (A) RDF for the atom pairs between hydrogen bound to backbone nitrogen and valine side-chain gamma carbons. (B) RDF for the atom pairs between backbone oxygen and valine side-chain gamma carbons..... 137

Figure 4. 20 Number of hydrogen bonds that each residue forms: V-F/1 denotes the first valine or phenylalanine (numbering starts from the lipophilic tail) on the corresponding PA; V-F/2 denotes second V or F, KK and EE denote merged results for two lysine and two glutamic acid residues, respectively..... 138

Figure 4. 21 Ramachandran plots for valine residues in L-VV and D-VV PAs. Black dots correspond to centers of dihedral angle populations for parallel and antiparallel β sheet conformations for valine residues reported by Hovmöller et. al. [152] N denotes for the counts..... 139

Figure 4. 22 Macro-scale mechanical investigation of peptide nanofiber networks by oscillatory rheology. (A) Viscoelastic analyses of peptide nanofibers by oscillatory rheology. Equilibrium storage and loss moduli of nanofiber networks during (B) time, (C) frequency and (D) strain sweeps..... 140

Figure 4. 23 SEM images of bulk hydrogels showing their nanofiber morphology similar for all groups, scale bars = 2 μm..... 141

Figure 4. 24 Nanomechanical characterization of peptide nanofibers by AFM; Elastic modulus comparison of peptide nanofibers. 142

Figure 4. 25 Representative height and adhesion maps of peptide nanofibers measured by AFM. 143

Figure 4. 26 Cellular viability measurements by Alamar Blue assay. 144

Figure 4. 27 Viability analyses of stem cells on peptide nanofibers after 1 day and 3 days of incubation by Live/Dead assay (Green cells are live cells, and red cells are dead cells). 145

Figure 4. 28 Cellular adhesion analyses of MSCs on peptide nanofibers and on TCP after 1 h and 5 h. 146

Figure 4. 29 Collagen adsorption on the peptide nanofibers were measured by ELISA. Collagen protein at 30 ng/mL was used as positive control. N.D. (Not Determined). 147

Figure 4. 30 (A) Cellular adhesion analyses of HUVECs 1 h and 5 h after seeding on peptide nanofibers and on TCP. (B) Cellular adhesion analyses of hFibs 1 h and 5 h after seeding on peptide nanofibers and on TCP. 148

Figure 4. 31 Cellular proliferation measurement of MSCs by BrdU assay through 5 days of culture (*p< 0.05, **p<0.01, ***p< 0.001 by two-way ANOVA with Bonferroni's post-hoc test, mean ± s.e.m.). 150

Figure 4. 32 Quantification of cellular spreading measurements of MSCs 24 h after seeding on peptide nanofibers, obtained by Image J analysis of cells stained with phalloidine and imaged by fluorescence microscopy (n>50 cell per group (*p<0.05, **p<0.01, ***p<0.001 by one-way ANOVA with Bonferroni's post-hoc test, mean ± s.e.m.). 151

Figure 4. 33 Representative fluorescent images of MSCs 24 h after seeding on peptide nanofibers, scale bar = 50 μm. 151

Figure 4. 34 Cellular spreading analyses for HUVECs and hFibs 24 h after seeding on nanofibers (*p< 0.05, **p<0.01, ***p< 0.001 by one-way ANOVA with Bonferroni's post-hoc test, mean ± s.e.m.) 153

Figure 4. 35 Osteogenic and chondrogenic differentiation analyses by qRT-PCR. Expression of Runx-2 and Sox-9 were quantified on day 7 (*p<0.05, **p<0.01, ***p<0.001 by one-way ANOVA with Bonferroni's post-hoc test, mean ± s.e.m.). 155

Figure 4. 36 Chondrogenic differentiation analyses by qRT-PCR on day 3 and day 7 of MSC cultures on peptide nanofibers. Expression of Sox 9 was quantified on day 3 (not significant by two-way ANOVA) and day 7 (*p<0.05, ***p<0.001, ****p<0.0001 by one-way ANOVA with Bonferroni's post-hoc test, mean ± s.e.m.). 156

Figure 4. 37 Safranin-O staining of MSCs on peptide nanofibers in both maintenance medium and chondrogenic medium, which stained the sulfated glycosaminoglycans, that are found mainly in cartilage tissue, as an indicator for chondrogenesis potential of MSCs, scale bar = 50 μm. 157

Figure 4. 38 Signaling pathway analyses of cellular mechanotransduction; (A) Integrin β1 expression on peptide nanofibers with different morphology and chirality, as analyzed by Western blotting (**p<0.01, ***p<0.001 by one-way ANOVA with Bonferroni's post-hoc test, mean ± s.e.m.); (B) Schematic representation of the signaling pathway activated in MSCs cultured on the L-form of cylindrical nanofibers; (C) pERK expression on peptide nanofibers, as analyzed by

Western blotting (**p<0.01 by one-way ANOVA with Bonferroni's post-hoc test, mean ± s.e.m.); (D) MEK expression on peptide nanofibers, as analyzed by Western blotting (*p<0.05 by one-way ANOVA with Bonferroni's post-hoc test, mean ± s.e.m.) 160

Figure 4. 39 Focal adhesion complex analyses of MSCs on peptide nanofibers with different morphology and chirality; Confocal images of MSCs on peptide nanofibers stained for the visualization of actin stress fibers (grey), vinculin (green), and nuclei (blue), scale bars = 20 μm.)..... 162

Figure 4. 40 Protein expression analyses of Integrin α2 and FAK. (A) Integrin α2 protein expression by Western blotting (B) Vinculin expression in MSCs on peptide nanofibers by flow cytometry analyses (C) FAK expression in MSCs on peptide nanofibers by flow cytometry analyses (*p<0.05, ***p<0.001 by one-way ANOVA with Bonferroni's post-hoc test, mean ± s.e.m.). 163

Figure 4. 41 Confocal images of MSCs on peptide nanofibers stained for the visualization of Actin filaments (grey), yellow arrows indicate the organized actin fibers and insert showed the zoomed cells with stress fibers, scale bars = 20 μm. . 164

Figure 4. 42 Schematic representation of MSC response on different PA nanofibers through activation/attenuation of YAP protein into the nucleus/cytosol. 165

Figure 4. 43 Confocal microscope images of MSCs stained for the visualization of YAP proteins (green) and nuclei (blue), scale bars = 20 μm. 166

Figure 4. 44 Cells with nuclear YAP localization were quantified from the confocal images, and were shown as percent of cells among all counted cells (**p<0.01 by one-way ANOVA with Bonferroni's post-hoc test, mean ± s.e.m.). 167

List of Tables

Table 1. 1 Examples of peptide sequences used in cartilage regeneration studies.... 15

Table 2. 1 3D PA gel combinations and bioactive groups presented on the nanofibers 24

Table 2. 2 Primers used in qRT-PCR analysis 28

Table 3. 1 Experimental plan & animal groups..... 75

Table 3. 2 Histological scoring. Adapted from Gerwin et.al. [109]..... 78

Table 4. 1 List of positively and negatively charged peptide amphiphiles 109

Table 4. 2 Peptide nanostructure compositions and their corresponding morphology and chirality..... 122

Abbreviations

AFM	Atomic force microscopy
ANOVA	Analysis of variance
BMP	Bone morphogenetic protein
BSA	Bovine serum albumin
CD	Circular dichroism
DCM	Dichloromethane
DIEA	*N*,*N*-diisopropylethylamine
DMEM	Dulbecco's modified Eagle's medium
DMF	N,N-Dimethylformamide
ECM	Extracellular matrix
ESI	Electrospray ionization
FBS	Fetal bovine serum
FGF	Fibroblast growth factor
Fmoc	9-Fluorenylmethoxycarbonyl
FTIR	Fourier transform infrared spectroscopy
GAG	Glycosaminoglycan
GAPDH	Glyceraldehyde 3-phosphate dehydrogenase
GF	Growth factor
HA	Hydroxyapatite
HBTU	*N*,*N*,*N*′,*N*′-Tetramethyl-O-(1*H*-benzotriazole-1-yl) uronium hexafluorophosphate
H&E	Hematoxylin and eosin
HPLC	High pressure liquid chromatography
IGF	Insulin-like growth factor
IM	Intramuscular
LC-MS	Liquid chromatography-mass spectroscopy
MSC	Mesenchymal stem cell
PA	Peptide amphiphile
PBS	Phosphate buffered saline
PDGF	Platelet-derived growth factor

rMSC	Rat mesenchymal stem cell
qRT-PCR	Quantitative real-time polymerase chain reaction
QTOF	Quadrapole time of flight
SD	Standard deviation
Sem	Standard error of mean
SEM	Scanning electron microscopy
TCP	Tissue culture plate
TEM	Transmission electron microscopy
TFA	Trifluoroacetic acid
TIS	Triisopropyl silane
TGF-β	Transforming growth factor-β
UV	Ultraviolet
VEGF	Vascular endothelial growth factor

Chapter 1. Introduction: Bioinspired Materials for Regenerative Medicine

This chapter of thesis was published in the following articles:

[1] Reprinted with permission from "Bioactive supramolecular peptide nanofibers for regenerative medicine"; Arslan, E.; Garip, C. I.; Gulseren, G.; Tekinay, A. B.; Guler, M. O. Advanced Healthcare Materials, 2014, 3, 1357 – 1376, Copyright (2014) John Wiley and Sons.

[2] Reprinted with permission from "Therapeutic Nanomaterials for Cartilage Regeneration"; Arslan, E.; Yaylaci, S.U.; Guler, M.O.; Tekinay, A.B., Therapeutic Nanomaterials, 59 , Copyright (2016) John Wiley and Sons.

1.1 Extracellular Matrix Mimetic Scaffolds

Advancement in biomaterials science and materials chemistry presents new opportunities for *de novo* synthesis of bioactive molecules that self-assemble into hierarchical supramolecular structures by excluding numerous problems for the generation of sophisticated networks. Material scientists are able to utilize necessary toolkits to alter cellular processes via engineered biomaterials with a deeper understanding of cell-materials and cell-matrix interactions, which have become indispensable for numerous applications in regenerative medicine. For the development of a proper scaffold, the material should enable the transport of nutrients and waste products, present an intrinsic biocompatibility, facilitate the

migration and development of cells, and provide the biochemical signals necessary for the survival and maintenance of cells.

To guide natural cellular activities, biomaterials should provide a microenvironment similar to that experienced by cells under natural conditions. The native extracellular matrix (ECM) not only provides a suitable physical environment but also incorporates the necessary set of biochemical and mechanical signals to ensure the normal function of cells, mediating their differentiation, morphogenesis and homeostasis (Figure 1.1) [3]. To initiate these cellular responses, biomaterials having specific bioactive signals interact with specific cell surface receptors. Moreover, in a synthetic environment, cells are affected by the physical and chemical features of the biomaterial [4, 5]. Hence, physical and chemical characteristics of scaffold also have direct roles on controlling the adhesion, migration, and differentiation of cells [6]. Therefore, material properties such as scaffold morphology chirality, hydrophilicity and surface charge should be considered for the development of functional scaffolds that can interact with the surrounding environment. Moreover, the time of implantation is also very critical in the design of tissue scaffolds, since it determines whether the construct is set to be implanted immediately or following an *in vitro* culture period. If constructs are needed to be implanted immediately, they should be stable in the physical environment of tissue and should protect the cells until neotissue formation is accomplished. On the other hand, if cell-laden scaffolds are needed to be used following an *in vitro* culture period, this kind of structural integrity and stability is not particularly necessary, since newly formed tissue can withstand in the native environment. In addition, for the successful tissue regeneration, the scaffold should also be able to fill the defect site and integrate with the surrounding

native tissue. Furthermore, degradation rate of biomaterilas in native tissue should be suitable to facilitate new tissue formation, as slow degradation interferes with the ingrowth of newly formed tissue, while faster degradation causes problems in maintenance of physical and mechanical support.

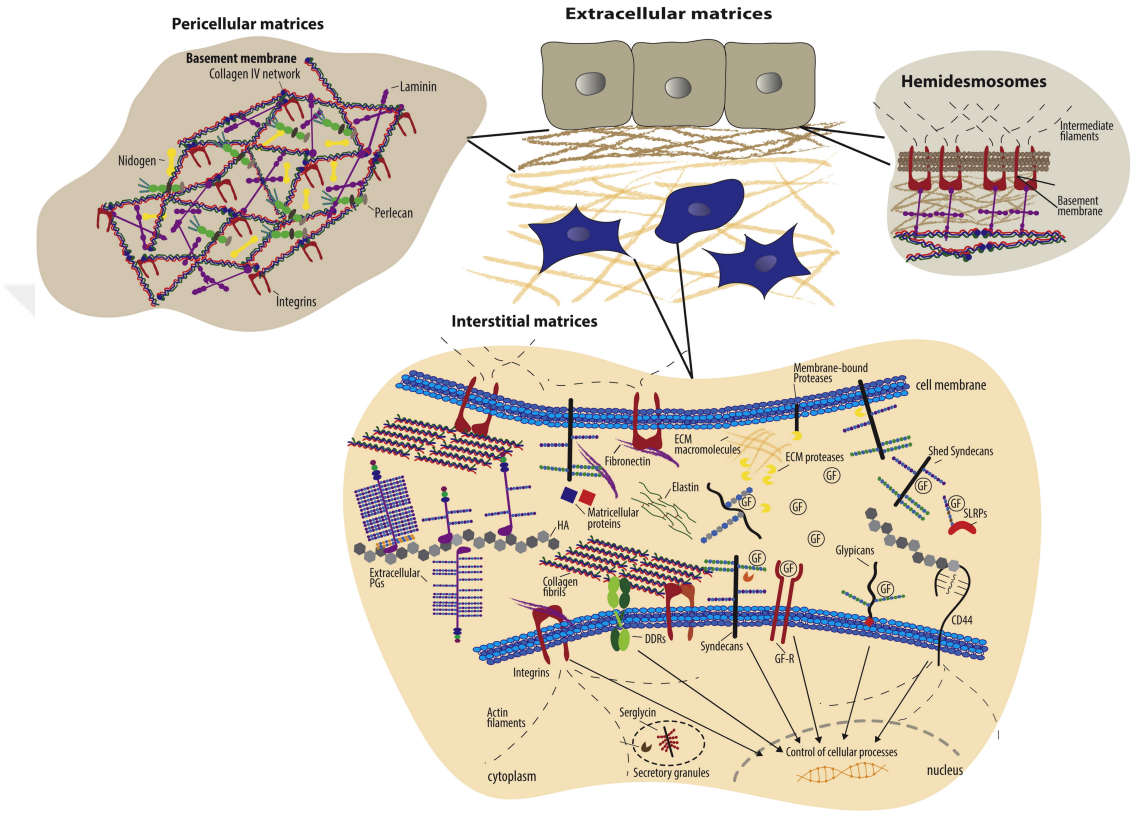


Figure 1. 1 Schematic representation ECM which is composed of two main types: interstitial and pericellular matrices. Interstitial matrices contain collagen fibrils, secreted proteoglycans (PGs), hyaluronic acid (HA), and other ECM proteins. These ECM macromolecules are associated with cells through receptors such as integrins, CD44, and DDRs (discoidin domain receptor). ECM components facilitate the presentation of growth factors (GF) to cells. Matrix degradation enzymes such as MMPs (matrix metalloproteases) are responsible for the turn over of the ECM (Reproduced from [7] with permission from Elsevier).

Several of natural and synthetic polymers have been investigated as ECM substitutes. Material source (natural or synthetic), biofunctionality, physical properties, and tissue integration capability designate application area of the scaffolds [8-10]. On one hand, natural materials such as agarose, alginate, hyaluronic acid, chitosan, and collagen are chosen due to their low costs and similarity to the native ECM, which facilitates their interaction with cells through functional groups, enables their natural degradation and ensures that the scaffold will be biocompatible [11]. Although they present several advantages, natural polymers lack the mechanical properties necessary in many tissues to withstand the high-stress environment, which casuses the rapid degradation of scaffold following implantation. On the other hand, synthetic scaffolds such as polymers, peptide–based materials, and composite materials introduce tailorable physical and chemical properties via different synthesis methods, which allow the production of various biomaterials having different sizes and shapes. Furthermore, they provide sparse immunogenic responses and toxicity with lower batch-to-batch variances compared to natural materials.

1.1.1 Self Assembling Peptide Nanofibers as ECM Mimetic Scaffolds

Self assembling peptide nanofibers comprise one of the major classes of bioactive synthetic materials. They present the complex architecture and biochemical properties of their natural counterparts through short amino acid-based biological signals. The use of short chains does not sterically hinder active epitopes and increases the stability of the structure [12, 13]. Therefore, peptide nanofibers are particularly advantageous, since they can be designed to display desirable structural properties, and they are formed through a relatively simple self-assembly process. Although hydrogels have several advantageous to be used in clinics such as higher

water storage capacity, biodegradability and oxygen permeability, these materials cannot adequately fulfill the strict physiological demands inherent to all human tissues. This problem rendered it crucial to develop biomimetic peptide scaffolds capable of activating specific biological responses and modulating a wide variety of cellular processes such as cell spreading, differentiation, tissue repair and regeneration (Figure 1.2).

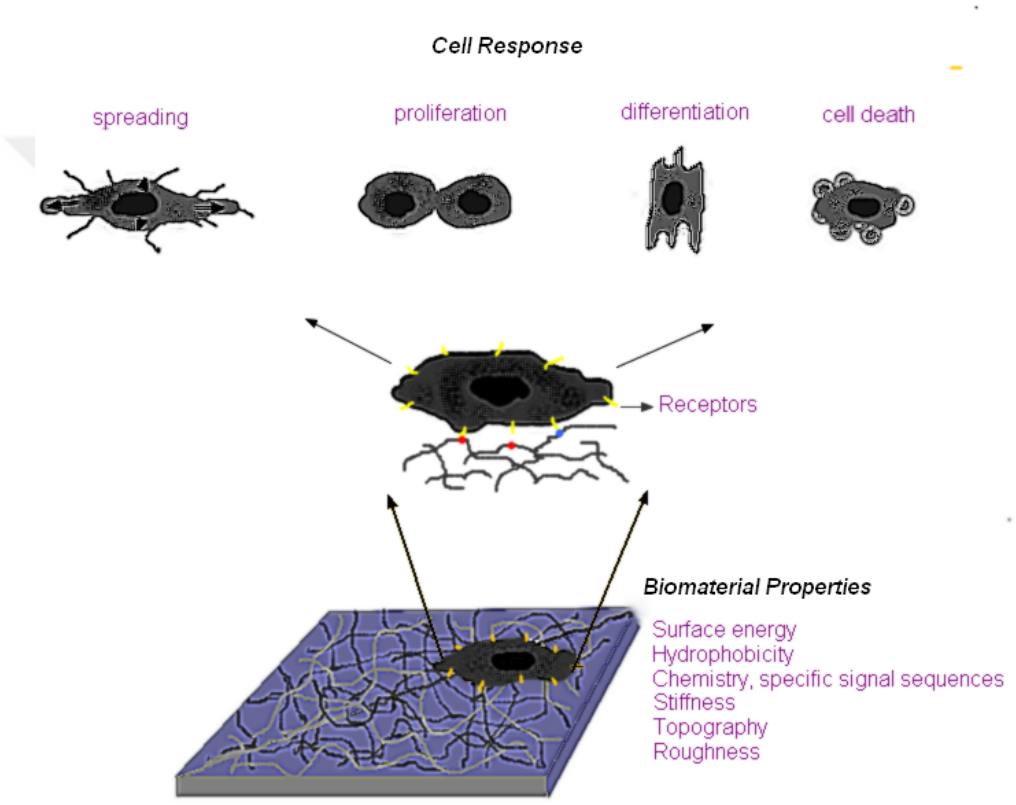


Figure 1. 2 Schematic illustration of biomaterial properties and their possible impact on cell fate (Reproduced from [1] with permission from John Wiley & Sons).

Peptide hydrogels are significant for their exceptional structural and functional features, which frequently present complex motifs such as α-helices, β-sheets, coiled-coils, β-hairpins and triple helices. In addition, basic peptide motifs can be chemically modified to utilize advanced and additional functions to nanofiber

matrices. One of the important structural characteristics of peptide nanofibers is the secondary structural motif. The β-sheet, being one of the most investigated secondary structures, is composed of two or more β-strands laterally attached by backbone hydrogen bonds to form a pleated sheet. Generally, two molar-equivalent solutions of oppositely charged peptides are mixed to assemble fibrous β-sheet scaffolds; however, acidic and amphiphilic β-sheet forming peptides could also be utilized for β-sheet formation. In addition, correlation between the hydrophobic parts and aromatic groups, and ionic strength of the molecules also play key roles in β-sheet assembly [14, 15].

Self-assembling amphiphilic peptides can be designed and assembled in various morphologies including fibers, ribbons, tubes, and vesicles [16]. These peptides contain both hydrophobic and hydrophilic residues, which affect assembly of amino acid sequence into specific secondary structures [17]. Multiple noncovalent interactions such as hydrogen bonding, van der Waals forces, electrostatic associations and hydrophobic interactions, drive the spontaneous self-assembly of individual peptide amphiphile molecules into supramolecular nanostructures under physiological conditions [12]. The hydrophobic alkyl group imitates the nonpolar "tail" region found in fatty acids. This hydrophobic segment can be modulated by using different chain lengths, components and structures. For example, by using less twisted β-sheet structures, stiffer materials can be formed [18]. Furthermore, charged residues can also be incorporated to provide aqueous solubility and control hydrogelation [19]. In addition, bioactive domains composed of different peptide epitopes presenting specially designed oligo-peptide sequences according to the purpose of design can be incorporated to induce cell adhesion, viability,

proliferation, migration, and differentiation [17, 20]. Consequently, three-dimensional fibrous networks are formed by these amphiphilic peptides. The representative structure of peptide amphiphile molecules (PAs) composed of one alkyl chain connecting with several amino acid sequences is shown in Figure 2 [12].

Peptide nanofibers, hence, can function cooperatively to achieve the required harmony of flexibility, strength, structural integrity and complexity of the native extracellular tissue through this fibrous organization and proper composition. Due to their superior features such as biocompatibility and biodegradability, peptide nanofibers have been used to regulate cellular bahaviour and repair damaged tissues in regenerative medicine both *in vitro* and *in vivo*. According to the application, tissue type specific bioactive peptide nanostructures can be designed. The order of epitopes to be presented to cells, and their intensity are significant factors for self assembling peptide nanofibers to direct cell behavior [21]. In addition, peptide nanofiber scaffolds engineered with porous structures and high surface to volume ratios provide a suitable spatiotemporal microenvironment for cells, and promote the material exchange between the scaffold and the environment. Cells continuously receive and process incoming information from the environment and remodel the extracellular structure by degrading it and depositing their own matrix components. This integrin-mediated dynamic and bidirectional interaction between cells and the environment is responsible for directing certain cellular processes to maintain tissue homeostasis [22].

1.2 Induction of Chondrogenesis and Cartilage Regeneration Through Self Assembling Peptide Nanofibers

Understanding specific cell-biomaterial and cell-extracellular matrix interactions is important to generate functional materials capable of inducing cartilage tissue regeneration. Cartilage matrix proteins responsible for organizing the cell microenvironment and regulating growth and differentiation are particularly promising candidates for research and their receptor recognition sequences are frequently utilized to generate peptide nanostructures. Hence, cartilage ECM protein mimics are extensively utilized to guide cell behavior in regenerative medicine, effectively simplifying their models' sophisticated structures without compromising their critical role in maintaining metabolic equilibrium in living systems [23]. In this respect, supramolecular peptide nanofibers have already demonstrated their potential to mimic native cartilage ECM with minimal complexity while retaining their desired chemical functions [1, 2]

1.2.1 Cartilage Structure

Cartilage, as load bearer of whole body mass, is distributed on multiple areas of body. Cartilage tissue is avascular, aneural, and alymphatic, and is classified into three different forms as hyaline cartilage, elastic cartilage and fibrocartilage. Mature cartilage cells are chondrocytes constituting 3-5 % of the adult articular cartilage [24]. In the deep part of the perichondrium, mesenchymal cells encircle the cartilage, which then differentiate into chondroblasts [25]. Cartilage tissue provides not only loading but also joint lubrication and articulation [24], and the ECM components have primary roles during these functions. The load-bearing function of cartilage tissue is mainly associated with its ECM components [26]. Mainly the fibrillar collagen network and proteoglycans are found in the extracellular microenvironment in the tissue [24]. In the collagen network, type II collagen is the primary collagen

fibril found in ECM. In addition, other collagens as types III, VI, IX, X,XI, XII and XIV, which all contribute to the mature extracellular framework [27]. Besides collagens, proteoglycans such as aggrecan, chondroitin sulfate glycosaminoglycan, keratin sulfate glycosaminoglycan, hyaluronan, and glycoprotein lubricin (PRG4) are also a major element of the cartilage ECM [28].

Water is also another important component of the articular cartilage. It is highly abundant in tissue and comprises 80% of the total weight. Hence, significant amount of water is combined within the collagen network in interfibrillar spaces [29]. Therefore, the load-bearing, articulative and lubricant functions of cartilage also depend on this water content of the tissue. This interfibrillar water within collagen network constructs a gelatinous structure and facilitates the spreading of the pressure gradient across the tissue and it provides to alleviation of excessive mechanical stress on the solid matrix [30, 31]. Therefore, healthy cartilage tissue can withstand to significant weight loads through two basic mechanisms of water: the frictional resistance of water flow and the pressurization of water within the matrix [32].

The joint cavity of the human body are composed of articular cartilage, synovial membranes, ligaments, subchondral bone and menisci [33]. Articular cartilage is a heterogeneous type of cartilage which is commonly affected by diseases and traumatic injuries, that necessitate therapeutic regeneration. It is composed of four tissue layers that are categorized with respect to their ECM composition and cellular morphology [34]. The superficial zone forms 10-20% of articular cartilage tissue by volume, consists of flattened chondrocytes and tightly packed collagens (mainly types II and IX), and is mainly responsible for the maintenance of tensile strength and protection of the underlying layers [32]. The middle (transitional) zone forms 40-

60% of cartilage tissue containing round chondrocytes, thicker collagen fibrils and proteoglycans, and it assists in the resisting of compressive forces [32]. The deep zone forms 30% of the tissue containing the thickest collagen fibers observed in cartilage. It is mainly composed of proteoglycans and has a role in resistance of cartilage against compressive forces [32]. The last layer, called the tidemark, is located between the deep zone and the calcified part of cartilage; and it has high proteoglycan content that also allows it to resist compression. In addition, there is an additional calcified layer between bone and cartilage, which integrates the two tissue types and contains hypertrophic chondrocytes. Furthermore, structural differences are seen into four layers with compositional, collagen-based and positional variations within the cells and matrix elements of a given cartilage layer. Hence, three types of cartilage ECM are classified: pericellular, territorial and interterritorial (Figure 1.3) [32]. The pericellular matrix is a thin layer that contains proteoglycans, non-collagenous proteins and glycoproteins, and it supports chondrocytes and play a role in establishing the signal transduction networks required for the proper functioning of cartilage tissue [35]. The pericellular matrix is encompassed by the territorial matrix, which contains mainly of a network of thin collagen fibrils that spread throughout the cartilage tissue. This matrix assists in the resistance of cartilage against mechanical stresses by withstanding the majority of the mechanical load on the tissue [36]. The interterritorial region is the largest region of the cartilage ECM, and most of the biochemical composition and function of articular cartilage depend on this region. This matrix has abundant proteoglycan content and collagen bundles that are arranged in parallel in the superficial zone, perpendicular on the surface of the deep zone, and in intermediate angles for middle zone collagens [37].

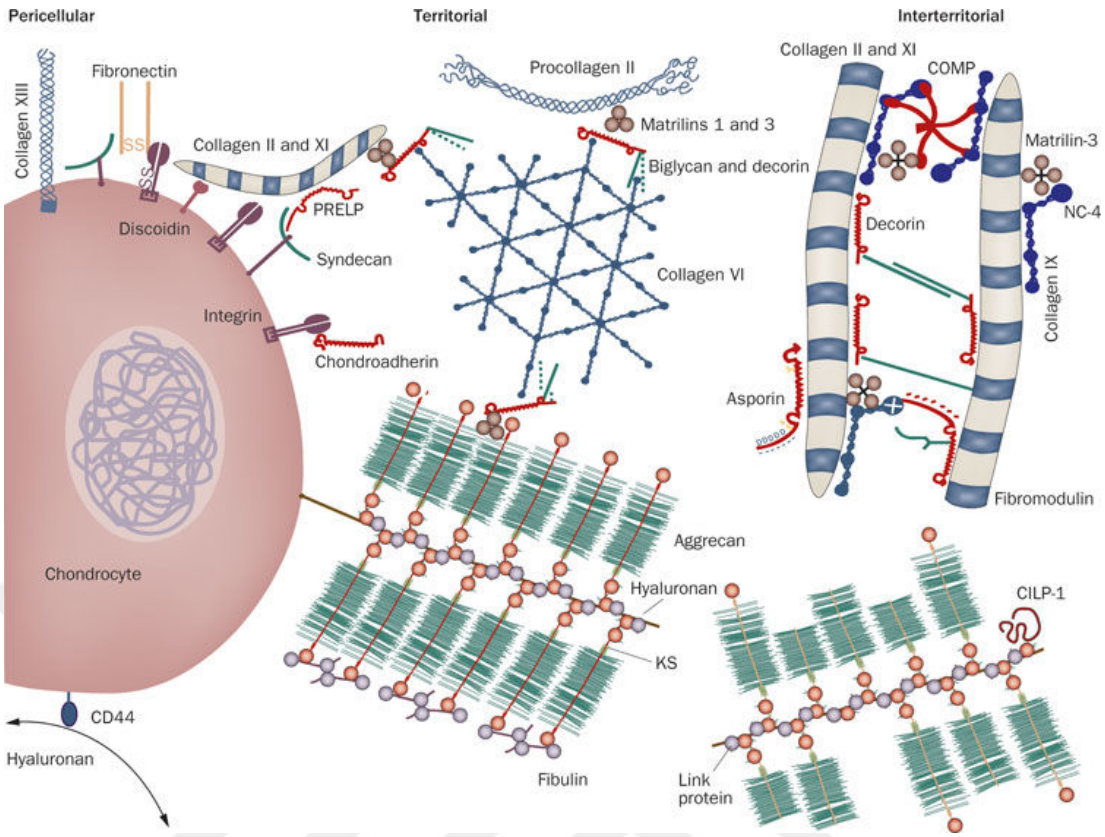


Figure 1. 3 Schematic representation of cartilage matrix surrounding chondrocytes with pericellular, territorial, interterritorial regions with essential macromolecules of ECM. Abbrevations: CS, chondroitin sulfate; KS, keratin sulfate; CILP-1, cartilage intermediate layer protein 1; PRELP, proline-arginine-rich leucine-rich repeat protein; COMP, cartilage oligomeric matrix protein. (Reproduced from [36] with permission from Nature Publishing Group).

The physiological metabolism of cartilage tissue is as crucial. Cartilage metabolism is mainly anaerobic, due to its avascular and alymphatic nature. Nutrition is provided by diffusion from the synovial fluid, through the pores of approximately 6 nm in diameter in cartilage matrix, which limits material exchange [31, 38]. Despite their low amount (approximately 3-5% of cartilage tissue), chondrocytes are the main effector cells of the metabolic activities of the tissue. Synthesis, maintenance, and

repair of the ECM are carried out by chondrocytes with several molecules such as proinflammatory cytokines and growth factors including transforming growth factor-1 (TGFβ), insulin-like growth factor, interleukin-1 and tumor necrosis factor-α [32, 39].

Healthy turnover of its ECM components is important for the homeostasis of cartilage and its structural stability. Therefore, deficiencies in turnover mechanisms lead to disease. The physiological metabolism of cartilage is controlled according to the stage of tissue growth. During embryonic development, chondrocytes rapidly synthesize ECM components and expand the new tissue, which requires high rates of activity. On the other hand, as the tissue ages or in the case of injury, expression levels of enzymes such as metalloproteinases and cathepsin increase, which initiate the degradation of ECM molecules [40, 41]. In addition, the chondrocytes of adult cartilage tissues are at a steady state and have limited function to replace degraded or damaged matrix materials [42].

Overall, chondrocytes and cartilage ECM are continuously interacted for the proper functioning of the tissue. Chondrocytes are mainly responsible for the development and maintenance of the ECM, while the ECM promotes nutrient exchange and determines which molecules can pass through the matrix to reach the chondrocytes. This function of the ECM depends on its composition and organization, and especially on its proteoglycan components [43]. The ECM itself also imparts physical and mechanical signals through the structural features of the fibrous network to the chondrocytes [39].

1.2.2 Cartilage Diseases

Cartilage defects and diseases are one of the major concerns causing disabilities. Osteoarthritis is one of these diseases affecting several parts of the cartilage tissue including articular cartilage, synovium and subchondral bone at molecular, cellular and tissue level. Therefore, osteoarthritis is mainly associated with decrease in articular cartilage thickness, bone thickening and bone outgrowth on the joint margin, and modification of the synovial fluid constituents [44]. Currently applied treatments are based on non-pharmacological therapies such as weight reduction and physical therapy; drug treatments such as pain relievers, chondro-protective molecules; and surgical interventions such as arthroplasty and osteotomy [44]. However, these treatments are only able to alleviate the symptoms of osteoarthritis and cannot reverse the condition itself; as such, significant advances in regenerative medicine and tissue engineering are necessary for the development of prospective clinical treatments and therapeutics for osteochondral diseases.

Osteoarthritis is an inflammatory cartilage disease accompanied with the erosion of the tissue. Combination of genetic, metabolic and biochemical factors play key roles in disease progression [45]. Aging with the mechanical deterioration in tissue is one of the main reasons of osteoarthritis in elderly patients. In addition to aging, joint diseases can also be seen in young people due to traumatic accident or obesity [46]. After an injury, day-to-day activities under body weight and limited regeneration capacity of cartilage to compensate the tissue degradation cause the gradual loss of tissue integrity. During disease progression, collagen degradation increases, proteoglycan content decreases-especially the amount and molecular size of hyaluronic acid reduces, types of the macromolecules change, and water content increases (Figure 1.4) [47-49]. Therefore, disruption of the anabolic and catabolic

activities of cartilage results in the pathophysiological formation of osteoarthritis, which leads in the progressive destruction of the tissue [49]. Such changes in tissue develop into severe degeneration, which necessitates the early treatment of disease to control the degeneration of the tissue [50, 51]. Hence, the effective treatment strategies for cartilage diseases are required by combination of novel treatment options and new multifunctional biomaterials.

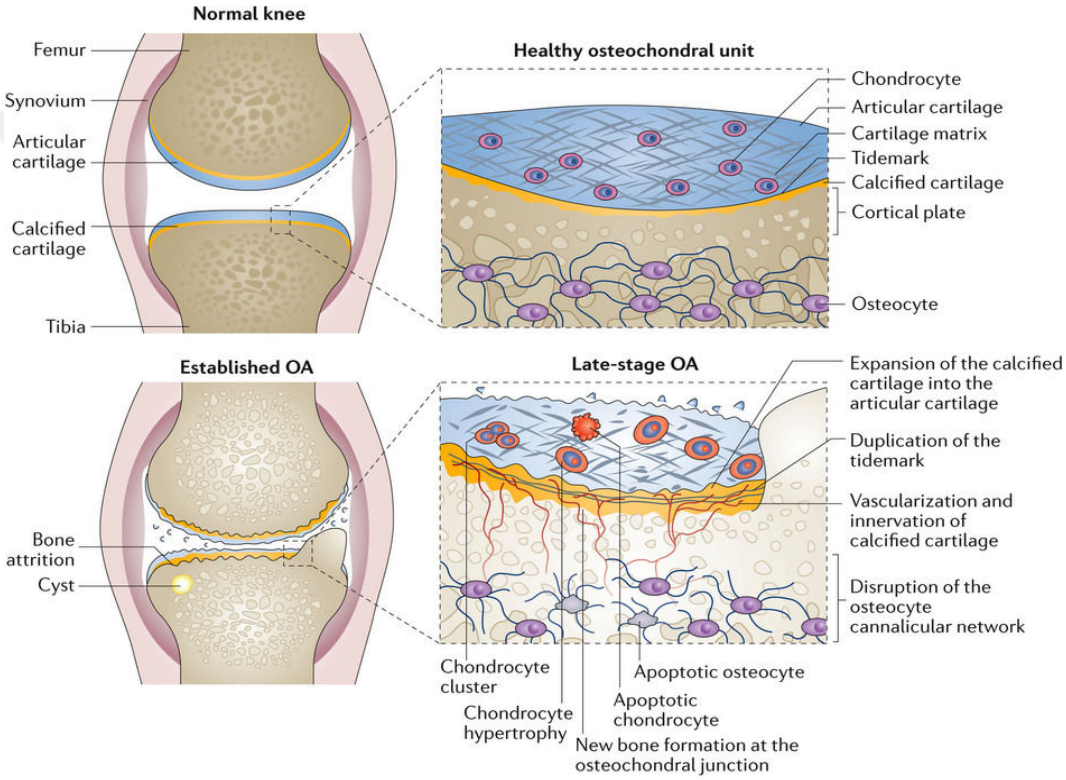


Figure 1. 4 The normal knee joint and the joint with established osteoarthritis are shown with structural elements of each stages (Reproduced from [52] with permission from Nature Publishing Group).

1.2.3 Cartilage Tissue Regeneration with Peptide Nanofibers

Tissue engineering holds great potential for the development of novel approaches to enhance cartilage tissue regeneration by recruiting a variety of biomaterials.

However, the regeneration of damaged cartilage tissue remains as a challenge despite rapid advances in other aspects of tissue engineering. Cartilage tissue engineering is primarily restricted by the low natural regenerative capacity of this tissue and its limited cell supplies. Hence, most of the scaffolds designed for cartilage regeneration have been dissatisfactory. Mimicking natural extracellular matrix, therefore, is now one of the crucial goals of cartilage tissue engineering in order to achieve efficient treatment. As self-assembled peptide amphiphiles are strong ECM-mimetic material candidates, much research has been performed regarding their potential use in cartilage regeneration. Some of the peptide sequences used in cartilage regeneration studies are shown in Table 1.1.

Table 1. 1 Examples of peptide sequences used in cartilage regeneration studies

Peptide sequence and bioactive peptide nanofibers	**Origin**	**Way of bioactivity**	**Reference**
TGF-β binding PA (HSNGLPL)	Binding affinity to TGF-β1	Articular cartilage regeneration	[53]
GAG-PA	Mimicking heparan sulfate found in native ECM	Promoting chondrogenesis of MSCs	[54]
KLD-12 (AcN-KLDLKLDLKLDL-	Self assembling	Encapsulation of chondrocytes in a 3D	[65]

NH_2),	peptide sequence	environment	
Glc-PA	Glucose conjugated self assembling peptide nanofiber	Induce chondrogenesis of MSCs *in vitro* and cartilage regeneration in defect model *in vivo*	[55]

The peptide KLD-12 (AcN-KLDLKLDLKLDL-NH_2), for example, was used as a self-assembled peptide hydrogel for encapsulation of chondrocytes in a 3D environment, and was demonstrated to be comparable to other cartilage ECM-derived scaffolds for the retention of chondrocyte morphology [56]. In addition, the peptide amphiphile nanofibers were demonstrated to induce cell proliferation, differentiation and the production of cartilage-like ECM *in vitro* as well as supporting regeneration of hyaline-like cartilage tissue *in vivo* [53, 57]. Furthermore, an integrated system composed of peptide nanofibers and polymers was demonstrated to have significant effect on the differentiation of hMSCs (human mesenchymal stem cells) into chondrocytes and augmented cartilage specific ECM production [58]. In this thesis, different ECM-mimetic peptide nanofiber formulations were designed and developed, which showed superior chondrogenic and therapeutic effect on stem cell differentiation *in vitro* and cartilage regeneration *in vivo*. Hence ECM-mimetic peptide amphiphiles are proposed to be highly promising for cartilage regeneration for further clinical applications.

Chapter 2. Glycosaminoglycan-mimetic signals direct the osteo/chondrogenic differentiation of mesenchymal stem cells in a three-dimensional peptide nanofiber extracellular matrix mimetic environment

This chapter of thesis was published in the following article [54]; Reprinted with permission from "Glycosaminoglycan-mimetic signals direct the osteo/chondrogenic differentiation of mesenchymal stem cells in a three-dimensional peptide nanofiber extracellular matrix mimetic environment"; Arslan, E.; Guler, M. O.; Tekinay, A. B., *Biomacromolecules,* 2016, 17, 1280 – 1291, Copyright (2016) American Chemical Society

2.1 Objective

Elucidation of complex cellular responses through the use of synthetic systems and understanding of cellular behaviors on natural and artificial scaffolds are recent efforts in bioactive scaffold development. Bioactive materials may therefore serve as models for understanding the cellular behaviors. Supramolecular assemblies of bioactive peptide nanostructures are especially promising for this purpose due to their ability to emulate both the biochemical and mechanical properties of native tissue environments. In this study, we developed GAG mimetic peptide nanofiber gel

as a three-dimensional (3D) platform to investigate how external factors in a system that closely mimics the structure and function of native extracellular matrix components alter the cell lineage commitment. We observed that specific culture medium components had synergistic effects on the ability of GAG-mimetic nanofiber gel to regulate the differentiation of mesenchymal stem cells into osteogenic and chondrogenic lineages. Specifically, FBS concentrations in the culture medium were demonstrated to control osteogenic and chondrogenic differentiation in tandem with the effects of the 3D peptide nanofiber network, even in the absence of externally administered growth factors. We therefore demonstrated that MSC differentiation can be specifically controlled by the combined influence of growth medium components and a 3D peptide nanofiber environment.

2.2 Introduction

The ECM is a dynamic niche that supports cellular activity by providing a physical framework for cell attachment and tissue formation, and enables the long-distance coordination of cellular activity by establishing biochemical and mechanical signaling networks [59]. Functional imitation of ECM elements is, therefore, a potent means of modulating cellular behavior for regenerative medicine and therapeutic purposes. The composition of the ECM is tissue-specific and heterogeneous, but generally features large macromolecule assemblies that serve as 3D scaffolds for the attachment of cells [59]. Conclusions of 2D experiments are, therefore, not readily applicable to physiological environments, despite the fact that *in vitro* studies are typically based on 2D cell cultures [60]. The 3D cell culture methods, however, are able to approximate the conditions found in the ECM of natural tissues, allowing non-epithelial cells to assume their native ellipsoidal morphology and produce

cellular responses similar to their *in vivo* behavior [61]. Culturing of MSCs via 2D seeding, in particular is problematic for cell differentiation studies, as the lack of a 3D scaffold introduces an unnatural factor to the growth environment by preventing cells from fully making contact with the material. In contrast, mesenchymal stem cells in 3D cultures retain their stellate morphology and polarization in the antero-posterior axis, which supports their survival by hindering apoptosis [60]. In addition, 3D culturing allows the growth of cells to very high confluency, which is critical for the differentiation of cells into specific lineages. 3D scaffolds may, therefore, shorten culture times and avoid issues such as contamination risks and genetic abnormalities that are associated with prolonged culturing [62]. As such, the development of 3D microenvironments capable of mimicking the function of natural ECM components is critical for both regenerative medicine and basic molecular biology research.

Due to their versatility and relative ease of isolation and cultivation, stem cells are used in many biomedical applications and clinical therapies. Stem cells may improve the wound healing process by migrating to sites of injury and differentiating into cell types necessary for the re-establishment of tissue integrity, enhancing the survival and proliferation of surrounding cells through paracrine secretions and/or modulating the immune and inflammatory responses created in response to tissue damage [63]. However, the resident stem cell population in both bone and cartilage tissues is insufficient to facilitate the complete regeneration of lost tissue [63]. The precise control of stem cell differentiation pathways is also a major issue in regenerative medicine, as the heterogeneous and unpredictable nature of stem cells makes their use problematic in medical applications [64]. As such, synthetic scaffolds are commonly used to provide an environment conductive for the regeneration of the

tissue of interest by assisting in the survival of stem cells or directing their commitment and differentiation. In particular, tunable scaffolds that incorporate bioactive signals can be used to overcome the problems associated with the direct administration of stem cells [1].

GAGs are the major components of the ECM of various tissues, including bone and cartilage. They are vital for the maintenance, differentiation and regeneration of these tissues, and also play a key role in tissue remodeling by interacting with native cells. Their effects result from a combination of their mechanical and biochemical properties, both of which can be imparted to synthetic scaffold materials to mimic their functions [1, 18, 62]. Considering their critical role in tissue remodeling, the inclusion of GAG-mimetic molecules in a 3D network is an advantageous strategy for the priming of stem cells for osteogenic and chondrogenic differentiation. Advances in peptide chemistry have also enabled the fabrication of peptide-based scaffold materials that closely emulate the structure of the native tissue environment, opening new avenues for biomedical research [1]. These biocompatible materials can be used in 3D cultures, and have been shown to serve as close analogs to natural scaffolds without exhibiting the limitations of naturally derived materials [65].

The cell culture medium is also critical as a modulatory element for lineage commitment in *in vitro* studies: Serum amount, growth factors and inhibitory elements in culture media must all be optimized to elicit the desired cell responses. A variety of media components and culture conditions have been demonstrated to exhibit distinctive effects on the differentiation of stem cells. For instance, FBS is known to increase the expression of osteogenic markers such as Runx-2 and Collagen type I, although cells exposed to FBS also exhibit a relative lack of mineral

deposition [66]. Chondrogenic differentiation, on the other hand, has been shown to be enhanced by DMEM supplemented with TGF-β, dexamethasone, and high glucose [67]. Consequently, the *in vitro* modulation of stem cells requires great insight into the roles played by each regulatory element found in culture conditions or incorporated into the scaffold design, and the use of these elements in the selective differentiation of stem cells is especially critical for the design of synthetic extracellular matrices for regenerative medicine. While a great variety of scaffolds have been devised for the selective differentiation of stem cells into specific niches; greater utility lies in the use of a single, versatile system that is able to direct the differentiation of multiple mature cell types depending on external factors provided alongside the scaffold.

Here, we investigated the ability of 3D GAG-mimetic peptide nanofiber gels to mediate the differentiation of MSCs into two fundamental mesenchyme-originated lineages in the presence of two distinct culture media containing different amounts of FBS. The differentiation patterns of the cells were determined and possible cell-material interactions responsible for causing these patterns were analyzed to determine the modulatory effect of serum on the culturing of stem cells in the context of bioactive signals provided by a 3D peptide network. The 3D GAG-mimetic peptide nanofiber gel niche was observed to demonstrate distinct effects on the osteogenesis and chondrogenesis of mesenchymal stem cells in low- and normal-serum environments, suggesting that serum presence can be used to directly alter the ability of a 3D scaffold to enhance stem cell differentiation towards osteogenic or chondrogenic lineage. Nonbioactive peptide nanofiber gels, however, did not exhibit this property, suggesting that the bioactivity of GAG-mimetic nanofibers was

necessary for the induction of differentiation by the culture medium. Our straightforward and simple design therefore demonstrates that the bioactivity of a peptide nanofiber scaffold, in tandem with the effect of serum amount in the culture medium, is able to exhibit strong modulatory effects on the differentiation of stem cells. n addition, 3D peptide nanofiber can be used for the investigation of the effects of other external factors on the differentiation of stem cells in bioactive scaffolds.

2.3 Experimental Section

2.3.1 Materials

Fluorenylmethoxycarbonyl (Fmoc) and tertbutoxycarbonyl (Boc) protected amino acids, [4-[α-(2′,4′-dimethoxyphenyl) Fmoc aminomethyl]enoxy] acetamidonorleucyl-MBHA resin (Rink amide MBHA resin), Fmoc-Glu(OtBu)-Wang resin and 2-(1H-benzotriazol-1-yl)-1,1,3,3-tetramethyluronium hexafluorophosphate (HBTU) were purchased from NovaBiochem and ABCR. Coverglasses and tissue culture plates (24-well) were purchased from Deckglaser and BD. All other chemicals and materials used were analytical grade and obtained from Invitrogen, Fisher, Merck, Alfa Aesar and Sigma-Aldrich. TGF-β, differentiation media and Collagen type I (C7661) were purchased from Sigma. Live/Dead Assay (L3224), Alamar Blue and other cell culture materials were purchased from Invitrogen. Antibodies were purchased from Abcam.

2.3.2 Synthesis and characterization of peptide amphiphile molecules

Fmoc solid phase peptide synthesis method was performed to synthesize Lauryl-Val-Val-Ala-Gly-Glu-Asp-Lys-(p-sulfobenzoyl)-Ser-Am (GAG-PA), Lauryl-Val-Val-Ala-Gly-K-Am (K-PA), Lauryl-Val-Val-Ala-Gly-Glu-Arg-Gly-Asp (RGD-PA), and Lauryl-Val-Val-Ala-Gly-E (E-PA). Rink amide MBHA resin (for GAG-PA and K-

PA), Fmoc-Glu-(OtBu)-Wang resin (for E-PA) and Fmoc-Asp-(OtBu)-Wang resin (for RGD-PA) were used as solid supports. All amino acid couplings were performed with 2 equivalents of Fmoc-protected amino acid, 1.95 equivalents of HBTU and 3 equivalents of N, N-diisopropylethylamine (DIEA) in DMF for 3 h. 20% piperidine/dimethylformamide (DMF) solution and 10% acetic anhydride−DMF solution were used for Fmoc deprotections for 20 min and acetylate the unreacted amine groups after each coupling step, respectively. Lauric acid as the source of the terminal lauryl group was coupled similar to amino acids. For GAG-PA synthesis, sulfobenzoic acid was added to the lysine side chain; lysine residues with 4-methytrityl (Mtt) side chain protection was used for the selective deprotection of amine groups. Mtt removal was performed by shaking resins for 5 min in TFA: TIS: H_2O: DCM in a ratio of 5:2.5:2.5:90. The cleavage of the peptides from the resin and deprotection of acid labile protected amino acids were carried out with a mixture of trifluoroacetic acid (TFA):triisoproplysilane (TIS):water in a ratio of 95:2.5:2.5 for 2.5 h. Excess TFA was removed by rotary evaporation. Ice-cold diethyl ether was used to triturate the remaining residue and the resulting white pellet was freeze-dried. Peptide amphiphile molecules were identified and analyzed by reverse phase HPLC on an Agilent 6530 accurate-Mass Q-TOF LC/MS equipped with an Agilent 1200 HPLC. K-PA was purified on an Agilent 1200 HPLC system by using a Zorbax prepHT 300CB-C8 column with a water–acetonitrile (0.1% TFA) gradient. GAG-PA, E-PA and RGD-PA have acidic characters, so Agilent Zorbax Extend-C18 (50 x 2.1 mm) column with a water/acetonitrile mixture (0.1% NH_4OH) was used. Their purification was performed on a Zorbax Extend C18 prep-HT with a water/acetonitrile (0.1% NH_4OH) gradient.

2.3.2 Preparation and characterization of self-assembled peptide gels for 3D cell culture experiments

Negatively charged PA solutions (GAG-PA, E-PA, RGD-PA) were prepared in cell culture medium (DMEM+10% FBS), while positively charged PA solutions were prepared in 0.25 M sucrose solution. For nanofiber formation, Lauryl-VVAGEGD-K (p-sulfobenzoyl)-S-Am (GAG-PA), Lauryl-VVAGRGD (RGD-PA) and Lauryl-VVAGK (K-PA) were mixed at a 3:1:5 molar ratio in order to form a GAG-mimetic peptide hydrogel. In a similar manner, Lauryl-VVAGE (E-PA), Lauryl-VVAGRGD (RGD-PA) and Lauryl-VVAGK (K-PA) were mixed at a 3:1:5 molar ratio for non-bioactive hydrogel formation. Mesenchymal stem cell pellets were suspended in RGD-PA solution (in culture medium) and mixed inside wells alongside either GAG-PA or E-PA with K-PA to produce 3D GAG-nanofiber (composed of GAG-PA/RGD-PA/K-PA) and E-nanofiber (composed of E-PA/RGD-PA/K-PA) scaffolds (Table 2.1). 3 mL of cell medium was added to the wells and the gels were incubated for 30 min at 37 °C. Collagen I (Life Technologies) gel was used as control.

Table 2. 1 3D PA gel combinations and bioactive groups presented on the nanofibers

PA Gels	Combinations	Bioactive Epitopes
GAG-Gel	GAG-RGD-K	GAG-mimetic/SO_3 group-functionalized/RGD epitope
E-Gel	E-RGD-K	RGD epitope

For SEM imaging, 3D peptide gels with cells were washed with PBS and fixed with 2% glutaraldehyde/PBS for 2 h. Peptide gels without cells were also prepared at identical concentrations to analyze the changes in the structural features of hydrogels in the presence of cells. Following three washing steps with PBS, samples were dehydrated in graded ethanol solutions, starting with 20% ethanol and proceeding to absolute ethanol for 10 min at each step. Samples were dried with a Tourismis Autosamdri-815B critical point drier, coated with 10 nm Au/Pd and imaged with a FEI Quanta 200 FEG SEM.

TEM analysis was performed with a FEI Tecnai G2 F30 TEM at 200 kV. A high-angle annular dark field (HAADF) detector was used for images taken in STEM mode. 7 mM of GAG and E-PA gel nanofiber systems were first diluted fifty-fold and then dropped on a 200-mesh copper TEM grid. Samples were left at room temperature for 7 min, stained by 2 wt % uranyl acetate for another 2 min and air dried prior to TEM imaging.

CD measurements were performed to analyze the secondary structures of PA nanofibers. A Jasco J-815 CD spectrophotometer was used for CD analysis. All samples were measured at hundred-fold dilutions of concentrations used in cell culture experiments. For each measurement, 300 μL of PA material was transferred into a 1 mm quartz cuvette, which was inverted gently to mix the sample without damaging the assembled nanostructures. Spectra were obtained at room temperature at a range of 300 nm to 190 nm, with a data interval of 1 nm and a scanning speed of 100 nm/min. The results are expressed as mean residue ellipticity and converted to the unit of $deg.cm^2.dmol^{-1}$.

Oscillatory rheology measurements were performed with an Anton Paar Physica MCR301 system. A 25 mm parallel plate with a gap distance of 0.5 mm was used at 25 °C for all measurements. The total gel volume was adjusted as 160 µL. PA solutions for 3D cell cultures were freshly prepared as 10 mM K-PA, 6 mM GAG-PA, 6 mM E-PA, and 2 mM RGD-PA, and then sonicated for 30 min. Gels were prepared using the GAG-RGD-K-PA and E-RGD-PA combinations. The negatively charged PA (GAG-PA or E-PA) was first loaded at the center of the stage and mixed with RGD-PA; the positively charged K-PA was then mixed with the sample in a spiral pattern. The upper plate was adjusted to the 0.5 mm position and the gel was incubated in this position for 15 min prior to measurement. For strain sweep measurements, angular frequency was kept constant at 10 rad/s, and strain was increased between 0.1 and 100%. Storage and loss moduli were recorded at each strain value. All rheology measurements were performed on gels with and without cells with three replicates.

2.3.3 3D cell culture and maintenance

rMSCs (rat mesenchymal stem cells, Invitrogen S1601-100) at passage 8 were used in all 3D cell culture experiments, including viability, rheology, GAG deposition and differentiation assays. rMSCs were initially cultured in DMEM supplemented with 10% FBS (Maintenance Media) in tissue culture plates at standard culture conditions (at 37 °C under 5% CO_2). After one day of incubation, maintenance medium (MT) was replaced with MT or DMEM supplemented with 2% FBS (low FBS medium). Maintenance medium supplemented with 10 mM β-glycerophosphate, 0.2 mM ascorbic acid and 100 nM dexamethasone was used for osteogenic differentiation on tissue culture plate (TCP).

2.3.4 Viability analyses

3D cell cultures were prepared in 24 well plates in MT medium, and cell viability was analyzed by Alamar Blue (Invitrogen) and Live/Dead (Life Technologies) assays. 5 x 10^5 rMSCs were seeded into gels and their viability was measured at days 3, 7 and 14 by measuring the fluorescence and absorbance of the reagent by spectrophotometry for the Alamar Blue assay, and imaging the cells by fluorescence microscopy and confocal microscopy for the Live/Dead Assay.

2.3.5 Sulfated glycosaminoglycan deposition analysis

Quantification of sulfated glycosaminoglycans was done by dimethylmethylene blue assay. Cell cultures were digested in papain digestion buffer (100 mM sodium phosphate buffer/10 mM Na_2EDTA/10 mM L-cysteine/0.125 mg/mL papain) overnight at 65 °C, and total DNA amount per gel was measured with a Qubit dsDNA quantitation kit (Invitrogen) to be used to normalize the sulfated glycosaminoglycan content. To produce standard curves, diluted chondroitin sulfate standards (from 0 to 35 μg mL^{-1}) were prepared for DMMB assay. 100 μL of DMMB solution (16 mg L^{-1}1,9-dimethylmethylene blue, 40 mM glycine, 40 mM NaCl, 9.5 mM HCl, pH 3.0) was added to 40 μL of papain-digested solutions and to standard samples. Then, optical densities (ODs) of the solutions were measured at 525 nm wavelength on a microplate reader. The absorbance of the control groups (gels without cells) was subtracted from the absorbance values of the experimental groups.

2.3.6 Gene and protein expression analysis

Gene expression analyses were performed by amplifying markers for chondrogenesis (Sox-9 and collagen II) and osteogenenesis (collagen I and Runx-2) by qRT-PCR.

Total RNAs of rMSCs in 3D PA gels were isolated using TRIzol (Invitrogen) according to the manufacturer's instructions. Yields and purities of extracted RNA were assessed by Nanodrop 2000 (Thermoscientific). Primer sequences were designed using Primer 3 software (Table 2.2). cDNA synthesis from RNA and qRT-PCR were performed using SuperScript III Platinum SYBR Green One-Step qRT-PCR Kit according to manufacturer's protocol. Reaction conditions were briefly as follows: 55 °C for 5 min, 95 °C for 5 min, 40 cycles of 95 °C for 15 s, 60 °C for 30 s, and 40 °C for 1 min, followed by a melting curve to confirm product specificity. Reaction efficiencies were evaluated for each primer set through standard curves using 5-fold serial dilutions of total RNA. For the analysis of expression, primary gene expression data were normalized by the expression level of GAPDH. A comparative Ct method was used to analyze the results.

Table 2. 2 Primers used in qRT-PCR analysis

Gene	***Primers*** ***Forward and Reverse***
Collagen I	5′- GAATATGTATCACCAGACGCAGA-3′
	5′- GGACATCTGGGAAGCAAAGT-3′
Collagen II	5′- CGAGGTGACAAAGGAGAAGC-3′
	5′- TCCCGGTCTTCATGGGACTA-3′
Runx-2	5'-GGACGAGGCAAGAGTTTCACT-3'
	5'-CCCTAAATCACTGAGGCGGT-3'

Sox-9	5′- CCACCCCGATTACAAGTACC-3′
	5′- CAGCCACCTGGGACTCTAA-3
Gapdh	5’- GTGCCAGCCTCGTCTCATA-3’
	5’- AACTTGCCGTGGGTAGAGTC-3’

Flow cytometry was performed to better quantify the differentiation potential of rMSCs in PA gels; expression of Sox-9 and Runx-2 proteins were analyzed to evaluate whether cells within gels have committed into osteogenic or chondrogenic lineages. Prior to flow cytometry analysis, the gel construct was disintegrated by collagenase/trypsin treatment and a cell strainer (Falcon®) was used to isolate cells from gels. The supernatant was then collected and centrifuged at 2500 rpm for 5 min. The cell pellet was washed twice with PBS, resuspended and fixed with 4% paraformaldehyde for 15 min at room temperature. The solution was then centrifuged at 2500 rpm for 5 min., and the cell pellet was resuspended and permeabilized in 0.2% Tween-20/PBS for 15 min at room temperature. A primary antibody solution of either Sox-9 [Anti-Sox9 antibody, (ab185230)] or Runx-2 [Anti-Runx2 antibody (ab76956)] or their corresponding isotypes, rabbit monoclonal IgG (ab172730) and mouse monoclonal IgG2a (ab170191), was prepared in 3% BSA/PBS solution at concentrations recommended by the manufacturer (Abcam) and used to stain the cells for 1 h. After primary antibody staining, cells were washed with permeabilizing solution, pelleted by centrifugation and stained with secondary antibodies [Goat Anti-Mouse IgG H&L (Alexa Fluor® 488) (ab150113) for Runx-2 and Goat Anti-Rabbit IgG H&L (Cy5 ®) preadsorbed (ab97077) for Sox-9] for 1 h. After washing

twice with permeabilizing agent, the cells were again pelleted by centrifugation and resuspended in PBS prior to cytometry analysis. Mesenchymal stem cells grown in corresponding differentiation media (either osteogenic or chondrogenic media) were used as positive controls. A BD Accuri^{TM} C6 flow cytometer system was used for cytometry and at least 50,000 events were analyzed for the measurements. For data analysis, BD Accuri^{TM} C6 software was used according to the manufacturer's instructions.

2.3.7 Statistical analysis

All data are presented as mean ± SEM (standard error of mean). The significance of differences between groups was determined with either one-way or two-way analysis of variance (ANOVA) with Tukey's/Bonferroni post tests. Differences were considered significant at $p < 0.05$, except where noted.

2.4 Results and Discussion

2.4.1 Design, preparation and characterization of self-Assembled PA molecules and 3D PA gels

The 3D gels provide a native-like microenvironment for the growth and differentiation of cells, thereby filling the gap between in vitro scaffold systems and in vivo tissue architectures. In this work, we studied the potential of a glycosaminoglycan-mimetic peptide nanofiber system for the induction of mesenchymal stem cell differentiation into osteo/chondrogenic lineages. Peptide nanofiber gels resemble the native tissue in having a nanofibrous structure akin to the collagenous fiber network found in the extracellular matrix. In addition to sharing a fibrous nature, both hydrogel and ECM environments are also rich in water and

present functional groups such as sulfonate, carboxylate and hydroxyl moieties (Figure 2.1).

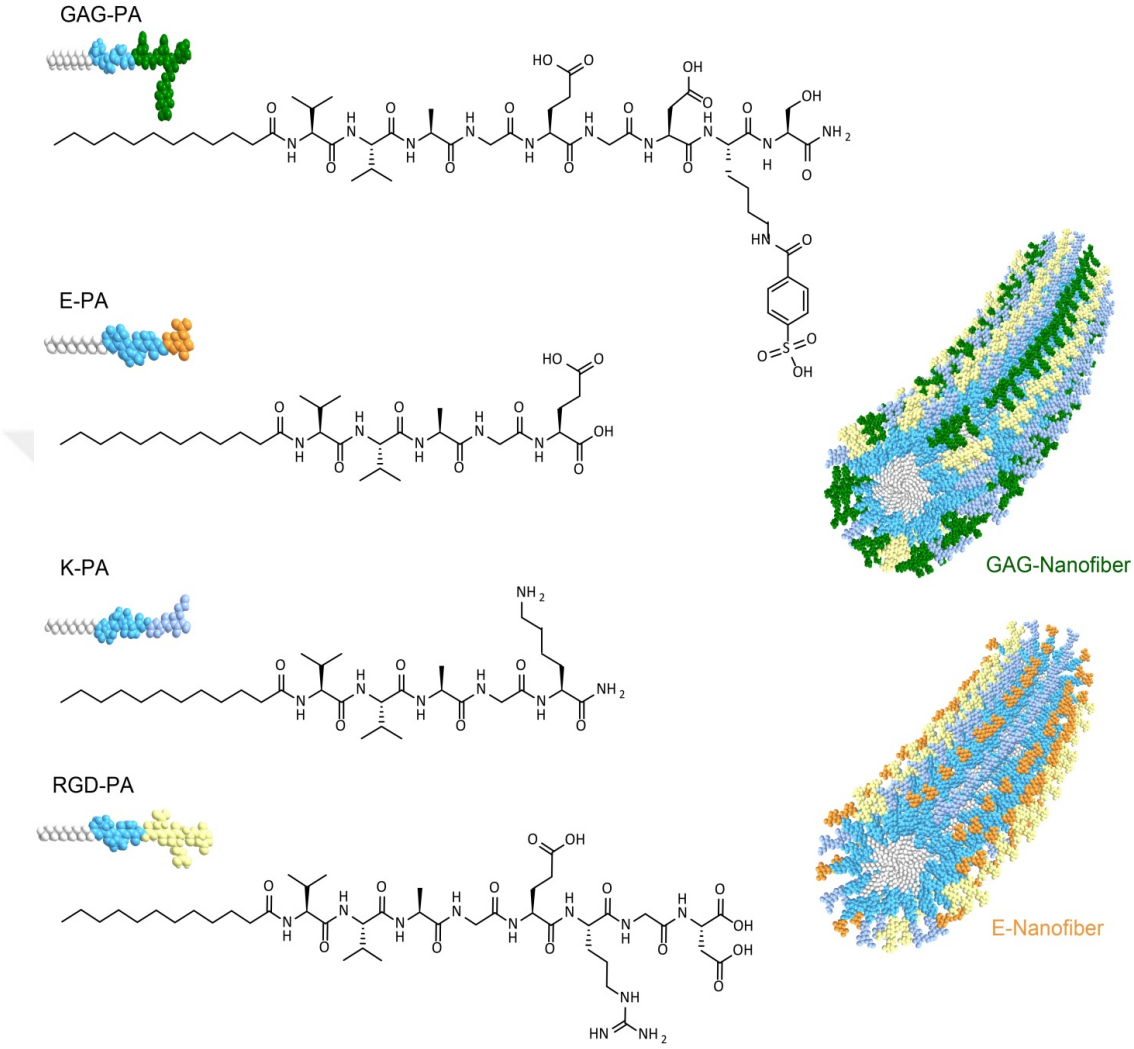


Figure 2. 1 Chemical structures of peptide amphiphile molecules. GAG-PA: Lauryl-VVAGEGD-K (p-sulfobenzoyl)-S; E-PA: Lauryl-VVAGE, K-PA: Lauryl-VVAGK; RGD-PA: Lauryl-VVAGRGD.

Two hydrogels were used for the present study: GAG-gel (GAG-PA/RGD-PA/K-PA) contains bioactive residues, while the control E-gel (E-PA/RGD-PA/K-PA) was used as experimental control (Table 2.1). GAG-gel was decorated with sulfonate, hydroxyl and carboxylate groups to imitate the structure of heparan sulfate

glycosaminoglycans, while the E-gel presented carboxylate and hydroxyl groups alone and lacked sulfonate groups. Both gels were formed by supramolecular interactions between peptide amphiphile molecules, which produce β-sheet containing nanofibers through self-assembly. This process is driven largely by charge neutralization between oppositely charged peptide amphiphiles, and further influenced by cohesive forces such as hydrogen bonding and van der Waals, hydrophobic and electrostatic interactions [1, 68]. Both gels contain RGD-PA, a bioactive sequence that enhances the adhesion of cells to the scaffold through integrin-mediated interactions between nanofiber surfaces and the cell membrane. The RGD sequence has been chosen as a well-established epitope for cell adhesion [69, 70], and in our optimization studies, we have observed that the presence of the RGD sequence (at a 1:7 RGD-PA: gel ratio) increases the attachment and survival of cells in peptide nanofiber gels.

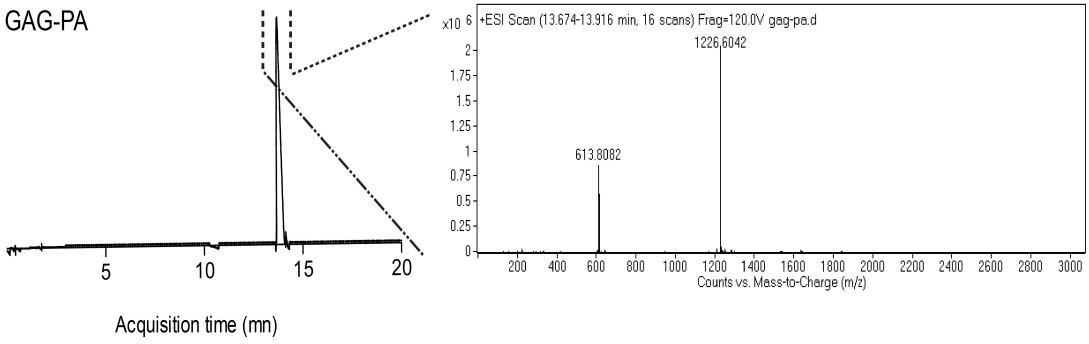


Figure 2. 2 Liquid chromatogram and mass spectra of GAG-PA, $[M-H]^-$ (calculated) = 1224.58, $[M-H]^-$ (observed) = 1226.6042 (observed $[M-2H]^{-2}$ m/z = 613.6082).

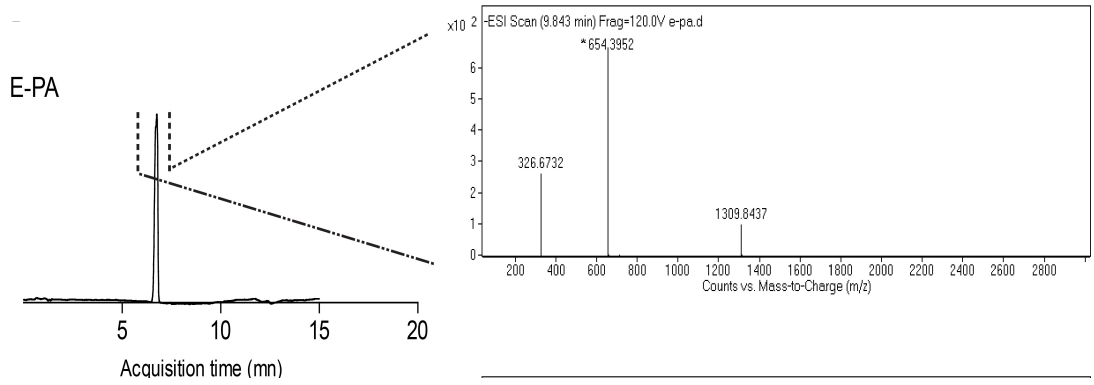


Figure 2. 3 Liquid chromatogram and mass spectra of E-PA, $[M-H]^-$ (calculated) = 654.4156, $[M-H]^-$ (observed) = 654.3952 (observed $[M-2H]^{-2}$ m/z = 326.6732 $[2M-H]^-$ m/z = 1309.8437).

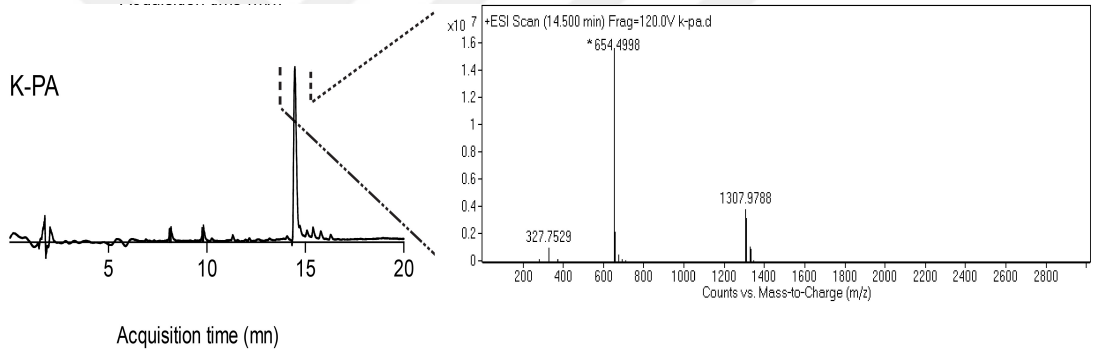


Figure 2. 4 Liquid chromatogram and mass spectra of K-PA, $[M+H]^+$ (calculated) = 654.4840, $[M+H]^+$ (observed) = 654.4998 (observed $[M+2H]^{+2}$ m/z = 327.7529, $[2M+H]^+$ = 1307.9788).

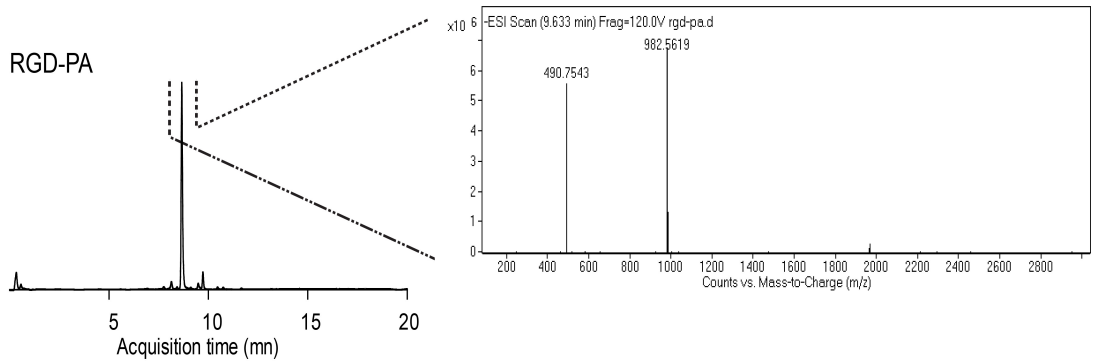


Figure 2. 5 Liquid chromatogram and mass spectra of RGD-PA, $[M+H]^+$ (calculated) = 983.57, $[M+H]^+$ (observed) = 982.5619 (observed $[M+2H]^{+2}$ m/z = 490.7543).

Peptide amphiphile molecules were characterized by liquid chromatography–mass spectrometry (LC–MS) and purified by preparative HPLC prior to use (Figures 2.2, 2.3, 2.4, 2.5). STEM (scanning transmission electron microscopy) of negatively stained co-assembled peptide nanofibers (Figure 2.6) revealed that two nanofiber networks were very similar to each other and that the peptide fibers comprising the gels had high aspect ratios and nanometer-scale diameters (10 nm-20 nm). The sizes of these nanofibers are similar to the fibrous collagen and glycoproteins found in the ECMs of both cartilage and bone[53, 71]. SEM images of gels (Figure 2.7) demonstrated the formation of a porous nanofiber network following the co-assembly of PA molecules. The secondary structures of both hydrogels were also analyzed by CD (Figure 2.8). CD spectra of both GAG- and E-gels were found to correspond to the β-sheet conformation, with a chiral absorbance at ~220 nm (Figure 2.8). In addition, pure GAG-PA, E-PA and K-PA molecules were not observed to form β-sheets at analyzed concentration. However, the CD spectrum of pure RGD-PA was found to show distinctive β-sheet features, which can be attributed to the

self-neutralization of this peptide due to the decreased electrostatic repulsion between peptide amphiphile molecules in the cell medium. As the gels used for cell culture experiments were higher in concentration (up to 7 mM = ~1% w/v) compared to those in CD measurements, β-sheet formation is expected to be prominent in all hydrogel scaffolds used. SEM images also suggest that the peptide nanofibers form a mesh-like structure that is similar to the fibrous environment of the extracellular matrix and therefore conductive to the attachment of cells.

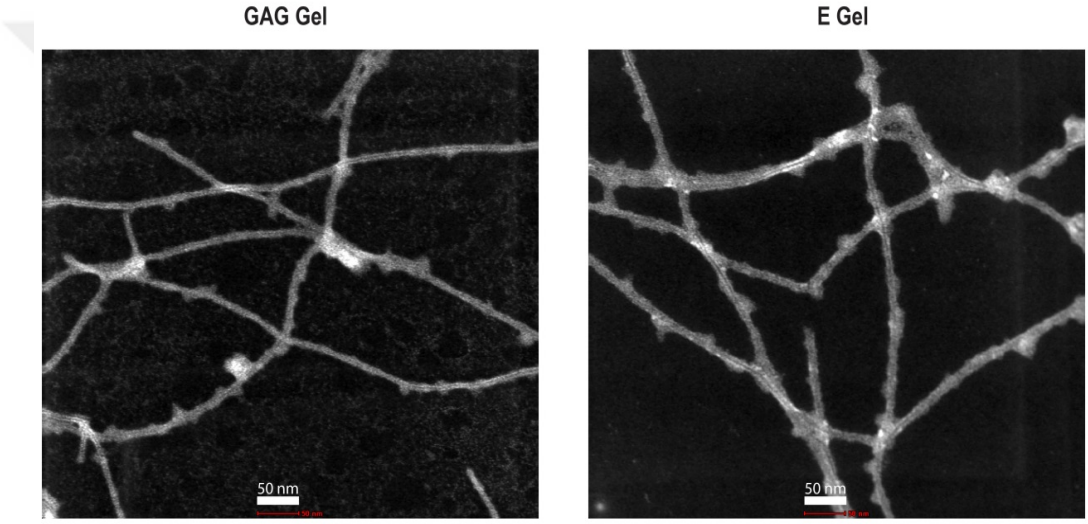


Figure 2. 6 STEM images of GAG and E nanofibers, scale bar = 50 nm. (B) SEM images of GAG- and E-gels, scale bar = 5 μm.

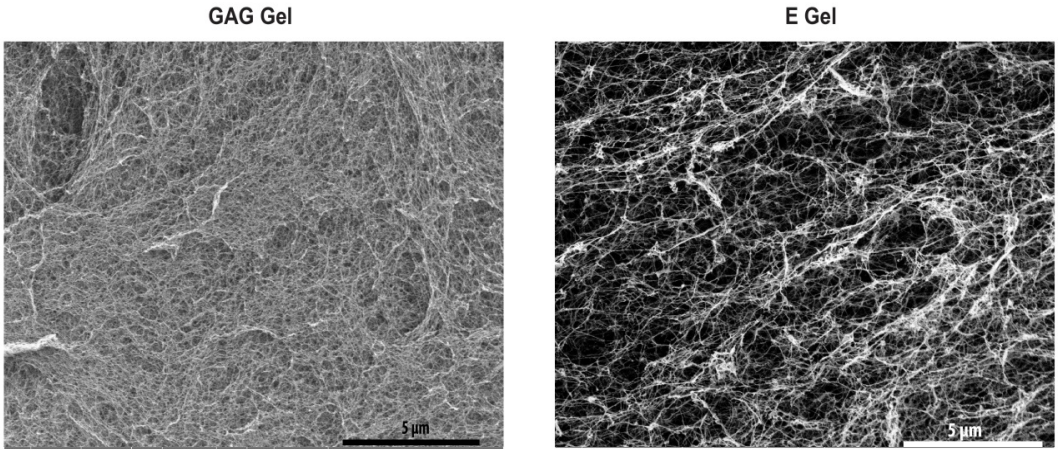


Figure 2. 7 SEM images of GAG- and E-gels, scale bar = 5 µm.

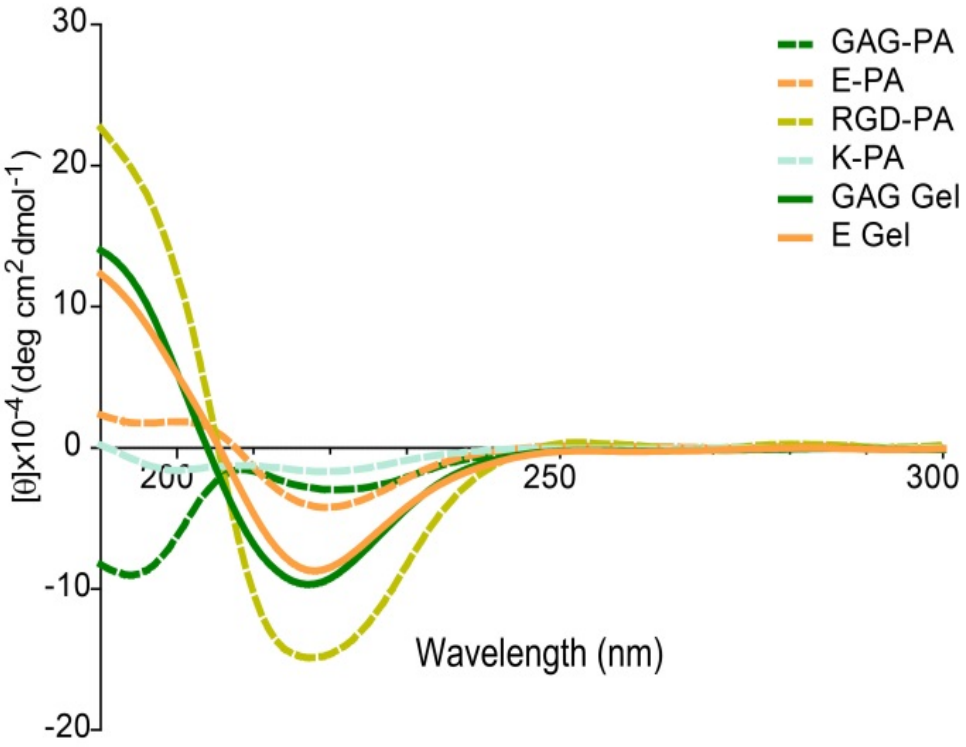


Figure 2. 8 CD spectra of peptide amphiphile solutions and gels.

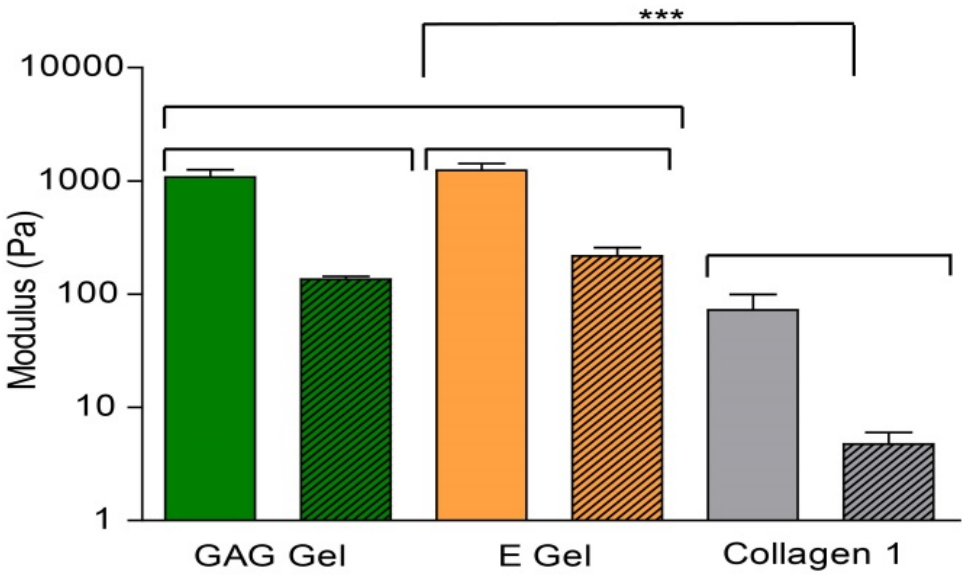


Figure 2. 9 Rheological analyses of peptide nanofiber gels and collagen I gel, ***p<0.001. Equilibrium moduli of the collagen I gel are significantly less than the equilibrium moduli of peptide nanofiber gels.

Oscillatory rheology analyses were performed to assess the mechanical properties of peptide nanofiber gels. Time sweep, frequency sweep and strain sweep rheology analyses were conducted in order to investigate the gel formation mechanics and viscoelastic properties of the scaffold material (Figure 2.9 and Figure 2.10). Storage moduli of both GAG- and E-gels are found to be higher than their loss moduli at their cell culture concentrations, suggesting that the materials are hydrogels in the strict sense. In addition, mechanical analyses were performed for gel niches containing encapsulated cells, and gels were observed to experience a slight decrease in stiffness moduli after 1 and 14 days of cell culture (Figure 2.11 and Figure 2.14). This can be attributed to their degradation by cellular enzymes and partial replacement with the native extracellular depositions of cells. Collagen I gel, a scaffold commonly used in bone and cartilage regeneration studies, was also used as

a control 3D gel environment for comparison [72]. Despite their mechanical properties to be used as scaffold in cell culture studies, collagen gels suffer from limitations such as immunogenicity, batch-to-batch variations and side effects resulting from viral and bacterial contamination, which are inherent to animal-derived scaffolds and necessitate the use of artificial matrices for the safe and efficient recovery of bone and cartilage injuries [73]. Equilibrium modulus values of peptide nanofiber gels and collagen I gel suggests that both GAG- and E-gels have similar moduli, while the modulus values associated with collagen I gel are significantly less than peptide gels. The higher storage moduli of peptide gels could be attributed to concentration differences, as higher polymer concentrations result in higher stiffness moduli. Differences in polymerization conditions, crosslinking degrees and molecular weights of peptide amphiphile molecules and collagen I also contribute to the discrepancy in the viscoelastic properties of their gels [74-76]. However, both control and bioactive peptide nanofiber gels are at the same concentration, display similar morphologies and exhibit comparable viscoelastic properties. As such, the possible bioactivity of the materials should be attributed to biochemical signatures presented in peptide gels rather than mechanical differences. Overall, rheological analysis revealed that the peptide amphiphile nanofibers displayed elastic solid-like behavior with high water content, which is consistent with the interwoven matrices both structures were observed to exhibit under electron microscopy imaging. In addition, the mechanical stability of the gels was strong enough to support cell growth in both peptide gels, which were found to exhibit similar elastic properties.

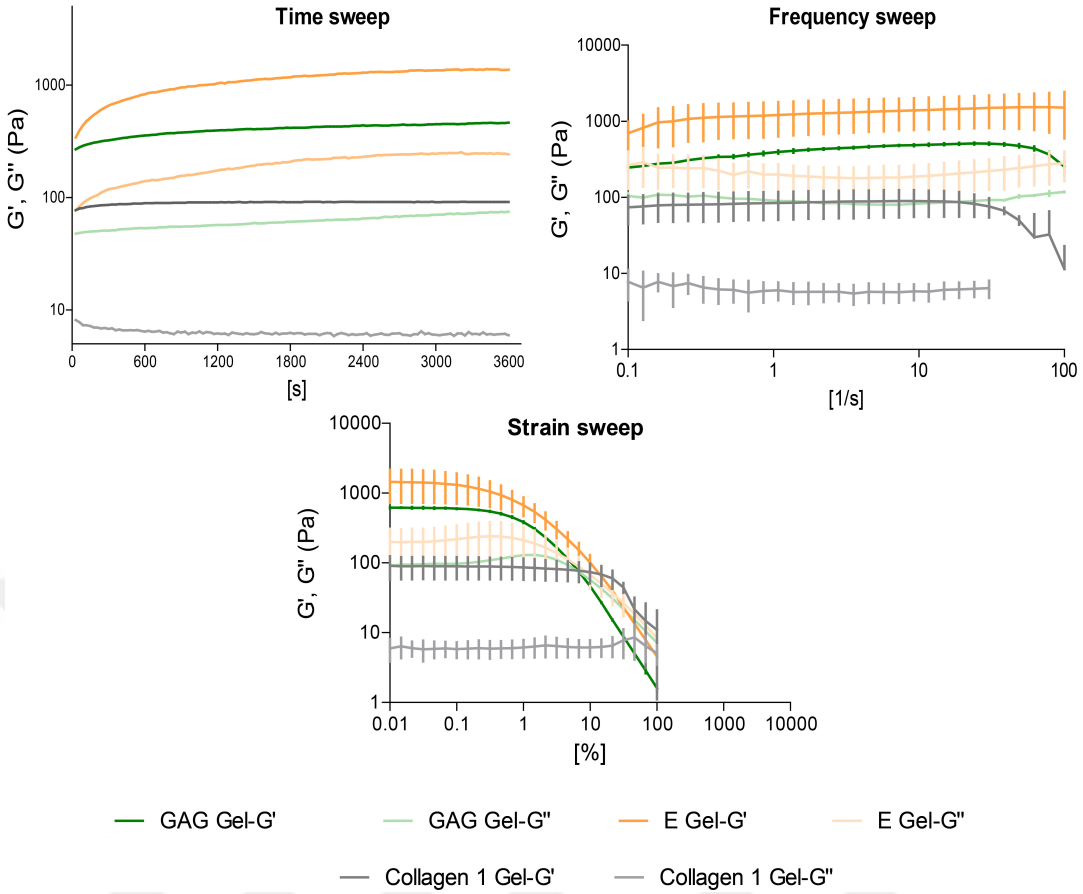


Figure 2. 10 Mechanical characterizations of PA gels by rheology. Equilibrium storage and loss moduli of GAG- and E-gels during time, frequency and strain sweeps.

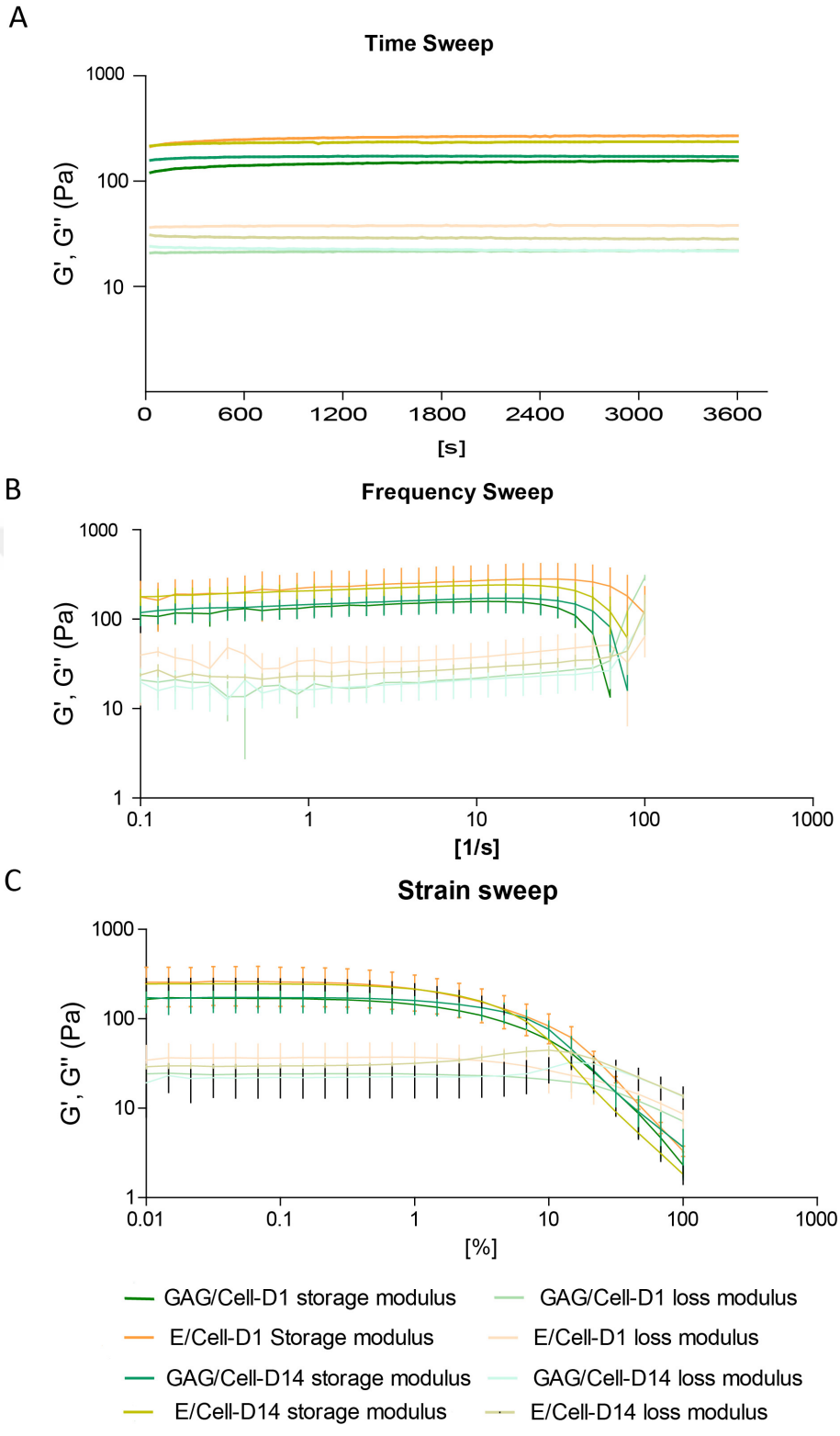


Figure 2. 11 Mechanical characterizations of GAG- and E-gel niche after 1 day and 14 days of cell culturing. Equilibrium storage and loss moduli of GAG- and E- gels during (A) time sweep, (B) frequency sweep, and (C) strain sweep.

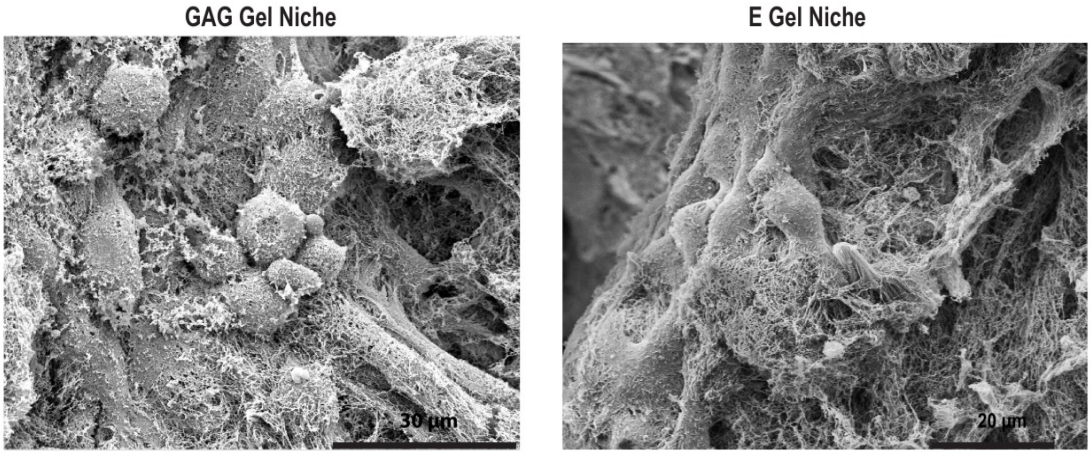


Figure 2. 12 SEM images of cells cultured within GAG- and E-gel niches at day 3, scale bar = 30 µm for GAG-gel and scale bar = 20 µm for E-gel.

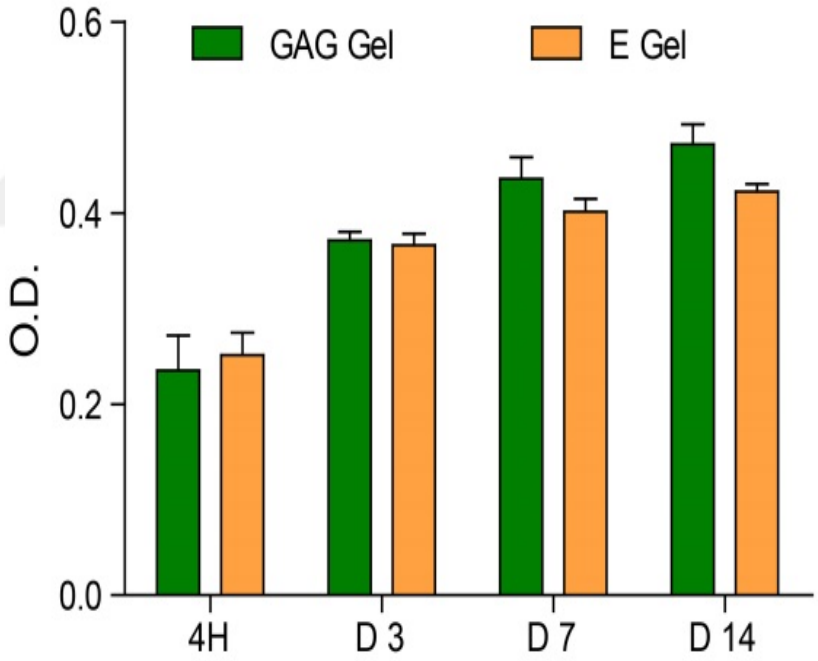


Figure 2. 13 Viability analyses of rMSCs within PA gel niches for 14 days (O.D. = optical density).

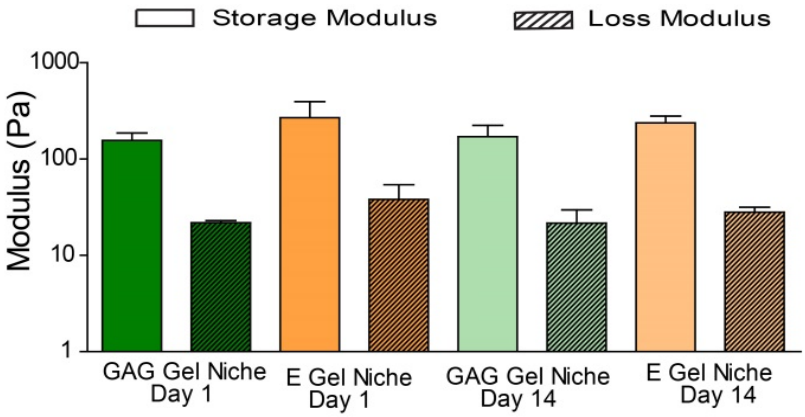


Figure 2. 14 Rheology analyses of peptide nanofiber gel niches incubated with cells for 1 day and 14 days.

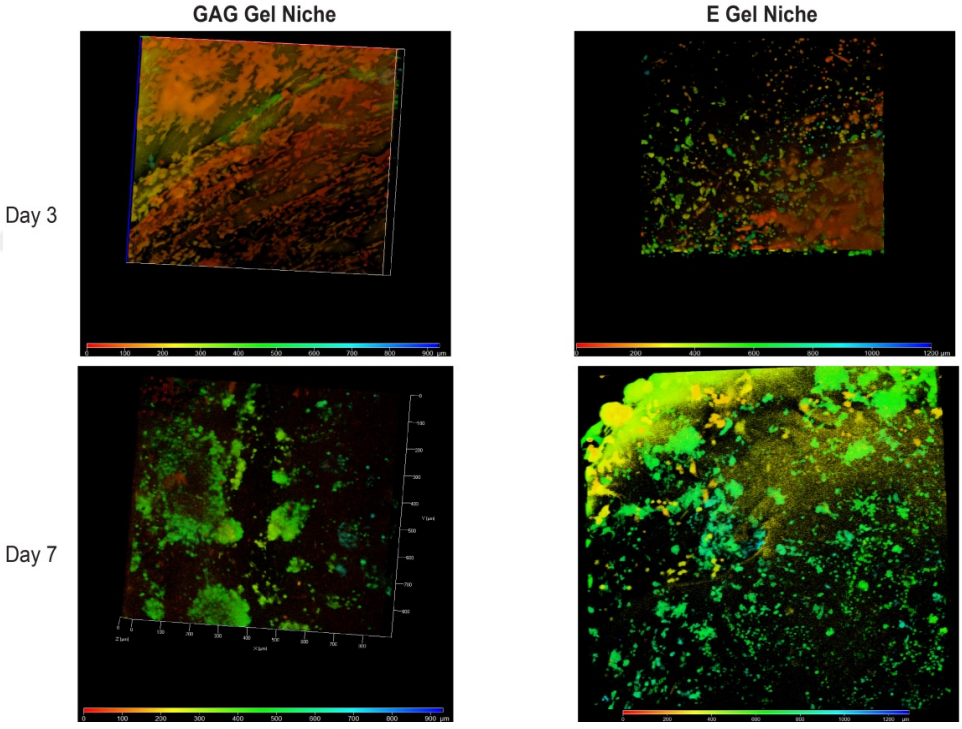


Figure 2. 15 Confocal microscopy analyses of cellular localization within peptide nanofiber gels following 3 and 7 days of culture. Colored-scale bars show the depth of gel niches; the corresponding cellular localizations are shown in depth-dependent colors (using a red to blue scale for surface-to bottom depth).

SEM images of gel niches (Figure 2.12) were acquired to evaluate the distribution and morphology of cells embedded within gels. The nanofiber network was observed to resemble native cartilage and bone ECMs, potentially providing mechanical support and instructive cues for cells. It should be stressed that while 3D microenvironments provide native-like material architectures for cells, they are often hindered by the insufficient transport of nutrients and waste products in and outside the scaffold [77]. In our design, however, the porous structure of gel niches facilitates nutrient and waste transport, as well as allowing cell migration to occur for cellular reorganization during differentiation (Figure 2.7 and Figure 2.12). Cells in gels displayed spherical morphologies similar to their *in vivo* condition, rather than the flattened shapes observed in 2D studies [77]. As such, 3D peptide nanofiber gels appear to exhibit an ECM-like structure that is suitable for supporting the attachment, viability and growth of cells.

2.4.2 3D peptide gels provide a biocompatible environment for MSCs

In vitro cell culture analysis of gels is vital for assessing their ability to induce the differentiation of stem cells towards a specific lineage. Cell-material interactions between mesenchymal stem cells and GAG-mimetic and non-mimetic gels were evaluated by optical, SEM and confocal microscopy. According to results of Alamar Blue assay, both GAG- and E-gels are biocompatible and support the growth and proliferation of cells (Figure 2.13). Live/Dead assay also showed that both living and dead cells were present in the scaffolds during 7 days of culture, and that the cells were distributed relatively uniformly within the gels (Figure 2.16). It is noteworthy that the 3D microenvironment of gels is much closer to the native tissue than 2D cell culture, which further enhances the survival of stem cells. In particular, the highly

porous structure of 3D scaffolds provides larger surface areas for cell attachment and proliferation, which enables the use of higher amount of cells in clinical applications [78]. However, in 2D control, most of the cells were dead at day 7 because of over confluency (Figure 2.16). Confocal analysis revealed that cells could migrate across the depth of the gel, and by day 7, exhibited a tendency to form clusters (Figure 2.15). The fact that extensive migration is possible within the 3D matrix suggests that cells may utilize proteolytic processes to locally modify matrix integrity [78]. As such, our system is suitable for facilitating the dynamic turnover of the extracellular matrix, which is necessary for the migration and remodeling of differentiating cells.

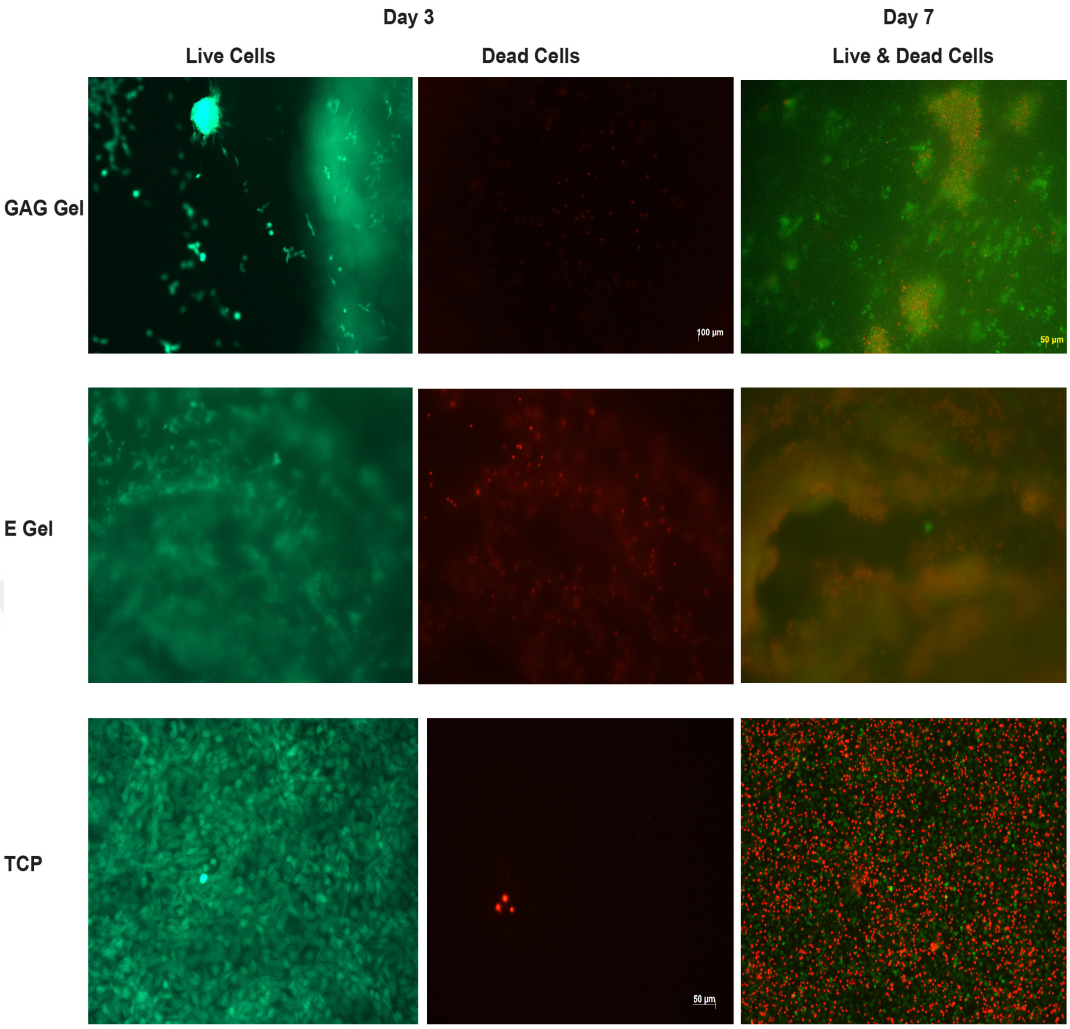


Figure 2. 16 Viability analyses of stem cells in 3D PA gel niches and cells on tissue culture plate by Live/Dead assay. Green cells are live cells, and red cells are dead cells.

Self-assembly is a major feature of supramolecular peptide amphiphile molecules and presents several opportunities in tissue engineering. The main advantage of self-assembling systems is their adaptive nature, as their primary sequence can be modified to a great extent without substantially altering the hydrogel's mechanical properties. In addition they provide a biocompatible, nanosized, porous, bioactive, and biodegradable gel environment that is well-suited for tissue engineering

applications [1, 79]. In contrast, other hydrogels used in regenerative medicine may suffer from drawbacks such as the lack of proper cell adhesion, insufficient bioactive signal delivery, non-biodegradability, constrained structural stability (e.*g.* for gas foaming), residual porogen problems (for solvent casting), and complex and high cost processing (for phase separation and photolithography) [80-86]. Self-assembling peptide systems therefore provide considerable advantages as artificial 3D scaffolds for tissue regeneration. In addition, peptide nanofiber gels can be used as injectable hydrogels to deliver cells into tissue defects, directly creating a cell/gel construct at the site of injury and allowing a more immediate tissue regeneration process compared to acellular scaffolds [87]. Both bone and cartilage tissue defects are especially suitable for injectable cell/gel systems.

2.4.3 Stem cell differentiation can be directed into chondrogenic and osteogenic lineages in 3D peptide gels

rMSCs were cultured on GAG-mimetic and non-mimetic gels for 7 days and their differentiation profiles were evaluated through the analysis of their morphology, gene expression levels, glycosaminoglycan and protein production by optical microscopy, qRT-PCR, DMMB and flow cytometry. The influence of GAG-PA nanofibers in 3D microenvironment was tested in tandem with different culture conditions to understand the processes underlying the lineage commitment of stem cells. Optical microscopy images of experimental groups suggest that mesenchymal stem cells in both GAG-PA and E-PA gels formed nodules, resulting in increased cell-to-cell interactions and cellular condensation (Figure 2.17). Cells embedded in the GAG-gel niche formed larger nodules when compared to E-gel in the presence of both types of culture media. For both cartilage and bone differentiation, nodule formation is an

important morphological change exhibited by stem cells, and is typically followed by mesenchymal condensation for the prefiguration of tissues. Therefore, morphology analysis suggests that stem cells in 3D gel environments follow the initial steps of osteo/chondrogenic differentiation. Upon this finding, differentiation capacities of mesenchymal stem cells at early (day 3) and middle/late (day 7) time periods were investigated in greater detail.

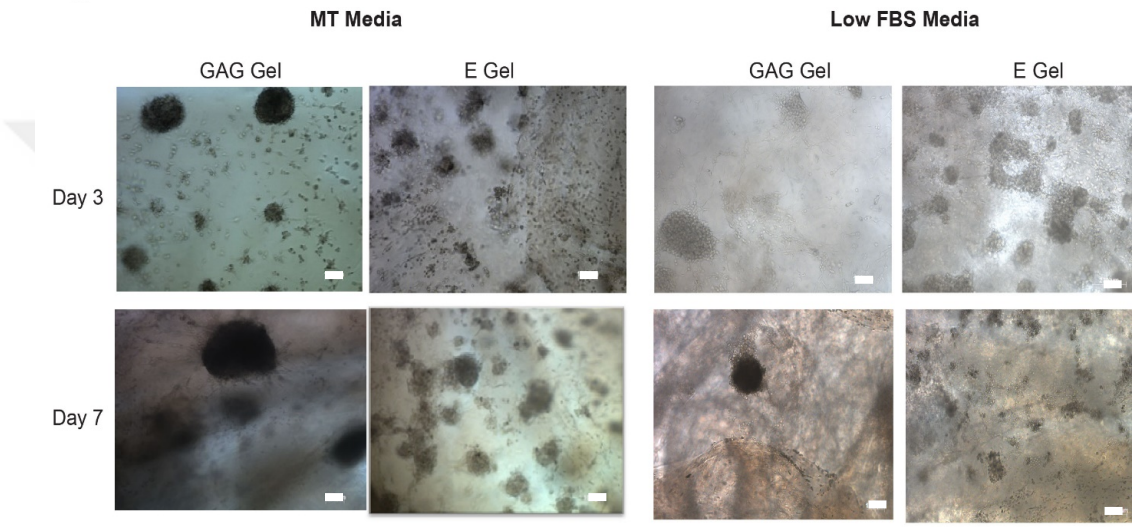


Figure 2. 17 Morphological tracking of cells in PA gel niches for 7 days, scale bars = 100 µm. (MT Media: 10% FBS containing growth media, Low FBS Media: 2% FBS containing media)

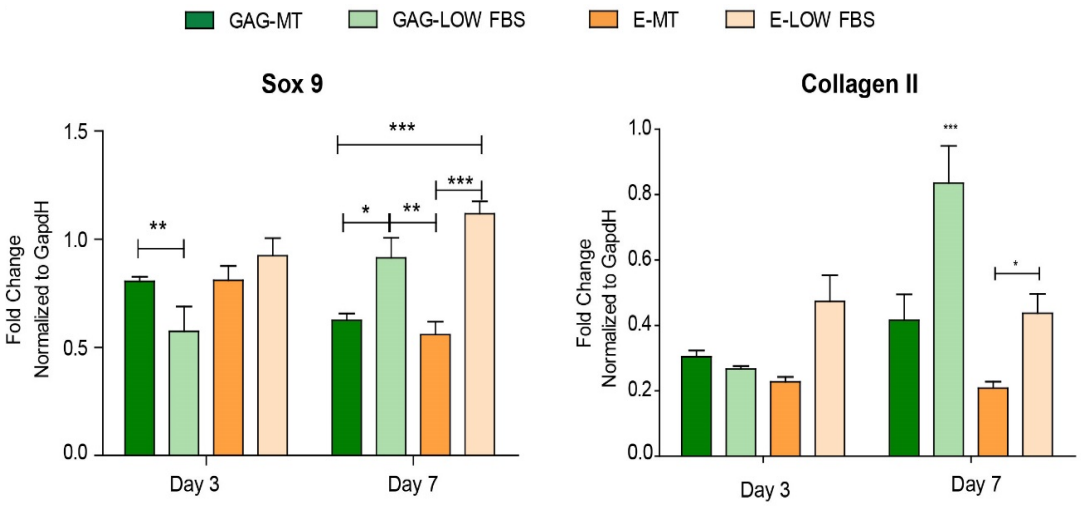


Figure 2. 18 Chondrogenic differentiation analyses by qRT-PCR. Expressions of Sox 9 and collagen II were quantified on days 3 and 7.

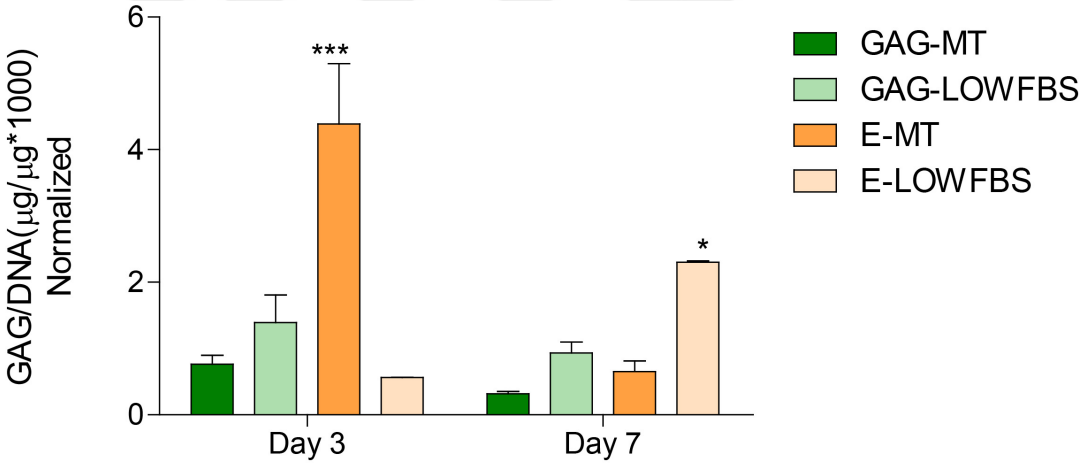


Figure 2. 19 Quantification of GAGs by dimethyl methylene blue (DMMB) assay on days 3 and 7 in both MT (10% FBS) and low FBS medium (Low FBS) (2% FBS). GAG concentrations were normalized to DNA. Error bars indicate SEM, n = 3, *p<0.05.

Cartilage differentiation was evaluated by the expression analysis of two cartilage specific markers, Sox-9 (early) and collagen II (middle/late), by qRT-PCR. A

significant difference was observed in the Sox-9 mRNA expression of GAG- and E-gel niches in maintenance medium and low-FBS medium (Figure 2.18): In the GAG-gel niche, the presence of low-FBS medium was found to downregulate Sox-9 expression at day 3, although this trend was reversed by day 7. In the E-gel niche, however, low-FBS medium increased Sox-9 expression at both days tested. Collagen II mRNA exhibited a trend similar to Sox-9, with a transient downregulation at day 3 followed by upregulation at day 7. Low-FBS media was observed to induce collagen II expression, but the level of fold changes exceeded 1 for only the E-low FBS group. In addition to the analysis of mRNA expressions, sulfated glycosaminoglycan production patterns were also investigated by using DMMB assay (Figure 2.19). The pattern of sulfated GAG production at day 7 was found to correlate with Sox-9 mRNA expression levels.

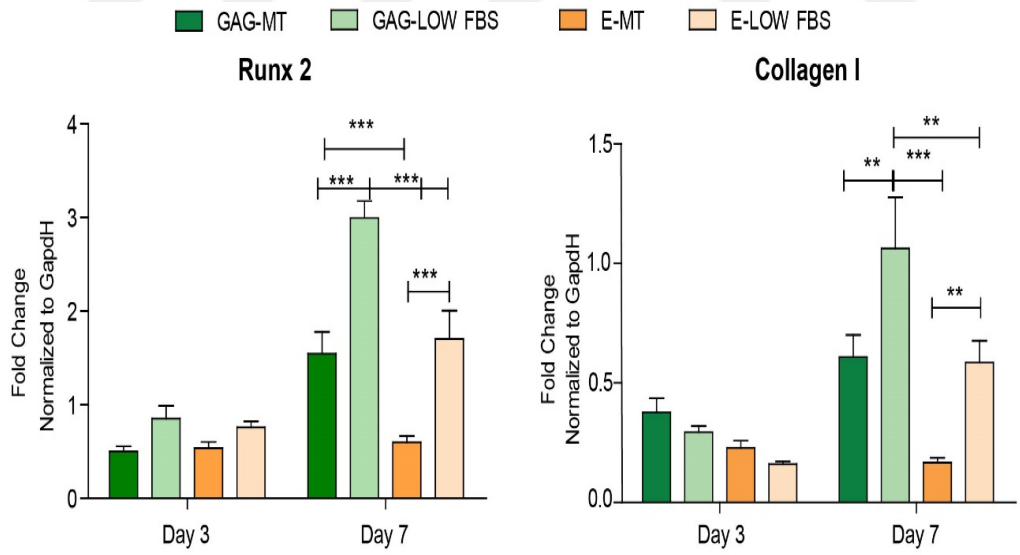


Figure 2. 20 Osteogenic differentiation analyses by qRT-PCR. Expressions of Runx 2 and collagen I were quantified on days 3 and 7.

Two markers, Runx-2 (early) and Collagen I (middle/late), were used for the evaluation of osteogenic differentiation (Figure 2.20). The pattern of expressions at day 7 was similar for both osteogenic markers, while the fold changes for Runx-2 expression were relatively higher compared to fold changes for Sox-9 expression. At day 3, no significant changes were observed for both markers across the groups. At day 7, however, expression levels of both osteogenic markers increased considerably in the GAG-gel group, suggesting that the combination of a GAG-like nanofiber scaffold and culture conditions had altered the differentiation pattern of the stem cells. This effect was especially pronounced in low FBS media. Indeed, the presence of a GAG-like nanofiber-containing culture environment and low levels of FBS can synergistically enhance the osteogenic differentiation of stem cells. Both culture conditions are also able to increase osteogenic differentiation to a lesser extent by themselves, as the GAG-gel group exhibited higher expressions of Runx-2 and collagen I compared to the non-bioactive scaffold, while cells in low-FBS medium likewise showed upregulated expressions of both genes compared to maintenance medium at day 7.

Expression profile analysis of cells revealed that the GAG-like scaffold instructs stem cells to differentiate into osteo/chondrogenic lineages in concert with the FBS concentration present in the growth medium, such that a reduction in the FBS concentration acts as an inducer for osteogenic differentiation. GAG mimetic signals, when grafted on peptide nanofibers, may therefore serve as insoluble ligands that are organized into a nanoscale spatial matrix and enable the differentiation of stem cells, while the FBS amount controls the direction towards which the cells are inclined to differentiate.

Overall, the investigation of stem cell differentiation into osteogenic and chondrogenic lineages in 3D scaffolds showed that peptide nanofiber gel niches may exhibit varying effects on the direction of lineage commitment. However, in addition to the differential effects of PA gels and culture conditions, the heterogenic features of mesenchymal stem cells may also contribute to the differentiation process. As such, the immunophenotypic features of the cultured cell population were also investigated to better understand the natural and induced variances in the differentiation capacities of stem cells.

2.4.4 Immunophenotypic characterization of stem cell differentiation into osteogenic and chondrogenic lineages

Analyzing the protein expression profile of mesenchymal stem cells is crucial for understanding the processes underlying the mechanism of their differentiation. However, one of the major problems of 3D cell culturing is the limitation of cellular and molecular analysis; for example, immunostaining of cells in 3D microenvironment is highly tricky and requires advanced imaging technology for quantification. In this study, we optimized a flow cytometer protocol for the immunophenotypic characterization of stem cells during their differentiation. Therefore, we were able to analyze the protein production level and quantify cellular populations to examine the lineage commitment of a cell population at the single-cell level. Since cellular differentiation patterns were previously observed to be evident on as early as the seventh day of culture, flow cytometer analyses were performed at day 7 for the immunophenotypic characterization of stem cells cultivated on PA gels in maintenance medium or low-FBS medium(Figure 2.21-Figure 2.24).

Sox-9 and Runx-2 antibodies were used to quantify cells as either chondro-committed or osteo-committed, respectively, and the percentile distribution of the cell population was calculated for each experimental group. Cells exposed to a combination of GAG-gel and maintenance medium were found to favor chondrogenesis instead of osteogenesis, exhibiting much higher Sox-9 expression than Runx-2. For other groups (GAG-gel/low FBS, E-gel/MT, E-gel/low FBS), however, cells with upregulated Runx-2 expression were more numerous, indicating a predominance of osteogenic commitment. The concentration of serum also had a substantial effect on the differentiation response, as both GAG-MT and E-MT combinations favored chondrogenesis to a greater extent than their low-FBS counterparts.

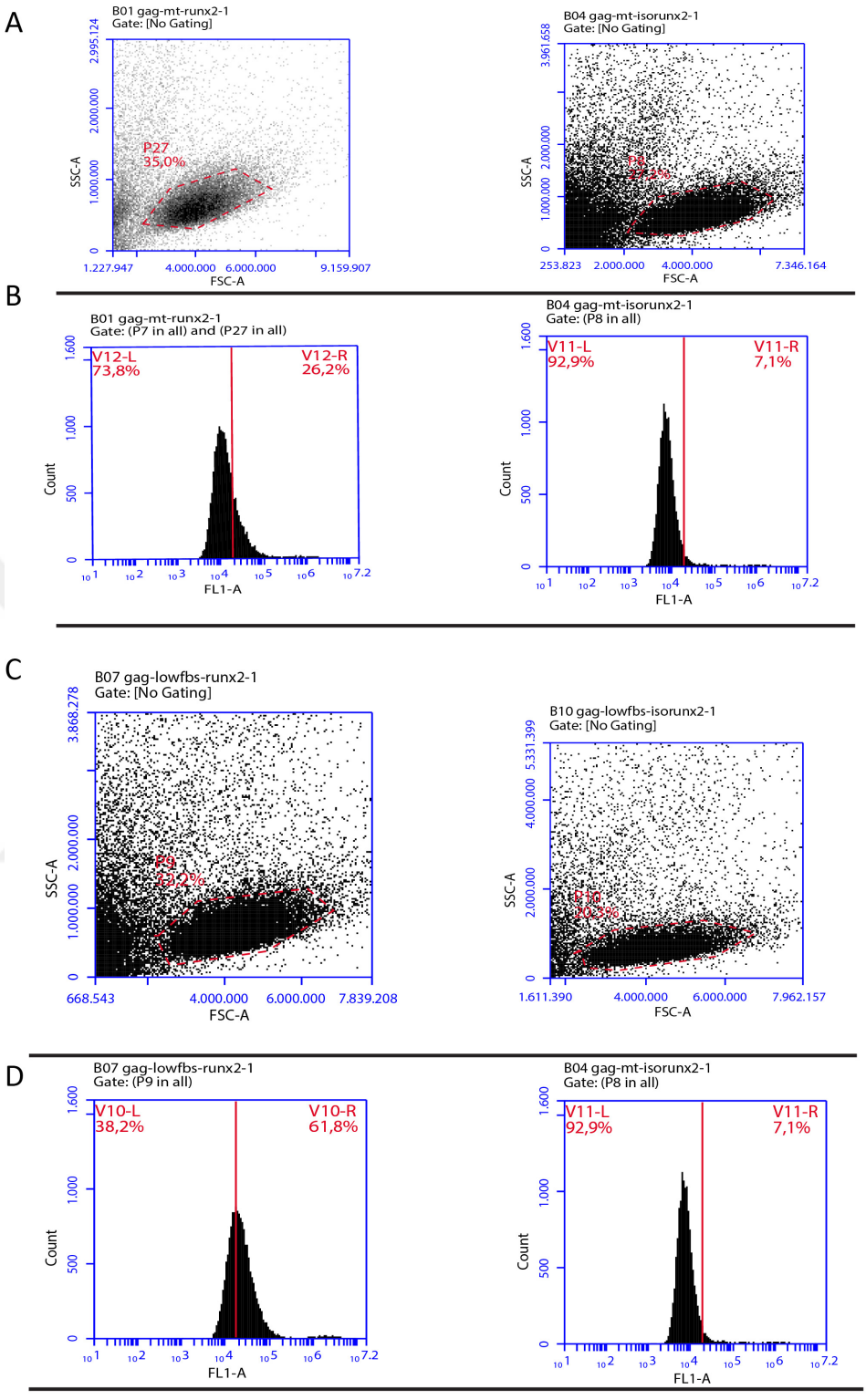


Figure 2. 21 Flow cytometry analyses of cells in GAG-gel within both MT and low FBS media. (A) Cell population and corresponding gating are shown for both Runx-2 and isotype labeling cells in GAG-MT niches. (B) Fluorescence signaling for

corresponding gated cell populations are shown for both Runx-2 and isotype labeling. Gating is applied for subtracting isotype labeling from Runx-2 labeled populations, and percent of remaining part is considered specifically stained with Runx-2 antibody. (C) Cell population and corresponding gating are shown for both Runx-2 and isotype labeling of cells in GAG-low FBS niches. (D) Fluorescence signaling for corresponding gated cell populations is shown for both Runx-2 and isotype labeling. Gating is applied for subtracting isotype labeling from Runx-2 labeled populations, and percent of remaining part is considered specifically stained with Runx-2 antibody.

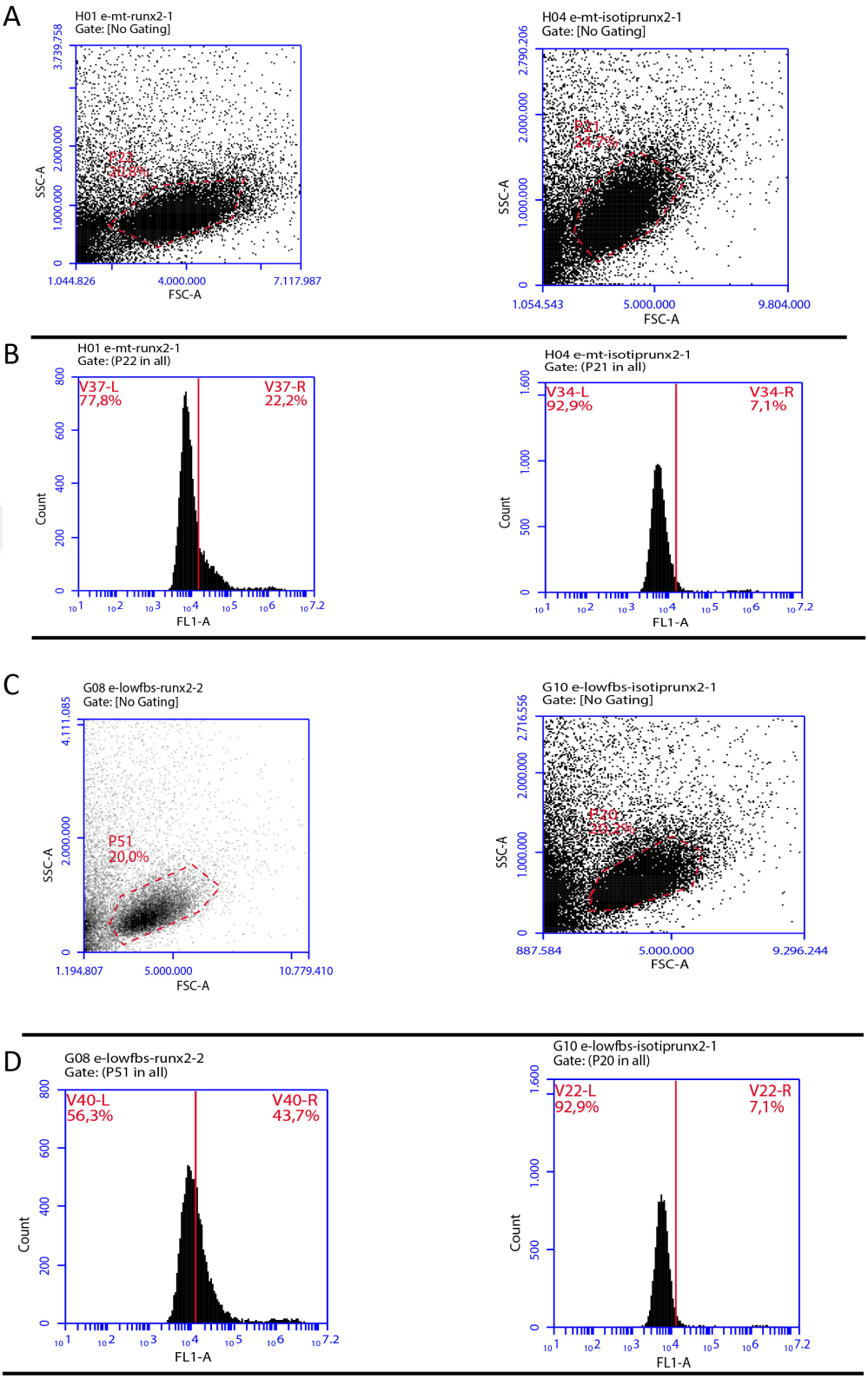


Figure 2. 22 Flow cytometry analyses of cells in E-gel within both MT and low FBS media. (A) Cell population and corresponding gating are shown for both Runx-2 and

isotype labeling cells in E-MT niches. (B) Fluorescence signaling for corresponding gated cell populations is shown for both Runx-2 and isotype labeling. Gating is applied for subtracting isotype labeling from Runx-2 labeled populations, and percent of remaining part is considered specifically stained with Runx-2 antibody. (C) Cell population and corresponding gating are shown for both Runx-2 and isotype labeling of cells in E-gel in low FBS media. (D) Fluorescence signaling for corresponding gated cell populations is shown for both Runx-2 and isotype labeling. Gating is applied for subtracting isotype labeling from Runx-2 labeled populations, and percent of remaining part is considered specifically stained with Runx-2 antibody.

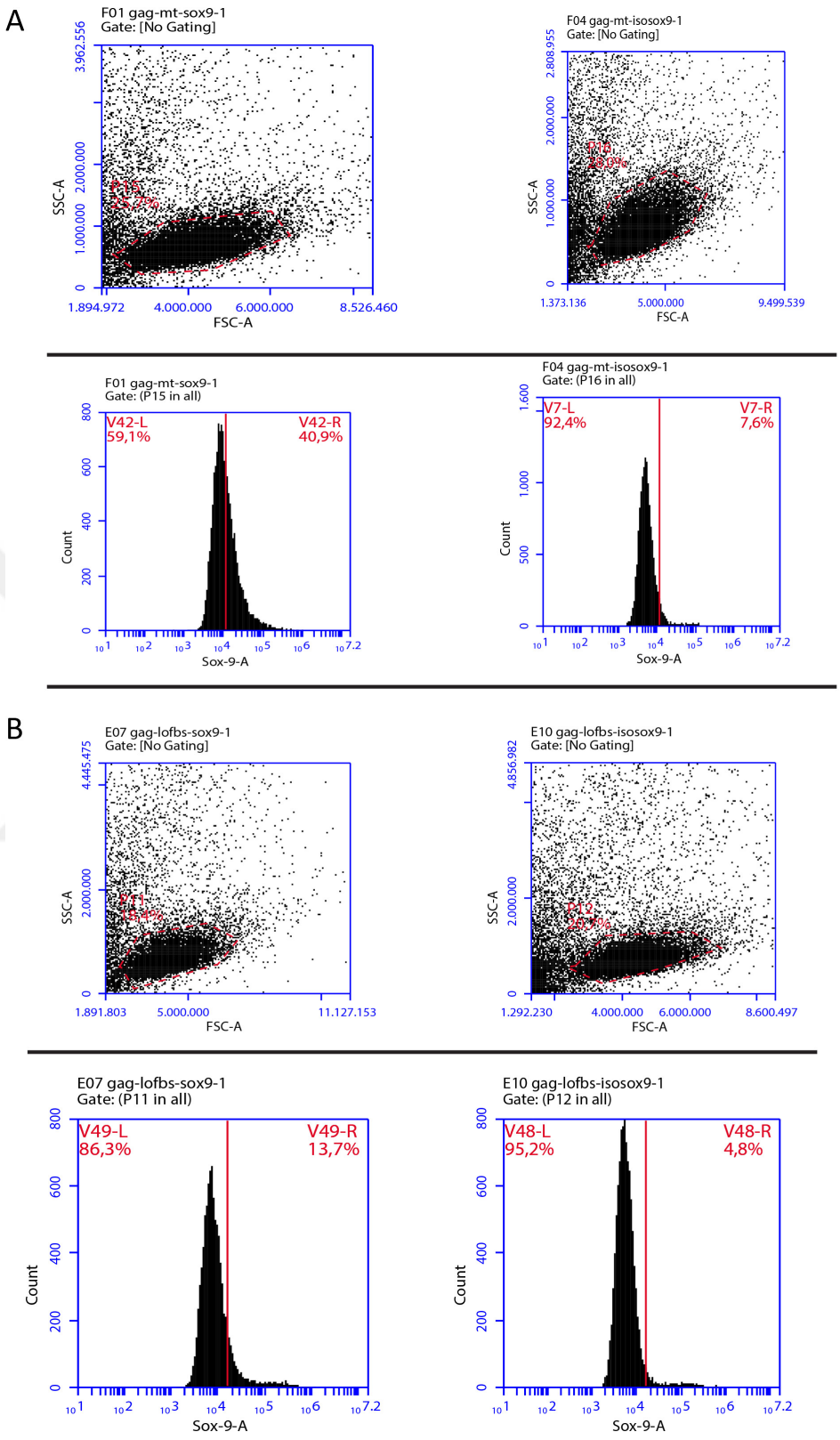


Figure 2. 23 Flow cytometry analyses of cells in GAG-gel within both MT and low FBS media. (A) Cell population and corresponding gating are shown for both Sox-9

and isotype labeling cells in GAG-MT niches. (B) Fluorescence signaling for corresponding gated cell populations are shown for both Sox-9 and isotype labeling. Gating is applied for subtracting isotype labeling from Sox-9 labeled populations, and percent of remaining part is considered specifically stained with Sox-9 antibody. (C) Cell population and corresponding gating are shown for both Sox-9 and isotype labeling of cells in GAG-low FBS niches. (D) Fluorescence signaling for corresponding gated cell populations are shown for both Sox-9 and isotype labeling. Gating is applied for subtracting isotype labeling from Sox-9 labeled populations, and percent of remaining part is considered specifically stained with Sox-9 antibody.

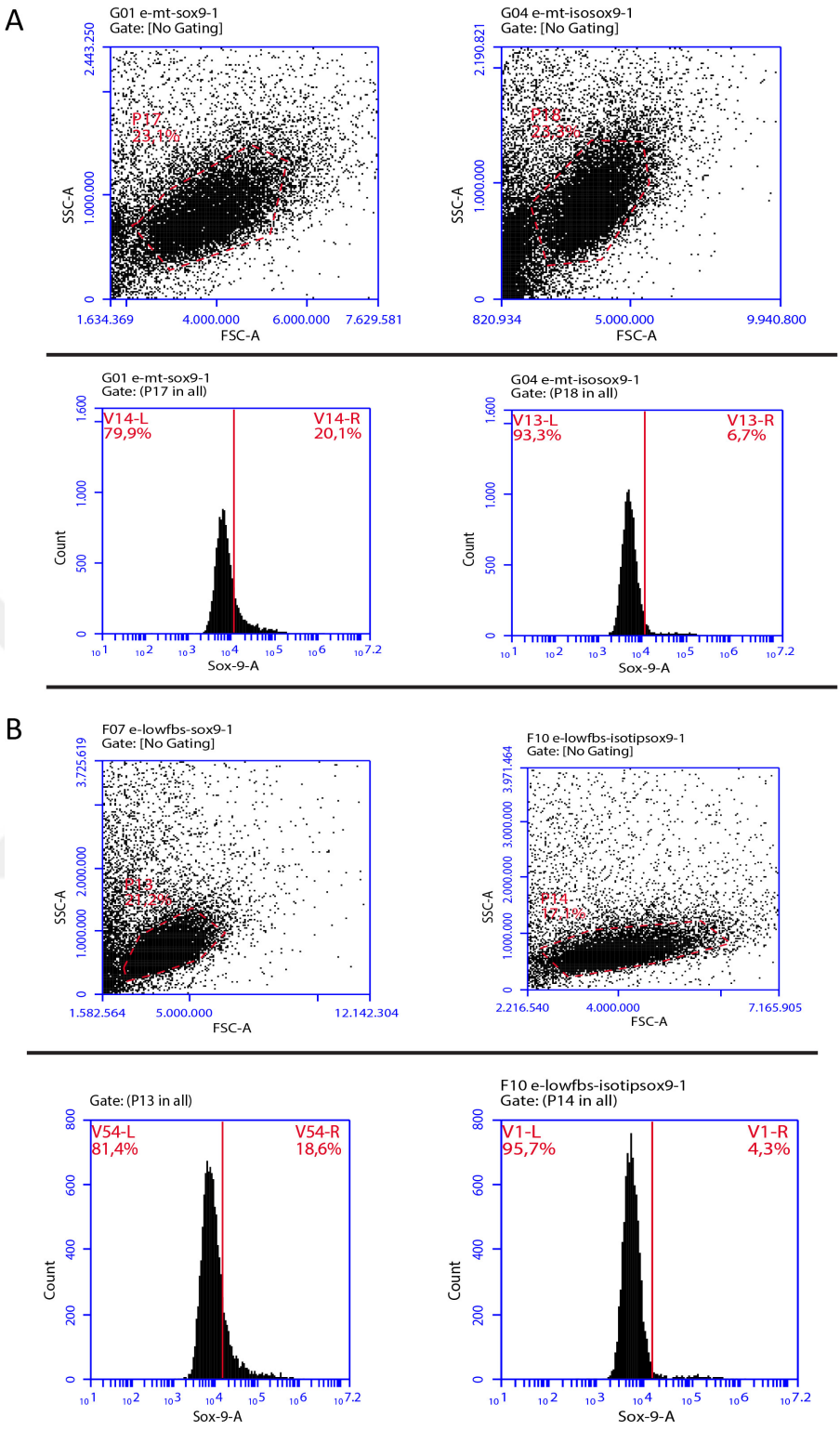


Figure 2. 24 Flow cytometry analyses of cells in E-gel within both MT and low FBS media. (A) Cell population and corresponding gating are shown for both Sox-9 and

isotype labeling cells in E-MT niches. (B) Fluorescence signaling for corresponding gated cell populations are shown for both Sox-9 and isotype labeling. Gating is applied for subtracting isotype labeling from Sox-9 labeled populations, and percent of remaining part is considered specifically stained with Sox-9 antibody. (C) Cell population and corresponding gating are shown for both Sox-9 and isotype labeling of cells in E-gel in low FBS media. (D) Fluorescence signaling for corresponding gated cell populations are shown for both Sox-9 and isotype labeling. Gating is applied for subtracting isotype labeling from Sox-9 labeled populations, and percent of remaining part is considered specifically stained with Sox-9 antibody.

Figures 2.25 and Figure 2.26 show the osteo- and chondrogenic protein expression of cells, as investigated by immunophenotypic analysis for Runx-2 and Sox-9. It is readily evident that the culture medium and the GAG-like 3D scaffold have separate and synergistic effects on the induction of stem cell differentiation. In maintenance medium, the GAG-like scaffold induced the upregulation of Sox-9 expression. Therefore, in the normal growth medium of stem cells, chemical and physical signatures presented in the GAG-gel niche are more likely to induce cells into chondrogenic differentiation. However, a lower concentration of FBS switches the effect of GAG-gel presence from pro-chondrogenic to pro-osteogenic. Even though low FBS media has pro-osteogenic effect in E-gel, it is notable that the effect of the maintenance media is considerably less prominent in the E-PA gel niche; *i.e.* a similar number of cells undergo osteogenic and chondrogenic differentiation in E-MT.

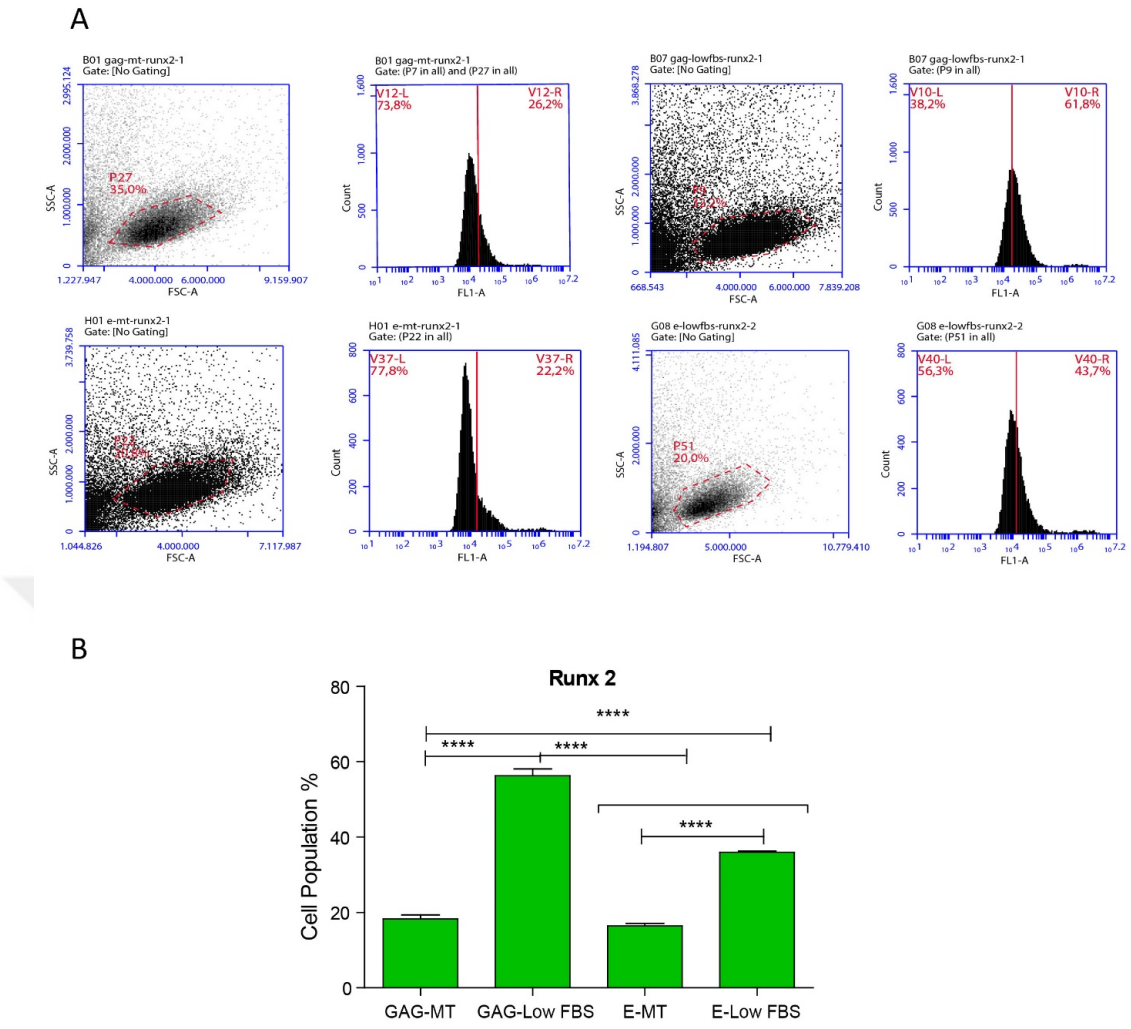


Figure 2. 25 Immunophenotypic characterization of stem cells encapsulated in GAG- and E-gel niches for Runx-2 expression on day 7. (A) Cell population and fluorescence signaling including corresponding gating are shown for both Runx-2 labeling of cells in GAG- and E-gel niches. Gating is applied for subtracting isotype labeling from Runx-2 labeled populations, and percent of remaining part is considered specifically stained with Runx-2 antibody. (B) Cell population percentage comparison for Runx-2 expression.

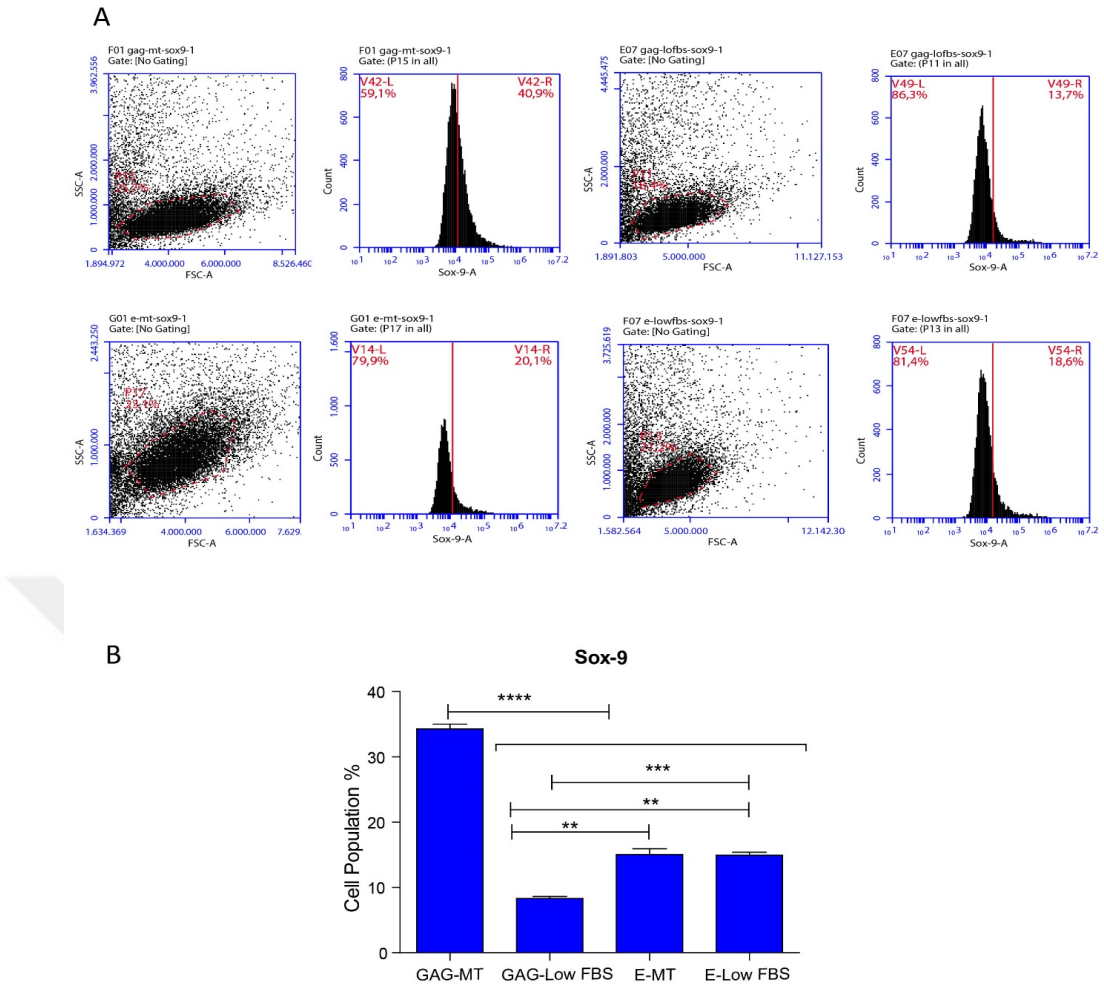


Figure 2. 26 Immunophenotypic characterization of stem cells encapsulated in GAG- and E-gel niches for Sox-9 expression on day 7. (A) Cell population and fluorescence signaling including corresponding gating are shown for Sox-9 labeling of cells in GAG- and E-gel niches. Gating is applied for subtracting isotype labeling from Sox-9 labeled populations, and percent of remaining part is considered specifically stained with Sox-9 antibody. (B) Cell population percentage comparison for Sox-9 expression.

It is well-recognized that stem cells lose their differentiation potential outside of their natural niche [78]. When designing artificial systems for the enhancement of tissue regeneration, various criteria should therefore be considered to ensure that cells are

exposed to a faithful replication of their native environment. In our work, we showed that the differentiation potential of stem cells could be modulated by controlling the synergistic effects of a GAG-mimetic scaffold and the cell medium. However, in addition to osteogenic and chondrogenic lineages, mesenchymal stem cells exhibit the potential to differentiate into adipogenic and some other cell types [88]. In addition, they are capable of self-renewal, which enables the rapid proliferation of stem cells for tissue repair, but by necessity requires a population of undifferentiated cells [89]. Our Sox-9 and Runx-2 expression results show that, in addition to osteo- and chondro-committed cells, a part of the population express neither of these markers and may be undifferentiated. Although these undifferentiated cells are generally underestimated and limit the utility of stem cells in regenerative medicine, we were able to decrease the percentage of non-differentiating cells in osteo- and chondro-committed niches in GAG-low FBS and GAG-MT niches, suggesting that the GAG network also promotes differentiation in general.

These results overall indicate that GAG-like nanofibers incorporated within 3D PA gels induce osteogenic differentiation in the presence of low FBS media, while chondrogenic differentiation dominates when FBS levels are increased. Indeed, chondrogenic differentiation is only prominent when cells are grown in GAG-gel scaffolds and treated with maintenance medium, while cells in other groups are largely predisposed towards osteogenesis. As such, GAG-mimetic bioactive signals are able to initiate chondrogenesis in a much greater population of cells in maintenance medium. A similar trend was also observed in the non-bioactive gel niche, although to a lesser extent. We therefore concluded that maintenance medium alone is not able to support a dominant chondrogenic profile and that synergistic

effects between the GAG-mimetic scaffold and the high-FBS medium is necessary for the majority of the cell population to commit to a chondrogenic differentiation pathway.

2.5 Conclusion

In this study, we investigated the potential of stem cells to differentiate into either osteogenic or chondrogenic lineages in 3D GAG-mimetic PA gel niches. GAG-like scaffolds were demonstrated to exhibit a distinctive effect on the differentiation of mesenchymal stem cells into osteo/chondrogenic lineages in media containing high and low concentrations of FBS. As mesenchymal stem cells are commonly used for the regeneration of cartilage and bone defects, characterization of their differentiation process is a topic of great interest for tissue engineering. We showed that 3D GAG-mimetic peptide nanofiber network could orchestrate the differentiation of mesenchymal stem cells in conjunction with environmental stimuli. It is noteworthy that differentiation potentials of stem cells could be regulated by altering medium components with the integrative effect of GAG mimetic scaffold. In addition, the 3D GAG gel was shown to be efficient for expanding of mesenchymal stem cells *ex vivo*, and the material can be developed further for *in vivo* applications. By combining this versatile GAG mimetic scaffold with optimum cell culture conditions, it is possible to direct the differentiation of stem cells into specific lineages with high efficiency. After the initial induction of cells into pre-osteogenic or pre-chondrogenic stages, the committed cells in these gels can also be selected (*e.g.* by using florescence activated cell sorting-FACS) for further clinical applications.

Chapter 3. Regenerative and Protective Effects of Peptide Amphiphile - Hyaluronic Acid Hybrid Nanofiber Membranes in *in vivo* Osteoarthritis Model

A partial content of this work is under preparation for a publication with the following authors:

Arslan, E.; Sardan Ekiz, M.; Eren Cimenci, C.; Çelik, I., Ozkan, H.; Guler, M. O.; Tekinay, A. B.

3.1 Objective

Osteoarthritis is a condition where tissue function is lost through a combination of secondary inflammation and deterioration in articular cartilage. One of the most common causes of OA is age-related tissue impairment because of wear and tear due to mechanical erosion. Hyaluronic acid-based viscoelastic supplements have been widely used as a treatment of knee injuries. However, they are unable to provide efficient healing and recovery. Here, a nanofiber-hyaluronic acid membrane system is presented for the efficient healing of arthritic cartilage tissue through the preservation of cartilage morphology with reduced osteophyte formation, protection of the subchondral region from deterioration, and maintenance of cartilage specific matrix proteins in vivo. In addition, the hybrid nanofiber membrane enabled

chondrocyte encapsulation and provided a suitable culturing environment for stem cell growth in vitro. The results showed that the superior therapeutic activity of hybrid nanofiber system was provided at relatively lower concentration than Hyalgan® and Synvisc® gels, which suggests that the membrane scaffold can be utilized as a potential candidate for further clinical studies for OA treatment.

3.2 Introduction

Cartilage tissue is distributed widely in the human body and plays essential roles in joint lubrication and the transmission of loads by withstanding high cyclic loads [32]. Chondrocytes are cartilage-specific cells that oversee the turnover of the non-cellular components of this tissue, but cannot repair major cartilage defects due to their low capacity for renewal [32]. Consequently, chondrocytes are assisted by MSCs that migrate to the defect site from the subchondral region during cartilage regeneration. This complex and lengthy repair process, in conjunction with repeated exposure to mechanical leading forces, makes cartilage defects highly susceptible to arthritic degeneration, which is one of the most common diseases of cartilage tissue. Osteoarthritis is a condition in which tissue function is lost through a combination of secondary inflammation, deterioration and erosion in joint cartilage [45]. Genetic, metabolic and biochemical factors all contribute to the etiology of osteoarthritis, and interactions between cartilage, bone and the synovium are crucial for the development of the disease. One of the most common causes of osteoarthritis is age-related tissue impairment.However, while wear and tear due to mechanical erosion usually manifest themselves in the elderly, joint problems may also occur in earlier ages due to causes such as traumatic accidents or obesity [33, 46]. Radiological

analyses have demonstrated that OA typically develops in less than 10 years in patients with untreated early cartilage injuries [50, 90].

Approximately 70% of cartilage tissue is composed of water by volume [32]. Proteoglycans interact with water, water-soluble molecules and various growth factors through their GAG moieties, such as the negatively-charged heparan sulfate, chondroitin sulfate, and hyaluronic acid [91]. GAGs electrostatically interact with growth factors to stabilize them and increase their availability to cells in aqueous media [91]. Collagen II is the most common fibrillar protein in cartilage and forms the functional skeleton of this tissue with collagen IX and collagen XI, which provide mechanical support and impart cartilage with the physical features required for its proper functioning [27, 92, 93]. Motifs on matrix proteins such as collagen and fibronectin, in conjunction with growth factors associated with GAGs, activate various intracellular signaling pathways through their interactions with cellular receptors, thereby initiating specific cellular responses [94-96]. During osteoarthritis formation, collagen degradation increases, proteoglycan content decreases, the prevalence of individual proteoglycans is altered, and water content increases [47, 48]. In addition, the amount and molecular size of hyaluronic acid in the synovial fluid is also reduced. Since OA alters the whole structure and function of cartilage tissue in a nigh-irreversible manner, the early prevention of this disease is critical for increasing the life quality of prospective patients. However, none of the current treatment methods can effectively provide healthy cartilage tissue formation [97-99].

Bone marrow stimulation techniques such as arthroscopic debridement, lavage and microfracture; osteochondral autograft and allograft techniques; and autologous chondrocyte implantation are some of the currently available methods that are used

to repair cartilage [100-102]. Today, these methods are used to ameliorate the symptoms of cartilage damage and partially restore mobility [103]. However, due to the mechanical weakness of the newly formed tissue, damage continues to occur at the defect site and degeneration eventually propagates into healthy cartilage even with treatment [104]. In addition, difficult surgical operations and high-cost and ineffectiveness of therapeutics used in clinics necessitate new therapeutic strategies. Therefore, tissue engineering applications employing three-dimensional scaffold-matrix systems that allow cellular infiltration and in situ differentiation are promising for the development of new approaches that can provide long-term joint function and durability [54, 105]. For this purpose, sustaining molecular components of the cartilage tissue and its structure with proper biochemical signals and mechanical support is critical for the regeneration of damaged tissue.

In this study, we developed a hybrid peptide nanofiber-hyaluronic acid membrane and examined its therapeutic effect in an in vivo osteoarthritis model in rats. At the liquid-liquid interface, the negatively charged high molecular weight hyaluronic acid solution contacts with positively charged peptide amphiphile molecules, which leads to the formation of a solid membrane. When two solutions are brought into contact, a physical layer is formed through the initial electrostatic complexation of the molecules, which prevents chaotic mixing of the two solutions by acting as a diffusion barrier. Hence, during the maturation of membrane, a unique scaffold structure develops, which contains three regions: an amorphous biopolymer layer, a layer of PA nanofibers parallel to the interface, and a layer of hybrid fibers perpendicular to the interface [106, 107]. Through this process, the nanofibers form micro-scale three-dimensional networks that are mechanically stable in aqueous

media. Here, we established hybrid nanofiber membranes by utilizing K-PA and Hyalgan®, which provided both the mechanical strength to support tissue and the bioactive signals for the activation of chondrocyte proliferation and functional cartilage-specific macromolecule synthesis. After the in vitro evaluation of hybrid nanofiber membranes using stem cell viability and chondrocyte proliferation assays in 2D and 3D environments, the protective and healing capacity of these membranes were investigated in vivo using early-stage and late-stage rat osteoarthritis models. The therapeutic effect of hybrid nanofiber membrane was found to be superior to the commercially available Hyalgan® and Synvisc® gel at a lower concentration and it provided a facile and feasible alternative to existing treatment methods for osteoarthritis.

3.3 Experimental Section

3.3.1 Materials

9-Fluorenylmethoxycarbonyl (Fmoc) and tertbutoxycarbonyl (Boc) protected amino acids, [4-[α-(2′,4′-dimethoxyphenyl) Fmoc aminomethyl]enoxy] acetamidonorleucyl-MBHA resin (Rink amide MBHA resin), Fmoc-Glu(OtBu)-Wang resin and 2-(1H-benzotriazol-1-yl)-1,1,3,3-tetramethyluronium hexafluorophosphate (HBTU) were purchased from NovaBiochem and ABCR. All other chemicals and materials used were analytical grade and were obtained from Invitrogen, Fisher, Merck, Alfa Aesar and Sigma-Aldrich. Coverglasses and tissue culture plates (24-well) were purchased from Deckglaser and BD. Hyalgan® and Synvisc (Hylan G_F20)® were commercially purchased. Chondrogenic differentiation media was purchased from Sigma. Live/Dead Assay (L3224), Alamar Blue and other cell culture materials were purchased from Invitrogen. Antibodies were purchased from Abcam.

3.3.2 Synthesis of peptide amphiphile molecules

The peptide amphiphile molecule, Lauryl-Val-Val-Ala-Gly-Lys-Am (K-PA), was synthesized by Fmoc solid phase peptide synthesis method. Rink amide MBHA resin was used as solid support for K-PA. For the amino acid coupling reactions, 2 equivalents of Fmoc-protected amino acid, 1.95 equivalents of HBTU and 3 equivalents of DIEA mixed in DMF for 3 h. 20% piperidine/DMF solution was used for Fmoc deprotection, while 10% acetic anhydride−DMF solution was used for 20 min for the acetylation of the unreacted amine groups after each coupling step. The terminal lauryl group was coupled by mixing lauric acid in a manner analogous to amino acid attachment. After couplings were finished, the cleavage of the peptides from the resin and deprotection of acid-labile protected amino acids were performed by a mixture of TFA : TIS: water at a ratio of 95:2.5:2.5 for 2.5 h. Then, rotary evaporation was performed to remove excess TFA. Ice-cold diethyl ether was used to triturate the remaining residue and the resulting white pellet was freeze-dried.

3.3.3 Chemical characterizations of peptide amphiphiles by LC-MS

Peptide amphiphile molecules were identified and analyzed by reverse phase HPLC on an Agilent 6530 accurate-Mass Q-TOF LC/MS equipped with an Agilent 1200 HPLC. K-PA was purified on an Agilent 1200 HPLC system by using a Zorbax prepHT 300CB-C8 column with a water–acetonitrile (0.1% TFA) gradient.

3.3.4 Preparation and characterization of self-assembled peptide amphiphile-HA hybrid nanofiber membrane

For nanofiber formation, K-PA was mixed with Hyalgan® at equal millimolar ratio in order to form a HA/K-PA hybrid membrane. The approximate molecular weight for Hyalgan® was determined as 615 kDa according to the manufacturer's guidelines.

3.3.5 Morphological analysis of hybrid nanofiber membrane by TEM imaging

Transmission electron microscopy (TEM) analysis of HA/K-PA hybrid membrane was performed with a FEI Tecnai G2 F30 TEM at 200 kV. For STEM mode images, a high-angle annular dark field detector was used. 5 mM HA/K-PA nanofiber system was diluted 100-200 times and then dropped on a 200-mesh copper TEM grid. Samples were left at room temperature for 7 min, stained by 2 wt % uranyl acetate for another 2 min and air dried prior to TEM imaging.

3.3.6 Secondary structure analysis of hybrid nanofiber membrane by CD

CD measurements were performed by Jasco J-815 CD spectrophotometer for the analysis of the secondary structures of the HA/K-PA membrane and Hyalgan® gel. All samples were measured at 100-fold dilutions of concentrations used in *in vitro* experiments. For each measurement, 300 μL of PA material was transferred into a 1 mm quartz cuvette, which was inverted gently to mix the sample without damaging the assembled nanostructures. Spectra were obtained at room temperature at a range of 300 nm to 190 nm, with a data interval of 1 nm and a scanning speed of 100 nm/min. The results were expressed as mean residue ellipticity and converted to the unit of $deg.cm^2.dmol^{-1}$.

3.3.7 Mechanical analysis of hybrid nanofiber membrane by oscillatory rheology

Oscillatory rheology measurements were performed with an Anton Paar Physica MCR301 system for the analysis of the mechanical characteristics of the HA/K-PA hybrid membrane. A 25 mm parallel plate with a gap distance of 0.5 mm was used at 25 °C for all measurements. The total membrane volume was adjusted as 250 µL. Hybrid membrane was freshly prepared as 1:1 ratio mixture of 5 mM K-PA and 5 mM Hyalgan®, and the mixture was then sonicated for 30 min. The upper plate was adjusted to the 0.5 mm position and the membrane was incubated in this position for 15 min prior to measurement. For strain sweep measurements, angular frequency was kept constant at 10 rad/s, and strain was increased between 0.1 and 100%. Storage and loss moduli were recorded at each strain value. All rheology measurements were performed on membrane with and without cells with three replicates.

3.3.8 Morphological analysis of hybrid nanofiber membrane by SEM imaging

For scanning electron microscopy (SEM) imaging, 1% (w/v) bulk peptide nanofiber membranes were prepared on silicon wafers. Samples were dehydrated in graded ethanol solutions, starting with 20% ethanol and proceeding to absolute ethanol for 10 min at each step. Samples were dried with a Tousimis Autosamdri-815B critical point drier, coated with 10 nm Au/Pd and imaged with a FEI Quanta 200 FEG SEM.

3.3.9 Cell culture experiments

The rMSCs (rat mesenchymal stem cells, Invitrogen S1601-100) at passage 8 were used in cell culture experiments, including viability and differentiation assays. The rMSCs were initially cultured in DMEM supplemented with 10% FBS (Maintenance Media) in tissue culture plates at standard culture conditions (at 37 °C under 5% CO_2).

Rat chondrocytes were isolated according to a protocol adapted from Gosset et. al [108]. All procedures on animals were approved by the Gulhane Military Medical Academy (GATA) Animal Ethics Committee. Briefly, femoral heads, femoral condyles and tibial plateau were isolated from one rat and placed in 1X PBS. Then, pieces of cartilage were incubated in 10 mL digestion solution for 45 min at 37 °C in a thermal incubator. After retrieving cartilage pieces using a 25-mL pipette, tissue fragments were agitated using a 25-mL pipette to detach soft tissues in 0.5 mg mL^{-1} collagenase D solution. Then, cartilage pieces were retrieved and placed in 10 mL of 0.5 mg mL^{-1} collagenase D solution for overnight at 37 °C. On the next day, the collagenase D solution containing residual cartilage was retrieved, and the cell solution was suspended through a cell strainer (Falcon™) and centrifuged for 10 min at 400 g at 20 °C. Then, cells were seeded into culture medium at a density of 8×10^3 cell per cm^2.

For *in vitro* studies, both 2D and 3D cell culture methods were performed to investigate the effect of bioactive hybrid membranes on both stem cells and chondrocytes. For 2D *in vitro* cell culture experiments, HA/K-PA (1 mM: 1 mM) membranes were prepared in wells and dried overnight. On the next day, rMSCs (were seeded on the coatings. Uncoated TCP was used as control group. For 3D *in vitro* cell culture experiments, rat chondrocytes were seeded in 3D peptide hybrid nanofiber membrane scaffolds prepared by the mixture of 5 mM Hyalgan gel and 5 mM K-PA at 1:1 ratio. Each solution was prepared in ddH_2O. Chondrocyte pellets were added to Hyalgan® and mixed with K-PA to facilitate their encapsulation in HA/K-PA membranes on glass slides in 24-well plates. For Hyalgan® and Synvisc® (Hylan G_F20) controls, chondrocyte pellets were encapsulated directly in Hyalgan®

or Synvisc® gels. Following scaffold preparation, 3 mL of cell medium was added to the wells and the gels were incubated for 30 min at 37 °C.

Cell viability was analyzed by Alamar Blue (Invitrogen) and Live/Dead (Life Technologies) assays. 5 x 10^5 rMSCs were seeded onto nanofiber membranes and their viability was measured at days 1, 2, and 3 by quantifying the fluorescence and absorbance of the reagent using spectrophotometry for the Alamar Blue assay, and imaging the cells by fluorescence microscopy and confocal microscopy for the Live/Dead Assay. In addition, for the biocompatibility analyses of the 3D hybrid membrane scaffold, chondrocytes were encapsulated into hybrid nanofiber membranes and Live/Dead assay was performed.

3.3.10 *In Vivo* osteoarthritis model in rat and intraarticular hybrid nanofiber membrane treatment

For the development of osteoarthritis in rats, medial meniscus destabilization was performed by the excision of connective tissues between femur and tibial bones in the knees of rats and osteoarthritis formation was observed due to cartilage wear. 6 rats were used for each group. Each rat was anesthetized by general anesthesia with ketamine-xylazine via intramuscular injection. Rats' knees were incised longitudinally from the upper patella to the tibialis tibia, followed by arthrotomy with the medial parapatellar. Then, locations of the medial meniscus and meniscotibial ligaments were determined, and the medial meniscotibial ligament was excised to destabilize the medial meniscus. The joint incisions were closed after observing that the medial meniscus had lost its stability and moved after the excision. After 1 week or 6 weeks from surgery (Table 1), each group was injected with corresponding scaffolds via insulin needle through intraarticular injection. At the end of the

specified periods, tissue regeneration was examined by the histopathological analysis of cartilage tissues.

Table 3. 1 Experimental plan & animal groups

Experimental Groups	**Animal Amount**	**Experimental Plan**
HA/K-PA	6	Intraarticular Injection: 1 week after degeneration Sacrification of Animals: 6 weeks after injection
	6	Intraarticular Injection: 6 weeks after degeneration Sacrification of Animals: 6 weeks after injection
Synvisc®	6	Intraarticular Injection: 1 week after degeneration Sacrification of Animals: 6 weeks after injection
	6	Intraarticular Injection: 6 weeks after degeneration Sacrification of Animals: 6 weeks after injection
Hyalgan®	6	Intraarticular Injection: 1 week after degeneration Sacrification of Animals: 6 weeks after injection
	6	Intraarticular Injection: 6 weeks after degeneration Sacrification of Animals: 6 weeks after injection
Sham	6	Intraarticular Injection: 1 week after degeneration

		Sacrification of Animals: 6 weeks after injection
	6	Intraarticular Injection: 6 weeks after degeneration Sacrification of Animals: 6 weeks after injection
Healthy Control	Healthy right knees of operated animals were used as healthy tissue control	

3.3.11 Histological and immunohistochemical stainings of tissue sections

Samples were fixed in 4% paraformaldeyde for 48 h at 4 °C and decalcified in 5% formic acid. 5% formic acid solution was exchanged every 2-3 days. The completion of decalcification was periodically tested with ammonium oxalate test. Decalcified samples were dehydrated in a graded series of ethanol and cleared via two changes of xylene. Samples were embedded in paraffin blocks and sectioned at 7-10 μm thickness by microtome. For histological and immunohistochemical evaluations, sections were deparaffinized and rehydrated through a series of graded alcohol solutions. Defect healing was monitored by the staining of representative slides taken at 20 section (~200 μm) intervals to determine the extent of cartilage regeneration through anterior to posterior regions of cartilage. For GAG imaging, sections were stained with Safranin-O for 5 min and Fast Green for 5 min. Masson's trichrome staining was performed to visualize the mature bone collagens, muscles, and collagens found in cartilage. For Masson's trichrome staining, after deparaffinization, slides were stained with hematoxylin for 45 sec, Biebrich Scarlett for 5 min, phosphomolibdic acid/ phosphotungistic acid solution for 5 min, and aniline blue for

5 min. Sirius red staining (Direct Red) was performed to visualize the organization of collagen fibers in the tissues. For staining, after deparaffinization, slides were stained with Weigert's hematoxylin for 8 min and pico-sirius red for 1 h. Then, sections were dehydrated in graded ethanol solutions and cleared in xylene. Slides were mounted with Histomount® mounting medium and imaged by light microscopy (Zeiss, Axio Scope).

For immunohistochemical stainings, slides were treated with an antigen retriever (Sigma) to uncover epitopes for 15 min at 37 °C after rehydration steps. After blocking for 2 h at room temperature, sections were incubated with primary Collagen II antibody (Pierce Antibodies) at 4 °C overnight. Sections were then washed extensively with TBS w/Triton-X (0.01% vol/vol) and treated with Goat anti-Mouse IgG-HRP at a dilution of 1:500 for 1 h at room temperature to detect bound primary antibodies. Secondary antibody binding was visualized with diaminobenzidine and nuclei were stained with hematoxylin (Sigma-Aldrich). Collagen II antibody was tested on positive control samples before staining of sections from experimental groups. Negative controls were obtained by omitting primary antibody and incubating with 1% normal goat serum/TBS. Slides were mounted with Histomount ® mounting medium.

3.3.12 Histological scoring

The histopathological assessment of osteoarthritis was performed to determine the extent of regeneration following hybrid nanofiber membrane treatment. A validated Osteoarthritis Research Society International (OARSI) scoring system was employed for the evaluation of the regenerative capacity of hybrid nanofiber membranes [109]. This scoring method includes the evaluation of cartilage matrix loss width, cartilage

degeneration score, total cartilage degeneration width, significant cartilage degeneration width, zonal depth ratio of lesions, osteophyte development and calcified cartilage and subchondral bone damage score in four major categories; the nature of the predominant tissue, structural characteristics, cellular evidence of degeneration and degenerative changes in adjacent cartilage.

Table 3. 2 Histological scoring. Adapted from Gerwin et.al. [109]

Cartilage Degeneration Grade	Description
0	No degeneration
1	Minimal degeneration: 5-10% of the total cartilage area is affected by matrix or chondrocyte loss
2	Mild degeneration; 11-25% affected
3	Moderate degeneration; 26-50% affected
4	Marked degeneration; 51-75% affected
5	Severe degeneration; greater than 75% affected

3.3.13 Statistical analysis

All data are presented as mean ± sem (standard error of mean). The significance of differences between groups was determined with Student's t-test and one-way analyses of variance (ANOVA) with Bonferroni posttests. Differences were considered significant at $p < 0.05$.

3.4 Results

3.4.1 Synthesis and characterization of hybrid nanofiber membranes

In this study, hybrid peptide nanofiber - hyaluronic acid membranes were formed to create an effective scaffold system for the regeneration of osteoarthritic cartilage tissue. The synergistic effect of the nanofibrous morphology of peptide amphiphiles and bioactivity of hyaluronic acid molecules were combined to create a mechanically stable regenerative nanofiber microenvironment. In addition, commercially available Hyalgan® gel and Synvisc® gel (which is the cross-linked counterpart of hyaluronic acid) were used as positive controls for *in vivo* studies. All PA molecules were produced by solid-phase peptide synthesis, and they were characterized and purified by LC-MS and preparative HPLC prior to use (Figure 3.1). Chemical structures of the PA molecule and Hyaluronic acid are shown in Figure 3.2.

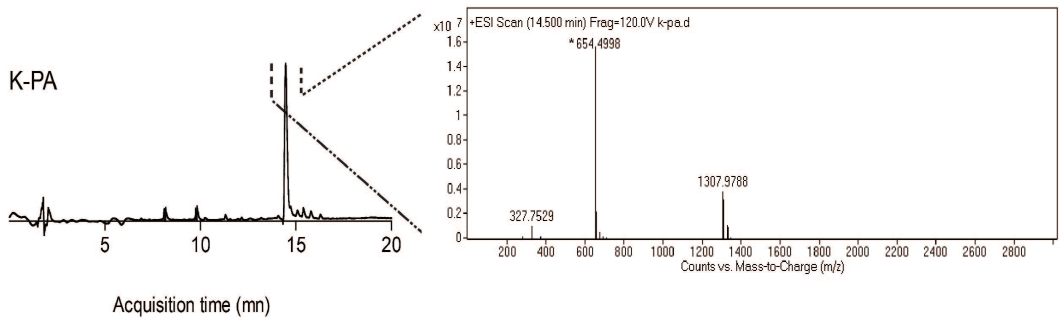


Figure 3. 1 Chemical characterization of K-PA molecule. Liquid chromatogram and mass spectra of L-VVAK, calculated exact mass [M] = 654.4998, $[M-2H]^{-}/2$ (m/z) = 327.7529.

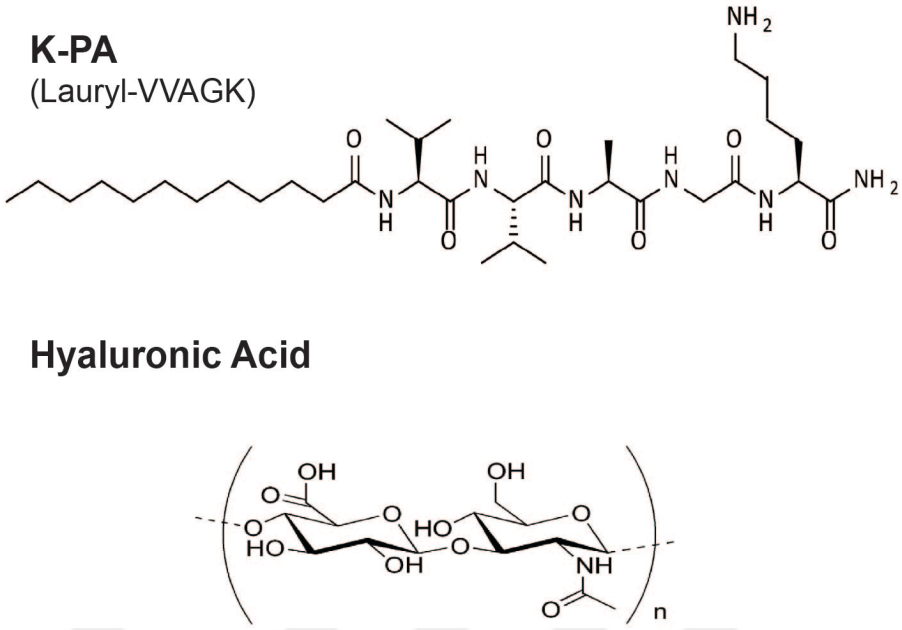


Figure 3. 2 Chemical structures of the K-PA and hyaluronic acid molecules.

STEM images of peptide nanofibers (Figure 3.3A) revealed that hybrid nanofiber networks were formed through the co-assembly of K-PA and Hyalgan® into nanofibers with high-aspect ratios and nanometer-scale diameters (10 nm-20 nm) through electrostatic interactions between positively and negatively charged building blocks presented in each molecule. Indeed, the sizes of the hybrid nanofibers were similar to the fibrous collagen and glycoproteins found in the cartilage ECM [53, 71]. In addition, SEM analyses of membranes (Figure 3.3B confirmed the formation of porous nanofiber networks within the membrane structure.

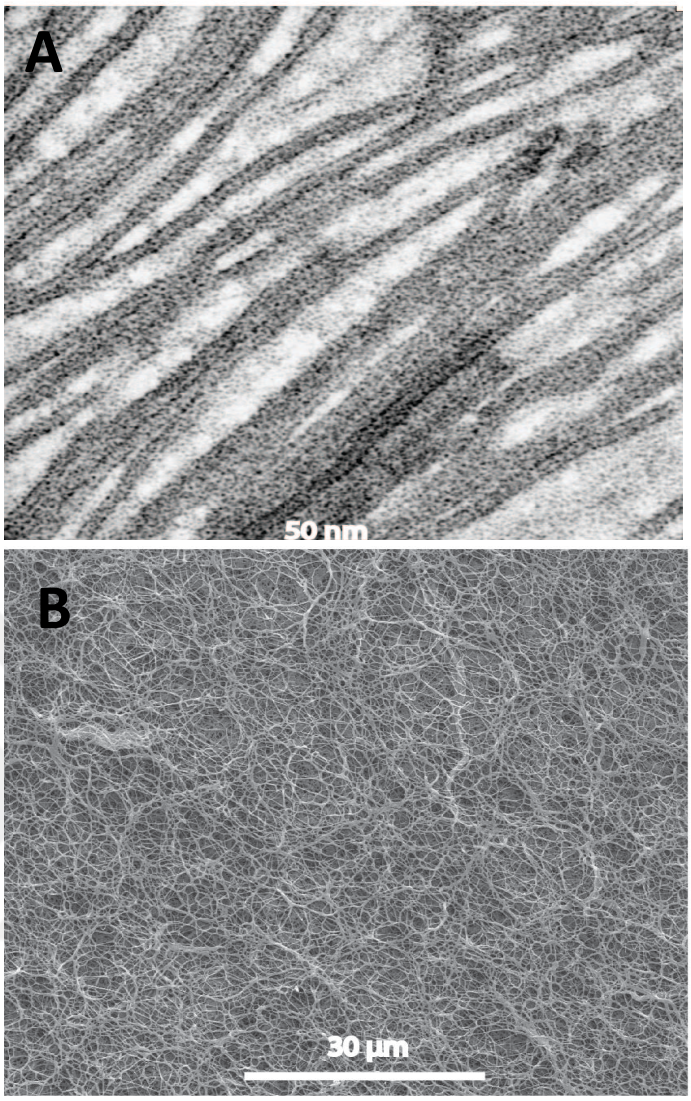


Figure 3. 3 (A) STEM image of hybrid nanofiber membrane (HA/K-PA), scale bar = 50 nm; (B) SEM image of hybrid nanofiber membrane at 5 mM, scale bar = 20 µm.

The secondary structures of the networks were characterized by CD spectroscopy. According to CD spectra, hybrid nanofiber membranes (HA/K-PA) had β-sheet conformation with peaks at ~220 nm (Figure 3.4A). On the other hand, pure K-PA and Hyalgan® molecules were not observed to form β-sheets at the analyzed concentrations. Oscillatory rheology analyses were also performed to investigate the mechanical properties of hybrid nanofiber membranes. Time sweep oscillatory

rheology analyses were conducted in order to assess the gel formation mechanics and viscoelastic properties of the scaffold material. The storage modulus of the hybrid nanofiber membrane was found to be higher than its loss modulus at *in vivo* experimental concentrations, suggesting that the material was hydrolytically stable and exhibited robust mechanical features (Figure 3.4B).

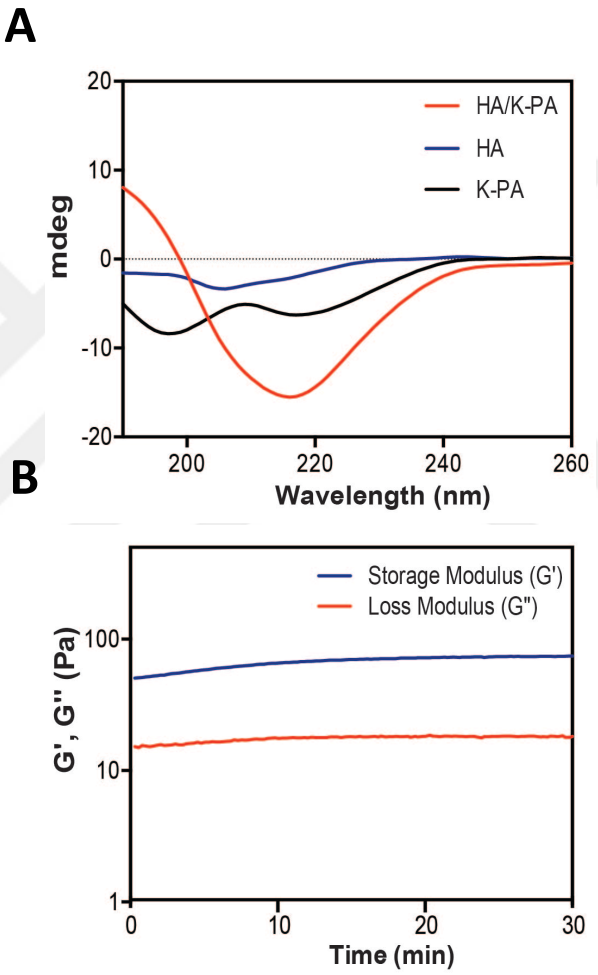


Figure 3. 4 (A) CD spectra of K-PA and Hyalgan• solutions and hybrid nanofiber membrane; (B) Rheological analyses of hybrid nanofibers.

3.4.2 Hybrid nanofiber membrane provide a biocompatible microenvironment for MSC and chondrocyte culturing and encapsulation in 2D and 3D *in vitro* environments

In vitro investigation of membranes is vital for assessing their biocompatibility and capability to be used for the encapsulation of cells. Hence, biocompatibility of membranes was evaluated through both 2D and 3D cell culturing. 2D *in vitro* cell culturing of mesenchymal stem cells (MSC) revealed that hybrid nanofiber membranes presented a suitable environment for the attachment and growth of stem cells (Figure 3.5).

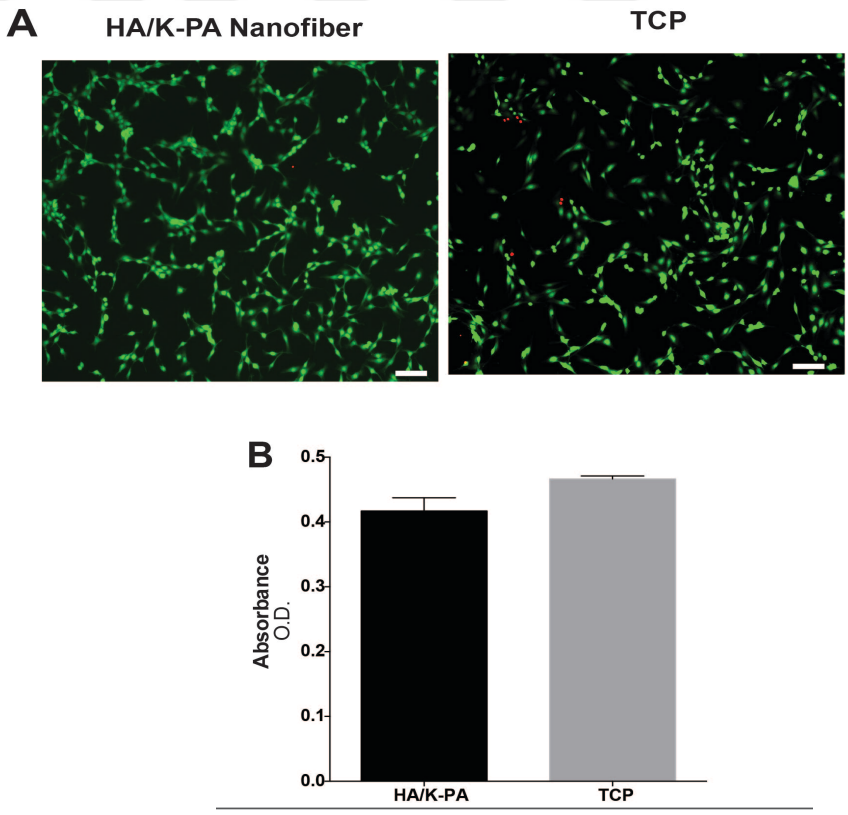


Figure 3. 5 (A) Live/Dead analyses of MSCs cultured on hybrid nanofiber membranes and on uncoated TCP; (B) Viability analyses of MSCs by Alamar Blue assay.

In addition, 3D *in vitro* autologous chondrocyte culturing was performed to evaluate the potential use of membranes for improved autologous chondrocyte implantation therapy (Figure 3.6). According to Live/Dead assay results, the hybrid nanofiber (HA/K-PA) membrane was biocompatible and supported the growth and proliferation of chondrocytes in 3D microenvironments (Figure 3.6). However, neither Hyalgan® nor Synvisc® gels was not mechanically stable as they dissolved in cell media and did not provide cell encapsulation for 3D chondrocyte culturing; rather, we observed 2D cellular adhesion similar to TCP control in these wells. When considering the importance of 3D microenvironments for cellular behaviors, it is essential to design and recruit mechanically stable scaffolds for further clinical applications. Our 3D hybrid nanofiber scaffold presents a highly porous structure that provides larger surface areas for cell attachment and proliferation, which enables the use of higher amounts of cells in clinical applications [78]. In addition, this hybrid nanofiber system is much closer to the native tissue morphology than 2D cell culture and enables the dynamic turnover of the extracellular matrix.

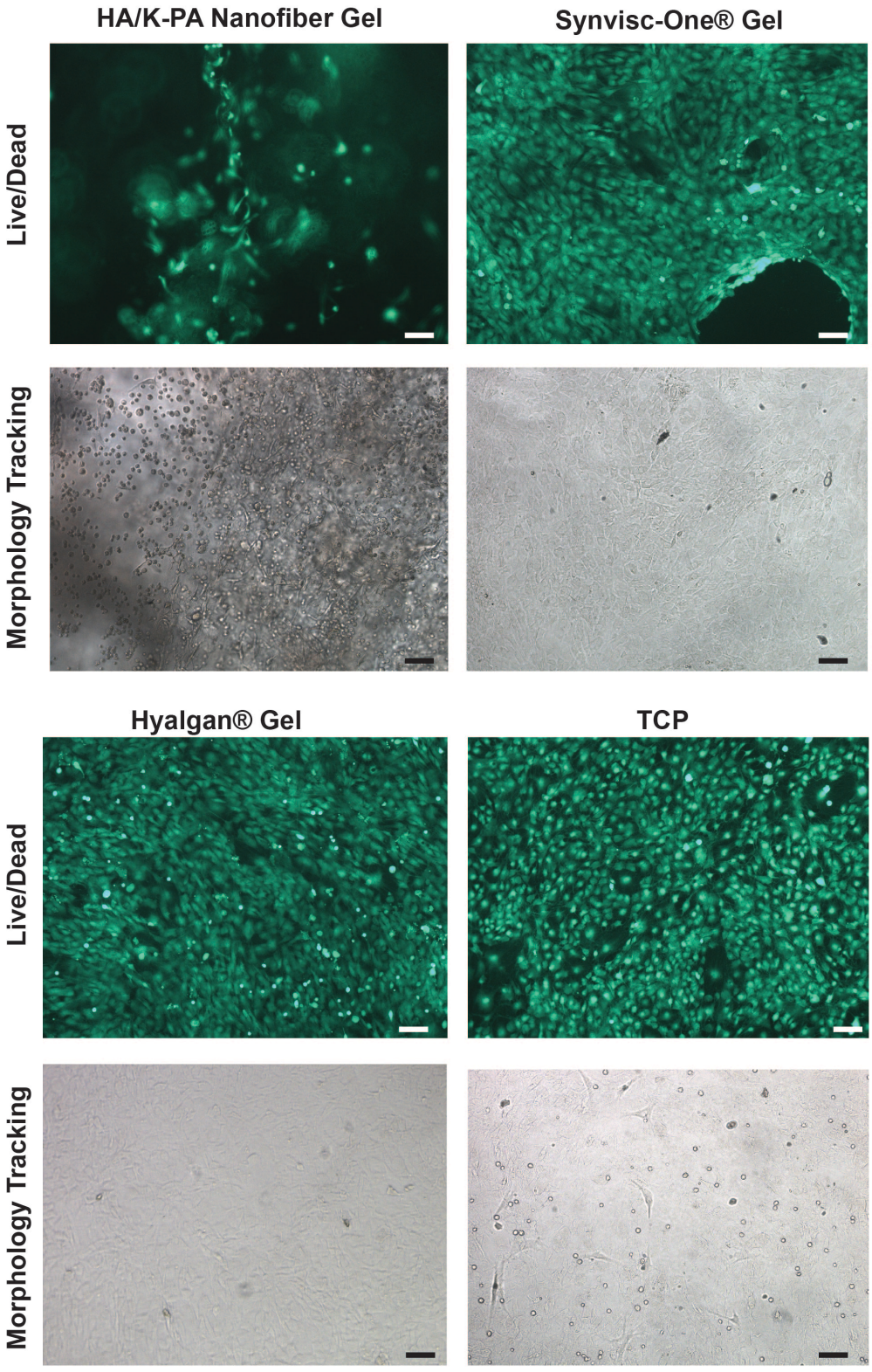


Figure 3. 6 Live/Dead analyses and morphology tracking of chondrocytes cultured in 3D scaffolds.

3.4.3 Hybrid nanofiber membrane promotes the regeneration of defected cartilage tissue in osteoarthritic rat knees

For the development of osteoarthritis model, medial meniscus destabilization was performed by the excision of connective tissues between femur and tibial bones in the knees of rats and subsequently osteoarthritis formation was observed due to cartilage wear [110]. The medial meniscotibial ligament (MMTL) is the connective tissue that fixes the tibial plateau to the medial meniscus (MM) [110]. MM provides an articular connection between the tibia and femur, as well as helping to transfer body weight on a wider surface, alleviating the load on the cartilaginous body. With the excision of MMTL and destabilization of MM, the MM structure was disturbed and the local mechanical stress increased with the concentration of body weight in a smaller area. In rats, increasing mechanical stress led to injuries at the back of the femur, in the center of the tibia, and in the medial cartilaginous region. Human osteoarthritis also manifests itself in the medial part of the knee, demonstrating the suitability of this model. Hence, *in vivo* efficacy of hybrid nanofiber membranes was investigated in osteoarthritic knees of rats.

For the evaluation of osteoarthritic tissue regeneration, an OARSI-recommended histopathology scoring method was performed [109]. According to this scoring method, total joint degeneration score was measured including the medial tibial and femur cartilage degeneration scoring, medial tibial osteophyte scoring, and bone scoring. Both early stage and late stage of osteoarthritis were modeled using two experimental groups that are 1W6W (Early group: scaffold injection 1 week after surgery & tissue extraction 6 weeks after injection) and 6W6W (Late group: scaffold injection 6 weeks after surgery & tissue extraction 6 weeks after injection) groups.

Both the protective effect and healing capacity of hybrid nanofiber membranes could be assessed through this two-arm experimental method. For the evaluation of cartilage degeneration scores, tissue sections were stained with Safranin-O/Fast green/Hematoxylin, and areas of cartilage, where proteoglycan loss was present without any chondrocyte death, were analyzed (Figure 3.7). Through this scoring, overall cartilage pathology and the important pathological parameters of collagen matrix fibrillation and loss/maintenance of matrix were determined. In addition, the tibial plateau was divided into 3 zones to effectively quantify the regeneration process (Figure 3.8). According to total degeneration scoring results, the hybrid nanofiber membrane had the lowest joint degeneration scoring and provided efficient regeneration and protection to the joint, performing significantly better than commercially available Hyalgan® gel and sham control. In addition, the hybrid nanofiber membrane provided comparable regeneration to Synvisc® gel, which is a crossed-linked, higher molecular weight version of hyaluronic acid that is more costly and has been shown to exhibit immunogenicity [97, 111].

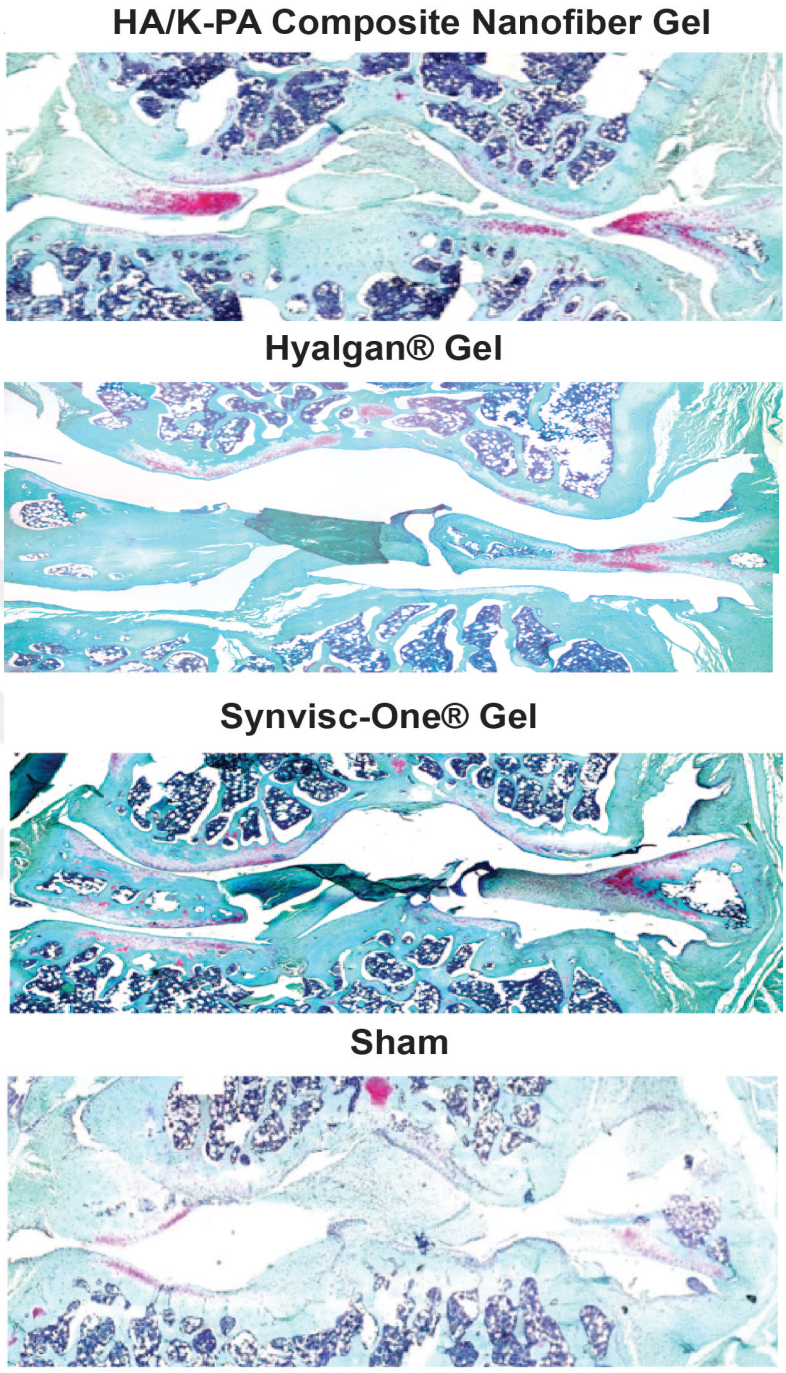


Figure 3. 7 Hyaline cartilage regeneration analyses through Safranin-O/Fast Green/Hematoxylin stainings of tissues for all groups.

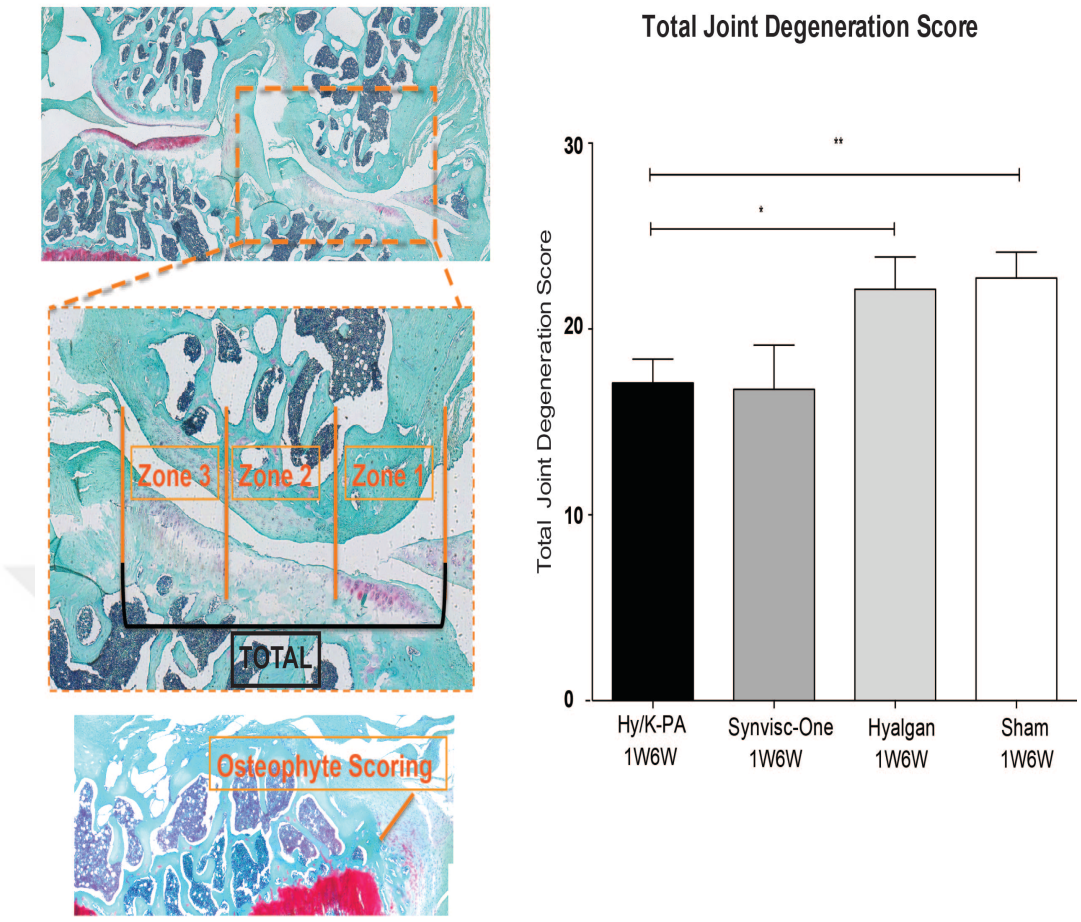


Figure 3. 8 Corresponding OARSI scoring for assessment of total joint score (Osteophyte scoring was evaluated as Grade 0: Marginal zone proliferative changes <200 µm; Grade 1: small 200-299 µm; Grade 2: moderate 300-399 µm; Grade 3: large 400-499 µM; Grade 4: very large >500 µm); Total joint score for scaffolds and sham (*p< 0.05, **p<0.01, by Student's t-test, mean ± s.e.m.).

In addition, Total Degeneration Width and Significant Degeneration Width of the medial tibial plateau were evaluated, and the hybrid nanofiber membrane was found to provide enhanced healing on cartilage through the surface (0% depth)-midzone (50% depth)-tide mark (100% depth) axis (Figure 3.9 and Figure 3.13) than the other scaffolds and sham group. Interestingly, Significant Degeneration Width

measurements demonstrated that the hybrid nanofiber membrane significantly protected cartilage tissue from severe degeneration (Figur 3.13). Furthermore, zonal depth ratios of lesions were measured and the hybrid nanofiber membrane had the lowest lesion depth, which was significantly lower than Hyalgan® gel and sham control and was comparable with Synvisc® gel (Figure 3.10).

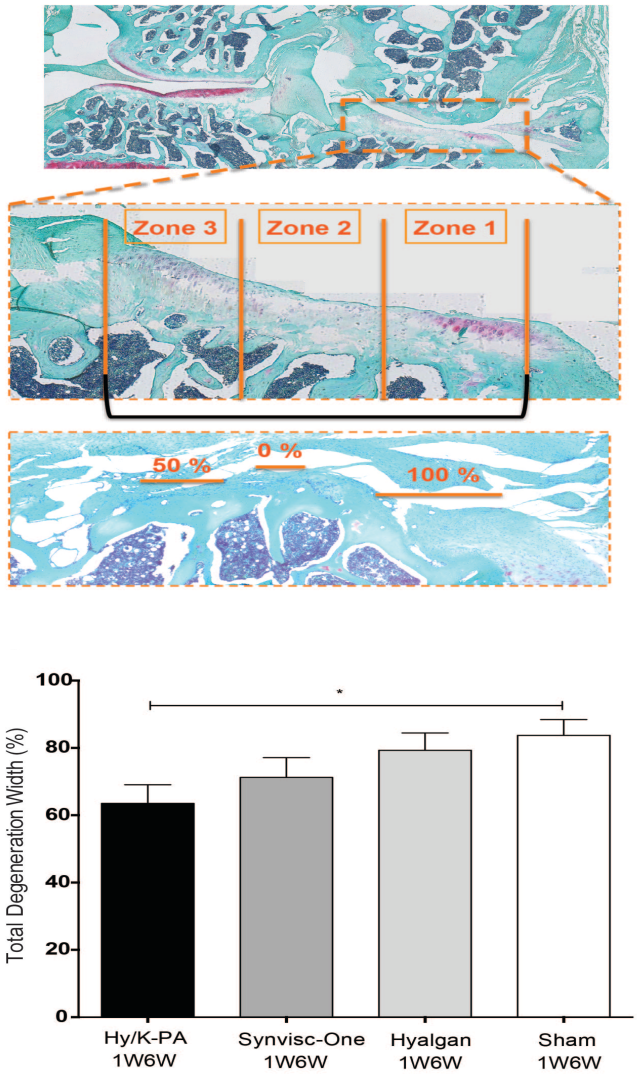


Figure 3. 9 Total degeneration width analyses across three zones (0%: degeneration on the cartilage surface; 50%: degeneration through the midzone; 100%: degeneration through the tidemark); Total degeneration width percent across the

whole cartilage tissue for all experimental groups (*p< 0.05, by Student's t-test, mean ± s.e.m.).

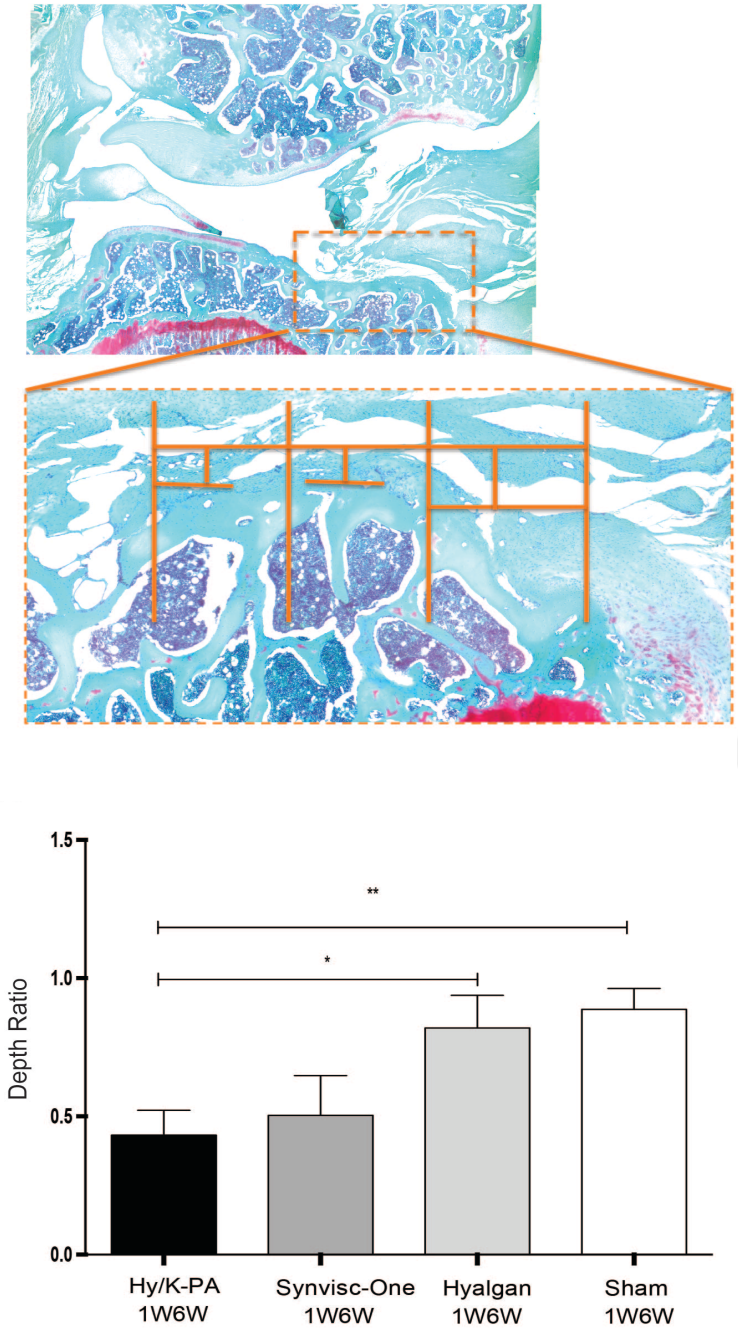


Figure 3. 10 Analyses methods for zonal depth ratio of lesions across three zones; Depth ratios of lesions across three zones for all experimental groups (1 and 0 are

maximum and minimum degeneration width, respectively) (*p< 0.05 and **p<0.01 by Student's t-test, mean ± s.e.m.).

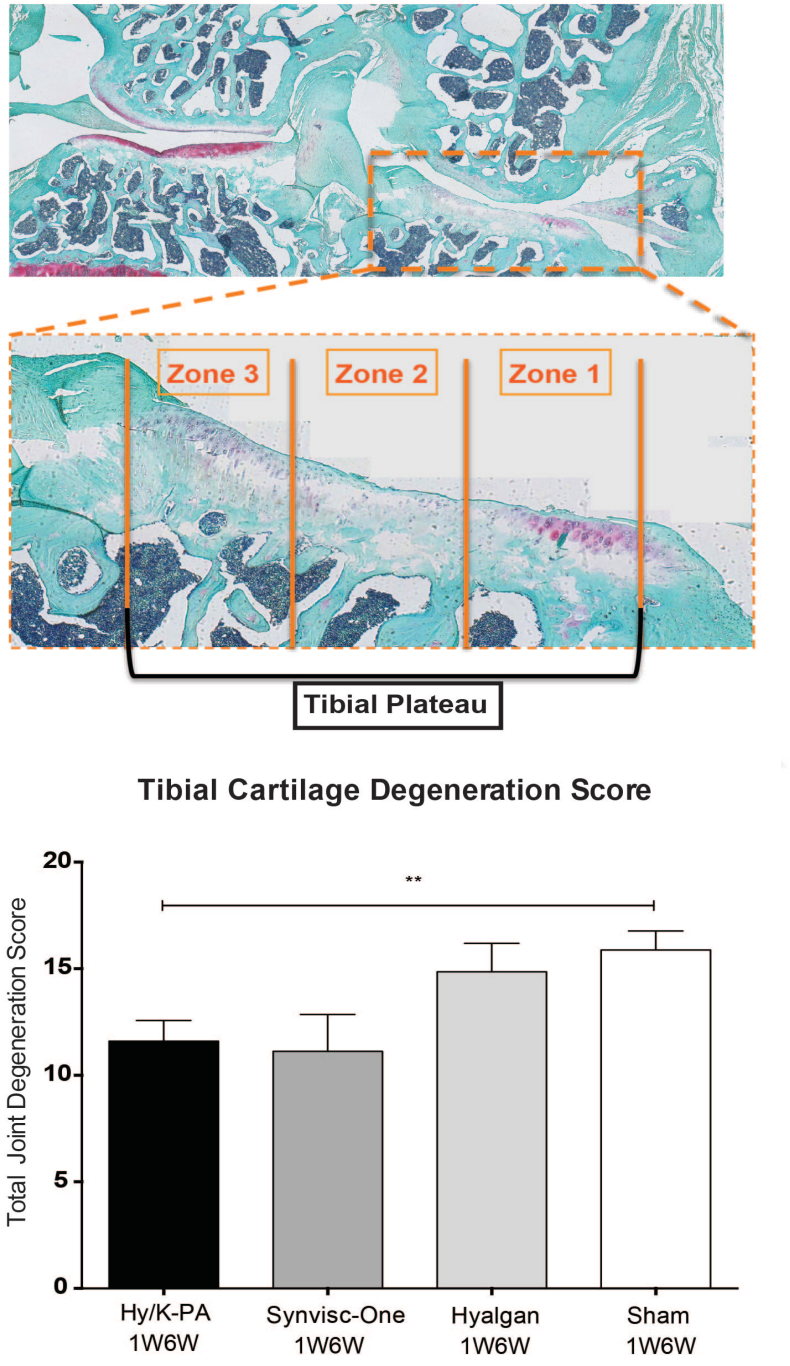


Figure 3. 11 Medial tibial cartilage scoring for experimental groups (**p<0.01, by Student's t-test, mean ± s.e.m.).

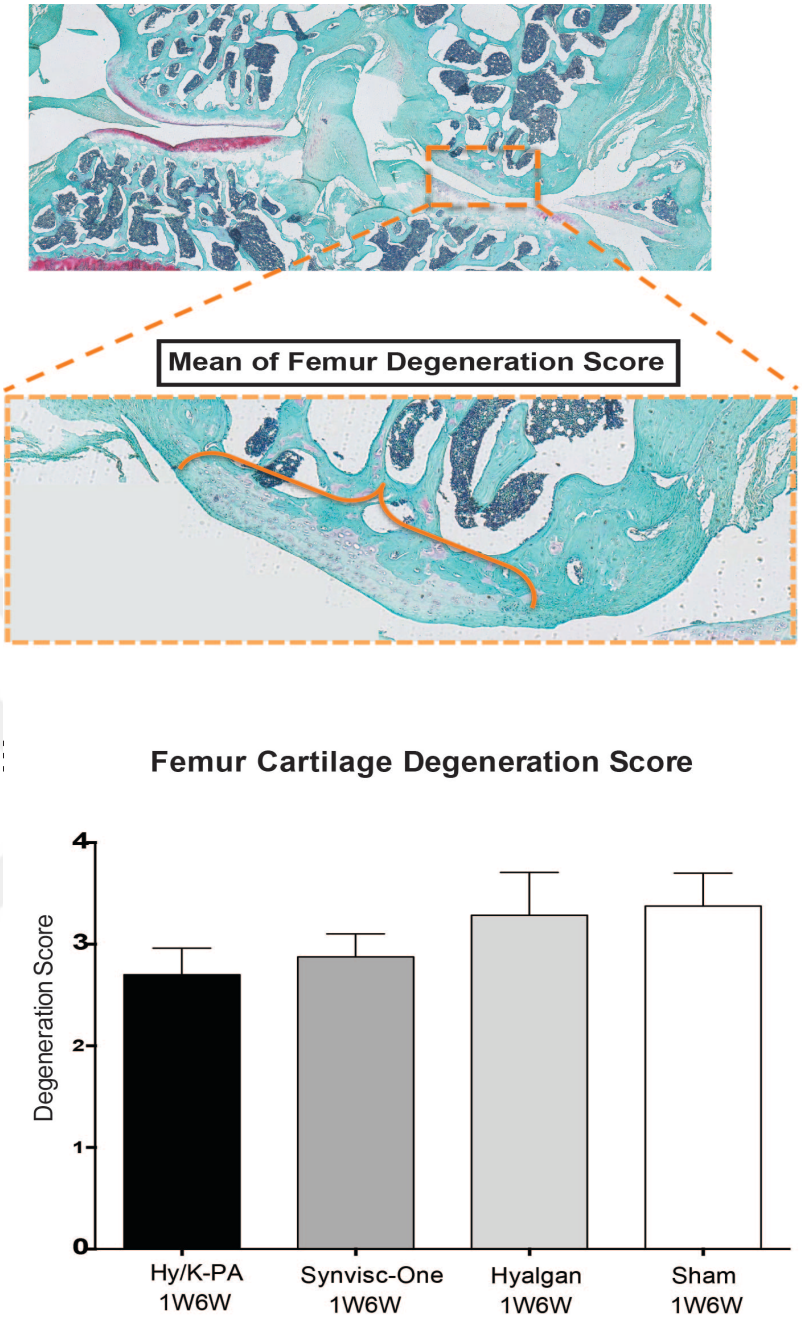
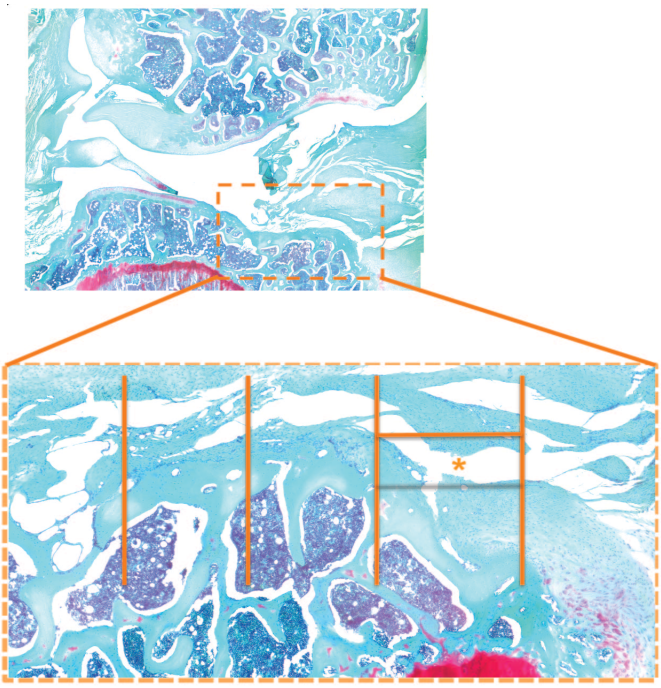


Figure 3. 12 Medial femur cartilage degeneration scoring for experimental groups.



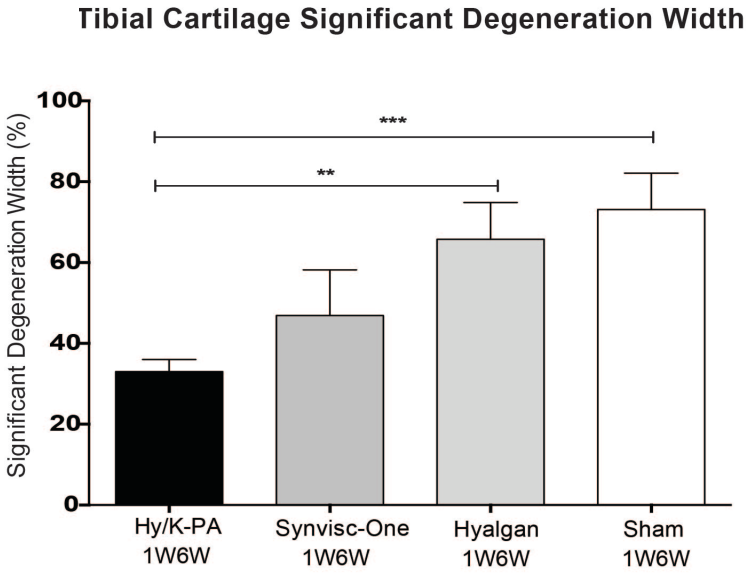


Figure 3. 13 Tibial cartilage significant degeneration width analyses for experimental groups (**p<0.01, *** p<0.001 by Student's t-test, mean ± s.e.m.).

Collagen II immunostaining demonstrated that cells in the hybrid nanofiber membrane-injected tissues had the highest collagen II deposition, whereas little-to-no collagen II presence was observed in the other groups, especially on the medial part

of tibial plateau (Figure 3.14). In addition, Sirius Red and Masson's Trichrome stainings were also performed to show the collagen structure and deposition on the tissue.

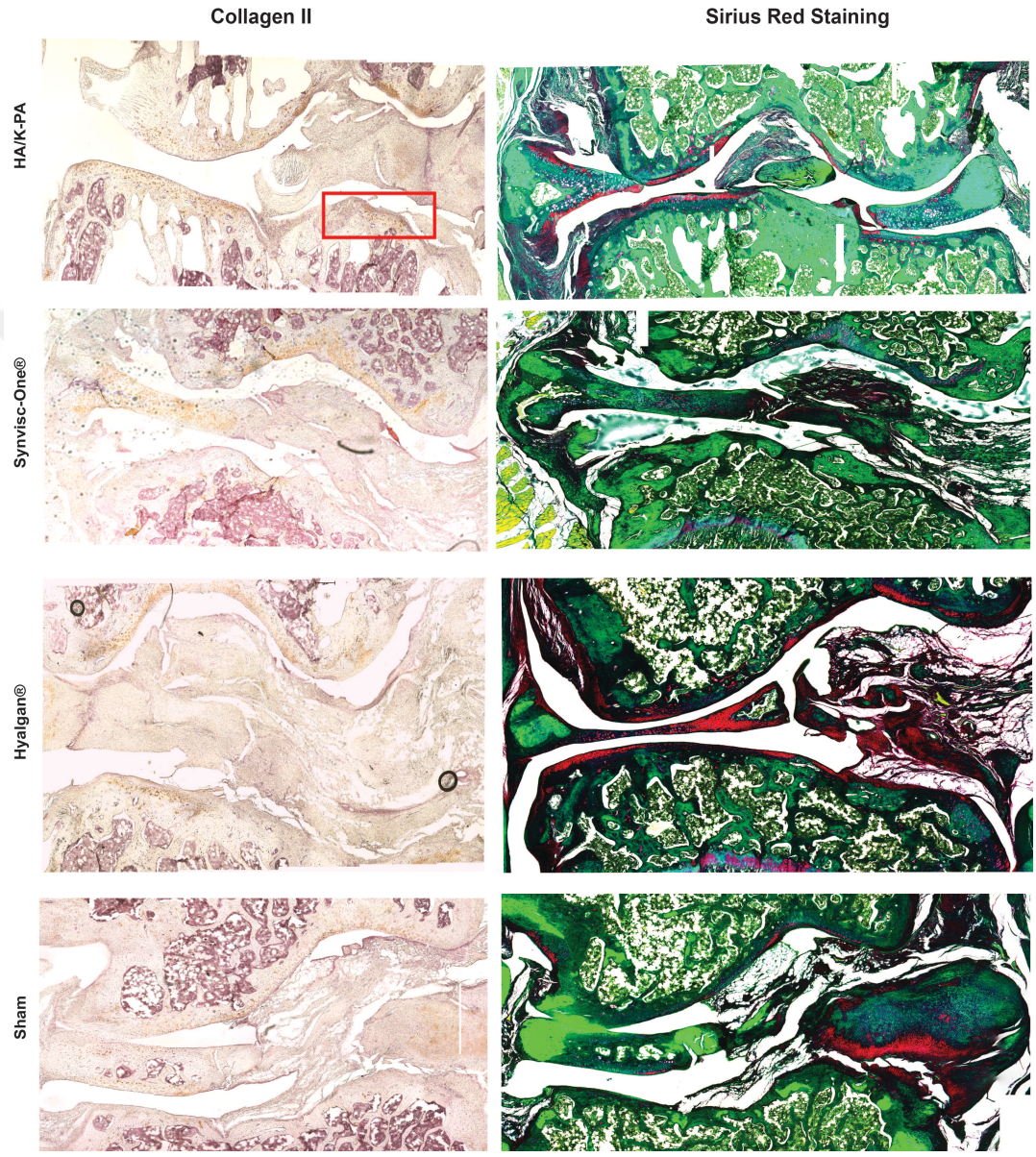


Figure 3. 14 Collagen deposition analyses; Collagen II immunostaining and Sirius Red stainings are shown for all experimental groups.

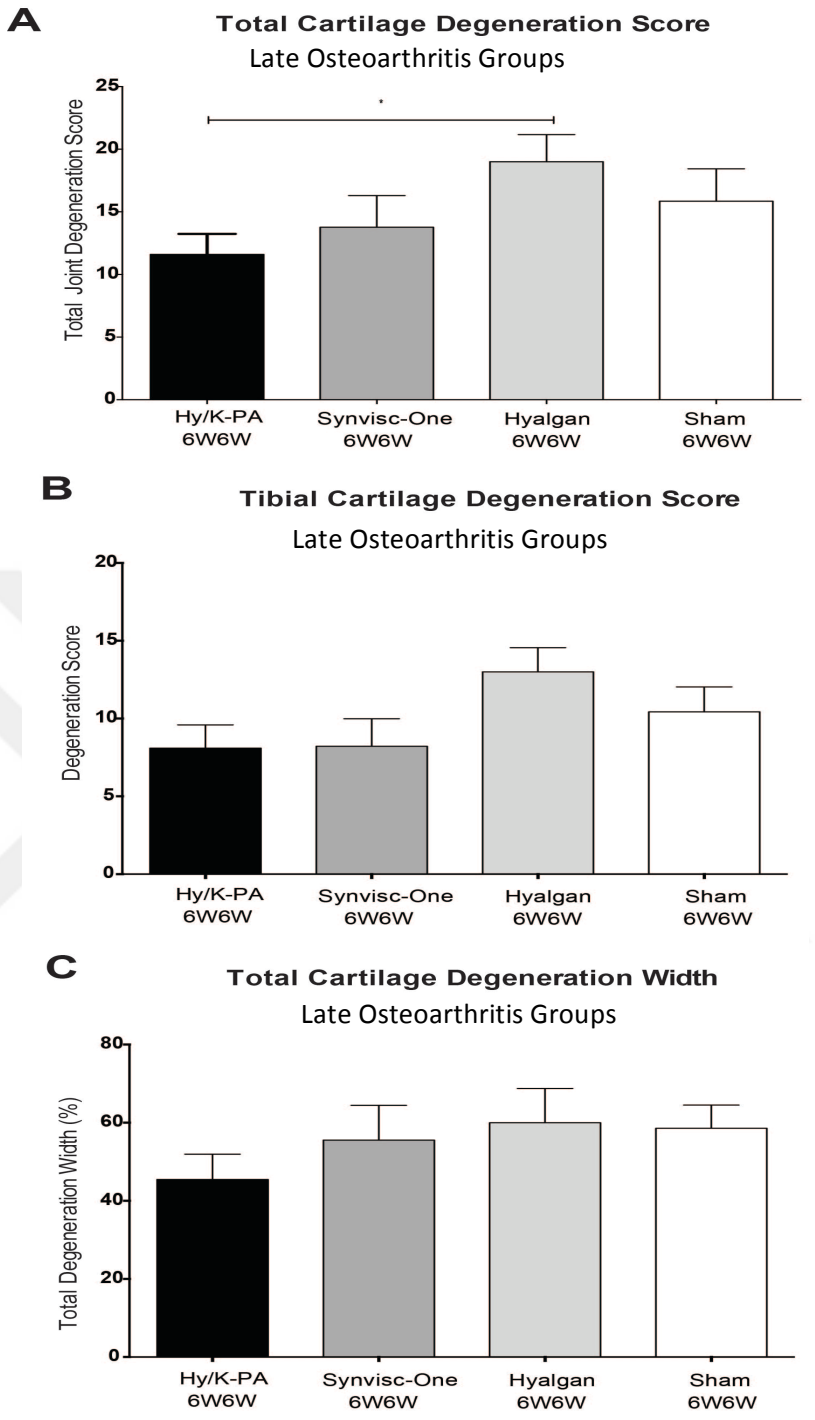


Figure 3. 15 (A) Total cartilage degeneration score for late osteoarthritis groups; (B) Tibial cartilage degeneration score for late osteoarthritis groups; (C) Total cartilage degeneration width for late osteoarthritis groups (*$p<0.05$ by Student's t-test, mean ± s.e.m.)

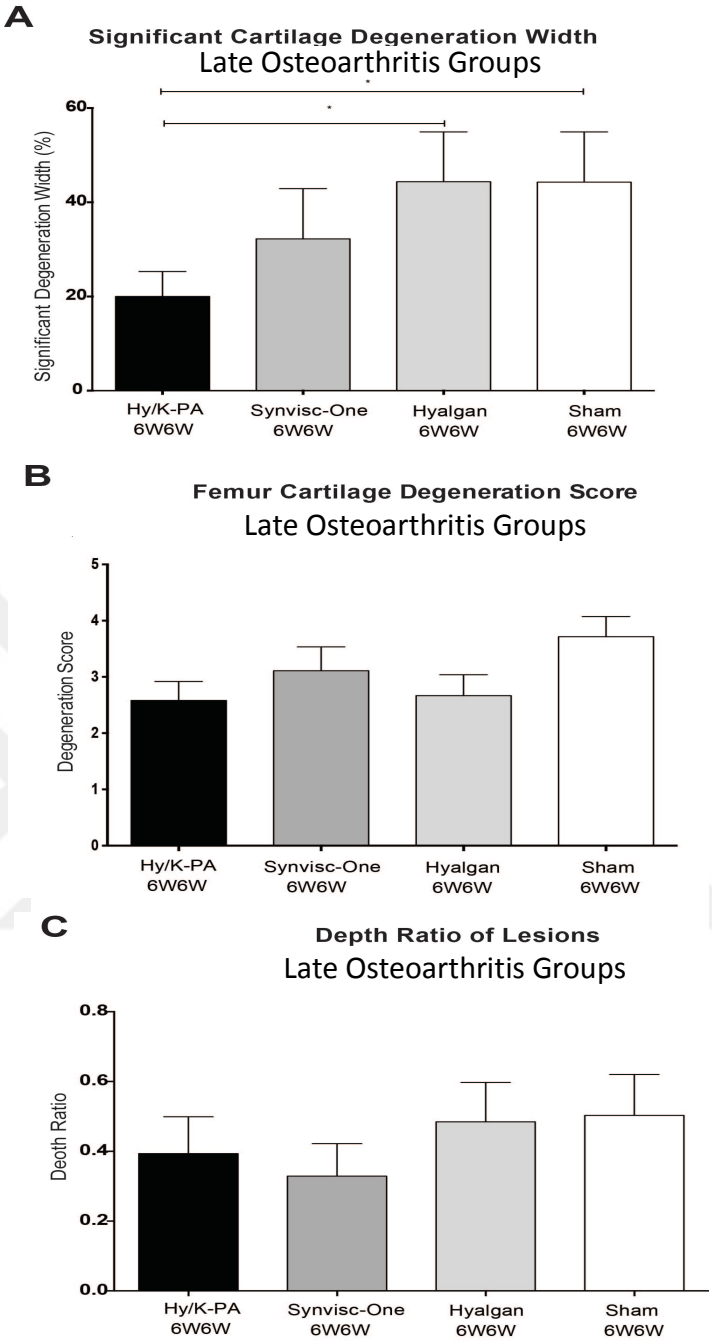


Figure 3. 16 (A) Significant cartilage degeneration width for late osteoarthritis groups; **(B)** Femur cartilage degeneration score for late osteoarthritis groups; **(C)** Depth ratio of lesions for late osteoarthritis groups (1 & 0 are max. and min. degeneration width, respectively) (*p< 0.05, by Student's t-test, mean ± s.e.m.).

3.5 Discussion

Osteoarthritis of the knee is an increasingly prevalent condition and has become one of the most common joint diseases in the aged population, as well as in populations having epidemic obesity [99]. Although pain and loss of function associated with osteoarthritis strongly affect the patients' quality of life, there is no effective treatment for this disease in clinics [99]. Failure of the damaged cartilage matrix to recover is essential for the etiology of osteoarthritis [99]. In addition, the progressive nature of osteoarthritis necessitates early intervention for its effective treatment. When damage occurs at earlier stages of osteoarthritis, chondrocyte clusters form at the damage site to compensate for matrix degradation through the action of tissue-destructive proteinases, and the local concentration of growth factors is increased to enhance the recovery attempt [112-114]. However, cartilage recovery is not effective and ultimately fails, which leads to imbalances in tissue anabolism/catabolism that favor catabolic activity. This process leads to the production of a mechanically weak matrix that cannot withstand the mechanical stresses that cartilage tissue is constantly exposed to. Therefore, especially at the early stages of disease, tissue-engineering strategies could be effective to enhance the recovery attempt of the tissue for the formation of a functional hyaline cartilage matrix. In this study, peptide amphiphile molecules were combined with commercially available Hyalgan® gel (which is composed of high molecular weight hyaluronic acid) which resulted in formation of hybrid nanofiber membranes with higher hydrolytic stability and mechanical strength even at ~1/4 of the concentration of the gels (Hyalgan® and Synvisc (Hylan G-F 20)®) used in clinics.

Autologous chondrocyte implantation is one of the leading osteoarthritis treatment options. Considering the essential role of chondrocyte clustering for matrix re-

synthesis and recovery at the early stages of osteoarthritis development, autologous chondrocyte implantation gained considerable attention for enhancing the healing capacity of degenerated matrix [114]. Hence, we also investigated the biocompatibility of the hybrid nanofiber membrane for chondrocyte implantation. HA/K-PA nanofiber membrane was found to support chondrocyte growth and provided a native ECM-like 3D microenvironment. On the other hand, both Hyalgan® and Synvisc® gels were not hydrolytically stable and disintegrated into culture media, which prevented the encapsulation of cells. Therefore, this hybrid nanofiber membrane scaffold can be also considered for further autologous chondrocyte implantation applications. In addition, the hybrid nanofiber membrane was shown to provide a suitable microenvironment for stem cell growth; which demonstrated the potential of this hybrid nanofiber membrane system for stem cell recruiting approaches in cartilage tissue engineering applications.

The shortcomings of current treatment options necessitate the investigation of possible therapeutics against osteoarthritis. Hence, the efficiency of HA/K-PA hybrid nanofiber membrane scaffold was analyzed through an *in vivo* osteoarthritis model. Both early stage and late stage of osteoarthritis were modeled using two experimental groups: 1W6W (Early group: scaffold injection 1 week after surgery & tissue extraction 6 weeks after injection) and 6W6W (Late group: scaffold injection 6 weeks after surgery & tissue extraction 6 weeks after injection) groups. According to the immunohistochemical results, the hybrid nanofiber membrane was found to exhibit significantly enhanced protective and healing capacity compared to clinically prescribed gels for early osteoarthritis groups. When defect healing was monitored by the staining of representative slides taken at 20 section (~200 μm) intervals to

determine the extent of cartilage regeneration through the anterior to posterior regions of cartilage, the cartilage tissue morphology was observed to be preserved better in HA/K-PA injected animals. In addition, the expression of cartilage-specific type II collagen was shown to increase in HA/K-PA group. Although we did not find statistically significant differences among late osteoarthritis groups, we also observed that degeneration score exhibited a downward trend for hybrid nanofiber membrane, which suggests that healing is enhanced for the late osteoarthritis groups (Figure 3.15 and 3.16). However, these findings also demonstrated that initiating treatment at early stages of osteoarthritis is crucial for the amelioration of disease symptoms.

Hyaluronan is one of the important components of synovial fluid in joints, and provides a viscoelastic environment and sufficient lubrication to reduce wear in cartilage [115]. In addition, it functions as a scaffold by retaining important macromolecules such as aggrecan and link proteins in joints, and stimulates the endogenous synthesis of hyaluronan by interacting with CD44 receptors on chondrocytes [115]. Despite of the fact that Hyalgan® and Synvisc® are prescribed in clinics as hyaluronan derivatives for osteoarthritis treatment at early/intermediate stages of disease, they have limited and short-term efficiency [98]. On the other hand, the hybrid scaffold both provided bioactivity by stimulating native ECM turnover through the presence of hyaluronic acid, and presented a mechanically stable viscoelastic microenvironment to maintain tissue function.

Self-assembly of molecules at structural interfaces is a major feature for the preparation of chemically well-defined and well-ordered materials and presents several opportunities in tissue engineering and clinical applications. It was previously demonstrated that the combination of small synthetic PA molecules with high-

molecular weight natural polysaccharide hyaluronic acid results in the formation of a solid membrane at the liquid-liquid interface [107]. Through this mechanism, HA/K-PA scaffold provided a mechanically robust network (Figure 3.4) due to the hierarchical order of K-PA and HA molecules. A similar membrane system was shown to be more stable than high molecular weight polysaccharide combination chitosan – gellan membranes, which were prone to disintegrating in aqueous environment [107]. In addition, this system allowed the formation of HA-filled membrane sacs that were shown to be robust enough to withstand suturing without tearing [107]. This feature is essential for the efficiency of membranes to be used in cartilage defects, because cartilage is constantly exposed to repetitive mechanical loading. Consequently, tear-resistance is crucial for the proper functioning of tissue substitutes. In addition, this hierarchically self-assembling membrane system facilitated the encapsulation of hyaluronic acid within the sacs, allowing its maintenance for a longer time following injection [107]. However, the use of hybrid PA/hyaluronic acid systems for osteoarthritis treatment has not been reported to date.

The nanofiber system described in the present study uses the same design principles as previously described hybrid membranes and can be effectively used for long-term treatment of osteoarthritis. Furthermore, the therapeutic activity of the HA/K-PA membrane was provided at a relatively lower concentration than Hyalgan® and Synvisc® gels, which further shows the superior therapeutic effect of this hybrid system at a lower production cost. Although the hybrid nanofiber membrane scaffold demonstrated comparable regenerative effect to Synvisc® gel, the latter material is associated with shortcomings due to its cost and immunogenicity problems [111]. In addition, the tailorable features of PAs present a broader opportunity to improve

membrane design and enhance therapeutic activity through the incorporation of specific bioactive epitopes. Furthermore, this membrane sac system allows the encapsulation and infiltration of large macromolecules such as proteins and growth factors. Hence, this system can be used for further drug delivery applications such as the delivery of nonsteroidal anti-inflammatory drugs against osteoarthritis.

3.6 Conclusion

Osteoarthritis is associated with severe pain and loss of function and is one of the leading causes of joint disabilities in older adults. The development of effective and novel treatment strategies against this disease is therefore of great importance for restoring damaged cartilage function. In this study, we have examined the *in vitro* and *in vivo* efficiency of a hybrid nanofiber membrane and observed that it enabled chondrocyte encapsulation and provided a suitable culturing environment for stem cell growth *in vitro*, while facilitating the preservation of cartilage morphology with reduced osteophyte formation, protecting the subchondral region from deterioration, and maintaining cartilage-specific matrix proteins *in vivo*. In addition, this system allows the formation of HA-filled membrane sacs that present a tear-resistant scaffold, which is crucial for the proper functioning of tissue substitutes under repetitive mechanical stress in joints. The hybrid nanofiber membrane system described in this study could therefore protect cartilage tissue from degeneration and enhance the repair process at the site of injury. Overall, the therapeutic activity of the hybrid nanofiber membrane system was provided at a relatively lower concentration than Hyalgan® and Synvisc® gels, which allows its use as a potential candidate for further clinical applications.

Chapter 4. Supramolecular Peptide Nanofiber Morphology Affects Mechanotransduction of Stem Cells

A partial content of this work is under preparation for a publication with the following authors:

Arslan, E.; Hatip Koc, M.; Uysal, O.; Dikecoglu, B.; Topal, A.E.; Garifullin, R.; Ozkan, A.; Dana, A.; Hermida-Merino, D.; Castelletto, V.; Edwards-Gayle, C.; Baday, S.; Hamley, I.; Tekinay, A. B.; Guler, M. O.

4.1 Objective

Chirality and morphology are essential factors for protein function and interactions with other biomacromolecules. ECM proteins are also similar to other proteins in this sense; however, the complexity of the natural ECM makes it difficult to study these factors at the cellular level. The synthetic peptide nanomaterials harbor great promise in mimicking specific ECM molecules as model systems. In this work, we demonstrate that mechanosensory responses of stem cells are directly regulated by the chirality and morphology of ECM-mimetic peptide nanofibers with strictly controlled characteristics. Structural signals presented on L-amino acid containing cylindrical nanofibers (L-VV) favored the formation of integrin β1-based focal adhesion complexes, which increased the osteogenic potential of stem cells through the activation of nuclear YAP. On the other hand, twisted ribbon-like nanofibers (L-

FF and D-FF) guided the cells into round shapes and decreased the formation of focal adhesion complexes resulting in the confinement of YAP proteins in the cytosol and a corresponding decrease in osteogenic potential. Interestingly, the D-form of twisted-ribbon like nanofibers (D-FF) increased the chondrogenic potential of stem cells more than their L-form (L-FF). Our results provide new insights into the importance and relevance of morphology and chirality of nanomaterials in their interactions with cells, and reveal that precise control over the chemical and physical properties of nanostructures can affect stem cell fate even without the incorporation of specific epitopes.

4.2 Introduction

In their native microenvironment, cells respond to a broad range of ECM signals by modulating their mechanical properties through cytoskeletal remodeling [116]. The ECM provides a physical scaffold that is integral for the transduction of biochemical and biomechanical signals necessary for proper functioning of cells and tissues. Structural and chemical features of ECM elements are essential for their ability to elicit specific cellular responses, and synergistic interactions between these signals are also crucial for the regulation of cellular behavior. For example, integrin-binding motifs such as GFOGER occur on collagen and only exhibit bioactivity when presented within a triple helix structure [117]. Thus, the macromolecular structure can substantially alter the context of even well-established biochemical signals by modulating their interactions with cellular receptors [118].

Stem cells adapt environmental signals as biochemical information through contractile forces acting on fibronectin fibrils [119]. In addition, fibrillar proteins in the ECM exhibit certain structural fingerprints that impart them with their

fundamental functions. For example, different collagen types in various supramolecular structures; including geometric networks, membrane-spanning fibrils, and beaded-filaments, contribute to a diverse range of functions such as providing tensile strength and enabling resistance to plastic deformation and rupture [120]. In addition, collagen fibrils exhibit a periodicity known as the D-band, which determines the stiffness of the microenvironment. Alterations in this periodicity are known to result in disease due to disorders in the shape and mechanical strength of the fibrillar structure [121].

Supramolecular structures of the ECM fibrillar proteins are tissue-specific and their mechanical properties are optimized to react to the specific range of external and internal forces that is routinely experienced by each tissue. Through these proteins, externally applied mechanical forces function at the molecular level by regulating focal adhesion (FA) point size, shape, and composition in cells [122]. In addition to supramolecular structures, chirality is also a characteristic of many biomacromolecular interactions that govern cellular behaviors [123-125]. In fact, a wide range of biomacromolecules function precisely due to specific enantiomeric interactions that fail to occur if both partners do not share a chiral configuration [126]. If any particular component was to be replaced by an unsuitable enantiomeric counterpart, the function of the whole system would be lost due to the ensuing destabilization effect that distorts the secondary structure of proteins and other biomacromolecules [127].

Inspired by the features of tissues and their natural ECM, a broad range of functional therapeutic biomaterials have been developed by emulating the physical, chemical and biological properties of native tissue microenvironments [1, 20, 23]. Among

these biomaterials, peptide nanofibers have great potential in mimicking natural ECM by incorporating specific signal sequences [128, 129]. While the biological activity of peptide nanofibers is typically based on the cellular recognition of their functional epitope sequences, their physical and chemical properties are also essential for mediating cell-biomaterials interactions [122]. Hence, self-assembled supramolecular peptide amphiphile nanofibers provide a useful toolkit for the investigation of cell-ECM interactions by exhibiting a variety of mechanical properties despite their simple, well-defined and highly bioactive structures [130-132]. Self-assembly can be triggered through different external and internal forces while providing an extremely large morphological diversity and various physical and chemical features as a result [133, 134]. Several studies have demonstrated that nanofibers with distinct morphology and chirality are able to selectively interact with cells to elicit specific cellular responses, but these studies only focus on one of these features in isolation from the others [84, 123, 124, 135]. However, emulating the complexity inherent to native tissues requires sophisticated biomaterials design integrating distinctive features to precisely regulate the distribution of cells, macromolecules and structural elements at various scales and dimensions [136].

In this work, we demonstrated peptide nanofibers with strictly controlled morphology and chirality to study the effects of these features on the cellular fate at the molecular and cellular levels. We monitored the control of cellular responses, including the differentiation of stem cells, by tuning the physical and chemical cues provided by the peptide nanofiber materials. Twisted ribbon-like nanofibers (L-FF and D-FF) reduced cellular spreading as well as ERK/MAPK pathway activity, resulting in genetic regulation through the repression of nuclear YAP (Yes-

associated protein) activity, which reduced the osteogenic differentiation of stem cells while favoring chondrogenesis by altering cell shape through matrix-induced cellular rounding. In contrast, the L- amino acid containing cylindrical nanofibers (L-VV) produced a greater mechanical feedback and enhanced cellular spreading through increased interaction with the integrin β1 receptor. Stem cells on L-VV scaffolds activated the ERK/MAPK pathway, which resulted in YAP/TAZ activation and nuclear YAP localization, which further increased the osteogenic differentiation of stem cells. These results demonstrate the importance of morphology and chirality on effect of ECM-mimetic nanofibers on stem and somatic cell behavior, and show that the behavior of stem cells could be tuned even without the incorporation of biologically relevant epitopes.

4.3 Experimental Section

4.3.1 Materials

9-Fluorenylmethoxycarbonyl (Fmoc) and tert-butoxycarbonyl (Boc) protected amino acids, [4-[α-(2′,4′-dimethoxyphenyl) Fmoc aminomethyl]enoxy] acetamidonorleucyl-MBHA resin (Rink amide MBHA resin), Fmoc-Glu(OtBu)-Wang resin and HBTU were purchased from NovaBiochem and ABCR. Cover glasses and tissue culture plates (24-well) were purchased from Deckglaser and BD. All other chemicals and materials used were analytical grade and obtained from Invitrogen, Fisher, Merck, Alfa Aesar and Sigma-Aldrich. Chondrogenic differentiation media were purchased from Sigma. Live/Dead Assay (L3224), Alamar Blue and other cell culture materials were purchased from Invitrogen. Western blotting, flow cytometry, and immunocytochemistry antibodies were purchased from Abcam, Millipore, or Santa Cruz Biotechnologies: anti-vinculin antibody, (Abcam, ab18058), anti-FAK antibody

(Abcam, ab72140), mouse monoclonal IgG2a (Abcam, ab170191), goat anti-mouse IgG H&L (Alexa Fluor® 488) (Abcam, ab150113), anti-Integrin α2 antibody [EPR17338] - C-terminal (Abcam, ab181548), anti-FAK antibody [63D5] (Abcam, ab72140), anti-phospho-FAK (Tyr397) antibody clone EP2160Y (Millipore, 04-974), anti-ERK1 + ERK2 antibody [IL-13] (Abcam, ab130004), anti-ERK1 (pT202/pY204) + ERK2 (pT185/pY187) antibody [MAPK-YT] (Abcam, ab50011), anti-MEK1 + MEK2 antibody (ab178876) or anti-phospho-MEK1 (Ser218/222)/MEK2 (Ser222/226) antibody (Millipore, 05-747), Goat Anti-Mouse IgG H&L (Alexa Fluor® 488) (Abcam, ab150113), YAP antibody (H-9) (SCBT, sc-271134).

4.3.2 Synthesis of peptide amphiphile molecules

All peptides were synthesized by using Fmoc solid phase peptide synthesis. All peptides including lauric acid were constructed on Fmoc-Rink Amide MBHA resin. Amino acid coupling reactions were performed with 2 equivalents of Fmoc-protected amino acid, 1.95 equivalents of HBTU and 3 equivalents of DIEA for 2 h. The Fmoc protecting group removal was performed with 20% piperidine/DMF solution for 25 min. Cleavage of the peptides from the resin was carried out with a mixture of TFA : TIS : H_2O at a ratio of 95 : 2.5 : 2.5 for 2 h. Excess TFA was removed by rotary evaporation. The remaining peptide was triturated with ice-cold diethyl ether and the resulting white precipitate was freeze-dried. All peptides were purified by Prep-HPLC and positively charged peptides were treated with 1 mM HCl.

Before each characterization, 1% (w/v) EE-PA solutions and KK-PA solutions were dissolved in water separately. Four samples; L-VV, D-VV, L-FF, D-FF, which are listed in Table 1, were prepared by mixing positively and negatively charged peptide

solution pairs at 1:1 volume ratio (Table 4.1). These neutralized samples were incubated overnight and all characterizations were done at the physiological pH.

Table 4. 1 List of positively and negatively charged peptide amphiphiles

Networks	Positive PA	Negative PA
L-VV	Lauryl-VVAGKK-Am	Lauryl-VVAGEE-Am
D-VV	Lauryl-vvaGkk-Am	Lauryl-vvaGee-Am
L-FF	Lauryl-FFAGKK-Am	Lauryl-FFAGEE-Am
D-FF	Lauryl-ffaGkk-Am	Lauryl-ffaGee-Am

4.3.3 Chemical characterizations of peptide amphiphiles by LC-MS

Agilent Technologies 6530 Accurate-Mass Q-TOF-MS equipped with HPLC using Zorbax SB-C8 column was used for LC-MS analysis. LC-MS sample was prepared in 0.5 mg/mL concentration. Mobile phase solutions were water (0.1% formic acid) and acetonitrile (ACN) (0.1% formic acid). LC-MS was run for 30 min for each sample and it started with 2% ACN and 98% H_2O for 5 min. Then, gradient of ACN reached 100% in 20 min. Finally, its concentration was dropped to 2% and it was kept running for 5 min. Solvent flow was 0.65 mL/min and 5 µL sample was injected.

4.3.4 Secondary structure analysis of peptide nanofibers by CD

A Jasco J-815 CD spectrophotometer was used for CD analysis. 1% (w/v) positively and negatively charged peptide solution mixtures were diluted first to 2 mM, then to 0.25 mM concentration, gradually. This prevented the disintegration of the co-assembled network through dilution. 0.25 mM solutions were used for the CD measurement in 1 mm quartz cell. Peptide solution was measured from 300 nm to

190 nm with 0.1 data pitch, 100 nm/min scanning speed, 1 nm bandwidth and 4 s D.I.T. Average of three measurements were used, and sensitivity was selected as standard.

4.3.5 Morphological analysis of peptide nanofibers by TEM

Imaging of the peptide nanostructures was achieved by TEM (FEI, Tecnai G2 F30) at 100 kV. For peptide nanofiber staining, uranyl acetate solution in water (2 wt %) was used. Each of four 1% (w/v) peptide stock solutions were gradually diluted to 2 mM solution, then to 50 μM TEM sample solution. These diluted samples were placed on a Lacey carbon coated copper grid. 10 μL of diluted sample solution was dropped on a grid and incubated for 8 min. The excess was removed by pipette. Then, 20 μL of 2 wt % uranyl acetate solution was put on a parafilm sheet. The grid was placed on the top of the drop with its upper side down and kept there for 5 min. Stained grids were dried in a fume hood at room temperature overnight.

4.3.6 Morphological analysis of peptide nanofibers by SAXS

Experiments on single component peptide solutions were performed on beamline B21 at Diamond Light Source, Harwell, UK. Solutions (1 wt % or 0.5 wt % for more viscous samples) were loaded into the 96 well plate of an EMBL BioSAXS robot. Aliquots of solutions (25 μL) were then injected via an automated sample exchanger at a slow and very reproducible flux into a quartz capillary (1.8 mm internal diameter) in the X-ray beam. For D-VVEE, the 1 wt % sample was too viscous to flow into the capillary, however, dilution to 0.5 wt % enabled sample delivery into the beam. The quartz capillary was enclosed in a vacuum chamber, in order to avoid parasitic scattering. After the sample was injected in the capillary and reached the X-ray beam, the flow was stopped during the SAXS data acquisition. SAXS frames

were collected with a duration of 20 s or 100 s. B21 operated with a fixed camera length (4.01 m) and fixed energy (12.4 keV). The images were captured using a Pilatus 2M detector. Data processing (background subtraction, radial averaging) was performed using the dedicated beamline software Scatter.

SAXS data were modeled using the software SASfit [137] with model "Bilayer Gauss". This model describes tape-like structures represented as bilayers with electron dense cores and lower electron density surfaces. The model, used in several previous papers [138, 139] was that of Pabst et al. [140]. In some cases (data for L-FFEE and D-FFKK) an alternative nanotube form factor provided a better fit to the data at low q where a maximum is observed in the intensity, corresponding to helically wrapped nanotapes. The fitting was done using SASfit [137]. A flat background was added in the model for all data.

Simultaneous SAXS/WAXS experiments on gel-forming mixtures were performed on beamline BM26B at the ESRF. Samples were placed in DSC pans modified with mica windows to enable transmission of the X-ray beam. The sample to SAXS detector distance was 3.16 m using a wavelength of 1.033 Å. A Dectris-Pilatus 1 M detector with a resolution of 981 × 1043 pixels and a pixel size of 172 × 172 μm was used to acquire the 2D SAXS scattering patterns. Standard corrections for sample absorption and background subtraction were performed. The data were normalized to the intensity of the incident beam (in order to correct for primary beam intensity fluctuations) and were corrected for absorption and background scattering. Diffraction from silver behenate was used to calibrate the wavevector scale of the scattering curve.

4.3.7 Molecular dynamics simulations of peptide nanofibers

All-atom explicit solvent simulation systems were prepared for four PA nanofibers. Each PA nanofiber system was constructed using 18 layers that were composed of 12 PAs. The starting configuration for each PA nanofiber was done based on previous simulations, such that 19 layer with 12 PA in each layer configuration gave rise to the most stable configuration for PAs having similar length compared with PAs given in this work [141]. In order to maintain 1:1 stoichiometry between glutamate (GLU-G) and lysine (LYS-K) having peptides, adjacent layers were constructed with either GLU only or LYS only peptides. To establish ionic interactions between the main simulation box and periodic images, 18 layers were chosen instead of 19 layers. Each layer was built by placing 12 PAs with 30° angle separation. Adjacent layers were put together with 5 Å distance away and 15° angle rotation (Figure 4.1). The PA nanofibers were solvated with TIP3 water molecules and, Na+ and Cl- ions were added to reach 0.15 M salt concentration. Resulting simulation system boxes contained around 120,000 atoms.

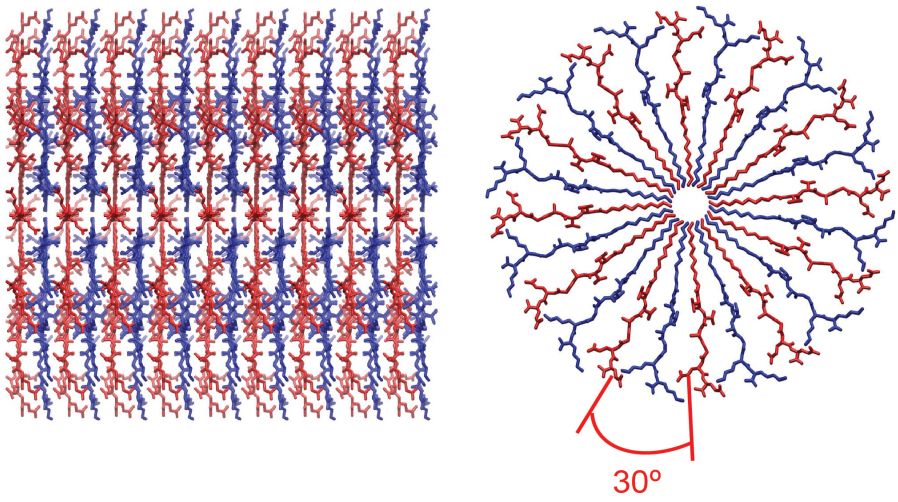


Figure 4. 1 Starting structures of the PA nanofibers for MD simulations. Nanofiber structures were built using 18 layers. Each layer contains 12 PAs that were placed by 30° angle separation. Adjacent layers contain only either glutamic acid (red) or lysine (blue) containing PAs and are constructed by 15° angle rotation with respect to each other.

MD simulations for the PA nanofibers were performed using NAMD program (version 2.9) with CHARMM force field [142, 143]. Prior to production simulations, simulation systems were minimized with 1000 minimization steps. 100 ns production simulations were carried out for each PA nanofiber system at 1 atm pressure and 310 K temperature. Electrostatic interactions were calculated using the particle-mesh Ewald method with a grid spacing [144]. The cutoff for van der Waals interactions was taken as 12 Å with a switching function after 10 Å. Simulation trajectories were integrated with a time step of 2 fs, with all interactions calculated at every time step. Atomic coordinates were collected every 10 ps. The analyses were applied to the last 20 ns of each trajectory. Hydrogen bonds and radial distribution functions (RDF)

were calculated using CPPTRAJ program [145]. Non-bonded interaction energy calculations on simulation trajectories were carried out using VMD program [146].

4.3.8 Nanomechanical analysis of peptide nanofibers by AFM

For AFM measurements, peptide nanofibers were prepared as 5 μM with the same method used for TEM imaging protocol, and were dropped onto a freshly cleaved mica surface. Silicon nitride (Budget Sensors) AFM probes were used for contact mode imaging of the self-assembled peptide nanofibers in liquid. For performing of force mapping in contact-mode, Asylum Research MFP-3D AFM was used. Force maps were taken at a resolution of 32 x 32 from a 1-5 μM area. A trigger point of 0.5 V was applied for curve measurements. Vertical deflection correction was performed before starting force map measurements. A total of more than 800 force curves were analyzed per peptide nanofiber group for AFM analysis. The Hertz model was applied to calculate elastic moduli from approach curves. The Poisson ratio of the nanofibers was assumed to be 0.33.

4.3.9 Bulk mechanical analysis of peptide nanofibers by oscillatory rheology

Oscillatory rheology measurements were performed with an Anton Paar Physica MCR301 system. A 25 mm parallel plate with a gap distance of 0.5 mm was used at 25 °C for all measurements. The total gel volume was adjusted as 250 μL. PA solutions were freshly prepared as 10 mM and sonicated for 30 min. Gels were prepared using the combinations seen in Table 4.2. The negatively charged PAs were first loaded at the center of the stage and mixed with the positively charged PAs. The upper plate was adjusted to the 0.5 mm position and the gel was incubated in this position for 15 min prior to measurement. For strain sweep measurements, angular frequency was kept constant at 10 rad/s, and strain was increased between 0.1 and

100%. Storage and loss moduli were recorded at each strain value. All rheology measurements were with three replicates.

4.3.10 Morphological analysis of peptide nanofibers by SEM

For SEM imaging, 1% (w/v) bulk peptide nanofiber gels were prepared on silicon wafers. Samples were dehydrated in graded ethanol solutions, starting with 20% ethanol and proceeding to absolute ethanol for 10 min at each step. Samples were dried with a Tourismis Autosamdri-815B critical point drier, coated with 10 nm Au/Pd and imaged with a FEI Quanta 200 FEG SEM.

4.3.11 *In vitro* cell culture experiments

Peptide amphiphile nanofiber scaffolds were prepared through the protocols used for chemical characterization experiments. Briefly, PA solutions were prepared in ddH_2O at a concentration of 2 mM and sterilized under UV for 1 h. Then, the corresponding well plates (96-well plates or 24-well plates, depending on the experiment) were coated with PA combinations (Table S1). Peptide coated plates were sealed and incubated at room temperature overnight for hydrogel consolidation before use. rMSCs (rat mesenchymal stem cells, Invitrogen S1601-100, at passage 6-8), HUVECs (HUVECs were kindly provided by Yeditepe University, Istanbul, Turkey) and primary human fibroblasts (hFib) (hFibs were kindly provided by Middle East Technical University, Ankara, Turkey) were used in in vitro cell culture experiments. All cells were initially cultured in DMEM supplemented with 10% fetal bovine serum (FBS) (maintenance medium) in tissue culture plates at standard culture conditions (at 37 °C under 5% CO_2). For differentiation analyses, after 1 day of incubation for cell attachment, the medium was replaced with fresh maintenance medium, chondrogenic differentiation medium (Gibco) or osteogenic medium.

Maintenance medium supplemented with 10 mM β-glycerophosphate, 0.2 mM ascorbic acid and 100 nM dexamethasone was used as an osteogenic medium for the osteogenic differentiation of rMSCs.

4.3.12 Viability assay

Cell cultures were prepared in 96 well plates in maintenance medium medium, and cellular viability was analyzed by Alamar Blue (Invitrogen) and Live/Dead (Life Technologies) assays. 5000 rMSCs, HUVECs, or hFibs were seeded onto peptide coatings and their viability was measured at 24 h, 48 h and 72 h by measuring the fluorescence and absorbance of the reagent by spectrophotometry for the Alamar Blue assay, and imaging the cells by fluorescence microscopy for the Live/Dead Assay.

4.3.13 Adhesion analysis

Cell cultures were prepared in 96-well plates (2000 cells/well, 3 replicas for each peptide nanofiber group) in maintenance medium medium and cellular adhesion was analyzed by using adhesion medium, which is serum free maintenance medium medium including 50 μg/mL cyclohexamide and 4 mg/mL BSA. Before seeding, cells were incubated in adhesion medium for 1 h and subsequently seeded onto peptide coatings in adhesion medium. After 1 h and 5 h, wells were washed with PBS and adherent cells were stained with Calcein Am for 20 min. The number of adherent cells were counted using Image J from fluorescence microscopy images.

4.3.14 Proliferation analysis

Cell cultures were prepared in 96-well plates in maintenance medium medium and cellular proliferation was analyzed by a colorimetric ELISA-based BrdU assay (Cell

Proliferation ELISA, BrdU; Roche) according to the manufacturer's protocol. Briefly, 5000 cells/well were seeded onto coatings, and after 1, 3 and 5 days, BrdU assay was performed by incubating cells with BrdU labeling reagent, fixing them, and staining them with anti-BrdU-POD. A manufacturer-provided colorimetric substrate was added to the wells for the development of antibody staining, and absorbance values were analyzed by a spectrophotometer.

4.3.15 Spreading analysis

For gene expression studies, Cell cultures were prepared in 24-well plates on glass cover slides in maintenance medium medium and cellular spreading was analyzed by staining cells with Phalloidine/TO-PRO-3 (Invitrogen). Images were taken by fluorescence microscopy, and analyzed by Image J software.

4.3.16 Gene expression analysis

Cell cultures (rMSC) were prepared in 24-well plates in maintenance medium or chondrogenic differentiation medium. Gene expression analyses were performed by amplifying markers for chondrogenesis (Sox-9) and osteogenesis (Runx-2) by quantitative RT-PCR (qRT-PCR). Total RNAs of rMSCs on peptide coatings were isolated using TRIzol (Invitrogen) according to the manufacturer's instructions. Yields and purities of extracted RNA were assessed by Nanodrop 2000 (Thermo Scientific). Primer sequences were designed using Primer 3 software. cDNA synthesis from RNA and qRT-PCR were performed using SuperScript III Platinum SYBR Green One-Step qRT-PCR Kit (Invitrogen) according to the manufacturer's protocol. Reaction conditions were briefly as follows: 55 °C for 5 min, 95 °C for 5 min, 40 cycles of 95 °C for 15 s, 60 °C for 30 s, and 40 °C for 1 min, followed by a melting curve to confirm product specificity. Reaction efficiencies were evaluated

for each primer set through standard curves using 5-fold serial dilutions of total RNA. For the analysis of expression, primary gene expression data were normalized by the expression level of GAPDH. A comparative Ct method was used to analyze the results.

4.3.17 Protein expression analyses by flow cytometry

Flow cytometry was performed to quantify the expression of Vinculin and FAK proteins, which are important regulators of focal adhesion and cellular mechanotransduction. Prior to flow cytometry analysis, the cells were disintegrated from peptide coatings by collagenase/trypsin treatment. The supernatant was then collected and centrifuged at 2500 rpm for 5 min. The cell pellet was washed twice with PBS, resuspended, and fixed with 4% paraformaldehyde for 15 min at room temperature. The solution was then centrifuged at 2500 rpm for 5 min, and the cell pellet was resuspended and permeabilized in 0.2% Tween-20/PBS for 15 min at room temperature. A primary antibody solution (either Vinculin [anti-Vinculin antibody, (ab18058)] or FAK [anti-FAK antibody (ab72140)]) or their corresponding isotype (mouse monoclonal IgG2a (ab170191)) was prepared in 3% BSA/PBS solution at concentrations recommended by the manufacturer (Abcam) and used to stain the cells for 1 h. After primary antibody staining, cells were washed with permeabilizing solution, pelleted by centrifugation and stained with secondary antibodies [goat anti-mouse IgG H&L (Alexa Fluor® 488) (ab150113)] for 1 h. After washing twice with permeabilizing agent, the cells were again pelleted by centrifugation and resuspended in PBS prior to cytometry analysis. A BD Accuri^{TM} C6 flow cytometer system was used for cytometry and at least 20,000 events were

analyzed for the measurements. For data analysis, BD Accuri™ C6 software was used according to the manufacturer's instructions.

4.3.18 Immunoblotting analysis of protein expression by western blotting

Western blotting analyses were performed to detect the expression levels of key proteins of mechanotransduction and the associated molecular pathways. Cells were isolated from their peptide coatings by RIPA buffer (including protease and phosphatase inhibitor cocktail), and the protein containing supernatant was removed and stored at -80 °C. Protein concentrations were determined using BCA Protein Assay Kit. Equal amounts of proteins per lane were separated by 12% SDS-PAGE and transferred to a polyvinylidene difluoride (PVDF) or nitrocellulose membrane. The membrane was blocked with 5% non-fat milk in TBS-T at room temperature for 2 h and then incubated with anti-Integrin α2 antibody [EPR17338] - C-terminal (Abcam, ab181548), anti-FAK antibody [63D5] (Abcam, ab72140), anti-phospho-FAK (Tyr397) antibody clone EP2160Y (Millipore, 04-974), anti-ERK1 + ERK2 antibody [IL-13] (Abcam, ab130004), anti-ERK1 (pT202/pY204) + ERK2 (pT185/pY187) antibody [MAPK-YT] (Abcam, ab50011), anti-MEK1 + MEK2 antibody (ab178876) or anti-phospho-MEK1 (Ser218/222)/MEK2 (Ser222/226) antibody (Millipore, 05-747) overnight at 4 °C. After washing in TBS-T, the blots were incubated with the corresponding horseradish-coupled secondary antibody (goat anti-rabbit IgG or goat anti-mouse IgG). The bands were visualized using Clarity™ Western ECL blotting substrate. GAPDH (Millipore) was used as the internal control and treated with the same protocol. Protein amounts in each sample were quantified using ImageJ software.

4.3.19 Immunocytochemical analyses of protein detection by confocal microscopy

The rMSCs on peptide coatings were fixed in 4% paraformaldehyde/PBS for 10 min and permeabilized in 0.1% Triton X-100 for 15 min. For blocking, samples were incubated with 3% (w/v) bovine serum albumin/PBS for 30 min and treated with either YAP antibody (H-9) (SCBT, sc-271134) or anti-Vinculin antibody [SPM227] (ab18058) overnight at 4 °C. Cells were then washed with PBS and incubated for 1 h at room temperature with goat anti-mouse IgG H&L (Alexa Fluor® 488). All samples were counterstained with 1 μM TO-PRO-3 (Invitrogen) in PBS for 20 min at room temperature and mounted with Prolong Gold Antifade Reagent (Invitrogen). Negative controls were obtained by omitting the primary antibody and incubating with 3% normal goat serum/PBS. Samples were imaged by confocal microscopy (Zeiss LSM510) and analyzed by Image J program for cell counting to determine the cell amount with nuclear YAP localization.

4.3.20 Collagen adsorption analyses by ELISA

For the determination collagen I adsorption on peptide nanofibers, indirect-ELISA was performed. ELISA plates were coated with peptide nanofibers. On the next day, plates were washed with washing buffer, dried by tapping, blocked with assay buffer (Life Technologies, DS98200) (2 h) and Collagen I (Millipore, 08-115) was added onto peptide coatings for overnight at 4 °C. Next day, plates were washed by washing buffer, dried by tapping, then they were incubated with anti-collagen I (1:500) (ab6308) primary antibody for overnight at 4 °C. After that, plates were washed 5 times with washing buffer and dried by tapping between each consecutive step. The HRP-conjugated anti-IgG antibody was used as a secondary antibody and

incubated for 2 h. The TMB (3,3′,5,5′-tetramethylbenzidine) substrate was added at the last step and the reaction was stopped after 15 min with stop solution (1.8 N H_2SO_4). Color formation was measured by using a microplate reader (Spectramax M5, Microplate reader) as absorbance at 450 nm wavelength (reference absorbance measured at 650 nm and subtracted from absorbance at 450 nm). All treatments were performed with at least four replicates and peptide nanofiber coatings without collagen I incubation were used as blank.

4.3.21 Statistical analysis

All data are presented as mean ± SEM (standard error of mean). All experiments were performed in at least three replicas. The significance of differences between groups was determined with either one-way or two-way analysis of variance (ANOVA) with Bonferroni's post-hoc test. Differences were considered significant at *$p<0.05$, except where noted.

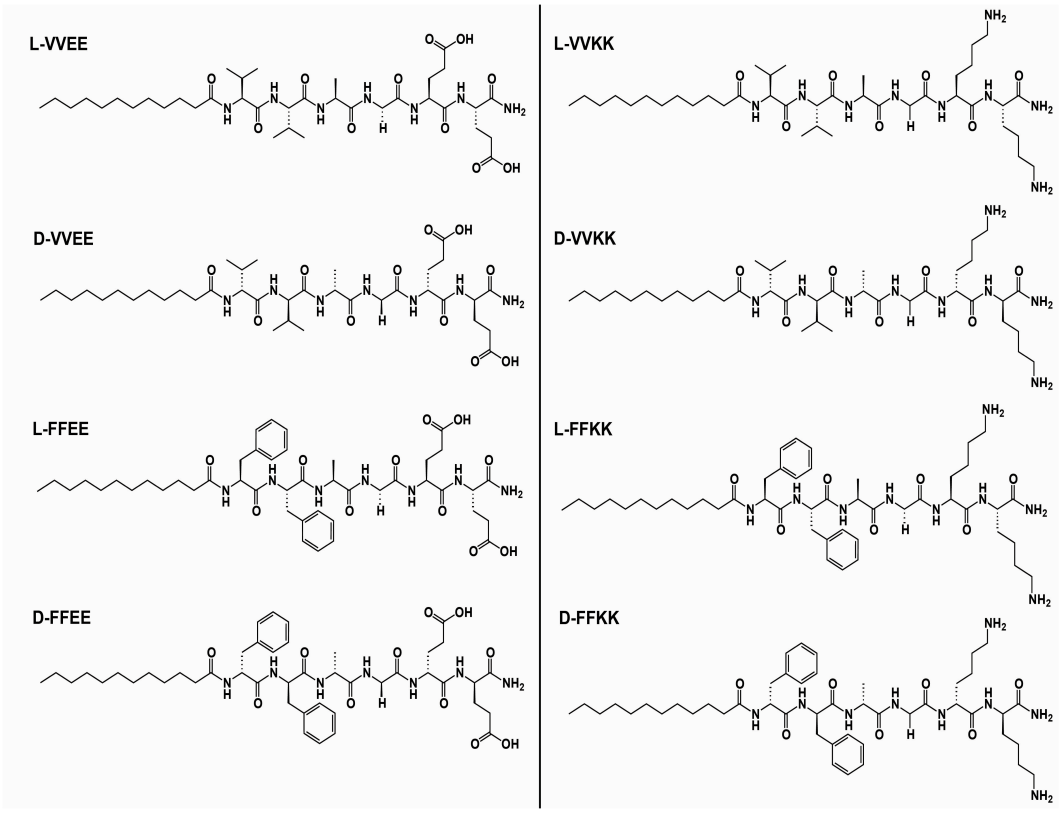
4.4 Results

4.4.1 Design, preparation and characterization of self-assembled PA molecule

Here we designed four different peptide nanofibers with distinct morphology and chirality, and evaluated their interactions with cells at the molecular level. Each nanofiber consisted of two oppositely charged peptide amphiphile (PA) molecules. In order to obtain four peptide nanofiber types (cylindrical L-form, cylindrical D-form, ribbon-like L-form, ribbon-like D-form), eight peptide amphiphile molecules, each consisting of a hydrophobic region, a β-sheet forming region, and a hydrophilic (or charged) region were designed and synthesized in two different chiral forms (Table 4.2).

Table 4. 2 Peptide nanostructure compositions and their corresponding morphology and chirality

PA	Combinations	Morphology
L-VV	L-VVEE/L-VVKK	Cylindrical Nanofibers
D-VV	D-VVEE/D-VVKK	Cylindrical Nanofibers
L-FF	L-FFEE/L-FFKK	Twisted Ribbon-like Nanofibers
D-FF	D-FFEE/D-FFKK	Twisted Ribbon-like Nanofibers



The hydrophobic region contained a lauric acid alkyl tail that is long enough to trigger specific nanofiber organization in water [54]. Either two glutamic acid or two lysine residues were used for the hydrophilic region. Four PA molecules were

synthesized with a charge of +2, and another four of them with a charge of -2 at the physiological conditions (Table 4.1). Two oppositely charged PA molecules co-assembled into high-aspect-ratio nanostructures through electrostatic interactions between positively and negatively charged building blocks to form each nanofiber network [68]. In addition, hydrophobic and hydrophilic regions of each PA molecule were linked together with a hydrogen bonding peptide region, which was essential for modulating self-assembly behavior to form cylindrical or ribbon-like structures. The valine-valine sequence caused the highest propensity for forming β-sheets for cylindrical nanofiber formation [54, 147]. The phenylalanine-phenylalanine sequence produced a twisted ribbon morphology through π–π stacking, which is the major promoting factor of the twisted morphology in the co-assembled network for ribbon-like nanostructure formation [148]. In addition, for achieving chiral differences in networks, all peptides were synthesized in both L and D enantiomeric forms [149]. Successful synthesis and purification of all eight PAs were confirmed by prep-HPLC and LC-MS (Figures from 4.2 to 4.9).

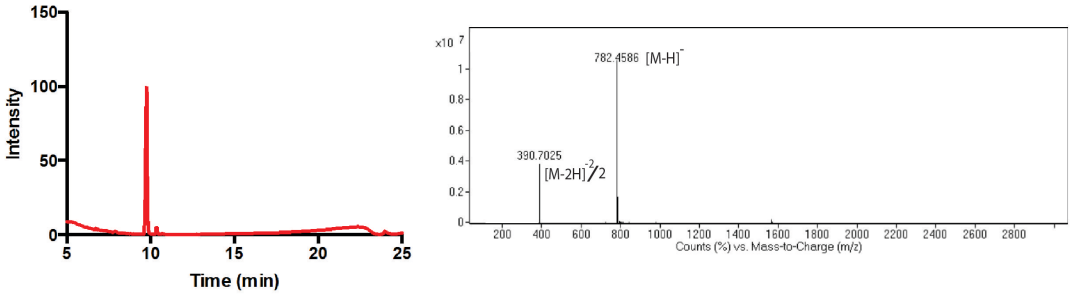


Figure 4. 2 Liquid chromatogram and mass spectra of L-VVEE, calculated exact mass [M] = 783.4742, $[M-H]^-$ (m/z) = 782.4586, $[M-2H]^-/2$ (m/z) = 390.7025.

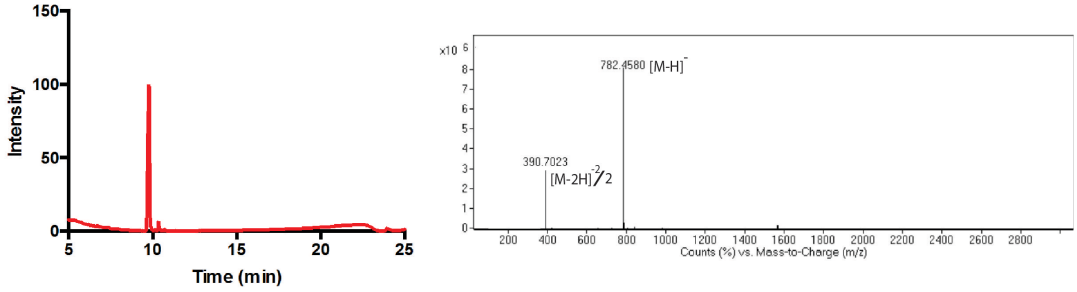


Figure 4. 3 Liquid chromatogram and mass spectra of D-VVEE, calculated exact mass [M] = 783.4742, $[M-H]^-$ (m/z) = 782.4580, $[M-2H]^{-2}/2$ (m/z) = 390.7023.

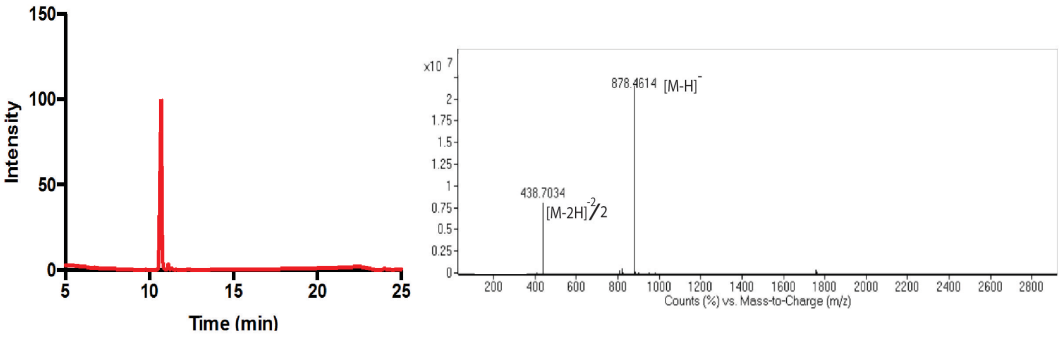


Figure 4. 4 Liquid chromatogram and mass spectra of L-FFEE, calculated exact mass [M] = 879.4742, $[M-H]^-$ (m/z) = 878.4614, $[M-2H]^{-2}/2$ (m/z) = 438.7034.

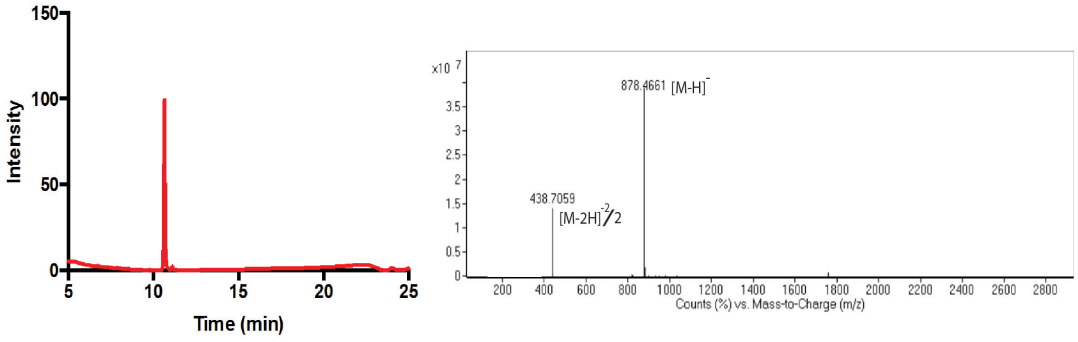


Figure 4. 5 Liquid chromatogram and mass spectra of D-FFEE, calculated exact mass [M] = 879.4742, $[M-H]^-$ (m/z) = 878.4661, $[M-2H]^{-2}/2$ (m/z) = 438.7059.

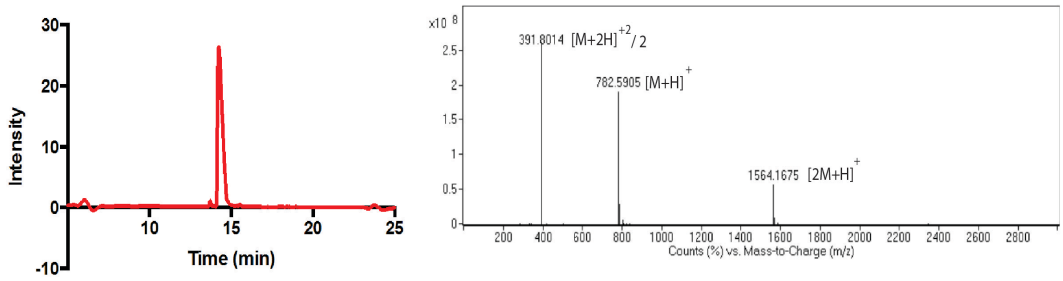


Figure 4. 6 Liquid chromatogram and mass spectra of L-VVKK, calculated exact mass [M] = 781.5789, $[M+H]^+$ (m/z) = 782.5905, $[M+2H]^{+2}/2$ (m/z) = 391.8014.

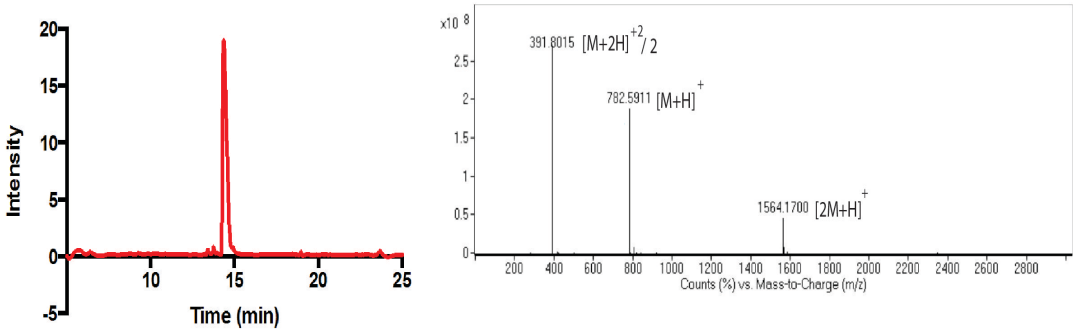


Figure 4. 7 Liquid chromatogram and mass spectra of D-VVKK, Calculated Exact Mass [M]= 781.5789, $[M+H]^+$ (m/z) = 782.5911, $[M+2H]^{+2}/2$ (m/z) = 391.8015.

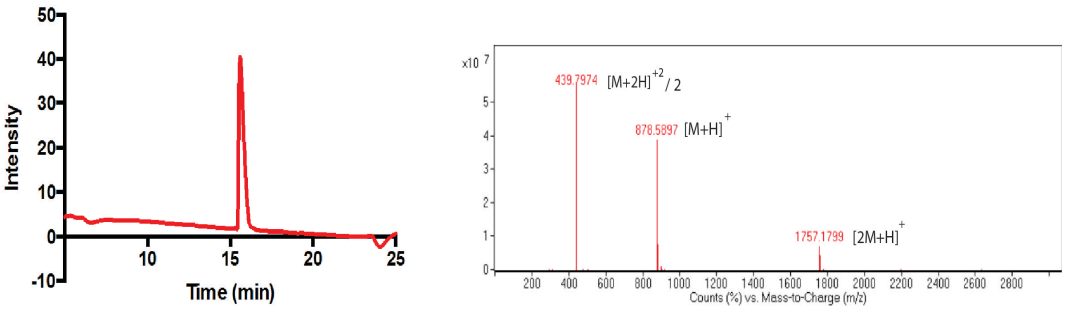


Figure 4. 8 Liquid chromatogram and mass spectra of L-FFKK, calculated exact mass [M] = 877.5789, $[M+H]^+$ = 878.5897 (m/z), $[M+2H]^{+2}/2$ (m/z) = 439.7974.

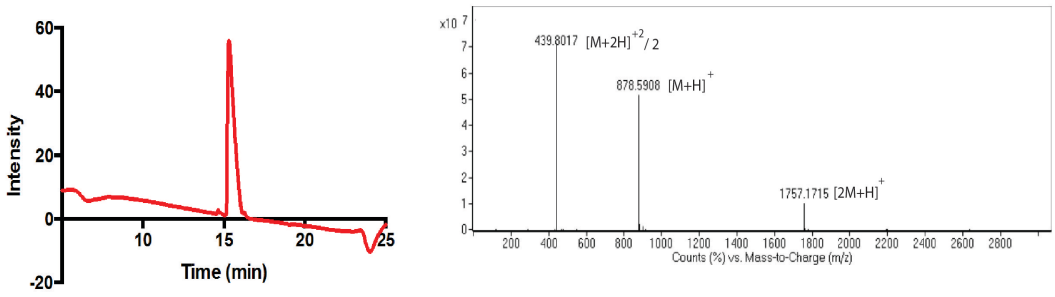


Figure 4. 9 Liquid chromatogram and mass spectra of D-FFKK, calculated exact mass [M] = 877.5789, $[M+H]^+$ (m/z) = 878.5908, $[M+2H]^{+2}/2$ (m/z) = 439.8017.

Morphology of the PA nanostructures was investigated by TEM (Figure 4.10). While L-VV and D-VV produced cylindrical nanofibers, twisted ribbon morphologies were observed for L-FF and D-FF. Uniform width and pitch sizes were obtained for L-FF and D-FF. The L-FF ribbons had 21.21 (±3.7) nm average diameters and 55.70 (±8.6) nm average pitch size, while D-FF formed ribbons that had an average diameter of 18.21 (±2.7) nm and pitch size of 48.21 (±7.3) nm (Figures 4.11 and 4.12).

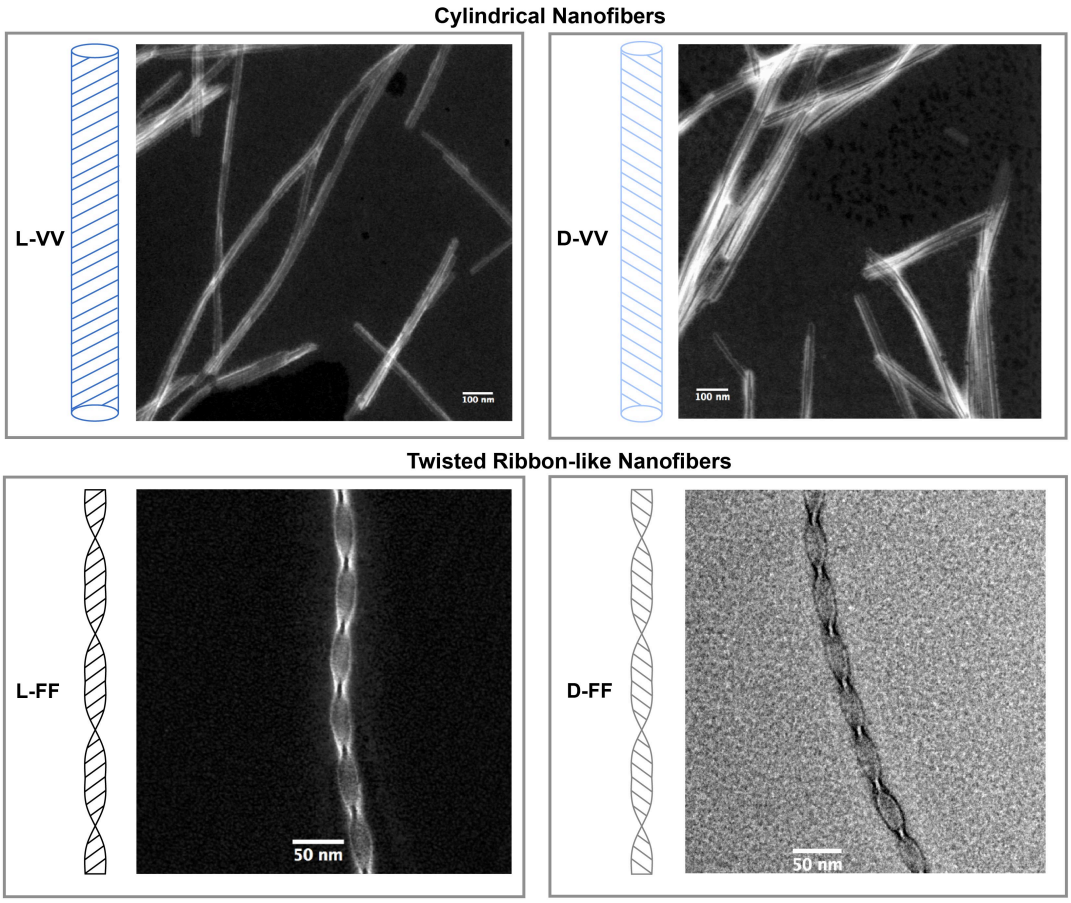


Figure 4. 10 Schematic representations of peptide nanofibers and their corresponding STEM images, scale bar = 100 nm (L-VV and D-VV), scale bar = 50 nm (L-FF and D-FF). L-VV: Lauryl-VVAGEE-Am / Lauryl-VVAGKK-Am, D-VV: Lauryl-vvaGee-Am / Lauryl-vvaGkk-Am, L-FF: Lauryl-FFAGEE-Am / Lauryl-FFAGKK-Am, D-FF: Lauryl-ffaGee-Am / Lauryl-ffaGkk-Am.

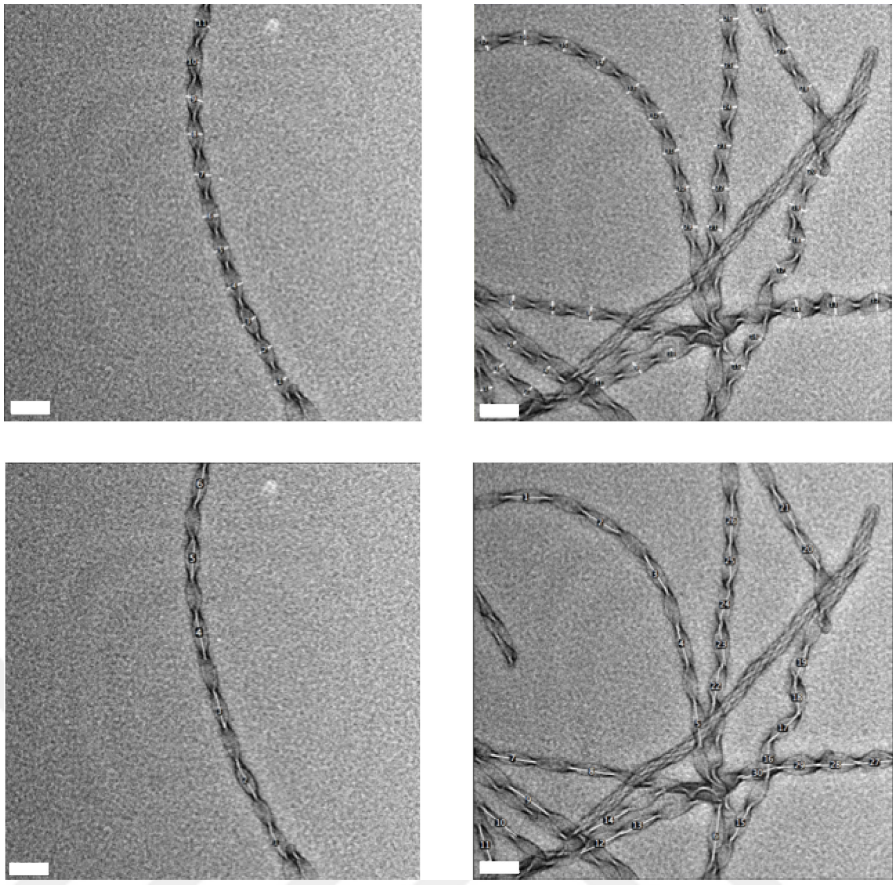


Figure 4. 11 TEM images showing diameter (top) and pitch size (bottom) measurements of L-FF networks. n =100 for diameter analysis, and n = 90 for pitch size analysis. Scale bars = 50 nm.

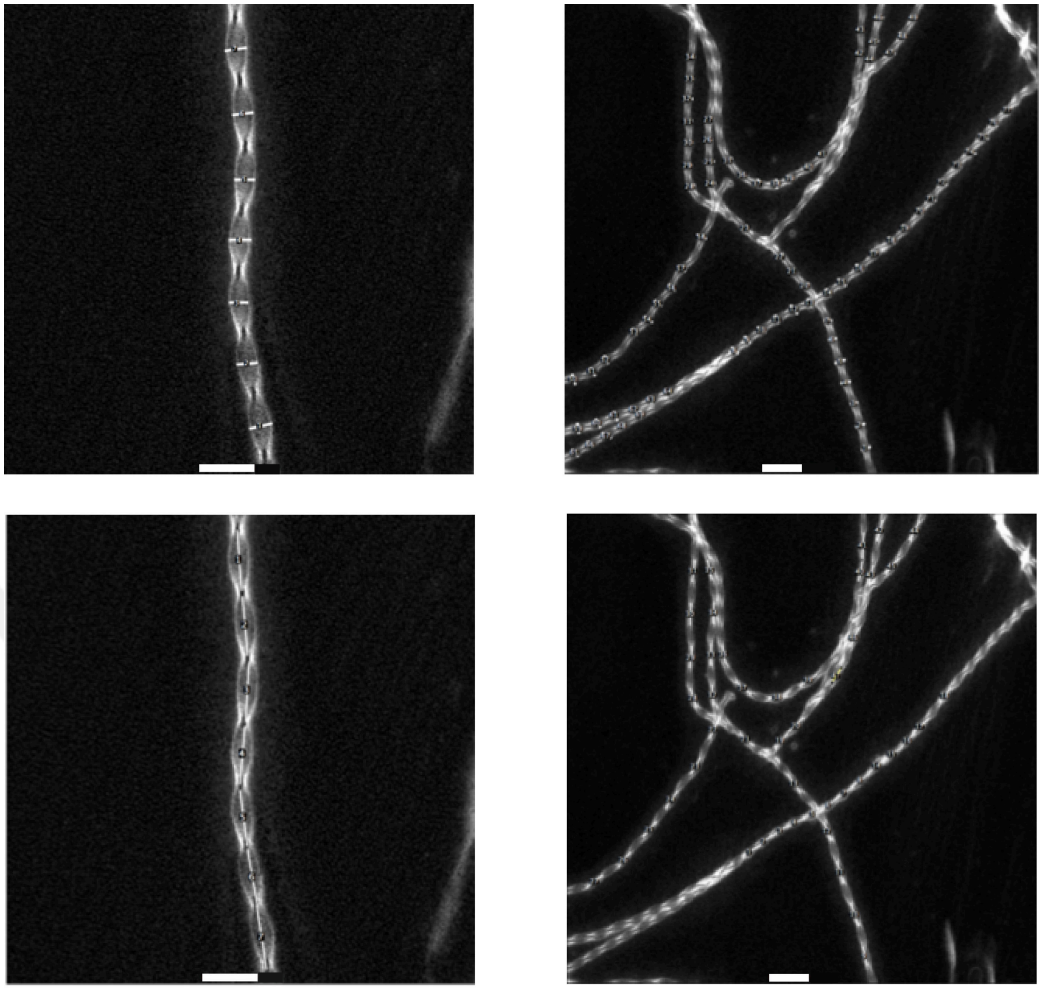


Figure 4. 12 STEM images showing diameter (top) and pitch size (bottom) measurement of D-FF networks. n = 100 for diameter analysis, and n = 90 for pitch size analysis. Scale bars = 50 nm (left), scale bars = 100 nm (right).

SAXS analysis showed that the form factor features of the eight PA solutions were characteristic of nanotape structures. SAXS data with model form factor fits are shown in Figure 4.13. The fits exhibited layer thicknesses of 38 ± 2 Å for L-VV and D-VV samples and 29 ± 1.5 Å for L-FF and D-FF samples. This is consistent with completely interdigitated bilayer structures (*i.e.* fully overlapped lipid chains in the bilayer interior), since the length of a PA molecule packed in a parallel β-sheet is

estimated to be 37 Å. For all four gels, SAXS showed very similar form factors (Figures 4.13 and 4.14) that exhibited features of twisted ribbons.

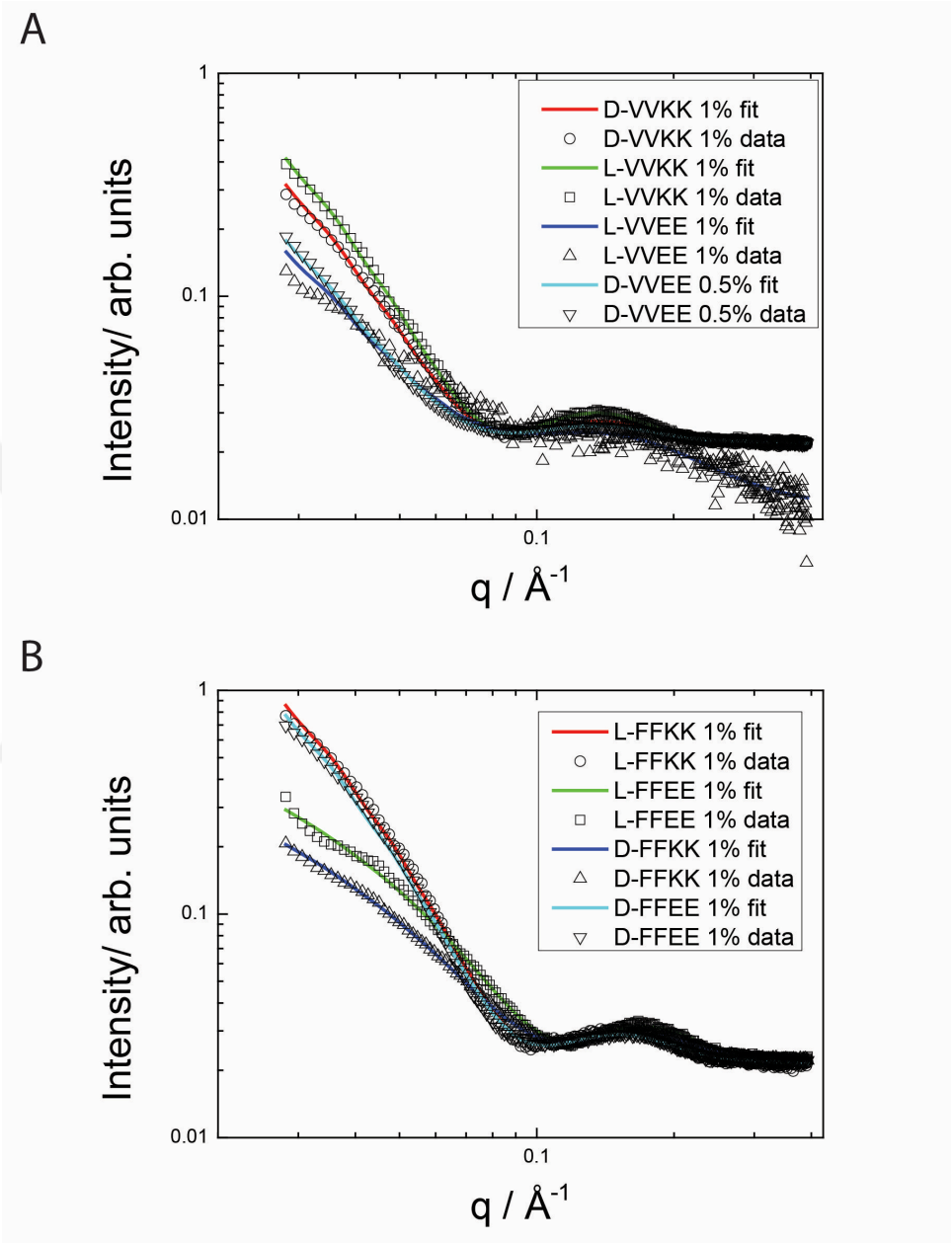


Figure 4. 13 SAXS patterns for unmixed PAs in aqueous solution, as indicated (open symbols) along with model form factor fits (solid lines) to describe nanotape structures, as described in the text, (A) VVxx series (data for D-VVEE multiplied by 5 for ease of comparison), (B) FFxx series.

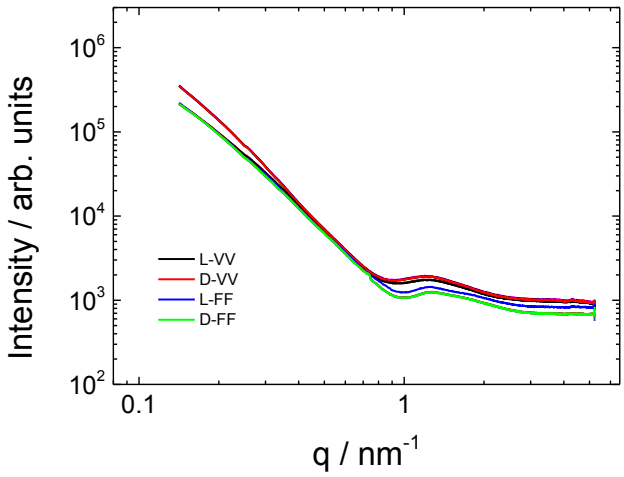


Figure 4. 14 SAXS patterns for gel mixtures, as indicated.

Hydrogen-bonding pattern and secondary structures of the networks were characterized by CD spectroscopy. For L-VV and D-VV ensembles, β-sheet secondary structure was detected by fingerprint bands at 221 nm and 200 nm (Figure 4.15) corresponding to n–π* and π–π* transitions, respectively [150]. CD spectra of L-FF and D-FF ensembles were more complicated, presumably a combination of absorptions of β-sheet motif and phenylalanine residues. In both cases, the CD spectra of L-form and D-form peptide nanofibers were mirror images of one another due to their opposite chirality. In the case of phenylalanine-containing L-FF and D-FF ensembles, a deviation was observed from perfect β-sheet structure because π-π interactions between aromatic side chains caused building blocks to assemble not with a 90° angle to the elongation axis, as with L-VV and D-VV, but with a narrower angle that rotated and twisted across the length of the fiber. This rotation in conformation has been reported as a twisted β-sheet secondary structure [147]. In twisted assemblies, relatively weaker hydrogen bonds are formed due to the increases in bond length. Therefore, a red shift was observed in the CD spectrum

(Figure 4.15). To get an estimate on contribution of phenylalanine residues, spectra of L-VV and D-VV ensembles were subtracted from spectra of L-FF and D-FF ensembles, respectively. CD difference spectra (Figure 4.16) are indicative of the contribution of the phenylalanine residues to higher energy transitions (n–π* and π–π*) of the amide group. The CD difference spectrum between L-isomer ensembles showed two positive peaks at 222 nm and 208 nm and a negative peak at 198 nm, which resemble CD spectrum of N-acetyl-L-phenylalanine amide [151].

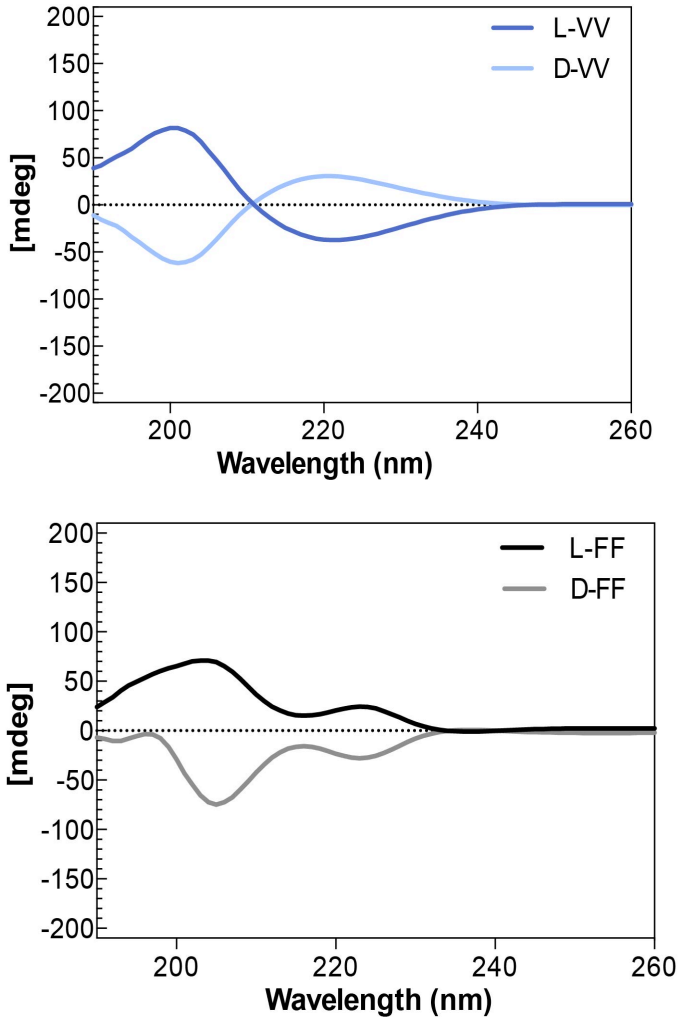


Figure 4. 15 CD spectra of peptide nanofibers.

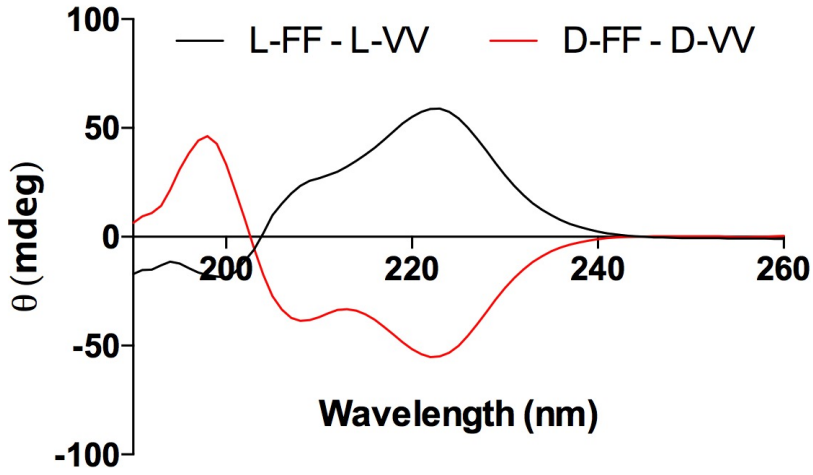


Figure 4. 16 CD difference spectra between L-FF and L-VV ensembles (black), and D-FF and D-VV ensembles (red).

All-atom explicit solvent classical molecular dynamics simulations were performed to investigate the molecular organization of the PAs at the atomic level (Figures 4.17, 4.18, and 4.19). Time series of the non-bonded interactions within peptide structures are shown in Figure 4.17A. Total non-bonded energies of L-FF and D-FF peptide nanofibers are similar to each other and higher than D-VV and L-VV nanofibers. On the other hand, L-VV nanofibers have lower non-bonded interaction energy than their D-VV counterparts. When only van der Waals interactions are considered, phenylalanine- and valine-containing PAs show different profiles. L-VV and D-VV nanofibers have lower energies, whereas L-FF and D-FF nanofibers have more van der Waals interactions. To elucidate this behavior, we calculated only the non-bonded interaction energies between atom pairs comprised of the side-chains of phenylalanine and valine amino acids (Figure 4.17B). We observed a high difference in the van der Waals interaction energy between peptide nanofibers having phenylalanine and valine residues. This suggests that van der Waals energy

difference between nanofibers containing phenylalanine and valine residues is due to high repulsion between phenylalanine side-chain atoms. It is also important to note that even though phenylalanine residues form favorable electrostatic interactions compared to valine residues, and the total non-bonded interaction energy is dominated by van der Waals interactions (Figure 4.17). High van der Waals repulsion between phenylalanine residues plays a critical role in the formation of twisted nanofibers. Even though the time scale of the simulations is not long enough to observe twisting in phenylalanine-containing nanofibers, energy analysis shows the driving force for formation of twisted nanofibers.

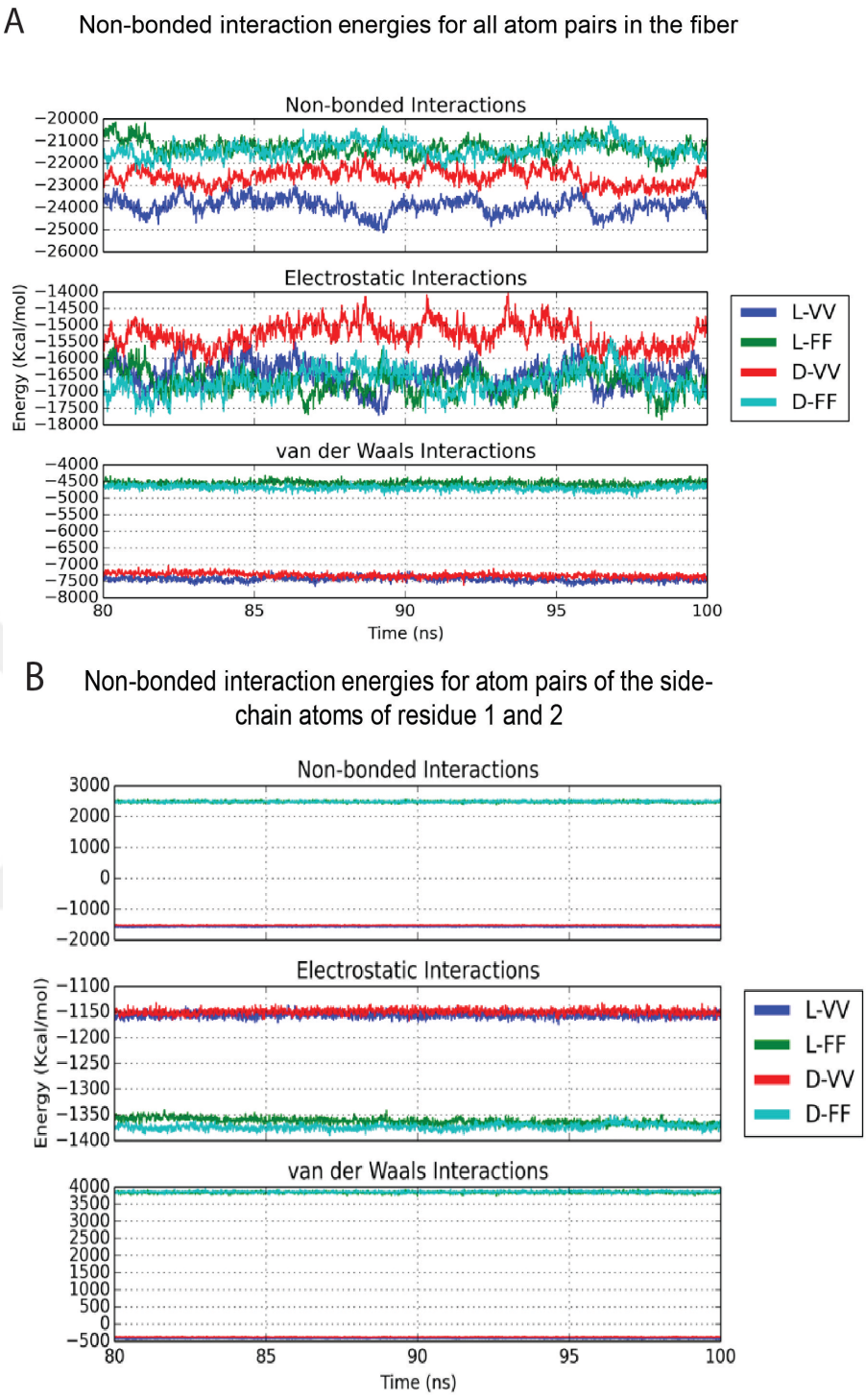


Figure 4. 17 Time series for non-bonded interaction energies for the last 20 ns of the simulations. (A) Energy calculation between PAs. (B) Energy calculations for the atom pairs of the side-chain atoms of the first and second residues on PAs.

Hydrogen bond analysis for the peptide nanofibers (Figure 4.18) shows the number of unique inter-peptide H-bond in each nanofiber as a function of simulation time. Phenylalanine-containing nanofibers have the lowest number of H-bonds; the number of H-bonds in D-FF and L-FF nanofibers fluctuates around 450. In contrast, the H-bond number in valine-containing peptide nanofibers increases up to 500 in D-VV and 650 in L-VV nanofibers. This difference in H-bond number between valine and phenylalanine-containing nanofibers suggests that bulky aromatic phenylalanine side-chains could limit the H-bond formation ability of phenylalanine-containing nanofibers. Interestingly, the number of H-bonds in D-VV is much lower than the number of H-bonds in L-VV nanofiber.

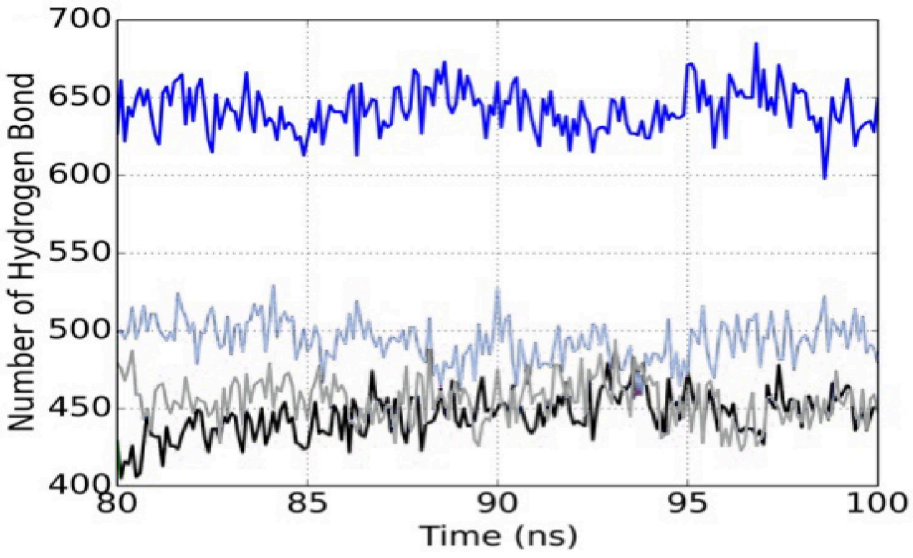


Figure 4. 18 Time series of hydrogen bond number for the last 20 ns of the simulations.

The contribution of each amino acid to the H-bond number is shown in Figure 4.20. Individual contribution of amino acids in phenylalanine-containing nanofibers does not differ considerably in L- and D- enantiomers. However, all amino acids except K

and E residues in valine-valine containing nanofibers have more H-bonds in L-form than in D-form. The two valine residues contribute substantially to the H-bond number difference between L- and D-forms of valine-containing PAs. Therefore, we investigated conformational and dynamic behavior of valine residues in L- and D-form to understand the H-bond number differences in valine residues. Valine residues sterically hinder H-bond formation in D-form as shown in radial distribution function (RDF) analysis. Figure 4.19 demonstrates atom-pair distribution as a function of pair-distance for the atom-pairs between valine side-chain gamma carbons and valine backbone oxygen, and the atom-pairs between valine side-chain gamma carbons and hydrogen atom bound to amide nitrogen. In these plots, the valine side-chain gamma carbons are closer to the valine backbone in D-form compared to the L-form. This result suggests that side-chain steric hindrance plays a role in hampering H-bond formation in D- amino acid-containing nanofibers.

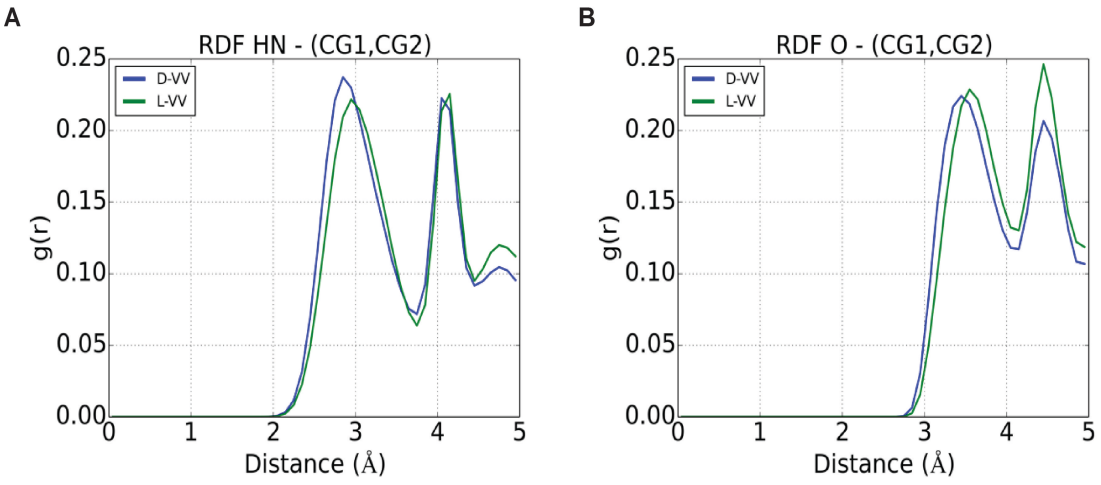


Figure 4. 19 Radial distribution function (RDF) plots. (A) RDF for the atom pairs between hydrogen bound to backbone nitrogen and valine side-chain gamma carbons. (B) RDF for the atom pairs between backbone oxygen and valine side-chain gamma carbons.

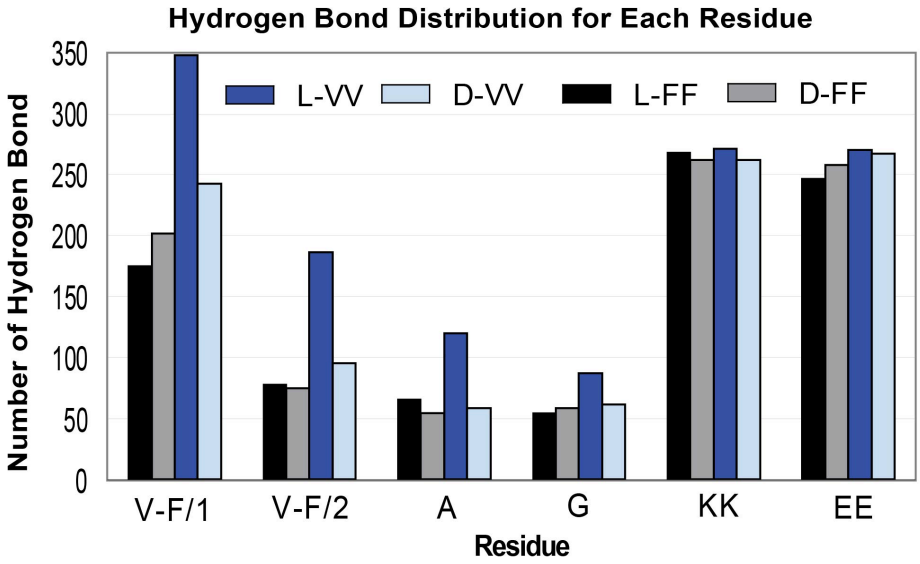


Figure 4. 20 Number of hydrogen bonds that each residue forms: V-F/1 denotes the first valine or phenylalanine (numbering starts from the lipophilic tail) on the corresponding PA; V-F/2 denotes second V or F, KK and EE denote merged results for two lysine and two glutamic acid residues, respectively.

Figure 4.21 shows Ramachandran plots for valine residues in L- and D- nanofibers. Dihedral angles for the first valine residue in L-form populated around phi = -110, psi = -135, which is close to the β-sheet region center (a study done by Hovmöller *et al.* on the analysis of protein structures reports that backbone dihedrals of valine amino acid for β-sheet forming conformations populate around the center where phi = -117.7 and psi = 127.8 for parallel beta strands, and phi = -121.2 and psi = 132.5 for antiparallel beta strands [152]). However, dihedral angle population for the first valine in D-form shifts to the center where phi and psi angles around -90 and -125 respectively. Dihedrals of the second valine in L-form nanofibers are not localized at a certain region; they can sample both regions near the ideal beta sheet region and regions where phi and psi are around -140 degrees. On the other hand, dihedral angle

population for the second valine in D-form PAs shifts towards the upper side of the Ramachandran plot. According to Hovmöller *et al.*, for conformations that form random coil structures, valine dihedrals shift towards higher phi and lower psi angles [152]. Hence, the dihedral angle population shift observed in our calculations for D-amino acid-containing nanofibers could imply that backbone conformation in D-amino acids deviates from the beta sheet region towards random coils. Hence, this could affect the H-bond forming ability of D-valine residues in PAs that form nanofibers.

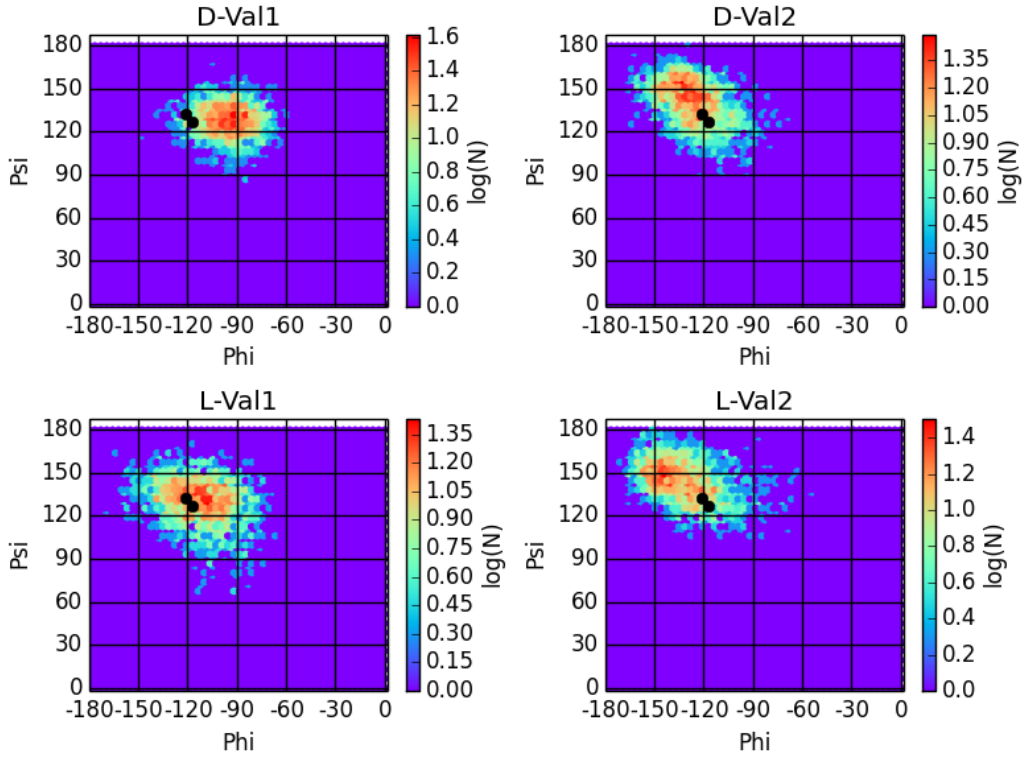


Figure 4. 21 Ramachandran plots for valine residues in L-VV and D-VV PAs. Black dots correspond to centers of dihedral angle populations for parallel and antiparallel β sheet conformations for valine residues reported by Hovmöller et. al. [152] N denotes for the counts.

Oscillatory rheology measurements were performed for mechanical analysis of the bulk gel. Time sweep, frequency sweep and strain sweep rheology analysis were conducted in order to investigate the gel formation mechanics and viscoelastic properties of the peptide nanofiber networks (Figure 4.22). Storage moduli of all nanofiber networks were found to be higher than their loss moduli suggesting that the materials are hydrogels. In addition, we found that cylindrical nanofiber networks have higher elastic moduli than twisted ribbon-like nanofiber networks. On the other hand, we did not detect any difference in elastic moduli of nanofibers between L- and D- forms.

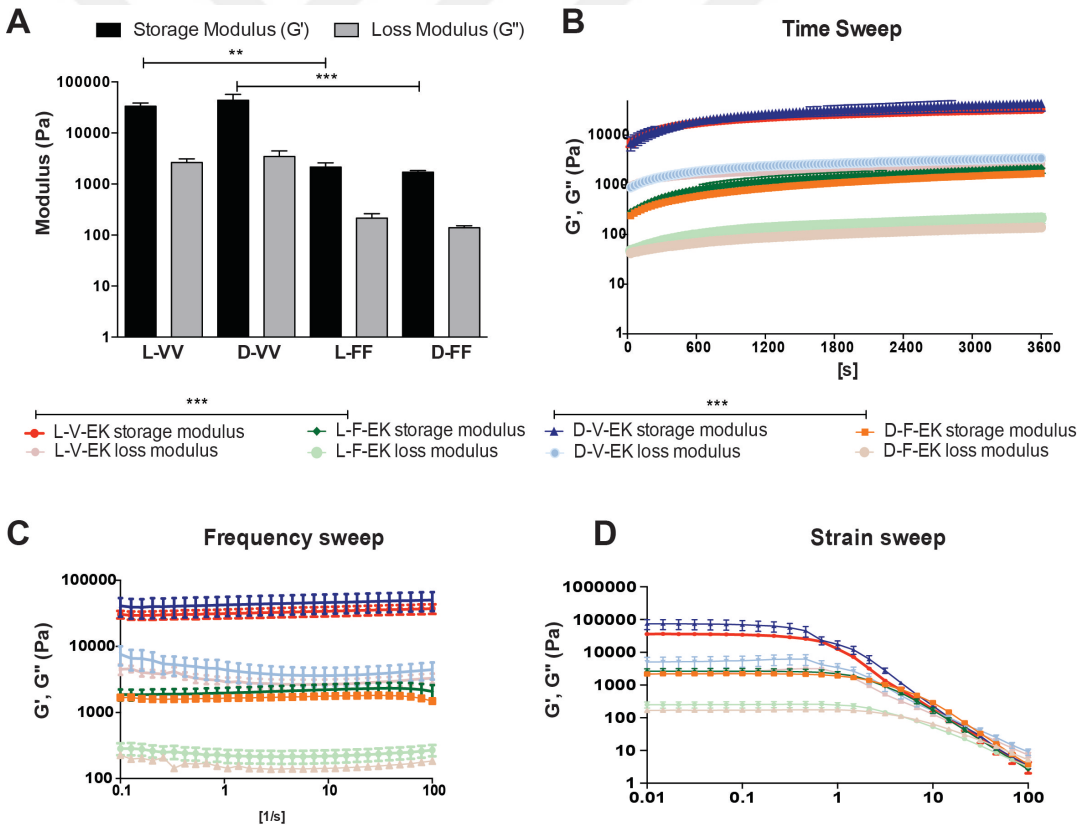


Figure 4. 22 Macro-scale mechanical investigation of peptide nanofiber networks by oscillatory rheology. (A) Viscoelastic analyses of peptide nanofibers by oscillatory

rheology. Equilibrium storage and loss moduli of nanofiber networks during (B) time, (C) frequency and (D) strain sweeps.

In addition, we performed SEM analyses which showed that the nanofiber morphology similar for all bulk hydrogel groups (Figure 4.23).

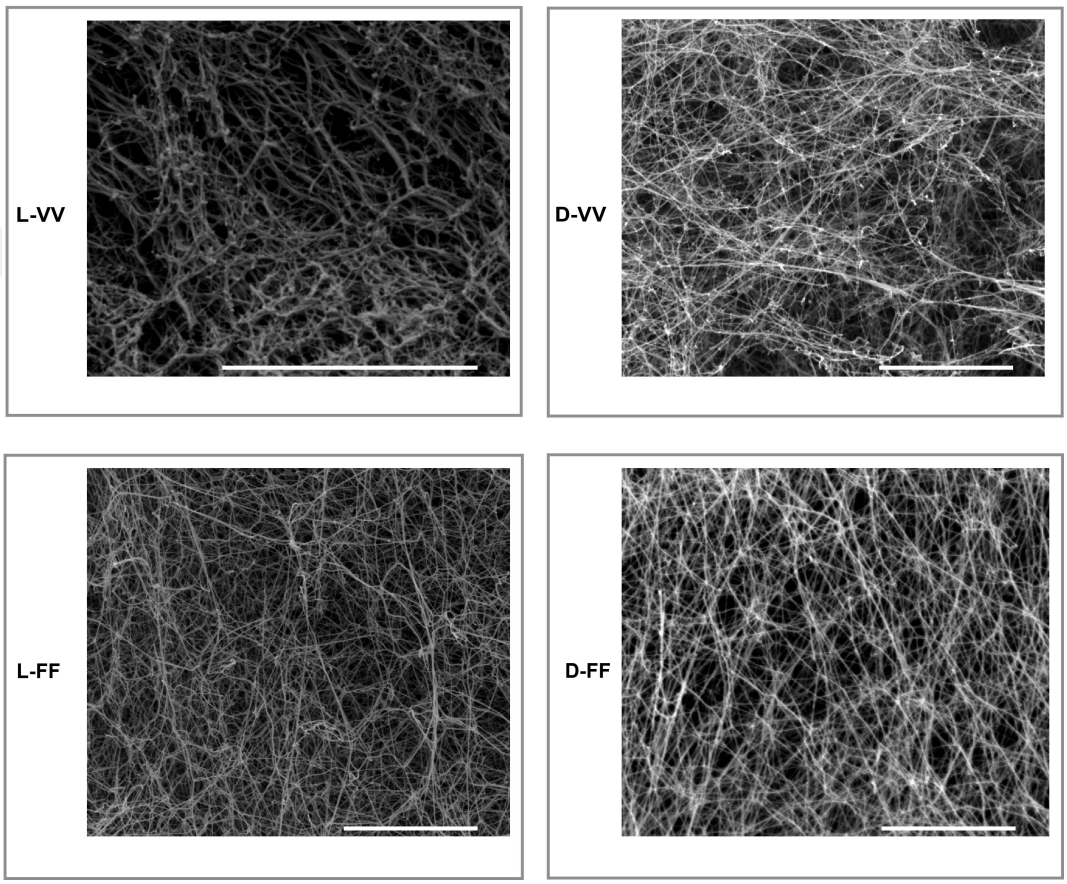


Figure 4. 23 SEM images of bulk hydrogels showing their nanofiber morphology similar for all groups, scale bars = 2 μm.

For nanomechanical characterization of peptide nanofibers, elastic behavior of peptide nanofibers was investigated by AFM measurements (Figures 4.24 and 4.25). Force mapping measurements were employed on nanofibers and nanobundles, and elastic modulus values were calculated by fitting approach curves using the Hertz

model in MATLAB (Figure 4.24). Both L-form of cylindrical and twisted ribbon-like nanofibers had significantly higher elastic moduli than their D-forms. L-VV nanofibers had the highest stiffness at 45.62 MPa, D-VV had 15.03 MPa, L-FF had 32.04 MPa and D-FF had 10.03 MPa. Interestingly, we observed that the difference in elastic moduli of L- and D- form of VV-nanofibers is consistent with the H-bond density according to molecular dynamic simulations.

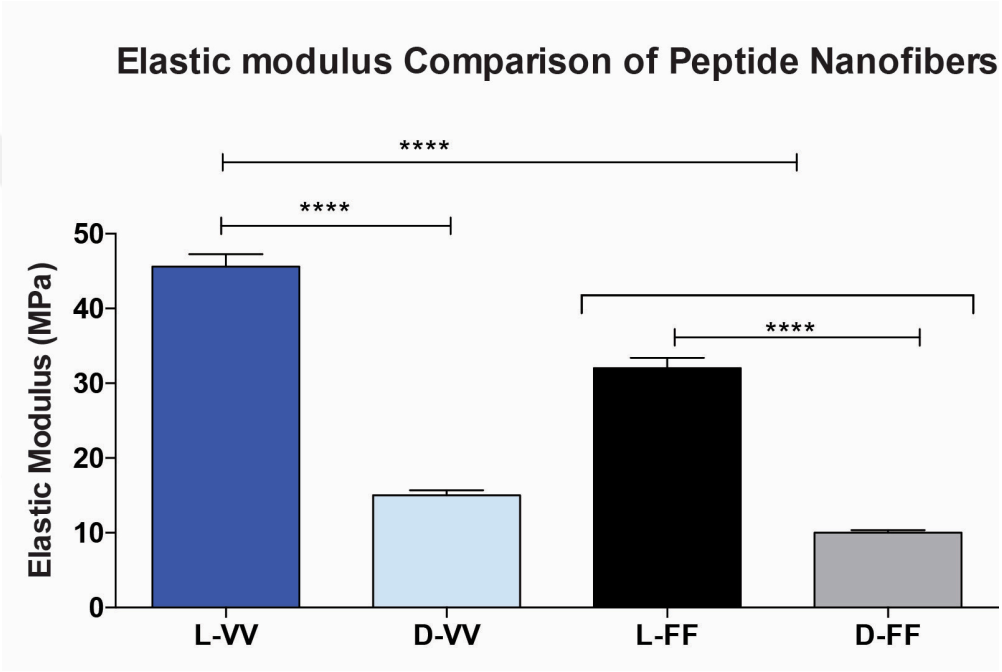


Figure 4. 24 Nanomechanical characterization of peptide nanofibers by AFM; Elastic modulus comparison of peptide nanofibers.

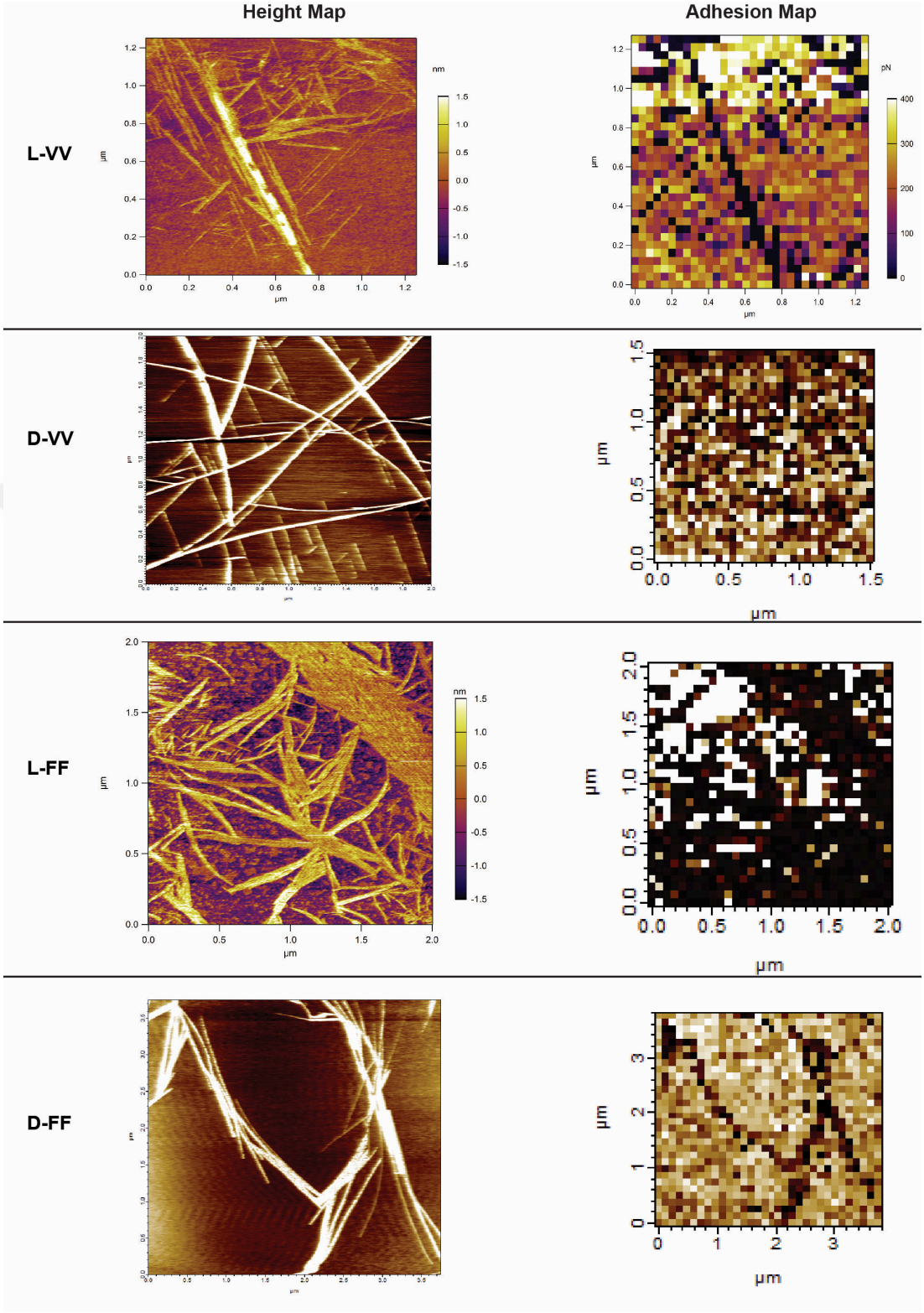


Figure 4. 25 Representative height and adhesion maps of peptide nanofibers measured by AFM.

4.4.2 Peptide nanofibers provide a biocompatible environment for cell culture

Cellular viability, adhesion, proliferation, and spreading were evaluated qualitatively and quantitatively prior to testing the effects of nanofiber morphology and chirality on cellular behavior. Viability analysis showed that all peptide nanofibers were biocompatible and conducive to the growth and proliferation of stem cells through 3 culture days (Figure 4.26). Live/Dead assay also showed that few to no dead cells were present on all scaffolds, which supports the results of Alamar Blue assay and demonstrates that these peptide nanofibers are highly biocompatible (Figure 4.27). In addition, Alamar Blue results indicated that the morphology and chirality of the peptide nanofibers do not affect the metabolic activity of cells.

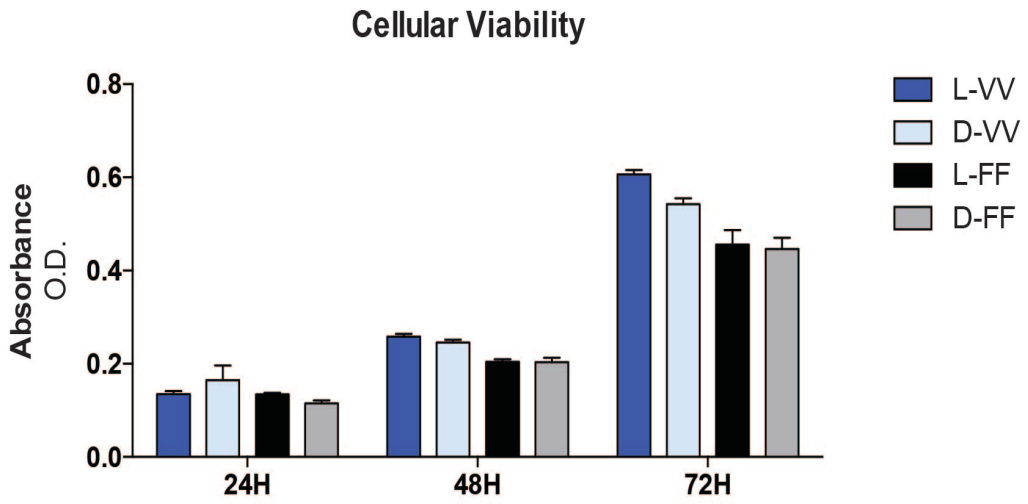


Figure 4. 26 Cellular viability measurements by Alamar Blue assay.

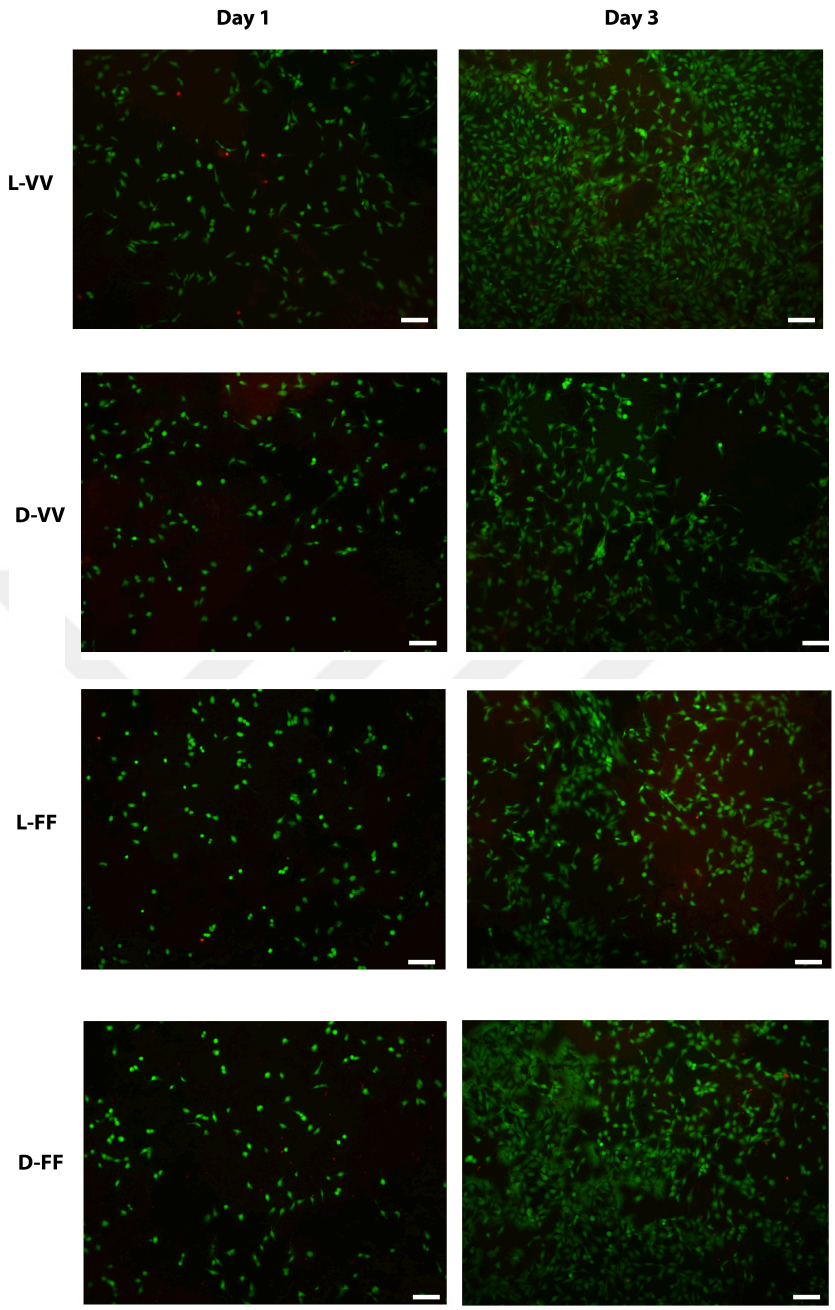


Figure 4. 27 Viability analyses of stem cells on peptide nanofibers after 1 day and 3 days of incubation by Live/Dead assay (Green cells are live cells, and red cells are dead cells).

When cells are exposed to a new microenvironment, cellular processes are initially altered to mediate substrate adhesion prior to the resumption of regular metabolic

pathways. At this initial step, the primary role of the nanostructure scaffold is to provide a suitable set of signals for cell attachment. Adhesion analysis of peptide nanofiber structures showed that all peptide nanofibers facilitated the initial attachment of stem cells after 1 h and 5 h of culturing (Figure 4.28). When compared to TCP, cells were found to immediately attach to peptide nanofiber surfaces within the first few hours (1-5 h) of culture, and no significant differences were observed in the initial attachment of cells among different morphological and chiral groups.

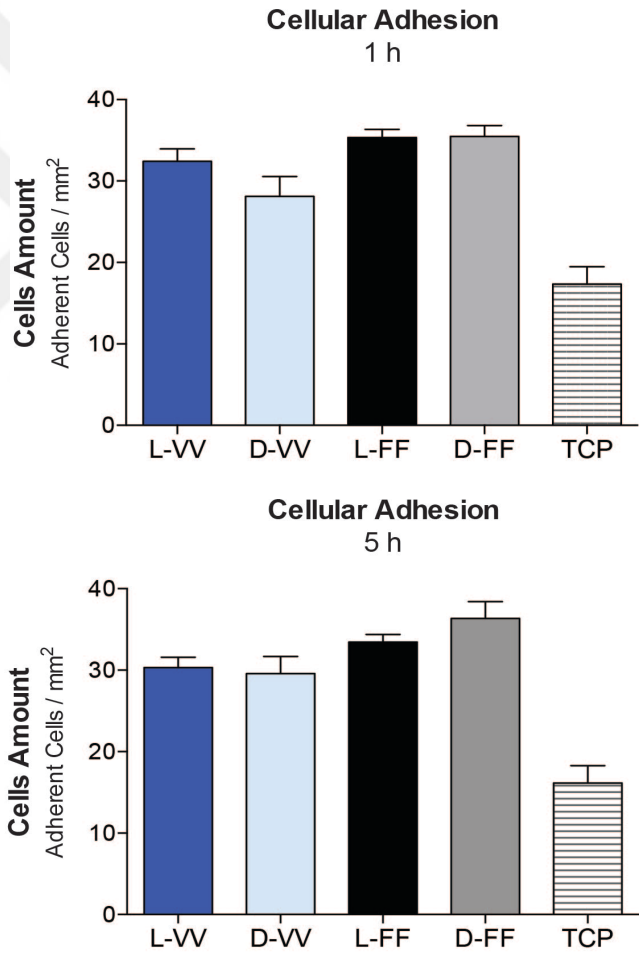


Figure 4. 28 Cellular adhesion analyses of MSCs on peptide nanofibers and on TCP after 1 h and 5 h.

In addition, we analyzed the collagen adsorption on the peptide nanofibers to examine whether there are any differential effects of these nanofibers on the matrix protein adsorption. We found that there was no specific collagen binding on any of the nanofiber groups (Figure 4.29).

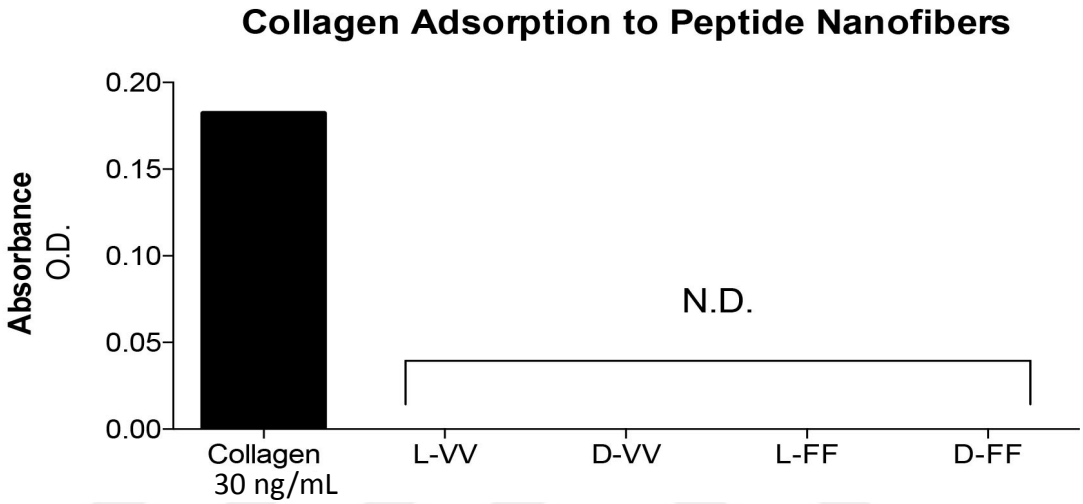


Figure 4. 29 Collagen adsorption on the peptide nanofibers were measured by ELISA. Collagen protein at 30 ng/mL was used as positive control. N.D. (Not Determined)

In addition to stem cells, an adherent primary human cell line (HUVECs) and human fibroblasts (hFibs) were also analyzed to determine the effect of peptide nanofibers morphology and chirality on cellular responses, and both cell types were found to readily adhere to peptide scaffolds (Figure 4.30). While HUVECs adhered significantly less on L-form of twisted-ribbon-like nanofibers (L-FF) among other groups, there were no significant differences between the groups for the adhesion of hFib cells (Figure 4.30B). Our adhesion results therefore show the number of cells that were able to initially establish themselves on the peptide materials.

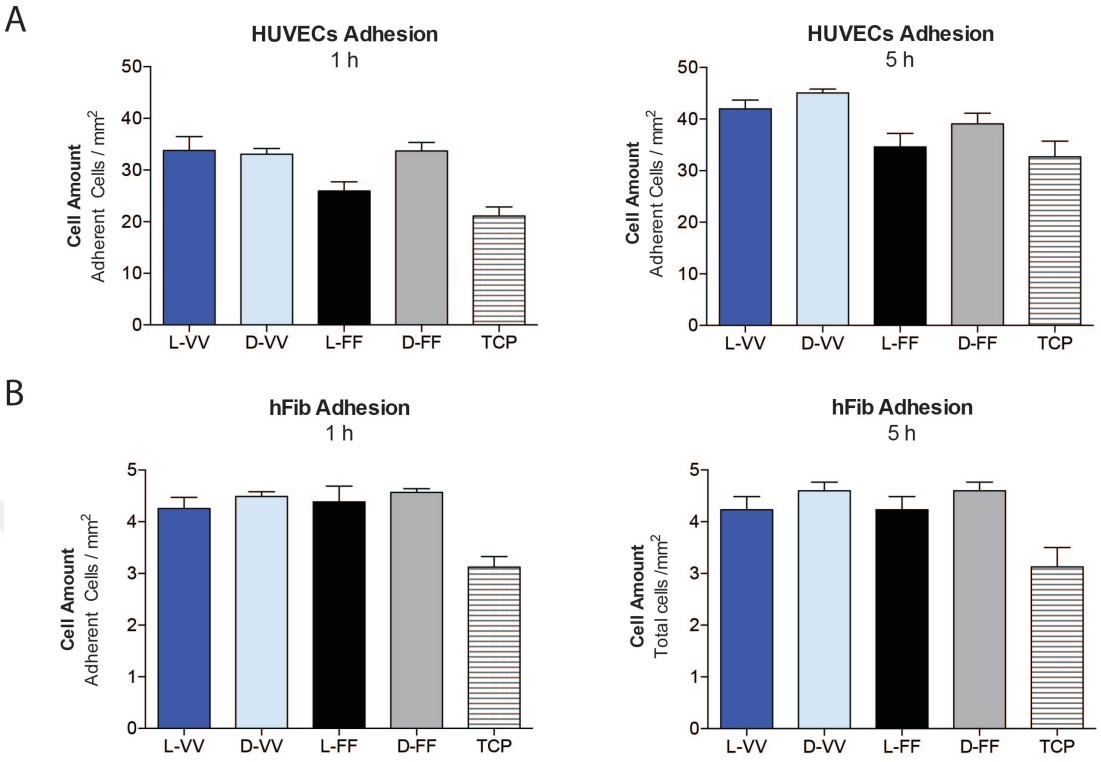


Figure 4. 30 (A) Cellular adhesion analyses of HUVECs 1 h and 5 h after seeding on peptide nanofibers and on TCP. (B) Cellular adhesion analyses of hFibs 1 h and 5 h after seeding on peptide nanofibers and on TCP.

4.4.3 Cellular proliferation and spreading is mediated by nanofiber morphology and chirality

Following cellular adhesion, a bioactive scaffold should ideally provide the necessary signals for activating cellular processes such as proliferation, spreading and differentiation. According to the proliferation analysis results (Figure 4.31), cells demonstrated different proliferation rates on different peptide nanofibers, suggesting that nanofiber morphology and chirality play an important role in mediating nanofiber-cell interactions. Proliferation of rMSCs was tracked for 5 days, and both

L- and D- forms of the twisted ribbon-like nanofibers (FF) were found to elicit significantly lower proliferation of rMSCs during 5 days of incubation. After 1 day of culture, cells proliferated on L- and D- forms of the cylindrical nanofibers (VV-PA) to a much greater extent than FF-nanofiber and TCP groups. Moreover, the importance of chiral differences for cylindrical nanofibers was seen even after 3 days of culture, where proliferation rates of rMSCs on L-VV decreased much more than D-VV. After 5 days, proliferation rates of rMSCs cultured on the L- and D- forms of VV-nanofibers had decreased, but were still higher than FF-nanofiber groups. Confluence is a likely reason for this effect, since cells cultured on L-VV and D-VV nanofibers would stop proliferating through contact inhibition after an early increase in their population. In contrast, L-FF and D-FF do not rapidly crowd the well plate and can sustain their growth for a longer period of time but do not increase the proliferation, which is probably due to cells undergoing into differentiation through different morphological signals than VV- nanofibers, which was also seen in chondrogenesis potential of cells on FF-nanofibers. In addition, studies on stem cells also showed that for particular differentiation lineages, proliferation of stem cells were decreased [153]. Overall, peptide nanofibers were found to strongly alter cellular processes even after short-term (24 h) culture, and proliferation on twisted ribbon-like nanofibers (FF-PAs) was limited compared to cylindrical nanofibers (VV-PAs).

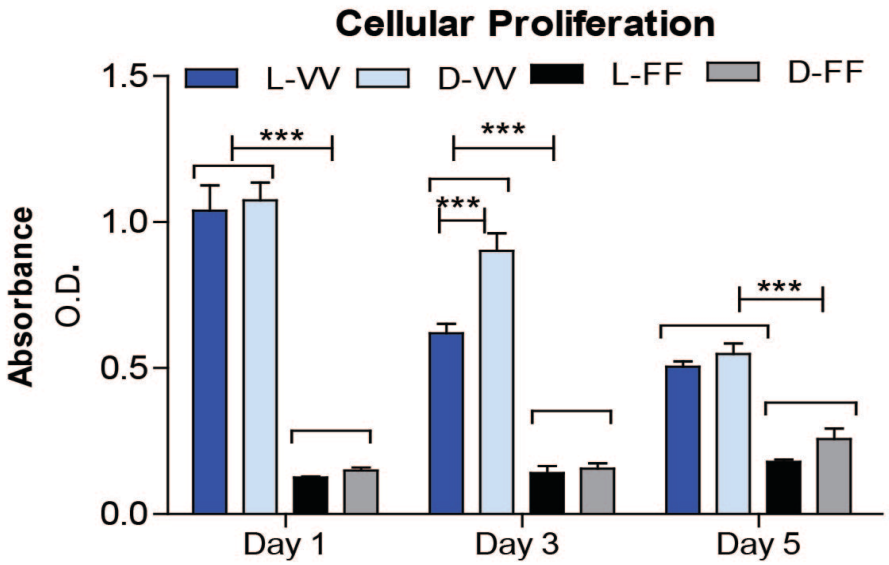


Figure 4. 31 Cellular proliferation measurement of MSCs by BrdU assay through 5 days of culture (*p< 0.05, **p<0.01, ***p< 0.001 by two-way ANOVA with Bonferroni's post-hoc test, mean ± s.e.m.).

After analyzing the collective response of cell cultures to different nanofibrous morphologies and chirality, cellular areas were measured to investigate the individual cellular responses (Figures 4.32 and 4.33). Although neighboring cells and cellular confluence may affect the spreading of cells, each cell spreads individually through its own receptors and specific receptor-ligand interactions [154]. Cells were seeded on all peptide nanofiber groups at the same cell concentration to avoid any initial confluency differences. We had already observed that the cells all adhered similarly (at the time of initial attachment of cells through 1-5 h) according to cellular adhesion analysis. The rMSCs cultured on L-and D- form of twisted ribbon-like nanofibers (FF-PA) exhibited significantly less cell spreading than those cultured on cylindrical nanofibers (VV-PA).

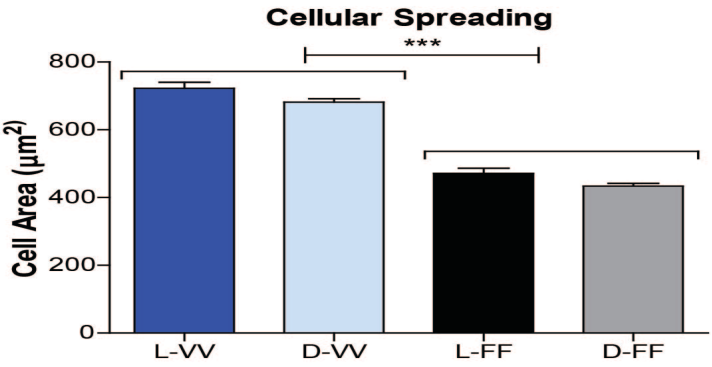


Figure 4. 32 Quantification of cellular spreading measurements of MSCs 24 h after seeding on peptide nanofibers, obtained by Image J analysis of cells stained with phalloidine and imaged by fluorescence microscopy (n>50 cell per group (*p<0.05, **p<0.01, ***p<0.001 by one-way ANOVA with Bonferroni's post-hoc test, mean ± s.e.m.).

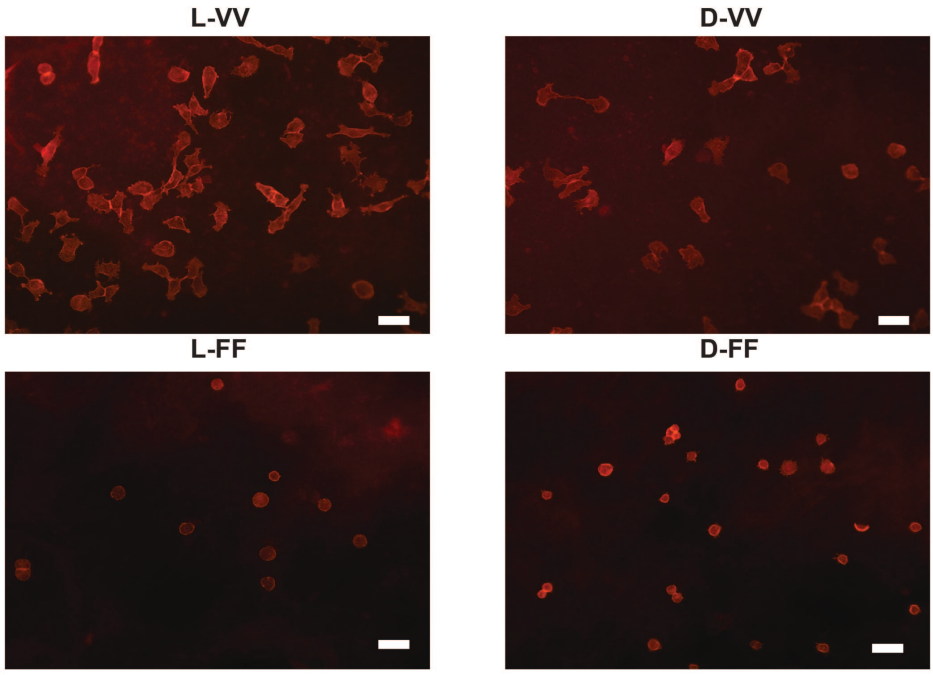


Figure 4. 33 Representative fluorescent images of MSCs 24 h after seeding on peptide nanofibers, scale bar = 50 µm.

In addition to rMSCs, the spreading of HUVECs and hFibs was also evaluated (Figure 4.34). Among peptide nanofibers with different morphology and chirality, HUVECs on the L-form of nanofibers (L-VV) exhibited less spreading than the D-form nanofibers (D-VV). As with other cell lines, the L-FF twisted ribbons limited the spreading of hFibs to a greater extent than the D-FF nanostructures, while the D-form of VV-nanofibers was much more inhibitory than the L-form for VV-nanofibers. As such, both the morphology of nanofibers and their chirality had distinctive effects on cellular responses. Twisted ribbon-like nanofibers exhibited a more pronounced restrictive effect on cellular spreading in the L-form; whereas cylindrical nanofibers were more inhibitory in their D-form, especially for fibroblasts. Although we observed similar mechanotransductive responses on peptide nanofibers for different cell types, we focused on stem cells for the analysis of cell-material interactions at the molecular level for further experiments to elaborate on the inherent effect of designed peptide nanofibers for future clinical applications.

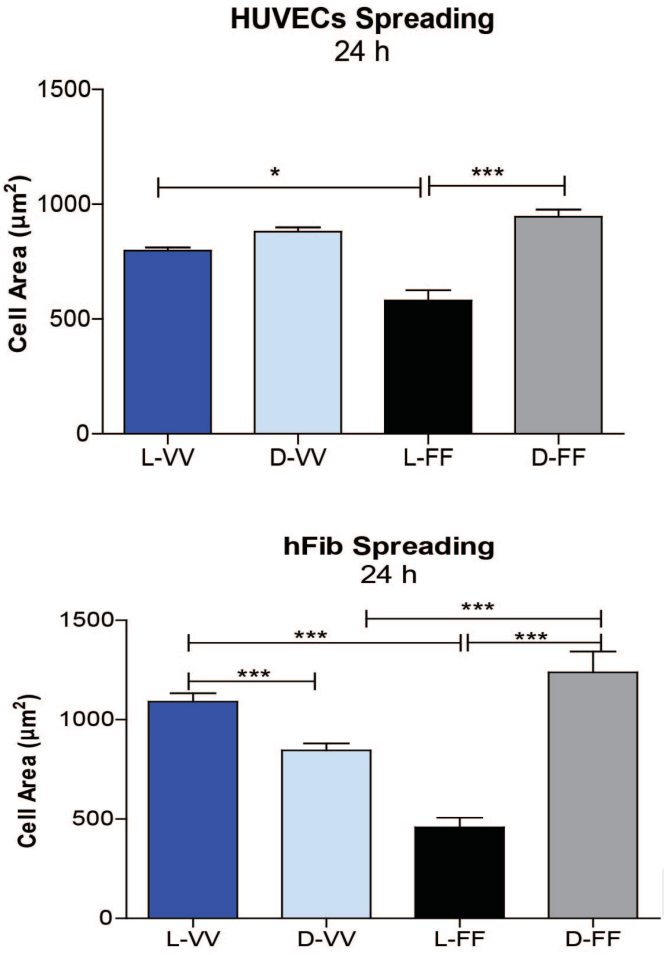


Figure 4. 34 Cellular spreading analyses for HUVECs and hFibs 24 h after seeding on nanofibers (*p< 0.05, **p<0.01, ***p< 0.001 by one-way ANOVA with Bonferroni's post-hoc test, mean ± s.e.m.)

4.4.4 Effects of peptide nanofibers with different morphologies on the osteochondrogenic differentiation of MSCs

When cells are exposed to a microenvironment, their morphology, spreading area, and proliferation rate are altered, resulting in the activation of specific response mechanisms that directly affect the organism at cell and tissue levels [155]. A thorough understanding of cell-materials interactions is essential to regulate these responses. These effects are also important for the clinical applicability of stem cells,

which are being utilized for the treatment of various diseases and biomedical applications. The primary advantage of stem cells is their ability to differentiate into multiple lineages, which can be mediated through their cultivation on peptide scaffolds or other biomaterials. Thus, the differentiation potential of rMSCs were analyzed on peptide nanofibers with different morphology and chirality. Mesenchyme-originated stem cells can differentiate into osteogenic, chondrogenic, and adipogenic lineages, and the initial commitment of cells to differentiate into the osteogenic and chondrogenic lineages was investigated by qRT-PCR analysis on day 7. Runx-2, a transcriptional factor, which is expressed during the osteogenic differentiation of stem cells to activate the synthesis of bone specific proteins, was found to be upregulated on both L- and D-forms of cylindrical nanofibers (L-VV and D-VV), with L-VV nanofibers exhibiting a more pronounced effect on Runx-2 expression than the D-form (Figure 4.35). In contrast, twisted ribbon-like nanofibers (L-FF and D-FF) significantly inhibited osteogenic differentiation of MSCs. These twisted ribbon-like nanofibers (L-FF and D-FF) instead increased the chondrogenesis of stem cells, as shown by increased Sox-9 expression, which was especially significant on D-FF nanofibers (Figures 4.36 and 4.37).

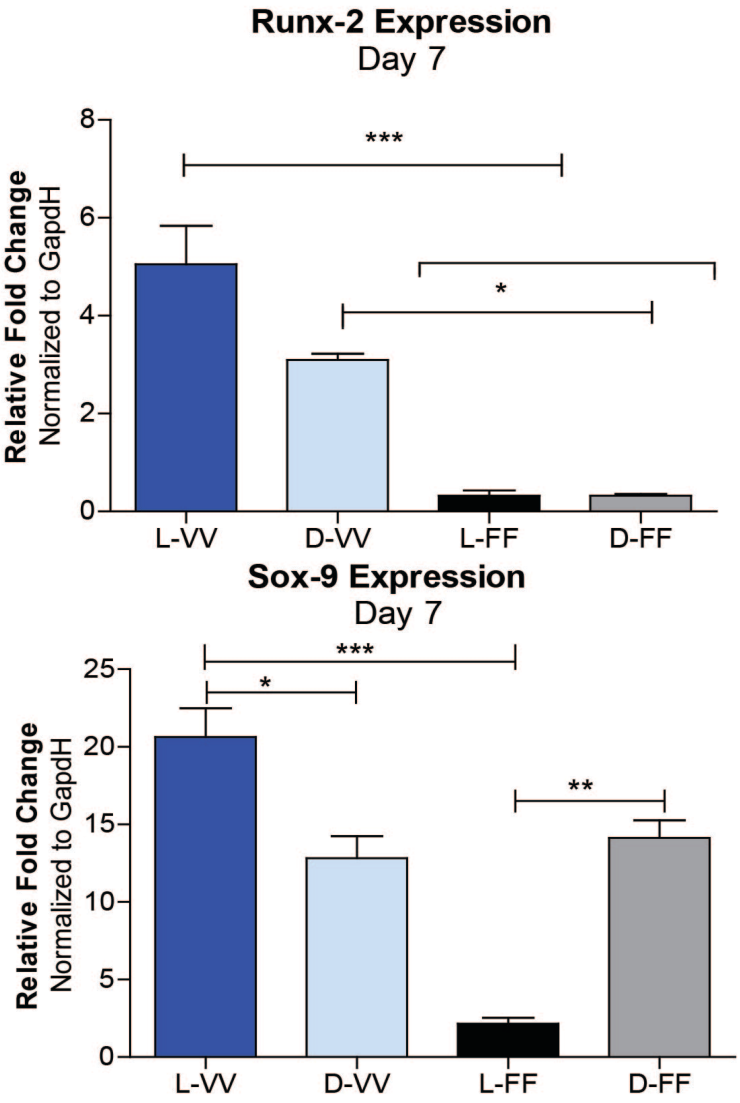


Figure 4. 35 Osteogenic and chondrogenic differentiation analyses by qRT-PCR. Expression of Runx-2 and Sox-9 were quantified on day 7 (*p<0.05, **p<0.01, ***p<0.001 by one-way ANOVA with Bonferroni's post-hoc test, mean ± s.e.m.).

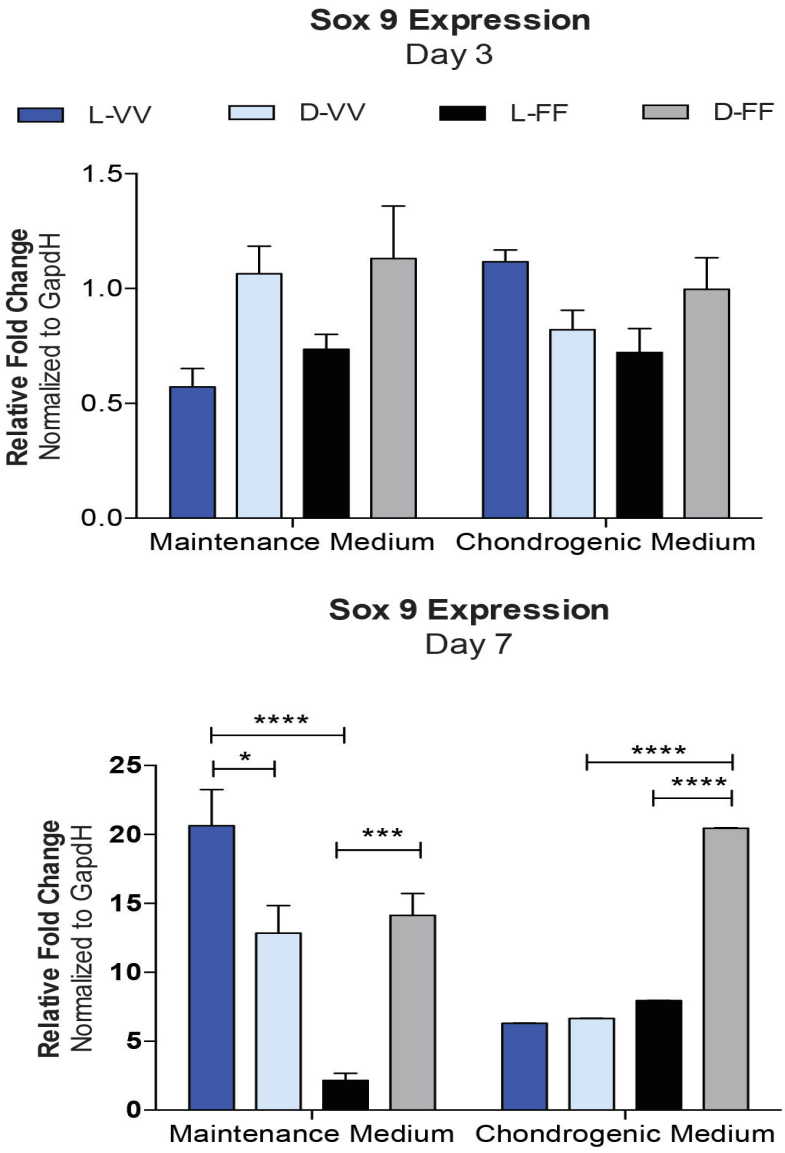


Figure 4. 36 Chondrogenic differentiation analyses by qRT-PCR on day 3 and day 7 of MSC cultures on peptide nanofibers. Expression of Sox 9 was quantified on day 3 (not significant by two-way ANOVA) and day 7 (*p<0.05, ***p<0.001, ****p<0.0001 by one-way ANOVA with Bonferroni's post-hoc test, mean ± s.e.m.).

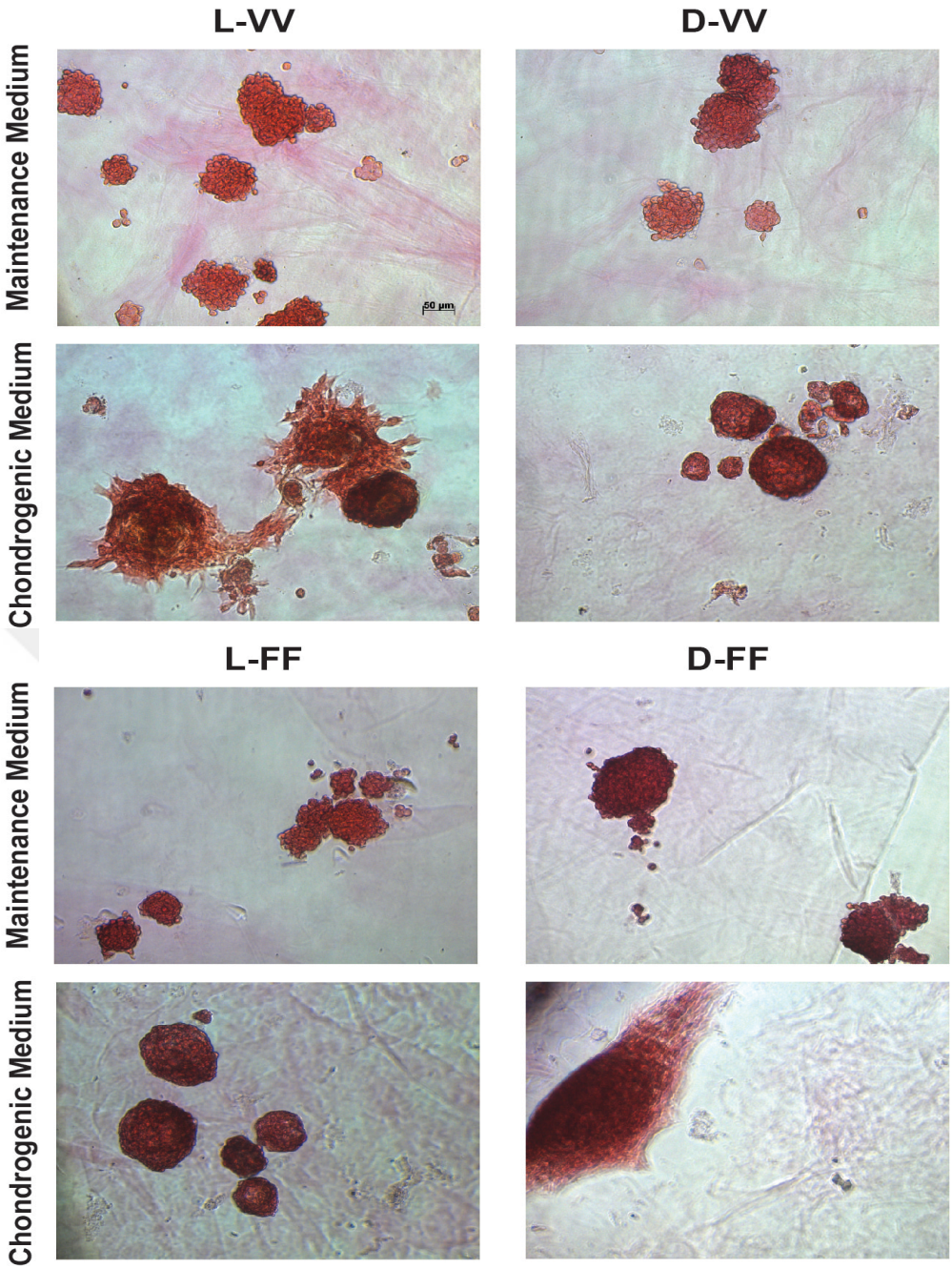


Figure 4. 37 Safranin-O staining of MSCs on peptide nanofibers in both maintenance medium and chondrogenic medium, which stained the sulfated glycosaminoglycans, that are found mainly in cartilage tissue, as an indicator for chondrogenesis potential of MSCs, scale bar = 50 μm.

4.4.5 Scaffold-mediated structural and chiral regulation of mechanotransduction

Since both twisted ribbon-like and cylindrical nanofiber systems presented the same amino acid sequences on their periphery, the differential bioactivity of these nanofibers was analyzed to investigate the effects of morphology and chirality on mechanotransduction of cells. Protein expression levels of key regulators for mechanotransduction-specific molecular pathways were investigated by Western blot analysis to further evaluate the effect of cell-material interactions of rMSCs on peptide nanofiber scaffolds. Cellular mechanotransduction is initiated by the binding of stretch receptors to nanofibers, which activates a protein cascade to convert mechanical information into biochemical signals [155]. Integrin β1 receptor is a key player in the early steps of this process and forms a heterodimeric complex with several integrin α receptors to bind fibrous proteins of the ECM and initiate the formation of focal adhesion complexes. Western blotting analysis of integrin β1 showed that its expression is upregulated on the L-forms of cylindrical (L-VV) and twisted ribbon-like nanofibers (L-FF) compared to the D-forms (Figure 4.38A). Between the two distinct morphologies, cylindrical nanofibers (VV-) significantly increased the expression of integrin β1 compared to twisted ribbon-like nanofibers. In addition, L-VV also had a greater capacity to induce integrin β1 expression in MSCs compared to D-VV, suggesting the importance of chirality for cell-ECM interactions.

While integrin receptors provide the initial interaction of peptide nanofibers with cells, the transduction of this information entails a complex signaling cascade (Figure 4.38B). The phosphorylation of ERK and MEK is an integral step in this process and

was investigated by Western blotting analysis. Significant differences were observed in the expression of MEK in MSCs on peptide nanofibers with different morphologies; in particular, rMSCs on L-form nanofibers invariably had higher MEK levels than their D-form counterparts, and cylindrical nanofibers (L-VV) had increased MEK expression compared to twisted ribbon (L-FF) nanofibers (Figure 4.37D). In addition, MSCs cultured on peptide nanofibers all expressed phosphorylated and activated ERK, but at different levels (Figure 4.37C; non-activated ERK was not detected in any of the groups and is not shown). The pERK expression patterns were similar to integrin β1, as L-forms of both VV- and FF-nanofibers had enhanced pERK expression, and cylindrical nanofibers enhanced phosphorylated ERK levels to a greater extent than twisted ribbon-like nanofibers.

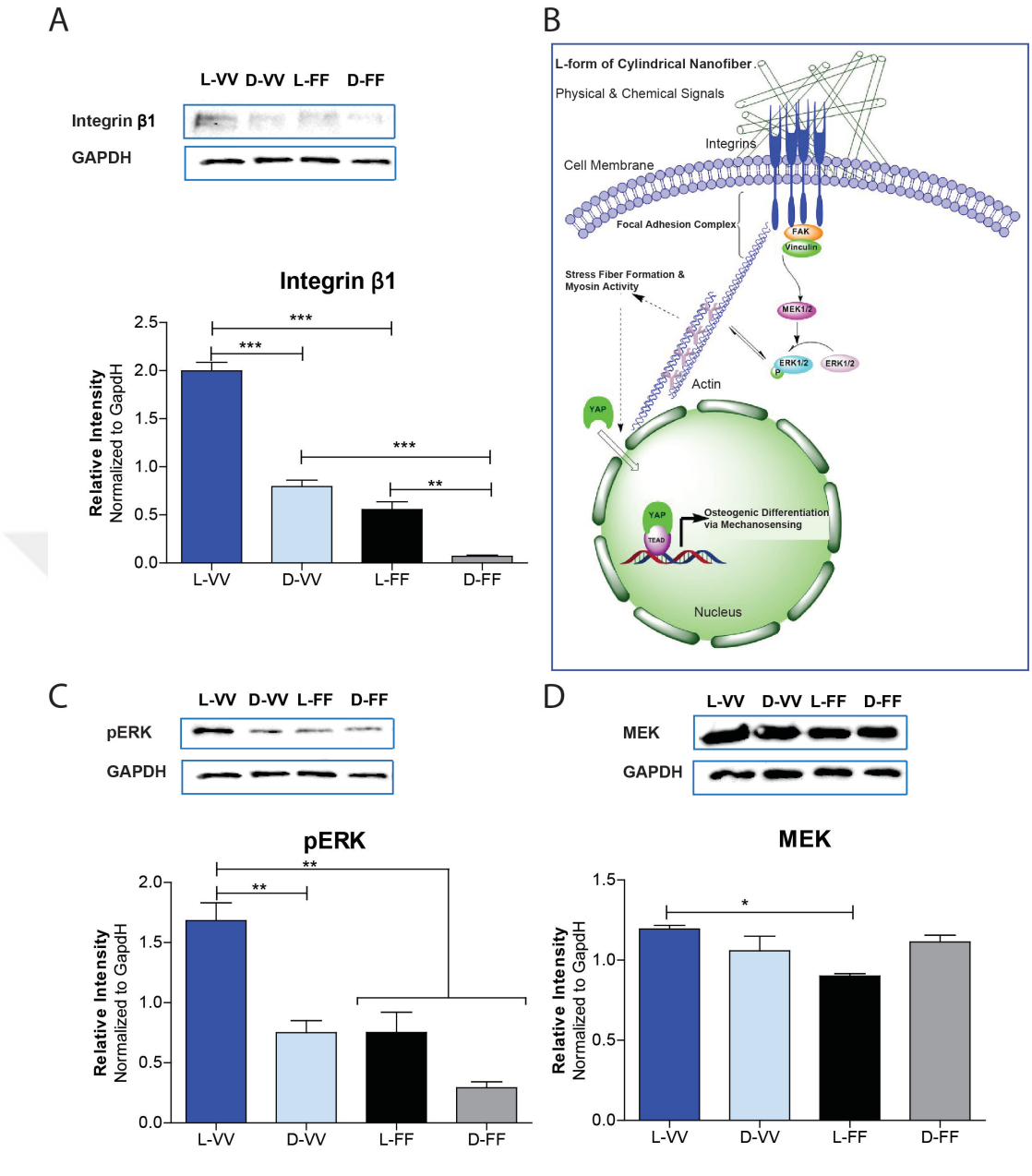


Figure 4. 38 Signaling pathway analyses of cellular mechanotransduction; (A) Integrin β1 expression on peptide nanofibers with different morphology and chirality, as analyzed by Western blotting (**p<0.01, ***p<0.001 by one-way ANOVA with Bonferroni's post-hoc test, mean ± s.e.m.); (B) Schematic representation of the signaling pathway activated in MSCs cultured on the L-form of cylindrical nanofibers; (C) pERK expression on peptide nanofibers, as analyzed by

Western blotting (**p<0.01 by one-way ANOVA with Bonferroni's post-hoc test, mean ± s.e.m.); (D) MEK expression on peptide nanofibers, as analyzed by Western blotting (*p<0.05 by one-way ANOVA with Bonferroni's post-hoc test, mean ± s.e.m.)

Vinculin expression was analyzed by both flow cytometry and confocal microscopy to determine the changes in focal adhesion point formation on peptide scaffolds (Figures 4.39 and 4.40). The localization of vinculin proteins is essential for the analysis of focal adhesion complexes, since vinculin plays an essential role in strengthening the adhesion complex by bearing force loads during the adhesion process [154, 156]. According to the confocal microscopy analysis, actin filaments were organized into well-defined stress fibers in cells on L-VV nanofibers (Figure 4.41). In addition, vinculin was strongly expressed on the protrusions of the cell membrane where focal adhesion complexes are formed. In contrast, on D-VV nanofibers, cells did not form stress fibers, vinculin proteins were observed in the cytosol, and the cells were not observed to develop long filopodia. Similarly, on twisted ribbon-like nanofibers (L-FF and D-FF), cells failed to develop stress fibers or form cellular protrusions; instead, they retained a spherical morphology with few adhesion points.

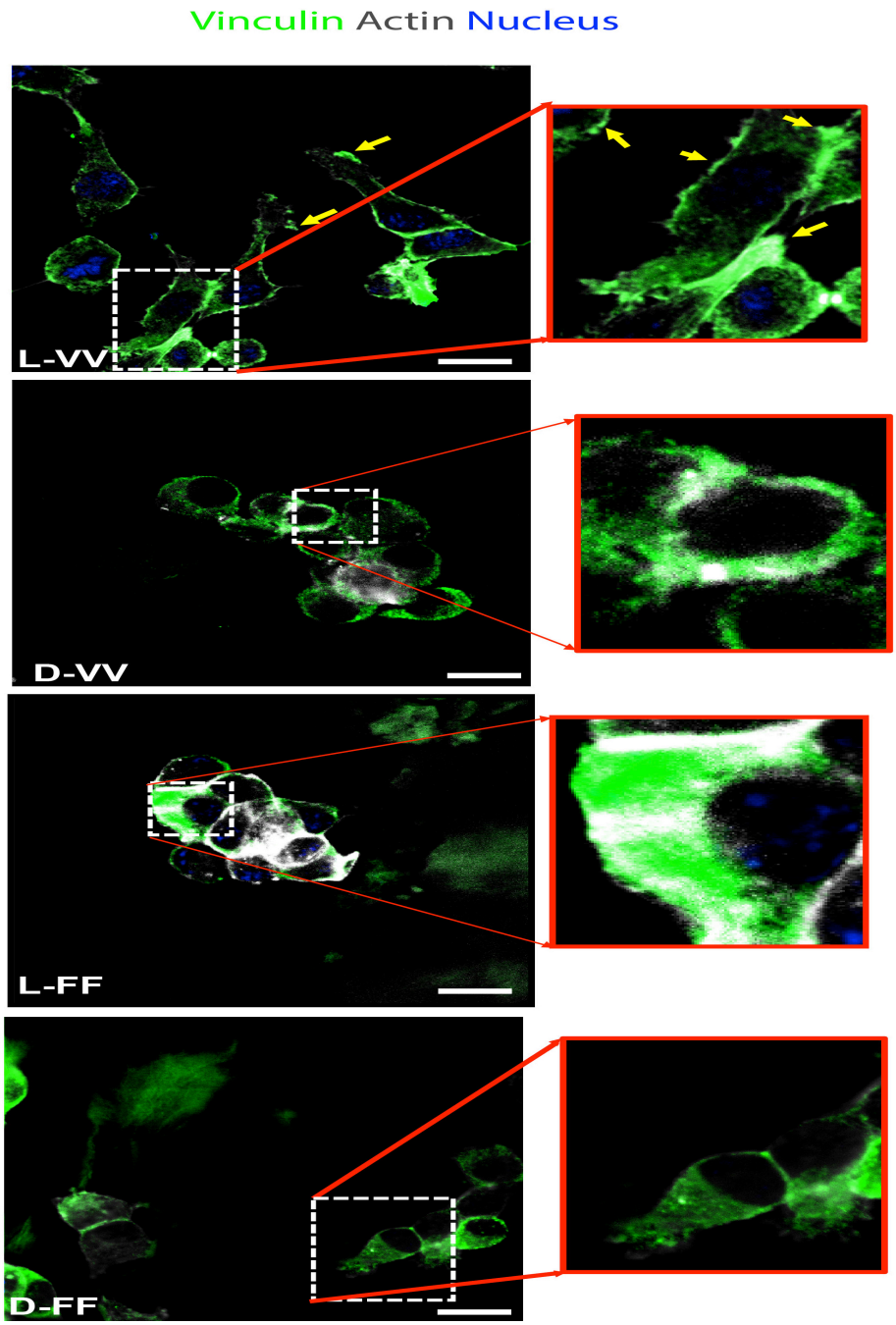


Figure 4. 39 Focal adhesion complex analyses of MSCs on peptide nanofibers with different morphology and chirality; Confocal images of MSCs on peptide nanofibers stained for the visualization of actin stress fibers (grey), vinculin (green), and nuclei (blue), scale bars = 20 μm.)

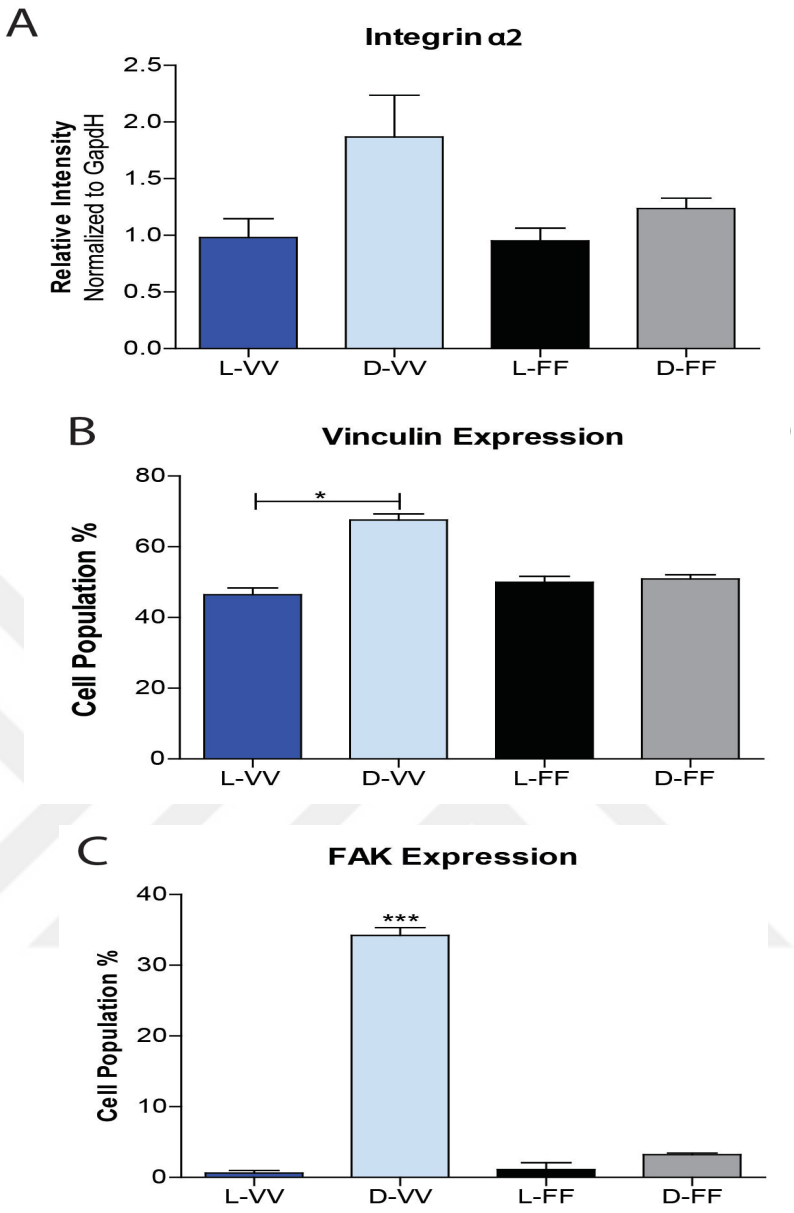


Figure 4. 40 Protein expression analyses of Integrin α2 and FAK. (A) Integrin α2 protein expression by Western blotting (B) Vinculin expression in MSCs on peptide nanofibers by flow cytometry analyses (C) FAK expression in MSCs on peptide nanofibers by flow cytometry analyses (*p<0.05, ***p<0.001 by one-way ANOVA with Bonferroni's post-hoc test, mean ± s.e.m.).

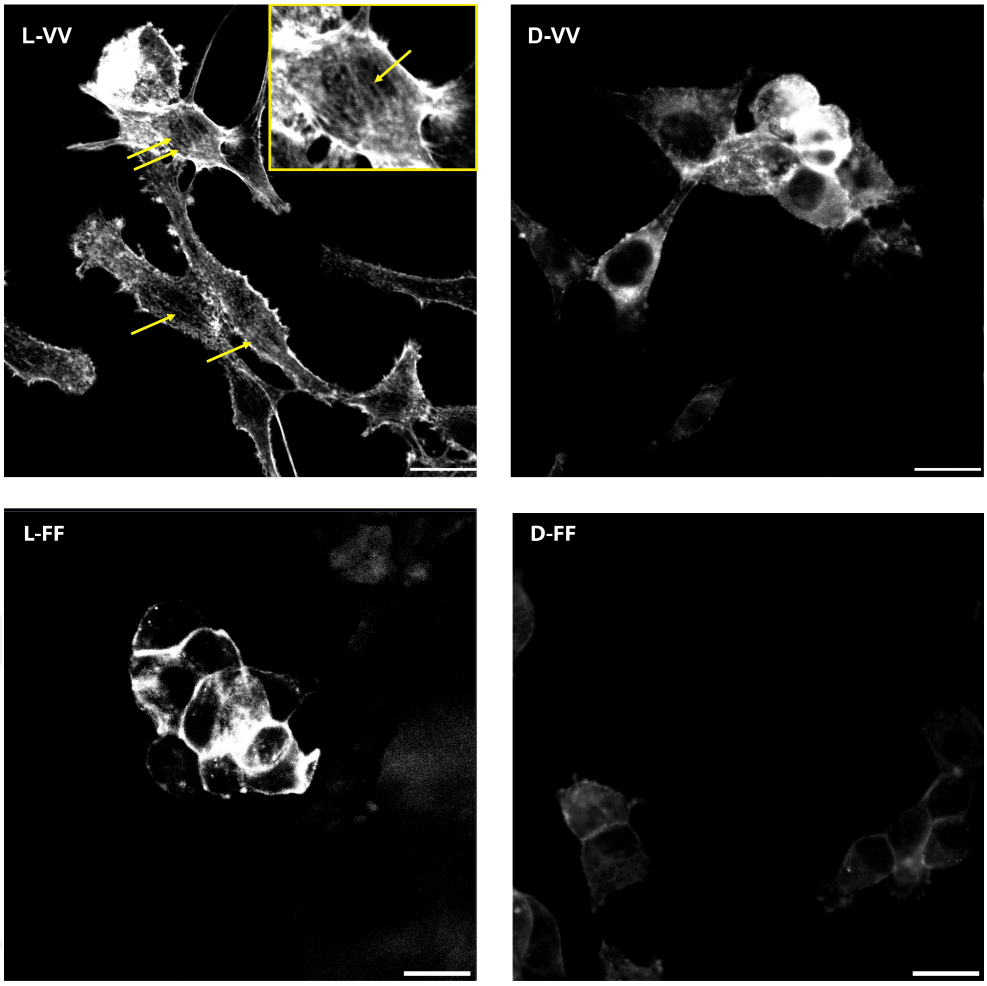


Figure 4. 41 Confocal images of MSCs on peptide nanofibers stained for the visualization of Actin filaments (grey), yellow arrows indicate the organized actin fibers and insert showed the zoomed cells with stress fibers, scale bars = 20 μm.

To demonstrate the molecular effect of peptide nanofiber morphology and chirality on cellular processes, the expression of YAP (Yes-associated protein, which is a transcriptional coactivator involved in organ growth) was assayed by immunocytochemical analyses. YAP is a transcription coactivator that regulates many cellular processes by shuttling between the nucleus and cytosol and interacting with transcription factors to inhibit or activate the transcription process [157]. The mechanical regulation of YAP activity involves the activation of F-actin

capping/severing proteins and the formation of stress fibers, which function as a mechanical rheostat in the mechanotransduction of cells [157, 158]. When YAP proteins are active, they localize into the nucleus and function as transcriptional co-activators; however, when they are inactive, they remain in the cytosol (Figure 4.42). According to confocal analyses, cells having nuclear YAP localization into all counted cells were quantified and it was found that significantly more cells cultured on L-VV had YAP proteins in their nuclei than other groups, suggesting that the activation of YAP occurs within 24 h of cell seeding on L-VV nanofibers (Figures 4.43 and 4.44). However, most of the MSCs cultured on the D-form of this cylindrical nanofiber (D-VV) had still inactive YAP proteins in their cytosol after 24 h incubation. Similarly, most of the cells on twisted ribbon-like nanofibers (both L- and D-from of FF- nanofibers) had inactive YAP proteins in their cytosols. Thus, the influence of supramolecular chirality on cells is decisive on even their gene-level regulation, and introduces an additional level of complexity to the structural and mechanical effects of nanofibers.

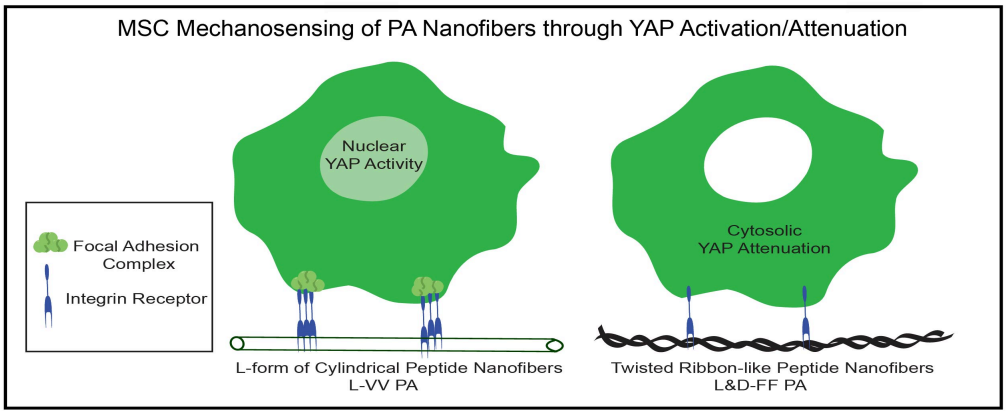


Figure 4. 42 Schematic representation of MSC response on different PA nanofibers through activation/attenuation of YAP protein into the nucleus/cytosol.

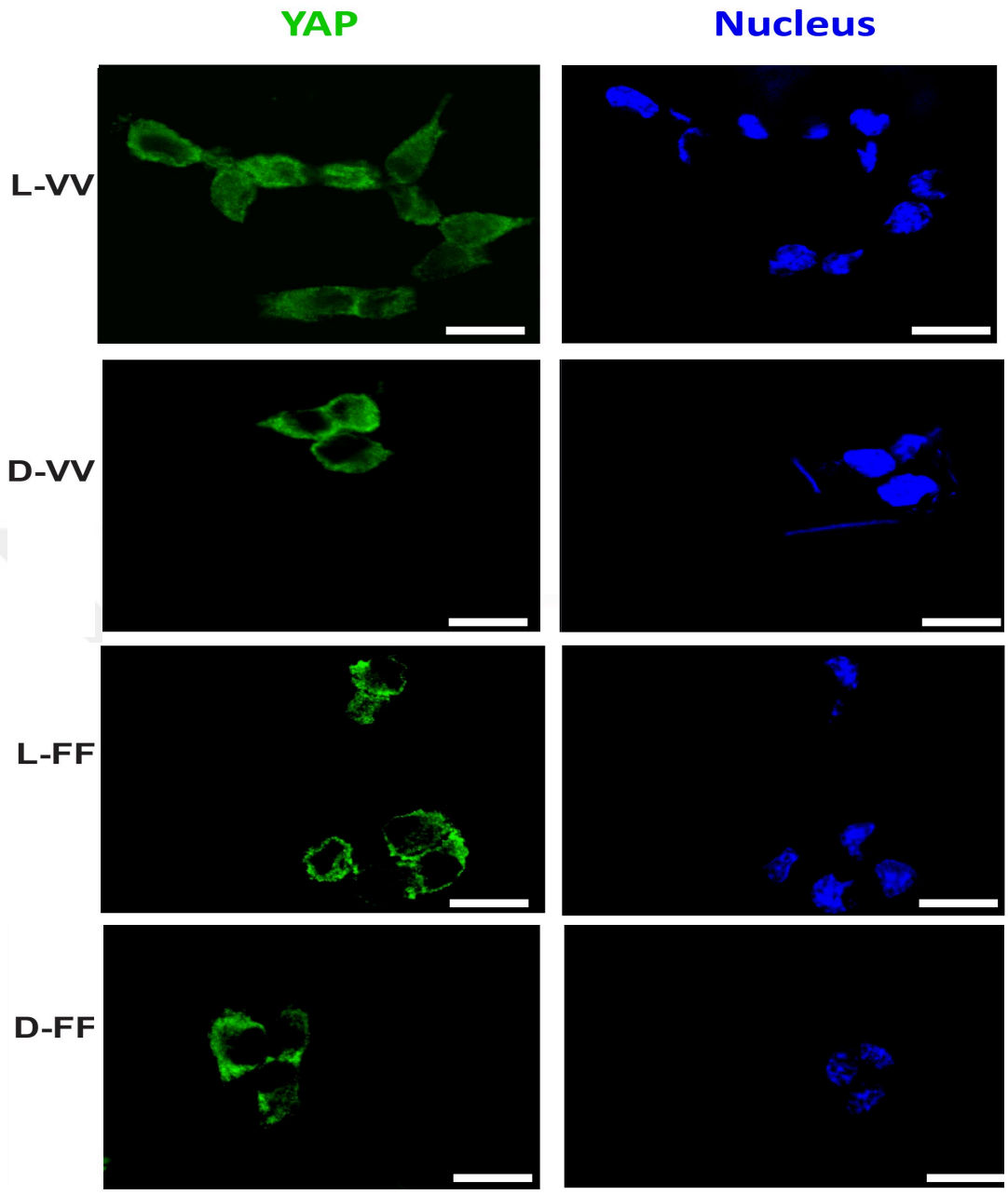


Figure 4. 43 Confocal microscope images of MSCs stained for the visualization of YAP proteins (green) and nuclei (blue), scale bars = 20 μm.

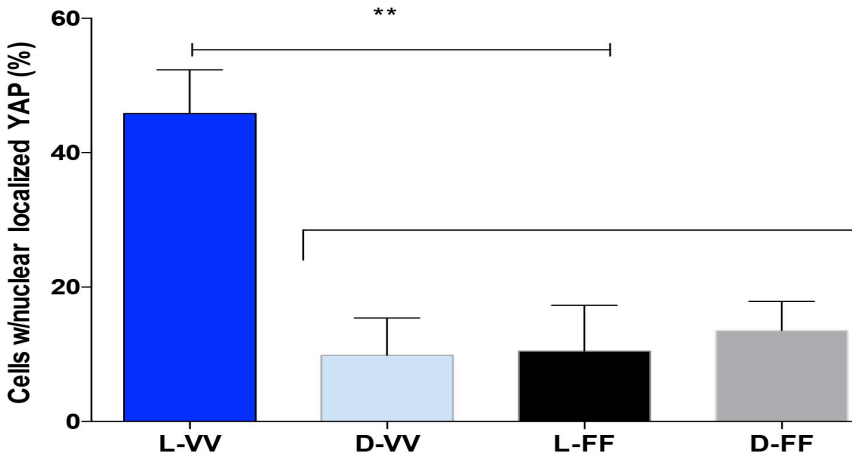


Figure 4. 44 Cells with nuclear YAP localization were quantified from the confocal images, and were shown as percent of cells among all counted cells (**p<0.01 by one-way ANOVA with Bonferroni's post-hoc test, mean ± s.e.m.).

4.5 Discussion

In addition to their successful use in medical applications, supramolecular nanostructures present a great opportunity to study cell-materials interactions by emulating the native ECM [1, 20]. Limitations in the in-depth analysis of cell-material interactions at the molecular level complicate potential investigations into the mechanical regulation of cells through morphological signals provided by the extracellular environment. Here we designed and synthesized a series of nanofiber scaffolds with well-defined structural properties, and used them to investigate the effects of fiber morphology and chirality on cellular behavior. Each peptide nanostructure was synthesized homogenously and showed no variance in physical and chemical features. L-VV and D-VV peptide nanofibers exhibited cylindrical morphology while L-FF and D-FF peptide nanofibers had a twisted ribbon-like morphology, as characterized by TEM analyses. Their chiral signatures were further analyzed and confirmed by CD measurements.

Peptides and proteins regulate their chirality through the self-assembly of their amino acid residues [159]. Therefore, different supramolecular systems with distinct structural features can be developed by altering assembly dynamics through the use of L- or D- enantiomers of amino acids [160]. In addition, self-assembly of nanomaterials can be reconfigured, and unique mechanical properties and complex topologies can be developed by controlling the interfacial tension of chiral materials [161]. Here we showed L- and D- forms of morphologically different nanofibers and observed that differences in chirality and morphology can result in the activation or repression of distinctive cellular processes. In rheology measurements, all peptide nanofiber networks displayed elastic solid-like behavior with high water content, and we did not detect any difference in elastic moduli of nanofibers between L- and D-forms. On the other hand, significant differences were observed in the elastic moduli of the L- and D- forms of peptide nanofibers through the AFM measurement of nanofibers and nanobundles (Figures 4.24 and 4.25). All nanofibers have megapascal-level elastic modulus values in aqueous environment, which emulates the conditions experienced by cells. Although the effect of stiffness on cellular behavior is well-documented in the literature, such studies generally focus on the mechanical properties of bulk gels [162]. In this study, AFM force map analysis provided deep insights for the elastic behavior of nanofibers, which were not detected by rheological analysis. When considering the concentration difference between two measurements, rheology provided bulk macro-scale measurement depending on the highly-concentrated nanofiber network properties, where molecular interactions could not be detected precisely. On the other hand, AFM provided nanoscale mechanical analyses, which is the scale at which cellular interactions

occur. In addition, it was previously indicated that, rather than bulk stiffness, mechanical feedback gathered from the interaction through collagen fibrils and integrin receptors has more pronounced effect on the stem cell behavior [163]. Similarly, we found that both morphology and chirality of nanofibers had profound effects on their mechanical stiffness: L-VV nanofibers formed more stiff fibrils than D-VV and FF-peptide nanofibers, which is relevant to their biological activity that we observed due to the well-known impact of stiffness on the initiation of osteochondral differentiation [164, 165]. As observed in the results of molecular dynamics simulations, D-VV had lower hydrogen bonding density than the L-form due to side-chain steric hindrance, which affects the rigidity of nanofiber formation. Similarly, twisted ribbon-like nanofibers had lower hydrogen bonding density according to molecular dynamics simulations, and the red shift in the CD spectrum of FF containing nanofibers is indicative of weaker hydrogen bond formation. L-VV, on the other hand, has a much higher H-bond density, which allows the rigid packing of structure and results in stiffer nanofiber formation, while lower H-bond density and weaker bond formation cause looser packing of PAs during self-assembly of nanofibers. The crucial role of the rigid backbone in viscoelastic properties was also shown in a previous study [166]. Hence, the nanofibers with different morphology and chirality were developed through strictly controlled modifications in the design of the peptide amphiphile molecules.

In this study, stem cells exhibited differential responses to different morphological and chiral signals. Osteogenesis and cell spreading were strongly stimulated on the L-form of cylindrical nanofibers (L-VV) compared to D-VV, L-FF and D-FF groups. This result is consistent with the previous reports, as a high spread area has been

reported to promote the osteogenic differentiation of MSCs [167]. The spreading of cells provides them with higher contractility through increased stress fiber formation, which increases their response to soluble factors such as autocrine/paracrine Wnt signals, as well as osteogenic media supplements [168]. In addition, Sox 9 expression was also detected in FF-groups as well. Sox-9 is indeed expressed during both osteogenic and chondrogenic differentiation at the earlier steps of mesenchymal differentiation; consequently, Sox-9 expression in the presence of osteogenic markers (*e.g.* Runx2) is considered to be an indicator of osteogenesis, while Sox-9 in the absence of osteogenic gene expression is a marker of chondrogenesis. Indeed, Akiyama *et.al.* showed that osteo-chondroprogenitor cells, as well as progenitors in a several tissues, are matured from Sox9-expressing precursors during mouse embryogenesis, and if Sox-9 is being inactivated, it results in prevention of mature osteoblast formation [169]. Hence, we also showed both L- and D- forms of cylindrical nanofibers increased the Sox-9 expression at mRNA level, where L-VV had more pronounced effect. On the other hand, twisted ribbon-like nanofibers increased Sox-9 expression in the absence of Runx2 and increased the chondrogenesis of MSCs. In fact, both L-and D- forms of the twisted ribbon nanofibers greatly reduced cellular proliferation as well as cellular spreading, which resulted in substantially lower osteogenesis. This restriction of cellular spreading was also seen for HUVECs and hFib cells cultured on the L-form of twisted ribbon-like nanofibers. Interestingly, the morphological effect on cellular spreading was more profoundly seen on the L-form of twisted ribbon-like nanofibers, which also indicates the importance of chiral signatures for the regulation of cellular behavior. For cellular adhesion, differences among nanofiber groups were only observed for

HUVECs, which is probably due to this cell line's inherent susceptibility towards physical changes in environment: endothelial cells are required to stretch, withstand strong shear forces, and prevent the development of atherosclerotic plaques and aberrant neovascularization in their native environment [170]. Therefore, the difference in the morphology of the nanofibers had a profound effect on the adhesion of HUVECs.

The minimal cellular proliferation and the spherical, non-adhering morphology of rMSCs on FF-PAs were conducive for chondrogenic differentiation, which was further enhanced when the cells were exposed to chondrogenic medium (Figure 4.36). The regulation of cell spreading is an essential requirement for optimal cellular differentiation, and high cell density have been reported to stimulate the chondrogenic differentiation of MSCs [167]; however, we observed a scaffold-driven chondrogenesis at a relatively lower cellular density on D-FF nanofibers. The combination of structural and morphological signals from the nanofiber surface and soluble chondrogenic factors from the differentiation medium further enhanced the chondrogenesis process on the D-form of ribbon-like nanofibers. Interestingly, while ribbon-like nanofibers significantly inhibited osteogenesis, they also strongly promoted chondrogenesis, especially in their D-form. As such, peptide scaffold morphology can be used to control the differentiation of MSCs into two closely related lineages. The spreading behavior of rMSCs on VV- and FF-nanofibers is also consistent with previous research [167, 171], as the less-spread cells on ribbon-like nanofibers differentiated into chondrogenic lineage, while the well-spread cells on cylindrical nanofibers committed to osteogenesis.

To better understand the underlying cellular mechanisms of these distinct responses, we further analyzed the specific components of the signaling pathways that are associated with the cellular adhesion, migration, and differentiation of MSCs. Kilian *et al.* previously showed that cell contractility, which is directly related to spreading of cells, activates the ERK/JUN pathway [168]. We also observed an increase in p-ERK expression in MSCs on L-VV nanofibers, and a significantly higher potential for osteogenesis through the activation of ERK/MAPK pathways even on the first day of culture [172, 173]. In addition, the MEK1-2 (MAP/ERK kinase 1-2) expressions of cells on L-VV nanofibers were significantly increased. ERK pathway activation is also strongly related to the increase of integrin β1 expression, and we found that both proteins were highly expressed in cells on L-VV nanofibers. Integrins interact with ECM fibrils and intracellular actin filaments through cytosolic linker proteins, which facilitate the mechanical connection of intracellular and extracellular environment of cells to raise specific cellular responses [154]. In addition, integrins act as transducers in the cellular sensing of physical forces that are exerted through the surrounding environment of cells [154, 155]. The L- form of cylindrical nanofibers increased integrin β1 expression and promoted the activation of ERK pathway, which stimulated the osteogenic differentiation of MSCs. This activation was also linked to the activation of F-actin, leading to the formation of well-organized stress fibers that were observed by confocal microscopy through actin staining. Interestingly, this effect of cylindrical nanofibers was much more advanced in the L-form compared to the D-form, which underlines the importance of the chiral signature of supramolecular nanofiber networks for the recognition by integrin receptors and the activation of signaling pathways.

For the analysis of focal adhesion complexes, vinculin expression was evaluated by using both confocal microscopy and flow cytometry (Figures 4.39 and 4.40). Vinculin is responsible for bearing the forces exerted on the focal adhesion complex, and its presence is essential for anchoring the complex to the surrounding actin network [154, 157]. According to confocal microscopy analyses, culturing on L-VV nanofibers significantly increased focal adhesion complex formation on the lamellipodial membranes of cells compared to other groups. In addition, flow cytometry results revealed a marked increase in the expression of vinculin in cells cultured on D-VV nanofibers, which may have enhanced the formation of focal adhesion complexes at later days of culture; albeit not as quickly as L-VV nanofibers. Interestingly, we also observed a similar increase in the expression of Integrin $\alpha 2$, which forms a heterodimer complex with Integrin $\beta 1$ and has been shown to bind to collagen and fibrinogen fibrils in ECM [155] (Figure 4.40A). This result further supported the hypothesis that D-VV nanofibers increased the expression of fibrillar protein-binding integrins, which can be later recruited for the formation of focal adhesion complexes, but not as quickly as on L-VV nanofibers. In addition, an increase in FAK protein expression was observed in most of the cells on D-VV nanofibers, at a level that was significantly higher than other peptide nanofibers (Figure 4.40C). Overall, these findings all indicate that culturing on D-VV nanofibers caused a delayed response in the formation of focal adhesion complexes when compared to L-VV nanofibers. While the spreading areas of L-VV and D-VV groups are similar, long-term adhesive forces have been shown to influence cellular behavior to a greater extent than spreading, suggesting that mechanotransduction may be more prominent on L-VV (as evidenced by higher

YAP nuclearization and osteogenic differentiation) despite comparable cell areas. In addition, while vinculin and FAK expression were higher on D-VV nanofibers, vinculin in this group was confined to the cytoplasm while focal adhesions were fewer in number compared to L-VV (Figures 4.39 and Figure 4.40). Consequently, we believe that D-VV shows an effect that is similar to but less pronounced than L-VV, such that the cells are able to spread but do not establish strong connections with the substrate. The higher expressions of integrin α2, FAK and vinculin may be a result of the fact that cells on D-VV are at a stage where focal adhesion complexes were in the process of being established, while the mature connections formed on L-VV are maintained by comparatively lower expressions of focal adhesion point-related proteins [174]. As a functional demonstration of this effect, cells spreaded more on D-VV after 3 days of incubation than 1 day incubation (Figure 4.27).

The twisted ribbon-like nanofibers limited the spreading of MSCs, decreased focal adhesion points and actin fibers, and deactivated the ERK pathway through diminished Integrin β1 expression. Matrix-induced cell rounding has previously been reported to correspond directly to decreases in focal adhesion and ERK pathway activation [163], which is caused by alterations in the mechanical feedback that occurs between collagen tethers and anchoring proteins on the cell membrane. As such, the suppression of integrin ligation in the twisted ribbon-like nanofibers appears to limit the adhesion of rMSCs resulting in insufficient mechanical feedback and limited ERK/MAPK pathway signaling. Although osteogenesis was not observed on FF containing nanofibers, chondrogenesis was significantly promoted on these scaffolds (especially on the D-FF form), which is an interesting result that

warrants further characterization and may be utilized for the development of smart biomaterial platforms for cartilage tissue engineering.

The effect of mechanical cues from the extracellular environment was also reflected on the gene expression profiles of rMSCs for the previously mentioned cellular signaling pathways. We observed that the cytosolic/nuclear localization of YAP protein was altered in cells grown on supramolecular peptide nanofibers. YAP/TAZ is a pair of transcriptional co-activators that play critical roles in organ growth and have been shown to be essential in the mechanotransduction of cells through their activity as nuclear sensors of stiffness [157, 175]. In particular, extracellular mechanical signals resulting from substrate effects or excessive cell growth trigger the organization of F-actin and enhance the nuclear localization of YAP [175]. Similarly, we found that MSCs on L-form cylindrical nanofibers (L-VV) had stronger integrin β1 expression, activated ERK signaling, and nuclear YAP activity compared to other groups. In contrast, cells on twisted ribbon-like nanofibers had low proliferation, confined cellular spreading and less focal adhesion, which resulted in the cytoplasmic retention of YAP. Even though the D-form of cylindrical nanofibers (D-VV) had a similar bulk morphology to the L-form, cells on the L-form had higher nuclear YAP activity compared to the D-form, suggesting that different chiral signals result in different routes of mechanotransduction in cells. The correlation between the decrease in proliferation and YAP activity also agrees with recent studies on the regulation of YAP/TAZ nuclear activity and proliferation by N-cadherin and RGD-incorporated hydrogels [158].

4.6 Conclusion

In summary, we showed that mechanosensitive pathways are selectively activated in stem cells depending on the morphology and chirality of the peptide nanofibers in the microenvironment. The mechanosensation and transduction controlled the activity of the YAP/TAZ complex, which relays the effects of the microenvironment to inside of the cells through integrin β1 receptor binding and subsequent cytosolic protein activations in the ERK pathway, ultimately results in the nuclear localization of YAP in response to L amino acid containing cylindrical nanofibers. However, this response was modulated not only by mechanical signaling, but also by the chemical signatures of the nanofibers and their chiral features. Morphology of the nanofibers was primarily responsible for initiating the cellular responses, but had synergistic effects with chiral signals. L-enantiomers found in natural proteins were observed to exhibit an increased effect on cell responses when introduced on cylindrical nanofibers; enhancing their capacity for promoting osteogenic differentiation even without incorporation of a bioactive epitope. D-enantiomers, on the other hand, had a pronounced effect on chondrogenesis when introduced in ribbon-like nanofibers. Overall, these results show that the morphology and chirality of the nanofibers can be exploited for selective differentiation of stem cells for regenerative medicine applications. In addition, it is interesting to note that the fundamental differences in hydrogen bond formation between peptide enantiomers may have played an important role during the early evolution of proteins, potentially accounting for the fundamental chiral asymmetry that exists in all known life.

Chapter 5. Conclusion and Future Prospects

Nanobiotechnology pave the way for the development of novel biomaterials with strictly controlled physical, chemical, and biological characteristics for regenerative medicine applications. In addition, nanobiotechnology research provides new opportunities for learning the pathophysiology of many diseases by enabling to study in-depth mechanisms of biological machinery. Self-assembling peptide nanofibers, in this respect, are versatile tools for generation of biomimetic materials having superior features similar to native tissue environment to induce tissue regeneration as therapeutic agents and to study biological machinery at cellular and organismal level. Peptide nanofibers, hence, can function cooperatively to achieve the required harmony of flexibility, strength, structural integrity and complexity of the native extracellular tissue through their fibrous organization and proper composition. Their superior features such as biocompatible and biodegradable nature, enable to regulate cellular behaviour and repair of damaged tissue both *in vitro* and *in vivo*. In this thesis, we proposed novel design strategies to develop peptide nanofiber scaffolds for stem cell differentiation and cartilage tissue regeneration.

GAG-mimetic peptide nanofiber gel as a 3D platform was used to investigate how cell lineage commitment is altered by external factors in a system that closely mimics the structure and function of native ECM components without influence of externally administered growth factors. Specific culture medium components were found to have synergistic effects with the GAG-mimetic nanofiber gel to regulate the differentiation of MSCs into osteogenic and chondrogenic lineages. In particular,

regulation of FBS concentrations in the culture medium modulated the osteogenic and chondrogenic differentiation of stem cells in tandem with the effects of the 3D peptide nanofiber network. Therefore, MSC differentiation can be specifically controlled by the combined influence of growth medium components and a 3D peptide nanofiber environment. This versatile GAG mimetic scaffold can be combined with optimum cell culture conditions, which present a suitable microenviroment for direction of the differentiation of stem cells into specific lineages with high efficiency. After the initial induction of cells into pre-osteogenic or pre-chondrogenic stages by these peptide nanofiber scaffolds, committed cells can also be selected (*e.g.* by using florescence activated cell sorting-FACS) for further clinical applications.

We also developed a hybrid peptide nanofiber-hyaluronic acid membrane and investigated its therapeutic effect in an *in vivo* osteoarthritis model. Hybrid nanofibers generated micro-scale three-dimensional networks that are mechanically stable in aqueous media and present bioactive signals for the activation of chondrocyte proliferation and cartilage regeneration. The protective and healing capacity of these membranes were investigated *in vivo* using early-stage and late-stage rat osteoarthritis models. Hybrid nanofiber membrane was found to have superior therapeutic effect than the commercially available Hyalgan® and Synvisc® gels at a lower concentration and presents a facile and feasible alternative treatment method for osteoarthritis.

In the last work, we demonstrated that peptide nanofibers with strictly controlled morphology and chirality have different effects on the cellular fate at the molecular and cellular levels. Through modulation of the physical and chemical cues provided

by the peptide nanofiber materials, cellular responses including the spreading and differentiation of stem cells can be controlled. The L- form of cylindrical nanofibers (L-VV) produced a greater mechanical feedback and promoted cellular spreading through increased interaction with the integrin β1 receptor, which resulted in the activation of the ERK/MAPK pathway, nuclear YAP localization, and increase in the osteogenic differentiation of stem cells. On the other hand, twisted ribbon-like nanofibers (L-FF and D-FF) decreased cellular spreading as well as ERK/MAPK pathway activity, resulting in the repression of nuclear YAP activity, which reduced the osteogenic differentiation of stem cells while favoring chondrogenesis in differentiation media. Our results demonstrate the importance of morphology and chirality of scaffold for cellular behavior, and show that the stem cells could be modulated even without the incorporation of biologically relevant epitopes.

In conclusion, we presented several regenerative medicine applications of peptide-based nanostructures. Despite the extensive advances and developments, many challenges yet remain to be solved. One of the major challenges is the understanding of mechanisms underlying cellular responses to further improve biomaterials to induce much more complex signaling pathways and to create more defined changes in cellular metabolism. Understanding of functional domains of tissue specific proteins and factors with the developments in proteomics may improve the strategies to generate stimuli responsive tissue specific scaffolds. In addition, improvement and optimization to enhance biocompatibility and biodegradability of these peptide-based biomaterials are required in their design, synthesis, and large-scale production. Furthermore, precise simulations for responses of these peptide systems in dynamic milieu of biological systems and control on their functions upon environmental

stimuli including chemical, mechanical, magnetic and electrical signals are very important. New characterization methods including TEM, AFM, spectroscopy, etc. and computational approaches recruiting mathematical algorithms for the precise simulations of the systems should be developed. Consequently, challenges of this highly active field of research provide also vast array of opportunities to work on for future progress and development of efficient biomaterials to overcome the current limitations.

Bibliography

[1] E. Arslan, I.C. Garip, G. Gulseren, A.B. Tekinay, M.O. Guler. (2014) Bioactive supramolecular peptide nanofibers for regenerative medicine. Advanced Healthcare Materials 3(9) 1357-1376.

[2] E. Arslan, S.U. Yaylacı, M.O. Guler, A.B. Tekinay. (2016) Therapeutic Nanomaterials for Cartilage Regeneration. Therapeutic Nanomaterials 59.

[3] C. Frantz, K.M. Stewart, V.M. Weaver. (2010) The extracellular matrix at a glance. Journal of Cell Science 123(24) 4195-4200.

[4] A. de Mel, A.M. Seifalian, M.A. Birchall. (2012) Orchestrating cell/material interactions for tissue engineering of surgical implants. Macromolecular Bioscience 12(8) 1010-1021.

[5] R.A. Gittens, T. McLachlan, R. Olivares-Navarrete, Y. Cai, S. Berner, R. Tannenbaum, Z. Schwartz, K.H. Sandhage, B.D. Boyan. (2011) The effects of combined micron-/submicron-scale surface roughness and nanoscale features on cell proliferation and differentiation. Biomaterials 32(13) 3395-3403.

[6] Z. Ma, M. Kotaki, R. Inai, S. Ramakrishna. (2005) Potential of nanofiber matrix as tissue-engineering scaffolds. Tissue Engineering 11(1-2) 101-109.

[7] A.D. Theocharis, S.S. Skandalis, C. Gialeli, N.K. Karamanos. (2016) Extracellular matrix structure. Advanced Drug Delivery Reviews 97 4-27.

[8] C. Chung, J.A. Burdick. (2008) Influence of three-dimensional hyaluronic acid microenvironments on mesenchymal stem cell chondrogenesis. Tissue Engineering Part A 15(2) 243-254.

[9] K. Benders, P. van Weeren, S. Badylak, D.l. Saris, W. Dhert, J. Malda. (2013) Extracellular matrix scaffolds for cartilage and bone regeneration. Trends in Biotechnology 31(3) 169-176.

[10] E.A. Makris, A.H. Gomoll, K.N. Malizos, J.C. Hu, K.A., Athanasiou. (2014) Repair and tissue engineering techniques for articular cartilage. Nature Reviews Rheumatology 11(1) 21-34.

[11] C. Zhao, A. Tan, G. Pastorin, H.K. Ho. (2013) Nanomaterial scaffolds for stem cell proliferation and differentiation in tissue engineering. Biotechnology Advances 31(5) 654-668.

[12] J.D. Hartgerink, E. Beniash, S.I. Stupp. (2002) Peptide-amphiphile nanofibers: a versatile scaffold for the preparation of self-assembling materials. Proceedings of the National Academy of Sciences 99(8) 5133-5138.

[13] B.V. Slaughter, S.S. Khurshid, O.Z. Fisher, A. Khademhosseini, N.A. Peppas. (2009) Hydrogels in regenerative medicine. Advanced Materials 21(32-33) 3307-3329.

[14] C.J. Bowerman, W. Liyanage, A.J. Federation, B.L. Nilsson. (2011) Tuning β-sheet peptide self-assembly and hydrogelation behavior by modification of sequence hydrophobicity and aromaticity. Biomacromolecules 12(7) 2735-2745.

[15] A. Mahler, M. Reches, M. Rechter, S. Cohen, E. Gazit, Rigid. (2006) Self-Assembled Hydrogel Composed of a Modified Aromatic Dipeptide. Advanced Materials 18(11) 1365-1370.

[16] S. Zhang, D.M. Marini, W. Hwang, S. Santoso. (2002) Design of nanostructured biological materials through self-assembly of peptides and proteins. Current Opinion in Chemical Biology 6(6) 865-871.

[17] S. Toksöz, M.O. Guler. (2009) Self-assembled peptidic nanostructures. Nano Today 4(6) 458-469.

[18] J.B. Matson, S.I. Stupp. (2012) Self-assembling peptide scaffolds for regenerative medicine. Chemical Communications 48(1) 26-33.

[19] J.B. Matson, R.H. Zha, S.I. Stupp. (2011) Peptide self-assembly for crafting functional biological materials. Current Opinion in Solid State and Materials Science 15(6) 225-235.

[20] M.J. Webber, J. Kessler, S.I. Stupp. (2010) Emerging peptide nanomedicine to regenerate tissues and organs. Journal of Internal Medicine 267(1) 71-88.

[21] H. Cui, M.J. Webber, S.I. Stupp. (2010) Self-assembly of peptide amphiphiles: From molecules to nanostructures to biomaterials. Peptide Science 94(1) 1-18.

[22] R.W. Sands, D.J. Mooney. (2007) Polymers to direct cell fate by controlling the microenvironment. Current Opinion in Biotechnology 18(5) 448-453.

[23] T.H. Barker. (2011) The role of ECM proteins and protein fragments in guiding cell behavior in regenerative medicine. Biomaterials 32(18) 4211-4214.

[24] L. Han, A. Grodzinsky, C. Ortiz. (2011) Nanomechanics of the Cartilage Extracellular Matrix. Annual Review of Materials Research 41133-168.

[25] L. Slomianka. (2009) Blue Histology - Skeletal Tissues - Cartilage. [ONLINE] Available at: http://www.lab.anhb.uwa.edu.au/mb140/CorePages/Cartilage/Cartil.htm#Hyaline. [Accessed 20 July 2017].

[26] H. Taipaleenmaki. (2010) Factors Regulating Chondrogenic Differentiation. (Doctoral Dissertation, University of Turku).

[27] D. Eyre. (2002) Collagen of articular cartilage. Arthritis Research 4(1) 30-35.

[28] Y. Lin, E. Luo, X. Chen, L. Liu, J. Qiao, Z. Yan, Z. Li, W. Tang, X. Zheng, W. Tian. (2005) Molecular and cellular characterization during chondrogenic differentiation of adipose tissue-derived stromal cells in vitro and cartilage formation in vivo. Journal of Cellular and Molecular Medicine 9(4) 929-939.

[29] Y. Lu, K. Parker, W. Wang. (2006) Effects of osmotic pressure in the extracellular matrix on tissue deformation. Philosophical Transactions of the Royal Society of London A: Mathematical, Physical and Engineering Sciences 364(1843) 1407-1422.

[30] V.C. Mow, S. Kuei, W.M. Lai, C.G. Armstrong. (1980) Biphasic creep and stress relaxation of articular cartilage in compression: theory and experiments. Journal of Biomechanical Engineering 102(1) 73-84.

[31] V.C. Mow, A. Ratcliffe, A.R. Poole. (1992) Cartilage and diarthrodial joints as paradigms for hierarchical materials and structures. Biomaterials 13(2) 67-97.

[32] A.J. Sophia Fox, A. Bedi, S.A. Rodeo. (2009) The basic science of articular cartilage: structure, composition, and function. Sports Health 1(6) 461-468.

[33] J. Clouet, C. Vinatier, C. Merceron, M. Pot-vaucel, Y. Maugars, P. Weiss, G. Grimandi, J. Guicheux. (2009) From osteoarthritis treatments to future regenerative therapies for cartilage. Drug Discovery Today 14(19-20) 913-25.

[34] S. Ströbel. (2007) Engineering of cartilage tissue constructs in a 3-dimensional perfusion bioreactor culture system under controlled oxygen tension. (Doctoral Dissertation, University of Basel).

[35] P.S. Eggli, W. Herrmann, E.B. Hunziker, R.K. Schenk. (1985) Matrix compartments in the growth plate of the proximal tibia of rats. The Anatomical Record 211(3) 246-257.

[36] D. Heinegård, T. Saxne. (2011) The role of the cartilage matrix in osteoarthritis. Nature Reviews Rheumatology 7(1) 50-56.

[37] V.C. Mow, X.E. Guo. (2002) Mechano-electrochemical properties of articular cartilage: their inhomogeneities and anisotropies. Annual Review of Biomedical Engineering 4(1) 175-209.

[38] A. Maroudas. (1968) Physicochemical properties of cartilage in the light of ion exchange theory. Biophysical Journal 8(5) 575-595.

[39] J. Buckwalter, H. Mankin, Instructional course lectures. (1997) The American Academy of Orthopaedic Surgeons-articular Cartilage. Part I: Tissue design and chondrocyte-matrix interactions. The Jornal of Bone and Joint Surgery 79(4) 600-11.

[40] V.M. Dejica, J.S. Mort, S. Laverty, M.D. Percival, J. Antoniou, D.J. Zukor, A.R. Poole. (1997) Cleavage of type II collagen by cathepsin K in human osteoarthritic cartilage. The American Journal of Pathology 173(1) 161-169.

[41] J.F. Woessner. (1991) Matrix metalloproteinases and their inhibitors in connective tissue remodeling. The FASEB Journal 5(8) 2145-2154.

[42] J.A. Buckwalter. (1995) Aging and degeneration of the human intervertebral disc. Spine 20(11) 1307-1314.

[43] J.A. Buckwalter, H.J. Mankin, A.J. Grodzinsky. (2005) Articular cartilage and osteoarthritis. Instructional Course Lectures-American Academy of Orthopaedic Surgeons 54 465.

[44] J. Clouet, C. Vinatier, C. Merceron, M. Pot-vaucel, Y. Maugars, P. Weiss, G.l. Grimandi, J.R.M. Guicheux. (2009) From osteoarthritis treatments to future regenerative therapies for cartilage. Drug Discovery Today 14(19-20) 913-925.

[45] D.T. Felson, Y. Zhang, M.T. Hannan, A. Naimark, B. Weissman, P. Aliabadi, D. Levy. (1997) Risk factors for incident radiographic knee osteoarthritis in the elderly: the Framingham Study. Arthritis Rheumatology 40.

[46] M. Grotle, K.B. Hagen, B. Natvig, F.A. Dahl, T.K. Kvien. (2008) Obesity and osteoarthritis in knee, hip and/or hand: An epidemiological study in the general population with 10 years follow-up. BMC Musculoskeletal Disorders 9(1471-2474) 1-5.

[47] C. Belcher, R. Yaqub, F. Fawthrop, M. Bayliss, M. Doherty. (1997) Synovial fluid chondroitin and keratan sulphate epitopes, glycosaminoglycans, and hyaluronan in arthritic and normal knees. Annals of the Rheumatic Diseases 56(5) 299-307.

[48] K.D. Brandt, G.N. Smith, L.S. Simon. (2000) Intraarticular injection of hyaluronan as treatment for knee osteoarthritis: what is the evidence? Arthritis & Rheumatism 43(6) 1192-1203.

[49] L.W. Moreland. (2003) Intra-articular hyaluronan (hyaluronic acid) and hylans for the treatment of osteoarthritis: mechanisms of action. Arthritis Research and Therapy 5(2) 54-67.

[50] D. Prakash, D. Learmonth. (2002) Natural progression of osteo-chondral defect in the femoral condyle. The Knee 9(1) 7-10.

[51] N.B. Kock, J.M. Smolders, J.L. Van Susante, P. Buma, A. Van Kampen, N. Verdonschot. (2008) A cadaveric analysis of contact stress restoration after osteochondral transplantation of a cylindrical cartilage defect, Knee Surgery, Sports Traumatology. Arthroscopy 16(5) 461-468.

[52] S.R. Goldring, M.B. Goldring. (2016) Changes in the osteochondral unit during osteoarthritis: structure, function and cartilage-bone crosstalk. Nature Reviews Rheumatology 12(11) 632-644.

[53] R.N. Shah, N.A. Shah, M.M.D.R. Lim, C. Hsieh, G. Nuber, S.I. Stupp. (2010) Supramolecular design of self-assembling nanofibers for cartilage regeneration, Proceedings of the National Academy of Sciences 107(8) 3293-3298.

[54] E. Arslan, M.O. Guler, A.B. Tekinay. (2016) Glycosaminoglycan-mimetic signals direct the osteo/chondrogenic differentiation of mesenchymal stem cells in a three-dimensional peptide nanofiber extracellular matrix mimetic environment. Biomacromolecules 17(4) 1280-1291.

[55] S. Ustun Yaylaci, M. Sardan Ekiz, E. Arslan, N. Can, E. Kilic, H. Ozkan, I. Orujalipoor, S. Ide, A.B. Tekinay, M.O. Guler. (2016) Supramolecular GAG-like Self-Assembled Glycopeptide Nanofibers Induce Chondrogenesis and Cartilage Regeneration. Biomacromolecules 17(2) 679-689.

[56] J. Kisiday, M. Jin, B. Kurz, H. Hung, C. Semino, S. Zhang, A. Grodzinsky. (2002) Self-assembling peptide hydrogel fosters chondrocyte extracellular matrix production and cell division: implications for cartilage tissue repair. Proceedings of the National Academy of Sciences of the United States of America 99(15) 9996-10001.

[57] P.W. Kopesky, E.J. Vanderploeg, J.D. Kisiday, D.D. Frisbie, J.D. Sandy, A.J. Grodzinsky. (2010) Controlled delivery of transforming growth factor β1 by self-assembling peptide hydrogels induces chondrogenesis of bone marrow stromal cells and modulates Smad2/3 signaling. Tissue Engineering Part A 17(1-2) 83-92.

[58] S.Q. Liu, Q. Tian, J.L. Hedrick, J.H.P. Hui, P.L.R. Ee, Y.Y. Yang. (2010) Biomimetic hydrogels for chondrogenic differentiation of human mesenchymal stem cells to neocartilage. Biomaterials 31(28) 7298-7307.

[59] C. Frantz, K.M. Stewart, V.M. Weaver. (2010) The extracellular matrix at a glance. Journal of Cell Science 123(24) 4195-4200.

[60] B.M. Baker, C.S. Chen. (2012) Deconstructing the third dimension,Äìhow 3D culture microenvironments alter cellular cues. Journal of Cell Science 125(13) 3015-3024.

[61] Knight, E., Murray, B., Carnachan, R., Przyborski, S. (2011). Alvetex®: polystyrene scaffold technology for routine three dimensional cell culture. 3D Cell Culture: Methods and Protocols 323-340.

[62] J. Kisiday, M. Jin, B. Kurz, H. Hung, C. Semino, S. Zhang, A. Grodzinsky. (2002) Self-assembling peptide hydrogel fosters chondrocyte extracellular matrix production and cell division: implications for cartilage tissue repair. Proceedings of the National Academy of Sciences 99(15) 9996-10001.

[63] N. Giuliani, G. Lisignoli, M. Magnani, C. Racano, M. Bolzoni, B. Dalla Palma, A. Spolzino, C. Manferdini, C. Abati, D. Toscani. (2013) New insights into osteogenic and chondrogenic differentiation of human bone marrow mesenchymal stem cells and their potential clinical applications for bone regeneration in pediatric orthopaedics. Stem Cells International 2013.

[64] S.K. Kang, I.S. Shin, M.S. Ko, J.Y. Jo, J.C. Ra. (2012) Journey of mesenchymal stem cells for homing: strategies to enhance efficacy and safety of stem cell therapy. Stem Cells International 2012.

[65] Kopesky, P. W., Vanderploeg, E. J., Sandy, J. S., Kurz, B., & Grodzinsky, A. J. (2010). Self-Assembling Peptide Hydrogels Modulate In Vitro Chondrogenesis of Bovine Bone Marrow Stromal Cells. Tissue Engineering. Part A, 16(2), 465–477. http://doi.org/10.1089/ten.tea.2009.0158

[66] L. Kyllönen, S. Haimi, B. Mannerström, H. Huhtala, K.M. Rajala, H. Skottman, G.K. Sándor, S. Miettinen. (2013) Effects of different serum conditions on osteogenic differentiation of human adipose stem cells in vitro. Stem Cell Research and Therapy 4(1) 17.

[67] A.M. Mackay, S.C. Beck, J.M. Murphy, F.P. Barry, C.O. Chichester, M.F. Pittenger. (1998) Chondrogenic differentiation of cultured human mesenchymal stem cells from marrow. Tissue Engineering 4(4) 415-428.

[68] K.L. Niece, J.D. Hartgerink, J.J. Donners, S.I. Stupp. (2003) Self-assembly combining two bioactive peptide-amphiphile molecules into nanofibers by electrostatic attraction. Journal of the American Chemical Society 125(24) 7146-7147.

[69] B.K. Hall, T. Miyake. (2000) All for one and one for all: condensations and the initiation of skeletal development. Bioessays 22(2) 138-147.

[70] Y. Xu, A.W. James, M.T. Longaker. (2008) Transforming Growth Factor-β Stimulates Chondrogenic Differentiation of Posterofrontal Suture-Derived Mesenchymal Cells In Vitro. Plastic and Reconstructive Surgery 122(6) 1649-1659.

[71] C. Phornphutkul, K.-Y. Wu, P.A. Gruppuso. (2006) The role of insulin in chondrogenesis. Molecular and Cellular Endocrinology 249(12) 107-115.

[72] H. Lodish, A. Berk, S.L. Zipursky, P. Matsudaira, D. Baltimore, J. Darnell. Molecular Cell Biology. 4th edition. New York: W. H. Freeman (2000) Section 17.3,

Overview of the Secretory Pathway. Available from: https://www .ncbi.nlm.nih.gov /books/NBK21471/

[73] C.H. Lee, A. Singla, Y. Lee. (2001) Biomedical applications of collagen. International Journal of Pharmaceutics 221(1) 1-22.

[74] Spinelli, F. J. (2008). Characterization of heparin-based hydrogel networks. (Doctoral Dissertation, University of Delaware).

[75] S. Lin, L. Gu. (2015) Influence of Crosslink Density and Stiffness on Mechanical Properties of Type I Collagen Gel. Materials 8(2) 551-560.

[76] J.A. Burdick, G.D. Prestwich. (2011) Hyaluronic acid hydrogels for biomedical applications. Advanced Materials 23(12) H41-H56.

[77] A.A. Worster, A.J. Nixon, B.D. Brower-Toland, J. Williams. (2000) Effect of transforming growth factor on chondrogenic differentiation of cultured equine mesenchymal stem cells. American Journal of Veterinary Research 61(9) 1003-1010.

[78] M. Lutolf, J. Hubbell. (2005) Synthetic biomaterials as instructive extracellular microenvironments for morphogenesis in tissue engineering. Nature Biotechnology 23(1) 47-55.

[79] H. Hosseinkhani, P.-D. Hong, D.-S. Yu. (2013) Self-assembled proteins and peptides for regenerative medicine. Chemical Reviews 113(7) 4837-4861.

[80] I. Zein, D.W. Hutmacher, K.C. Tan, S.H. Teoh. (2002) Fused deposition modeling of novel scaffold architectures for tissue engineering applications. Biomaterials 23(4) 1169-1185.

[81] A.S. Lin, T.H. Barrows, S.H. Cartmell, R.E. Guldberg. (2003) Microarchitectural and mechanical characterization of oriented porous polymer scaffolds. Biomaterials 24(3) 481-489.

[82] H. Oxley, P. Corkhill, J. Fitton, B. Tighe. (1993) Macroporous hydrogels for biomedical applications: methodology and morphology. Biomaterials 14(14) 1064-1072.

[83] T.V. Chirila, I.J. Constable, G.J. Crawford, S. Vijayasekaran, D.E. Thompson, Y.-C. Chen, W.A. Fletcher, B.J. Griffin. (1993) Poly (2-hydroxyethyl methacrylate) sponges as implant materials: in vivo and in vitro evaluation of cellular invasion. Biomaterials 14(1) 26-38.

[84] G. Chen, T. Ushida, T. Tateishi. (2001) Development of biodegradable porous scaffolds for tissue engineering. Materials Science and Engineering: C 17(1) 63-69.

[85] J. Taboas, R. Maddox, P. Krebsbach, S. Hollister. (2003) Indirect solid free form fabrication of local and global porous, biomimetic and composite 3D polymer-ceramic scaffolds. Biomaterials 24(1) 181-194.

[86] H. Hosseinkhani, P.-D. Hong, D.-S. Yu, Y.-R. Chen, D. Ickowicz, I.-Y. Farber, A.J. Domb. (2012) Development of 3D in vitro platform technology to engineer mesenchymal stem cells. International Journal of Nanomedicine 7 3035.

[87] L. Haines-Butterick, K. Rajagopal, M. Branco, D. Salick, R. Rughani, M. Pilarz, M.S. Lamm, D.J. Pochan, J.P. Schneider. (2007) Controlling hydrogelation kinetics by peptide design for three-dimensional encapsulation and injectable delivery of cells. Proceedings of the National Academy of Sciences 104(19) 7791-7796.

[88] H. Kalervo Väänänen. (2005) Mesenchymal stem cells. Annals of Medicine 37(7) 469-479.

[89] S. Kumar, D. Chanda, S. Ponnazhagan. (2008) Therapeutic potential of genetically modified mesenchymal stem cells. Gene Therapy 15(10) 711-715.

[90] G.E. Gold, S.B. Reeder, H. Yu, P. Kornaat, A.S. Shimakawa, J.W. Johnson, N.J. Pelc, C.F. Beaulieu, J.H. Brittain. (2006) Articular Cartilage of the Knee: Rapid Three-dimensional MR Imaging at 3.0 T with IDEAL Balanced Steady-State Free Precession—Initial Experience 1. Radiology 240(2) 546-551.

[91] J. Taipale, J. Keski-Oja. (1997) Growth factors in the extracellular matrix. The FASEB Journal 11(1) 51-59.

[92] D. Eyre. (2001) Articular cartilage and changes in arthritis: collagen of articular cartilage. Arthritis Research and Therapy 4(1) 30.

[93] S.W. Li, M. Takanosu, M. Arita, Y. Bao, Z.X. Ren, A. Maier, D.J. Prockop, R. Mayne. (2001) Targeted disruption of Col11a2 produces a mild cartilage phenotype in transgenic mice: comparison with the human disorder otospondylomegaepiphyseal dysplasia (OSMED). Developmental Dynamics 222(2) 141-152.

[94] E. Zamir, B. Geiger. (2001) Molecular complexity and dynamics of cell-matrix adhesions. Journal of Cell Science 114(20) 3583-3590.

[95] A. Gigout, M. Jolicoeur, M. Nelea, N. Raynal, R. Farndale, M.D. Buschmann. (2008) Chondrocyte aggregation in suspension culture is GFOGER-GPP-and β1 integrin-dependent. Journal of Biological Chemistry 283(46) 31522-31530.

[96] P.M. van der Kraan, M.-J. Goumans, E.B. Davidson, P. Ten Dijke. (2012) Age-dependent alteration of TGF-β signalling in osteoarthritis. Cell and Tissue Research 347(1) 257-265.

[97] V. Dasa, M. DeKoven, K. Sun, A. Scott, S. Lim. (2016) Clinical and cost outcomes from different hyaluronic acid treatments in patients with knee osteoarthritis: evidence from a US health plan claims database. Drugs in Context 5.

[98] V.M. Goldberg, L. Goldberg. (2010) Intra-articular hyaluronans: the treatment of knee pain in osteoarthritis. Journal of Pain Research 3 51.

[99] J.W.J. Bijlsma, F. Berenbaum, F.P.J.G. Lafeber. (2011) Osteoarthritis: an update with relevance for clinical practice. The Lancet 377(9783) 2115-2126.

[100] M.R. Baumgaertner, W.D. Cannon, J.M. Vittori, E.S. Schmidt, R.C. Maurer. (1990) Arthroscopic debridement of the arthritic knee. Clinical Orthopaedics and Related Research 253 197-202.

[101] W.D. Bugbee, F.R. Convery. (1999) Osteochondral allograft transplantation. Clinics in Sports Medicine 18(1) 67-75.

[102] T.J. Gill, P.C. McCulloch, S.S. Glasson, T. Blanchet, E.A. Morris. (2005) Chondral Defect Repair After the Microfracture Procedure A Nonhuman Primate Model. The American Journal of Sports Medicine 33(5) 680-685.

[103] E.B. Hunziker. (2002) Articular cartilage repair: basic science and clinical progress. A review of the current status and prospects. Osteoarthritis and Cartilage 10(6) 432-463.

[104] T. Minas, S. Nehrer. (1997) Current concepts in the treatment of articular cartilage defects. Orthopedics 20(6) 525-538.

[105] D.W. Hutmacher. (2000) Scaffolds in tissue engineering bone and cartilage. Biomaterials 21(24) 2529-2543.

[106] D. Carvajal, R. Bitton, J.R. Mantei, Y.S. Velichko, S.I. Stupp, K.R. Shull. (2010) Physical properties of hierarchically ordered self-assembled planar and spherical membranes. Soft Matter 6(8) 1816-1823.

[107] R.M. Capito, H.S. Azevedo, Y.S. Velichko, A. Mata, S.I. Stupp. (2008) Self-Assembly of Large and Small Molecules into Hierarchically Ordered Sacs and Membranes. Science 319(5871) 1812-1816.

[108] M. Gosset, F. Berenbaum, S. Thirion, C. Jacques. (2008) Primary culture and phenotyping of murine chondrocytes. Nature Protocols 3(8) 1253-1260.

[109] N. Gerwin, A. Bendele, S. Glasson, C. Carlson. (2010) The OARSI histopathology initiative–recommendations for histological assessments of osteoarthritis in the rat. Osteoarthritis and Cartilage 18 S24-S34.

[110] S. Glasson, T. Blanchet, E. Morris. (2007) The surgical destabilization of the medial meniscus (DMM) model of osteoarthritis in the 129/SvEv mouse. Osteoarthritis and Cartilage 15(9) 1061-1069.

[111] M. Ishikawa, K. Yoshioka, K. Urano, Y. Tanaka, T. Hatanaka, A. Nii. (2014) Biocompatibility of cross-linked hyaluronate (Gel-200) for the treatment of knee osteoarthritis. Osteoarthritis and Cartilage 22(11) 1902-1909.

[112] P.S. Burrage, K.S. Mix, C.E. Brinckerhoff. (2006) Matrix metalloproteinases: role in arthritis. Frontiers Bioscience 11(1) 529-543.

[113] M. Aurich, G.R. Squires, A. Reiner, J.A. Mollenhauer, K.E. Kuettner, A.R. Poole, A.A. Cole. (2005) Differential matrix degradation and turnover in early cartilage lesions of human knee and ankle joints. Arthritis and Rheumatology 52(1) 112-119.

[114] M.B. Goldring. (2000) The role of the chondrocyte in osteoarthritis. Arthritis and Rheumatology 43(9) 1916-1926.

[115] D.D. Allison, K.J. Grande-Allen. (2006) Hyaluronan: a powerful tissue engineering tool. Tissue Engineering 12(8) 2131-2140.

[116] F. Guilak, D.M. Cohen, B.T. Estes, J.M. Gimble, W. Liedtke, C.S. Chen. (2009) Control of stem cell fate by physical interactions with the extracellular matrix. Cell Stem Cell 5(1) 17-26.

[117] T. Koide. (2007) Designed triple-helical peptides as tools for collagen biochemistry and matrix engineering. Philosophical Transactions of the Royal Society of London B: Biological Sciences 362(1484) 1281-1291.

[118] C.G. Knight, L.F. Morton, A.R. Peachey, D.S. Tuckwell, R.W. Farndale, M.J. Barnes. (2000) The Collagen-binding A-domains of Integrins α1β1 and α2β1Recognize the Same Specific Amino Acid Sequence, GFOGER, in Native (Triple-helical) Collagens. Journal of Biological Chemistry 275(1) 35-40.

[119] B. Li, C. Moshfegh, Z. Lin, J. Albuschies, V. Vogel. (2013) Mesenchymal stem cells exploit extracellular matrix as mechanotransducer. Scientific Reports 3.

[120] L.D. Muiznieks, F.W. Keeley. (2013) Molecular assembly and mechanical properties of the extracellular matrix: A fibrous protein perspective. Biochimica et Biophysica Acta (BBA) - Molecular Basis of Disease 1832(7) 866-875.

[121] R.K. Das, O.F. Zouani, C. Labrugere, R. Oda, M.-C. Durrieu. (2013) Influence of nanohelical shape and periodicity on stem cell fate, ACS Nano 7(4) 3351-3361.

[122] A. Buxboim, I.L. Ivanovska, D.E. Discher. (2010) Matrix elasticity, cytoskeletal forces and physics of the nucleus: how deeply do cells ‘feel’outside and in? Journal of Cell Science 123(3) 297-308.

[123] G.F. Liu, D. Zhang, C.L. Feng. (2014) Control of Three-Dimensional Cell Adhesion by the Chirality of Nanofibers in Hydrogels. Angewandte Chemie International Edition 53(30) 7789-7793.

[124] T. Sun, D. Han, K. Rhemann, L. Chi, H. Fuchs. (2007) Stereospecific interaction between immune cells and chiral surfaces. Journal of the American Chemical Society 129(6) 1496-1497.

[125] M. Zhang, G. Qing, T. Sun. (2014) Chiral biointerface materials. Chemical Society Reviews 41(5) 1972-1984.

[126] T.A. Jakschitz, B.M. Rode. (2014) Chemical evolution from simple inorganic compounds to chiral peptides, Chemical Society Reviews 41(16) 5484-5489.

[127] E. Krause, M. Bienert, P. Schmieder, H. Wenschuh. (2000) The helix-destabilizing propensity scale of D-amino acids: the influence of side chain steric effects. Journal of the American Chemical Society 122(20) 4865-4870.

[128] G. Tansik, E. Kilic, M. Beter, B. Demiralp, G.K. Sendur, N. Can, H. Ozkan, E. Ergul, M.O. Guler, A.B. Tekinay. (2016) A glycosaminoglycan mimetic peptide nanofiber gel as an osteoinductive scaffold. Biomaterials Science 4(9) 1328-1339.

[129] H. Ceylan, S. Kocabey, A.B. Tekinay, M.O. Guler. (2012) Surface-adhesive and osteogenic self-assembled peptide nanofibers for bioinspired functionalization of titanium surfaces. Soft Matter 8(14) 3929-3937.

[130] G. Gulseren, I.C. Yasa, O. Ustahuseyin, E.D. Tekin, A.B. Tekinay, M.O. Guler. (2015) Alkaline phosphatase-mimicking peptide nanofibers for osteogenic differentiation. Biomacromolecules 16(7) 2198-2208.

[131] B. Senturk, M.O. Cubuk, M.C. Ozmen, B. Aydin, M.O. Guler, A.B. Tekinay. (2016) Inhibition of VEGF mediated corneal neovascularization by anti-angiogenic peptide nanofibers. Biomaterials 107 124-132.

[132] I.C. Yasa, N. Gunduz, M. Kilinc, M.O. Guler, A.B. Tekinay. (2015) Basal Lamina Mimetic Nanofibrous Peptide Networks for Skeletal Myogenesis. Scientific Reports 5 16460-16460.

[133] A.J. Markvoort, H.M. Ten Eikelder, P.A. Hilbers, T.F. de Greef, E. Meijer. (2011) Theoretical models of nonlinear effects in two-component cooperative supramolecular copolymerizations. Nature Communications 2 509.

[134] L. Zhang, X. Wang, T. Wang, M. Liu. (2015) Supramolecular Gels: Tuning Soft Nanostructures in Self-assembled Supramolecular Gels: From Morphology Control to Morphology-Dependent Functions. (Small 9-10/2015), Small 11(9-10) 1024-1024.

[135] R.K. Das, O.F. Zouani, C. Labrugère, R. Oda, M.-C. Durrieu. (2013) Influence of Nanohelical Shape and Periodicity on Stem Cell Fate. ACS Nano 7(4) 3351-3361.

[136] D.W. Green, J.M. Lee, E.J. Kim, D.J. Lee, H.S. Jung. (2016) Chiral Biomaterials: From Molecular Design to Regenerative Medicine. Advanced Materials Interfaces 3(6).

[137] I. Breßler, J. Kohlbrecher, A.F. Thünemann. (2015) SASfit: a tool for small-angle scattering data analysis using a library of analytical expressions. Journal of Applied Crystallography 48(5) 1587-1598.

[138] V. Castelletto, G. Cheng, C. Stain, C. Connon, I. Hamley. (2012) Self-assembly of a peptide amphiphile containing L-carnosine and its mixtures with a multilamellar vesicle forming lipid. Langmuir 28(31) 11599-11608.

[139] V. Castelletto, R.M. Gouveia, C.J. Connon, I.W. Hamley. (2013) New RGD-peptide amphiphile mixtures containing a negatively charged diluent. Faraday Discussions 166 381-397.

[140] G. Pabst, M. Rappolt, H. Amenitsch, P. Laggner. (2000) Structural information from multilamellar liposomes at full hydration: full q-range fitting with high quality x-ray data. Physical Review E 62(3) 4000.

[141] E.D. Tekin. (2015) Molecular dynamics simulations of self-assembled peptide amphiphile based cylindrical nanofibers. RSC Advances 5(82) 66582-66590.

[142] J.C. Phillips, R. Braun, W. Wang, J. Gumbart, E. Tajkhorshid, E. Villa, C. Chipot, R.D. Skeel, L. Kale, K. Schulten. (2005) Scalable molecular dynamics with NAMD. Journal of Computational Chemistry 26(16) 1781-1802.

[143] A.D. MacKerell Jr, D. Bashford, M. Bellott, R.L. Dunbrack Jr, J.D. Evanseck, M.J. Field, S. Fischer, J. Gao, H. Guo, S. Ha. (1998) All-atom empirical potential for molecular modeling and dynamics studies of proteins. The Journal of Physical Chemistry B 102(18) 3586-3616.

[144] U. Essmann, L. Perera, M.L. Berkowitz, T. Darden, H. Lee, L.G. Pedersen. (1995) A smooth particle mesh Ewald method. The Journal of Chemical Physics 103(19) 8577-8593.

[145] D.R. Roe, T.E. Cheatham III. (2013) PTRAJ and CPPTRAJ: software for processing and analysis of molecular dynamics trajectory data. Journal of Chemical Theory and Computation 9(7) 3084-3095.

[146] W. Humphrey, A. Dalke, K. Schulten. (1996) VMD: visual molecular dynamics. Journal of Molecular Graphics 14(1) 33-38.

[147] E.T. Pashuck, H. Cui, S.I. Stupp. (2010) Tuning supramolecular rigidity of peptide fibers through molecular structure. Journal of the American Chemical Society 132(17) 6041-6046.

[148] E.T. Pashuck, S.I. Stupp. (2010) Direct observation of morphological tranformation from twisted ribbons into helical ribbons. Journal of the American Chemical Society 132(26) 8819-8821.

[149] R. Garifullin, M.O. Guler. (2015) Supramolecular chirality in self-assembled peptide amphiphile nanostructures. Chemical Communications 51(62) 12470-12473.

[150] A. Micsonai, F. Wien, L. Kernya, Y.-H. Lee, Y. Goto, M. Réfrégiers, J. Kardos. (2015) Accurate secondary structure prediction and fold recognition for circular dichroism spectroscopy. Proceedings of the National Academy of Sciences 112(24) E3095-E3103.

[151] A.J. Adler, N.J. Greenfield, G.D. Fasman. (1973) Circular dichroism and optical rotatory dispersion of proteins and polypeptides. Methods in Enzymology 27 675-735.

[152] S. Hovmöller, T. Zhou, T. Ohlson. (2002) Conformations of amino acids in proteins. Acta Crystallographica Section D: Biological Crystallography 58(5) 768-776.

[153] Y.B. Park, Y.Y. Kim, S.K. Oh, S.G. Chung, S.-Y. Ku, S.H. Kim, Y.M. Choi, S.Y. Moon. (2008) Alterations of proliferative and differentiation potentials of human embryonic stem cells during long-term culture. Experimental & Molecular Medicine 40(1) 98-108.

[154] M.A. Schwartz. (2010) Integrins and extracellular matrix in mechanotransduction. Cold Spring Harbor Perspectives in Biology 2(12) a005066.

[155] A.B.J. Prowse, F. Chong, P.P. Gray, T.P. Munro. (2011) Stem cell integrins: Implications for ex-vivo culture and cellular therapies. Stem Cell Research 6(1) 1-12.

[156] S. Chanet, A.C. Martin. (2014) Mechanical force sensing in tissues. Progress in Molecular Biology and Translational Science 126 317.

[157] M. Aragona, T. Panciera, A. Manfrin, S. Giulitti, F. Michielin, N. Elvassore, S. Dupont, S. Piccolo. (2013) A mechanical checkpoint controls multicellular growth through YAP/TAZ regulation by actin-processing factors. Cell 154(5) 1047-1059.

[158] B.D. Cosgrove, K.L. Mui, T.P. Driscoll, S.R. Caliari, K.D. Mehta, R.K. Assoian, J.A. Burdick, R.L. Mauck. (2016) N-cadherin adhesive interactions modulate matrix mechanosensing and fate commitment of mesenchymal stem cells. Nature Materials 15(12) 1297-1306.

[159] Z. Luo, S. Zhang. (2012) Designer nanomaterials using chiral self-assembling peptide systems and their emerging benefit for society. Chemical Society Reviews 41(13) 4736-4754.

[160] A. Aggeli, I.A. Nyrkova, M. Bell, R. Harding, L. Carrick, T.C. McLeish, A.N. Semenov, N. Boden. (2001) Hierarchical self-assembly of chiral rod-like molecules as a model for peptide β-sheet tapes, ribbons, fibrils, and fibers. Proceedings of the National Academy of Sciences 98(21) 11857-11862.

[161] T. Gibaud, E. Barry, M.J. Zakhary, M. Henglin, A. Ward, Y. Yang, C. Berciu, R. Oldenbourg, M.F. Hagan, D. Nicastro. (2012) Reconfigurable self-assembly through chiral control of interfacial tension. Nature 481(7381) 348-351.

[162] A.J. Engler, S. Sen, H.L. Sweeney, D.E. Discher. (2006) Matrix elasticity directs stem cell lineage specification. Cell 126(4) 677-689.

[163] B. Trappmann, J.E. Gautrot, J.T. Connelly, D.G. Strange, Y. Li, M.L. Oyen, M.A.C. Stuart, H. Boehm, B. Li, V. Vogel. (2012) Extracellular-matrix tethering regulates stem-cell fate. Nature Materials 11(7) 642-649.

[164] J.S. Park, J.S. Chu, A.D. Tsou, R. Diop, Z. Tang, A. Wang, S. Li. (2011) The effect of matrix stiffness on the differentiation of mesenchymal stem cells in response to TGF-β. Biomaterials 32(16) 3921-3930.

[165] N.D. Evans, C. Minelli, E. Gentleman, V. LaPointe, S.N. Patankar, M. Kallivretaki, X. Chen, C.J. Roberts, M.M. Stevens. (2009) Substrate stiffness affects early differentiation events in embryonic stem cells. European Cells and Materials 18(1) e13.

[166] S. Mondal, M. Varenik, D.N. Bloch, Y. Atsmon-Raz, G. Jacoby, L. Adler-Abramovich, L.J. Shimon, R. Beck, Y. Miller, O. Regev. (2017) A minimal length rigid helical peptide motif allows rational design of modular surfactants. Nature Communications 8 14018.

[167] J. Eyckmans, G.L. Lin, C.S. Chen. (2012) Adhesive and mechanical regulation of mesenchymal stem cell differentiation in human bone marrow and periosteum-derived progenitor cells. Biology Open 1(11) 1058-1068.

[168] K.A. Kilian, B. Bugarija, B.T. Lahn, M. Mrksich. (2010) Geometric cues for directing the differentiation of mesenchymal stem cells. Proceedings of the National Academy of Sciences 107(11) 4872-4877.

[169] H. Akiyama, J.-E. Kim, K. Nakashima, G. Balmes, N. Iwai, J.M. Deng, Z. Zhang, J.F. Martin, R.R. Behringer, T. Nakamura. (2005) Osteo-chondroprogenitor cells are derived from Sox9 expressing precursors. Proceedings of the National Academy of Sciences of the United States of America 102(41) 14665-14670.

[170] H.-J. Park, Y. Zhang, S.P. Georgescu, K.L. Johnson, D. Kong, J.B. Galper. (2006) Human umbilical vein endothelial cells and human dermal microvascular

endothelial cells offer new insights into the relationship between lipid metabolism and angiogenesis. Stem Cell Reviews and Reports 2(2) 93-101.

[171] L. Gao, R. McBeath, C.S. Chen. (2010) Stem Cell Shape Regulates a Chondrogenic versus Myogenic Fate through Rac1 and N-cadherin. Stem Cells (Dayton, Ohio) 28(3) 564-572.

[172] R.K. Jaiswal, N. Jaiswal, S.P. Bruder, G. Mbalaviele, D.R. Marshak, M.F. Pittenger. (2000) Adult Human Mesenchymal Stem Cell Differentiation to the Osteogenic or Adipogenic Lineage Is Regulated by Mitogen-activated Protein Kinase. Journal of Biological Chemistry 275(13) 9645-9652.

[173] C.-S. Li, Z. Zheng, X.-X. Su, F. Wang, M. Ling, M. Zou, H. Zhou. (2016) Activation of the Extracellular Signal-Regulated Kinase Signaling Is Critical for Human Umbilical Cord Mesenchymal Stem Cell Osteogenic Differentiation. BioMed Research International 2016 10.

[174] D. Hanein, A.R. Horwitz. (2012) The structure of cell–matrix adhesions: the new frontier. Current Opinion in Cell Biology 24(1) 134-140.

[175] W. Chen, Y. Shao, X. Li, G. Zhao, J. Fu. (2014) Nanotopographical surfaces for stem cell fate control: Engineering mechanobiology from the bottom. Nano Today 9(6) 759-784.